MODELING DRAG FORCES AND VELOCITY FLUCTUATION STATISTICS IN WALL-BOUNDED FLOWS AT HIGH REYNOLDS NUMBERS

by

Xiang I. A. Yang

A dissertation submitted to The Johns Hopkins University in conformity with the requirements for the degree of Doctor of Philosophy.

Baltimore, Maryland

June, 2016

Abstract

In this two-part thesis, the long-standing problems of modeling drag forces over smooth and rough surfaces, as well as understanding and modeling velocity fluctuation statistics, are addressed. In part I, we focus on simulating and modelling rough wall boundary layers. We introduce two techniques to facilitate wall-modeled large-eddy simulations (LES) of turbulent boundary layers: an integral wall modelling technique and a rescaling-recycling inflow generation technique for LES of rough wall turbulent boundary layers. The integral wall model uses the von Karman Polhausen integral method and therefore is algebraic instead of differential. Because of its algebraic nature, the cost of the wall model is Reynolds number independent. Using the integral method, non-equilibrium effects, including flow acceleration, pressure gradient, etc. can be included by solving the vertically integrated momentum equation. The rough wall rescaling-recycling method is a generalization of the flat plate rescaling-recycling inflow generation technique. For the velocity fluctuations at a downstream plane to be recycled for an inflow condition, the downstream velocity signals need to be rescaled according to an inner and an outer length scale. For rough wall boundary layers,

the inner layer length scale is imposed by the roughness. To dynamically compute this length scale, we diagnose the dispersive stress and define the inner layer length scale to be the height at which the dispersive stress drops to 10% of its local maximum. Next, an analytical rough wall model that relates the rough wall topology to its aerodynamic properties is developed and tested by comparing the model predictions with existing experimental and computational measurements. In this analytical rough wall model, the velocity profile within the roughness layer (the layer occupied by the roughness) is modelled as follows: $U = \exp(a(z-h)/h)$, where U is the mean velocity, z is the wall normal coordinate, h is the roughness height and a is the attenuation coefficient; above the roughness, a logarithmic profile $U/u_\tau = 1/\kappa \log((z-d)/z_o)$ is used, where u_τ is the friction velocity, d is the zero-plane displacement, z_o is the effective roughness height and κ is the von Karman constants. Initially unknown parameters including d and z_o are determined using fundamental constraints based on velocity continuity, momentum conservation as well as a geometric sheltering model, in which the mutual sheltering among the roughness elements is explicitly accounted for. The model is tested for various rough surfaces, including aligned and staggered arranged cubes, cubes with bi-modal height distribution, cube arrays with Gaussian height distribution, etc. Generally good agreement between the model predictions and LES measurements is found. In part II of the thesis, new insights for modeling velocity fluctuations in the log region in wall bounded flows at high Reynolds number are presented. First we reformulate the Townsend attached eddy hypothe-

ABSTRACT

sis and introduce the Hierarchical-Random-Additive-Process formalism. Instead of resorting to a specifically-shaped typical wall eddy, the HRAP formalism represents the space-filling, self-similar, wall-attached eddies as identically, independently distributed random additives. This HRAP formalism is then used to probe the flow physics in the log region. Power-law scaling of the single-point moment generating function of the streamwise velocity fluctuations $\langle \exp(qu) \rangle$, where u is the streamwise velocity fluctuation normalized by friction velocity and q is an independent parameter, is predicted. Moreover, a scaling transition in the two-point moment generating function $\langle \exp(qu(x) - qu(x+r)) \rangle$, where x and $x+r$ are two points separated in the streamwise direction by a distance r, is predicted. Those predictions are confirmed using hot-wire measurements from boundary layers at $Re_\tau \sim O(10^4)$, where Re_τ is the friction Reynolds number, defined based on the boundary layer height and the friction velocity. The measurements are taken from the Melbourne High-Reynolds-Number-Boundary-Layer-Wind-Tunnel. Next, the HRAP model is used to identify new generalized logarithmic scalings that feature a scaling behavior $\log(\delta/r)$, where δ is the boundary layer thickness and r is, again, the two-point displacement in the streamwise direction. The same experimental measurements are used to provide empirical support for the new logarithmic laws.

Primary Reader: Professor Charles Meneveau

Secondary Reader: Professor Rajat Mittal, Tamer Zaki

ABSTRACT

Acknowledgments

Foremost, many thanks to my PhD advisor Dr. Charles Meneveau for his patience and intelligence in guiding me on turbulence research and my co-advisor Dr. Rajat Mittal for helpful discussion and generous help. Many results in this thesis came from fruitful collaborations encouraged by Dr. Meneveau with Dr. Ivan Marusic from the University of Melbourne, Dr. Mike Schultz from the Naval Academy, Dr. Stefano Leonardi from the University of Texas at Dallas, Dr. Luca Biferale from the University of Rome, Tor Vergata. Much work in this thesis could not have be done without my colleague Jasim Sadique. I acknowledge Dr. Dennice Gayme, Dr. Di Yang, Dr. Richard Stevens, Dr. Jung-Hee Seo, Dr. Kourosh Shoele, Dr. Chao Zhang, Shigan Chu, Ismail Hameduddin, Luis Martinez, Eshwan Ramudu, Joel Bretheim, Parastou Eslami, Aron Rips, Anirban Gosh, especially Dr. Vijay Vedula, Perry Johnson for their insights on turbulence research, as well as the fun they brought to my Ph.D.. For reading and correcting this thesis, I thank again Dr. Meneveau, Dr. Mittal and also Dr. Tamer Zaki.

I acknowledge Dr. A. Prosperetti for his exceptional courses on fluid dynamics and

mathematics, Dr. Meneveau for his lectures on turbulence and dimensional analysis, Dr. Mittal for his teaching on numerical methods and computational fluid dynamics, Dr. Tony Darymple for his course on GPU computing, and Dr. Peter Olson for the lectures on earth and planetary science. I acknowledge Office of Naval Research and National Science Foundation for financial support. Numerical simulations were conducted on the DoD, Xsede, HHPC, MARCC, Panoramix machines.

Last, my acknowledgement to my fiance Ting Zhou for her patience, thoughtfullness and understanding.

Dedication

To my parents, Xiaoping Yang, Lifen Yu

Contents

List of Tables

List of Figures

Chapter 1

Introduction

1.1 Overview

Wall-bounded turbulence has been one of the centerpieces of turbulence research for many decades. This rich phenomenon has been studied from various perspectives using tools including laboratory experiments, numerical simulations and theoretical modelling. For the study presented in this thesis, we focus on the following topics of wall-bounded flows at high Reynolds number, (i) drag prediction for rough wall turbulent boundary layers, (ii) modelling of velocity fluctuations for smooth-wall boundary layers. The data on rough wall boundary layers are mainly from numerical simulations, specifically large-eddy simulations (LES). LES simulates the energetic eddy motions and resorts to sub-grid stress (SGS) models for less-energetic fluid motions, hence is quite cost-efficient (although could be less accurate compared to a DNS or a

laboratory experiment). Despite the use of SGS models, wall-resolved LES, in which the near wall region is resolved almost as in DNS to avoid the use of wall models, can still be prohibitively expensive, especially for rough-wall LES. LES wall modelling is therefore a pacing field in turbulence modelling. An over-view of LES wall modelling, including the commonly used equilibrium modelling technique and zonal technique, is given in Sect 1.2.1. A compromise of the zonal models and the equilibrium models leads to the integral wall model that is discussed in this work. Besides the wall modelling, turbulent inflow generation is required, which can be quite non-trivial. To simulate fully developed boundary layers that have a constant outer length scale (e.g. channel flows, pipe flows), periodic condition in the streamwise direciton is usually sufficient to provide the inflow condition, but for spatially-growing turbulent boundary layers, techniques including concurrent library generation and non-concurrent library generation need to be used. An over-view of those inflow generation methods is given in Sect 1.2.2. In this thesis, one of the concurrent library generation method, the resaling-recycling method, is generalized for rough wall boundary layers. Having the near wall turbulence modelled using the integral wall model and the inflow generated using the rough-wall rescaling-recycling method, we use the in-house code Vicar3D to conduct LES of rough wall turbulence. The Reynolds number is high and we are interested in the fully rough regime. The main quantity of interest here is the drag force. Drag prediction has been one of the most studied topic in rough wall turbulence. Empirical relations and physics based models for rough wall drag prediction

are briefly reviewed in Sect 1.2.3. Here an analytical rough wall model is developed. The second topic of this thesis is describing and modelling of velocity fluctuation statistics in smooth-wall turbulent boundary layers. In the past decade, data of boundary layers at ever-high Reynolds number have become available. With the high Reynolds number datasets, scaling laws that were not possible to be confirmed (e.g. the logarithmic scaling of the variance of the streamwise velocity fluctuations) can be studied, moreover, new scalings are found by analyzing those datasets. An over-view of recent developments are given in Sect. 1.3.1. We present results of analysis of the data from the Melbourne High-Reynolds-Number-Boundary-Layer-Wind-Tunnel. We present empirical evidence of a power-law scaling of the single-point moment generating functions and logarithmic scalings featuring $\log(\delta/r)$. Those scalings and the ones that are already known can be understood based on the hierarchical random additive process (HRAP) model. This model is a reformulation of the Townsend attached eddy model. A brief overview of the attached model is given in Sect. 1.3.1. Further motivation and background of each study is given in sect. 1.2 and an outline of the thesis is given in sect. 1.4.

1.2 Background and Motivation, Part I

1.2.1 LES wall modelling

Near wall resolution requirements continue to be a significant challenge for Large-Eddy-Simulation (LES) of high Reynolds number flows. The number of required grid points to resolve the inner layer in LES scales with streamwise-distance based Reynolds number Re_x as $\sim Re_x^{2.4}$.[17,18] Full wall modeling, in which a much weaker dependence on Re_x can be achieved, is therefore a practical necessity to apply LES to high Reynolds number flows.

A variety of wall models have been proposed for LES. A review of the most important models can be found in Refs.18, 19. The two types of wall layer models used most frequently are the (i) equilibrium and (ii) zonal and/or hybrid models. The equilibrium wall models are based on the assumption of a constant stress layer to relate the wall stress to the velocity in the logarithmic (equilibrium) layer over surfaces. Some versions make use of the observed inclination of vortical structures.[20,21] The equilibrium model for rough surfaces is often used in geophysical applications owing to the very large Reynolds numbers and irregular surfaces prevalent in those applications.[22–26] For rough surfaces, the wall model also requires specification of a roughness scale y_0 which must be obtained empirically. We note that for the special case of scale-invariant surfaces, a dynamic approach has recently been proposed in which y_0 can be determined from the resolved, larger-scale features of the surface-flow

interactions.[27] However, this dynamic roughness model still requires the assumption of equilibrium conditions.

The equilibrium assumption excludes effects associated with unsteadiness, pressure gradients, low Reynolds numbers, etc., and therefore its general applicability is limited. On the other hand, so-called zonal and hybrid RANS/LES approaches can include such effects in the near-wall region. They are based on consideration of the full boundary layer equation, including unsteadiness, viscous and advective terms. Inside the near-wall region, the modeling is based on Reynolds averaging of the Navier-Stokes equations (RANS), since the three-dimensional motions, even those at the local integral scale of turbulence, become smaller than the computational grid. Thus, the entirety of the turbulence spectrum must be parameterized. The RANS equations are then integrated along a grid that can be very fine in the wall-normal direction but remains coarse (comparable to the resolution in the LES domain) in the directions parallel to the boundary. Many examples of such zonal models exist.[28,29] The one-dimensional turbulence model (ODT) can also be considered a zonal model.[30–32] The Detached Eddy Simulation method is a hybrid, combining LES away from the wall with RANS near the wall on the same grid, but typically using severe grid refinement in the wall-normal direction.[33] A number of these various methods are reviewed in Refs. 18, 19, 34. Several challenges associated with these models can be identified. (i) The first is cost, arising from the required numerical solution on a one-dimensional, wall normal grid with a resolution that requires grid points in the

viscous sub-layer. (ii) Many zonal methods require matching of different numerical integration techniques in the RANS and the LES regions. Thus the near wall zone requires a number of user-specific decisions to be made such as grid distribution and number of grid points in the RANS region. This leads to additional complexities and challenges in reproducibility of results. (iii) Also, there has not been much development of zonal or hybrid modeling of rough-wall boundary layers in which the RANS portion must represent flow over a rough rather than smooth surface. (iv) Finally, an important issue is that velocity fluctuations near the crossover region between RANS and LES tend to be excessively damped or are not generated at the correct rate, causing a deficit of turbulent fluctuations in the LES portion near the surface.[35] Remedies based on addition stochastic forcings have been proposed.[35] Recent insights about coupling of wall stress fluctuations with outer-layer fluctuations may be useful in this regard and this knowledge is beginning to be explored.[36,37]

We note that there have been several further efforts that aim to include near-wall physics in LES that do not fall in the equilibrium type, zonal or hybrid-type model classes. The approaches includes optimal control[38] and ideas from neural nets to relate wall stresses with velocities in the bulk of the flow.[39] Recently, another method used a dynamic slip boundary condition to incorporate Reynolds number effects.[40] They use a diffusive filter that reproduces some viscous (Reynolds number) effects with smooth transitions between several regimes. However, other near wall physics represented by the unsteady term, convective terms, pressure gradients, etc. are still

not incorporated explicitly and modeling effects of surface roughness with unresolved surface features remains a challenge.

1.2.2 Inflow generation

Direct Numerical as well as Large Eddy Simulations of spatially evolving turbulent boundary layers over rough surfaces remains an important topic.[41–43] Applications include flow over plant canopies,[44,45] urban boundary layers[46] and geophysical flows in general,[47,48] flows involved in heat transfer,[49] and aerodynamic applications.[50–52] It can be prohibitively expensive to begin a simulation from the laminar regime, trigger turbulence, and extend the simulation in the streamwise direction until reaching the region of interest. Unless one resolves this entire transitional process, numerical computation of a turbulent region of interest in the boundary layer requires the prescription of turbulent inflow boundary conditions. Prescription of turbulent flow at the inlet boundary remains a challenge, especially for boundary layers developing over rough surfaces.

In practice, the commonly used techniques for inflow generation can be categorized into synthesized turbulence methods and precursor simulation methods.[53] The synthesized turbulent methods construct turbulent fluctuations and superimpose the synthesized turbulent fluctuations on a prescribed mean flow. Inflow generation techniques that fall into this category include the Fourier methods,[54–56] the POD methods,[57–59] the digital filtering methods,[60–62] and the synthetic eddy method.[63] To use

these types of methods, the full velocity spatial/temporal correlations or wavenumber-frequency turbulence energy spectrum is required. Since typically Gaussian statistics must be assumed, a significant adjustment length is needed until physically realistic flow structures (e.g. elongated streaks) and non-Gaussian statistics are allowed to develop. The precursor simulation methods, on the other hand, do not require prior knowledge about the turbulence statistics. Methods that fall into this category require the generation of a 'library' of turbulence data which can be pre-generated,[64,65] or generated concurrently.[2,66,67] A particularly effective concurrent method uses rescaling and recycling of the outflow[2] as the inlet boundary condition. This rescale-recycling method[2] was first proposed for smooth-wall simulations, and then extended for simulations of boundary layers over surfaces with moderate roughness (the equivalent sand-grain roughness must be specified).[68] However, inflow generation for boundary layers developing over surfaces with large roughness elements that are resolved on the computational grid remains a challenge.

1.2.3 Rough wall modelling

The problem of predicting the friction drag exerted by turbulent flow on a surface based on knowledge about the surface geometry has received extensive and enduring attention. Efforts on this topic date back to the early experimental work in Ref 69 and 70. Since 1944 the Moody diagram that relates the friction drag with the equivalent sand-grain roughness height k_s[71] has been a most commonly employed engineering

tool. There have been many further efforts since then to correlate the surface topology with the hydrodynamic response through equivalent sandgrain roughness height, friction factor,[72] effective slope,[73,74] surface skewness factor,[75] and examinations of Reynolds number similarity for rough walls see e.g. Ref. 76. For reviews, see Ref. 75, 77.

Researchers working on modeling urban canopy flows have been interested in parameterizations of the hydrodynamic roughness length (z_o, note that at some places we also denote this quantity as y_0 since at places we use y as the wall-nomral coordinate), displacement height (d), and drag coefficient for the specific case of rectangular prism roughness elements due to the typically cubiform shapes of buildings. Part of the extensive efforts have been reviewed in Refs. 77, 78. For particular applications of various models for z_o and d see Refs. 79–81. Among the parameters expected to be the most important for z_o and d are the solidity λ_f (defined as the projected frontal area per unit lot area), the planar density λ_p (defined as the projected horizontal area per unit lot area), and the characteristic height h of individual roughness elements.[77] The morphometric models usually include explicit dependencies of, e.g. z_o, on these parameters determined through empirical approaches such as fitting with experimental or numerical data. Models that fall into this category include those introduced in Refs. 82–85. Calibrated for certain surface roughness and over a given range of λ_f, λ_p, such models can provide reasonably accurate predictions of z_0 and d for practical applications. Nevertheless, to a great extent they remain dependent upon much

empirical input. Thus the problem of relating hydrodynamic and geometrical roughness remains open since local flow conditions may depend on details of the roughness elements in a highly case-specific fashion.

In order to develop physics-based models for flows over surfaces with attached roughness elements, some detailed understanding of the averaged velocity profile within the roughness layer (defined here as the region between the surface and the top of roughness elements) must be developed. This is similar to the situation where knowledge about the logarithmic law has led to physically based drag laws for smooth boundary layers. One option is to examine the differential momentum equation, as done in differential urban canopy models e.g. Refs. 8, 9, 86, 87 that focus on predicting the horizontally $(x-y)$ and temporally averaged velocity profile inside and above the canopy using integration of the momentum differential equation. To obtain the mean velocity profile as function of height, the modeling task focuses on the Reynolds stress (that arises due to temporal averaging over turbulence), dispersive stress (that arises due to spatial averaging of mean velocity across spatial heterogeneities in the temporal mean velocity distribution) and the form drag (which arises due to the direct momentum extraction by the roughness elements interacting with the flow). The Reynolds stress is usually modeled with a Prandtl mixing-length eddy-viscosity model; the dispersive stress is commonly neglected; and the drag is typically modeled using a quadratic law for a body force associated with the form drag $F = C_d \rho U^2 \delta A_f / \delta V$, where ρ is the fluid density, C_d is the drag coefficient, U is a mean streamwise refer-

ence velocity, and δA_f is the projected frontal area within a volume δV. The mixing length (denoted as l_m) and the drag coefficient C_d need to be specified. With these models for stresses and the force, the spatially and temporally averaged streamwise momentum equation can be integrated in the wall normal direction to obtain the mean velocity profile.

To increase the accuracy of the predictions from such models, various empirical inputs have been employed by different authors. Examples include the approach in Ref.[9] requiring an attenuation factor to be specified a-priori as a function of solidity $\lambda_f = A_f/A_T$ (where A_f and A_T are the projected frontal and horizontal lot areas, respectively), while in Ref.,[8] the authors employ an empirical function to model the displacement height d. As mentioned before, it is quite established that solidity λ_f is the most important parameter characterizing the surface morphology and most currently available rough wall models are insensitive to more detailed characterizations of the roughness distribution (see reviews by Ref. 77, 78). While typically the wake interactions are not explicitly modeled, there have been some attempts (e.g. Refs. 42, 88) to model the mutual sheltering between roughness elements.

Thus, while significant progress has been achieved in roughness modeling over the past several years, shortcomings in the models reviewed above can be identified. Morphometric and urban canopy models depend significantly on empirical input such as ad-hoc specifications of the mixing length l_m on λ_f, height from the bottom surface, etc. Moreover, although the differential urban canopy models can make more detailed

predictions than the morphometric models, being differential instead of algebraic (e.g. Refs. 8,87), they are more costly to evaluate. This can be an obstacle when attempting to combine these models with numerical weather prediction codes. Lastly, mutual sheltering among roughness elements, while being a commonly accepted concept, lacks a clear operational definition and there is still no simple, yet accurate model that can include mutual sheltering in the context of a practical roughness model.

1.3 Backgroud and Motivation, Part II

1.3.1 The log layer in wall turbulence at high Reynolds number

An important feature of wall boundary layer flows is the logarithmic law for the mean velocity profile $U/u_\tau \equiv U^+ = \kappa^{-1}\ln(zu_\tau/\nu) + B$ valid in the inertial region, where z is the distance to the wall, u_τ is the friction velocity based on the wall-stress τ_w ($u_\tau = \sqrt{\tau_w/\rho}$, ρ is the fluid density), ν is the kinematic viscosity, κ is the von Kármán constant, and B is another constant (see results in Refs. 89, 90 for recent empirical evidence for logarithmic scaling of the mean velocity). Even if only approximately valid under realistic conditions, such a basic property of wall-bounded turbulent flows continues to provide predictions in many practical applications, and it helps to test models, calibrate parameters, and guide the development of theories.

Recently, a logarithmic behavior has also been observed in the inertial region for the variance of the fluctuations in the streamwise velocity component. Such behavior can be motivated by model predictions based on the 'attached eddy hypothesis' in Refs. 15, 91. There has been growing evidence[92,93] for a logarithmic behavior of the form $\langle {u^+}^2 \rangle = B_1 - A_1 \ln(z/\delta)$, where u^+ is the normalized stream-wise velocity fluctuation and δ is an outer length-scale. For developing boundary layers the outer scale is the boundary-layer thickness, while it is the radius for pipes, and the half-height for plane channels. Empirical data are mostly consistent with a value of $A_1 \approx 1.25$ (the Townsend-Perry constant), whereas B_1 is flow-dependent and thus not universal. The logarithmic structure extends to higher order moments,[94] and high-order structure functions also exhibit logarithmic behavior in the relevant range of streamwise separation between two points.[95]

One particularly effective conceptual model of wall turbulence dates back to Townsend,[15] who hypothesized that the logarithmic region consists of space-filling, self-similar eddies as shown schematically in figure 5.1(a), whose sizes scale with their distance from the wall. This attached eddy hypothesis has proven to be quite useful in providing (non-trivial) estimates on the scalings in various turbulence quantities including turbulence intensity, Reynolds stress, single-point moments, two-point statistics, pressure fluctuations etc. in wall-bounded flows at high Reynolds number.[14,15,91,94–98] The hypothesis has also guided studies of flow structures,[99,100] including near-wall hairpins,[101–105] coherent vortex packets/clusters;[106–112] and has provided

insights into modelling of flow spectra.[113–115]

Therefore it is not surprising that many efforts have been devoted to various formal mathematical formulations of the Townsend attached eddy hypothesis.[14,15,96,116,117] While details might vary among the various formalisms, all attached eddy models are based on an eddy population density that is inversely proportional to the wall distance, i.e. $P(z) \sim 1/z$, which is a direct consequence of the space-filling property of the hierarchical attached eddies.[14]

From the perspective of statistical descriptions of wall bounded turbulence, high positive moments emphasize those intense events that deviate significantly from the mean. In fact, the most extreme value can be obtained from the limit of very high-order moments since $\max(u) = \lim_{p\to+\infty} \langle u^p \rangle^{1/p}$. Those intense events, from a phenomenological perspective, can indicate the presence of certain flow structures, for example, high and low velocity streak structures that are known to be important in momentum transport in wall turbulence. However, moments do not provide a natural way to distinguish between the positive and negative fluctuations. Even order moments mix the contributions from both positive and negative sides of the distribution. Odd-order moments emphasize the difference between the contributions of positive and negative fluctuations, which does not facilitate emphasizing positive and negative contributions separately. Conditional moments can be used for such discrimination but they depend on both the threshold and the order of the moment, increasing complexity. There is a need for more advanced statistical tools to better characterize

fluctuations in wall bounded turbulence.

1.4 Thesis outline

The thesis is organized as follows. The integral wall model is presented in Chap 2 followed by a chapter devoted to the rescaling-recycling inflow generation technique. In Chap 4 the analytical rough wall model is developed and tested. In Chap 5 the hierarchical random additive model is discussed in detail along with empirical evidence on newly found logarithmic scalings. Statistical behaviors of various moment-generating-functions in wall bounded flows are studied in Chap 6. Last, concluding remarks are given in Chap 7.

Chapter 2

Integral wall model for LES

2.1 Introduction

Taking zonal/hybrid models into a new direction, an interesting method has been proposed in Refs. 118–120 that has a cost that is significantly less than typical zonal/hybrid models. Their approach is based on a vertically integrated boundary layer equation in which the (RANS) stresses are modeled. They use a Reynolds stress model based on streamwise vortices (such vortex structures also used in the vortex based subgrid-scale model in LES[121]). The resulting wall-layer equation is an ordinary differential equation in time for the wall stress at every point, and the approach includes non-equilibrium terms that are approximated based on the local, outer LES-layer velocities and pressure gradient.

Following the approach of Ref. 118, the presently proposed model is based on

vertical integration of the boundary layer equations. Additionally, we aim to include information about the velocity distribution profile below the first LES grid point, and in particular how the velocity distribution affects the unsteady and advective (non-equilibrium) terms in the boundary layer equations. Such information is captured in the zonal/hybrid models based on explicit numerical integration of a vertical fine grid.

In our proposed method, we argue that the velocity profiles typically expected in the thin layer arising from RANS equations are of fairly restricted functional forms that are amenable to be parameterized with a small number of coefficients. The classical integral method by Von Karman-Pohlhausen[122] is based on such parameterized, assumed functional forms (they used polynomial forms for laminar flow), followed by analytical vertical integration of the boundary layer equations to enable relating the stress at the surface with the velocity at some distance from it. We propose here to use this method with suitably formulated test-functions appropriate for turbulent boundary layers. The approach can be considered to be a compromise between the equilibrium models and the zonal/hybrid models. Because the integral equation is derived from the full boundary layer approximation, physical effects such as pressure gradient and acceleration effects can be taken into account, at least in an approximate fashion. We shall denote the proposed method as iWMLES (integral wall model LES). As opposed to traditional zonal wall models, no near-wall region with another fine mesh or with mesh refinement in the wall normal direction is necessary, since

the relevant wall normal information is condensed into an assumed velocity profile that is analytically tractable. Moreover, since the outer velocity obtained from LES is prescribed at a certain specified height from the wall, the boundary layer thickness needs not to be solved for. As a result, the model is local and algebraic, instead of differential in space.

We consider iWMLES of turbulent boundary layers over smooth or rough surfaces. We assume that large scale roughness (larger than the LES grid-scale) can be resolved explicitly on the numerical grid, for instance using the immersed boundary method. Effects of small scale roughness elements must be modeled, i.e. must be included in the wall model. Referring back to the challenges associated with zonal methods enumerated above, the method to be proposed here addresses issues (i), since it is far less expensive than solving the wall-layer equations numerically, (ii) the method avoids the additional complexities of user-dependent choices of numerical near-wall grid resolution, and (iii) it can include rough-wall effects. However, issue (iv) associated with the turbulent velocity fluctuations in the LES portion of the domain is not addressed as of now, and is left for future work. Regarding the coupling to the fluctuations in the LES portion, we point out that the constrained LES approach (CLES)[123] may become an attractive option for this purpose. In CLES, in the LES portion, one adjusts the subgrid-scale model parameter so as to enforce consistency with the Reynolds stresses from the RANS portion of the domain. Moreover, we will be concerned here with modeling the mean wall stress and not short-time (inner-scale)

wall stress fluctuations, for which other modeling strategies may be called for.[37] The material presented in this chapter has appeared in Ref. 124.

2.2 Governing equations

In this section we summarize the RANS governing equations applied in the wall-layer. We adopt a coordinate system with x, z axes parallel to — and y axis normal to — the immersed boundary. The x, z axes are fixed in time, i.e. do not change as function of the tangential resolved velocity vector. We denote the velocity components on the wall-parallel plane as u and w, whereas the wall-normal velocity component is denoted by v. Sometimes, we use index notation u_i $(i = 1, 2, 3)$ for convenience.

2.2.1 Spatial and temporal filtering

We apply two averaging operations onto the variables and dynamical equations: (i) a spatial (2D) filtering in the x, z directions at a scale commensurate to that of the LES spatial resolution, $\Delta_x \times \Delta_z$, similar to that used in Ref. 118, and (b) a one-sided exponential relaxation temporal filtering with a time-scale T_{wall} which is meant to represent the appropriate (long) time-scale associated with vertical turbulent and laminar diffusion in the near-wall region:

$$\langle u \rangle(y; x, z, t) \equiv \int_{-\infty}^{t} \int_{x',z'} u(x', y', z', t')\; G_{\Delta}(|x - x'|, |z - z'|)\; \frac{e^{-(t-t')/T_{\text{wall}}}}{T_{\text{wall}}}\; dt' dx' dz'. \quad (2.1)$$

The particular reasons for the need for temporal filtering at time scale T_{wall} will be explained in greater detail in §2.3.4 below. The expression for the filtered z-direction velocity component $\langle w \rangle$ is similar. These filtered velocities depend mainly on wall normal direction y, while a "slow" spatial dependence on x, z at LES resolution, and dependence of time over time-scales on the order of T_{wall} also exist. The filtering of the nonlinear terms, $\langle u_i u_j \rangle$, gives rise to Reynolds stresses that are modeled using an eddy-viscosity closure, according to

$$\left[\langle u_i u_j \rangle - \langle u_i \rangle \langle u_j \rangle\right]^d = -\nu_T \left(\frac{\partial \langle u_i \rangle}{\partial x_j} + \frac{\partial \langle u_j \rangle}{\partial x_i} \right), \tag{2.2}$$

where $i, j = 1, 2, 3$, and the superscript d denotes the trace-free part of the tensor.

2.2.2 Wall layer equations

Applying boundary layer approximations to the resulting RANS-type equations yields

$$\frac{\partial \langle u \rangle}{\partial t} + \frac{\partial \langle u \rangle \langle u \rangle}{\partial x} + \frac{\partial \langle u \rangle \langle v \rangle}{\partial y} + \frac{\partial \langle u \rangle \langle w \rangle}{\partial z} = -\frac{1}{\rho}\frac{\partial \langle p \rangle}{\partial x} + \frac{\partial}{\partial y}\left[(\nu + \nu_T) \frac{\partial \langle u \rangle}{\partial y} \right] + \langle f_x \rangle$$

$$\frac{\partial \langle w \rangle}{\partial t} + \frac{\partial \langle w \rangle \langle u \rangle}{\partial x} + \frac{\partial \langle w \rangle \langle v \rangle}{\partial y} + \frac{\partial \langle w \rangle \langle w \rangle}{\partial z} = -\frac{1}{\rho}\frac{\partial \langle p \rangle}{\partial z} + \frac{\partial}{\partial y}\left[(\nu + \nu_T) \frac{\partial \langle w \rangle}{\partial y} \right] + \langle f_z \rangle$$

$$\frac{\partial \langle u \rangle}{\partial x} + \frac{\partial \langle v \rangle}{\partial y} + \frac{\partial \langle w \rangle}{\partial z} = 0, \qquad \frac{\partial \langle p \rangle}{\partial y} = 0 \tag{2.3}$$

where ρ, p are density and pressure, and f_x and f_z are body forces that will be used to model roughness effects.

For the eddy viscosity ν_T, we adopt a classical mixing-length formulation,

$$\nu_T = \ell_m^2 \left| \frac{\partial \langle U \rangle}{\partial y} \right|, \tag{2.4}$$

where $\langle U \rangle = (\langle u \rangle^2 + \langle w \rangle^2)^{1/2}$ is the velocity magnitude. As usual, ν_T requires a model for the mixing length ℓ_m. Details of the mixing length expressions used in the model are provided in Appendix A. The terms including f_x, f_z represent distributed volume forces used to model unresolved roughness elements. As in flow through porous media, we use a classic canopy-stress model[125] to represent the form drag introduced by unresolved roughness. Details about the parameterization of the filtered force terms $\langle f_x \rangle$ and $\langle f_z \rangle$ are given in Appendix A. We remark that the effects of local surface (and streamline) curvature are not included in this initial version of the model but it is not difficult to consider more generally applicable formulations, including, e.g. effects of curvature, buoyancy, surface transpiration, etc.

2.2.3 Vertical Integration

We integrate Eq.2.3 from $y = 0$ to certain specified distance from the wall, $y = \Delta_y$. The x and z direction velocities at $y = \Delta_y$ will be denoted as $\langle u \rangle|_{y=\Delta_y} = U_{LES}$ and $\langle w \rangle|_{y=\Delta_y} = W_{LES}$. These are assumed to be known from the LES and will be filtered

in time to comply with the time-scale separation requirement as enunciated in Eq.2.1. The corresponding vertical velocity $\langle v \rangle|_{y=\Delta_y}$ is obtained from integrating the filtered continuity equation from 0 to Δ_y:

$$\langle v \rangle|_{y=\Delta_y} = -\frac{\partial}{\partial x}\int_0^{\Delta_y} \langle u \rangle dy - \frac{\partial}{\partial z}\int_0^{\Delta_y} \langle w \rangle dy \tag{2.5}$$

Replacing into the integrated horizontal momentum equations yields

$$\frac{\partial L_x}{\partial t} + M_x = \tau_{\Delta_y,x} - \tau_{w,x} \quad \text{and} \quad \frac{\partial L_z}{\partial t} + M_z = \tau_{\Delta_y,z} - \tau_{w,z}, \tag{2.6}$$

where M_x and M_z are the contribution from the convective and pressure terms

$$\begin{aligned} M_x &= \frac{1}{\rho}\frac{\partial \langle p \rangle}{\partial x}\Delta_y + \left[\frac{\partial L_{xx}}{\partial x} + \frac{\partial L_{xz}}{\partial z} - U_{LES}\left(\frac{\partial L_x}{\partial x} + \frac{\partial L_z}{\partial z}\right)\right] \\ M_z &= \frac{1}{\rho}\frac{\partial \langle p \rangle}{\partial z}\Delta_y + \left[\frac{\partial L_{xz}}{\partial x} + \frac{\partial L_{zz}}{\partial z} - W_{LES}\left(\frac{\partial L_x}{\partial x} + \frac{\partial L_z}{\partial z}\right)\right]. \end{aligned} \tag{2.7}$$

We define L_x, L_{xx}, L_z, L_{zz}, L_{xz}:

$$L_x = \int_0^{\Delta_y} \langle u \rangle dy,\ L_{xx} = \int_0^{\Delta_y} \langle u \rangle^2 dy,\ L_z = \int_0^{\Delta_y} \langle w \rangle dy,\ L_{zz} = \int_0^{\Delta_y} \langle w \rangle^2 dy,\ L_{xz} = \int_0^{\Delta_y} \langle u \rangle \langle w \rangle dy. \tag{2.8}$$

The stresses $\tau_{\Delta_y,x}$ and $\tau_{\Delta_y,z}$ denote the wall-normal momentum flux at $y = \Delta_y$:

$$\tau_{\Delta_y,x} = (\nu + \nu_T)\left.\frac{\partial \langle u \rangle}{\partial y}\right|_{y=\Delta_y}, \quad \tau_{\Delta_y,z} = (\nu + \nu_T)\left.\frac{\partial \langle w \rangle}{\partial y}\right|_{y=\Delta_y}, \tag{2.9}$$

with ν_T given by Eq.2.4 evaluated at $y = \Delta_y$. $\tau_{w,x}$ and $\tau_{w,z}$ in Eq.2.6 are the total wall-stress in the x and z directions. Notice that this represents momentum loss due

to both viscous friction and possible form drag on unresolved roughness:

$$\begin{aligned}\tau_{w,x} &= (\nu+\nu_T)\left.\frac{\partial\langle u\rangle}{\partial y}\right|_{y=0} + \int_0^{\Delta_y} C_d\ a_{\mathrm{Lx}}\ |\langle U\rangle|\,\langle u\rangle\ dy \\ \tau_{w,z} &= (\nu+\nu_T)\left.\frac{\partial\langle w\rangle}{\partial y}\right|_{y=0} + \int_0^{\Delta_y} C_d\ a_{\mathrm{Lz}}\ |\langle U\rangle|\,\langle w\rangle\ dy.\end{aligned} \tag{2.10}$$

For some applications (typically surfaces with a roughness layer) ℓ_m may not vanish at $y = 0$ and therefore ν_T is kept for generality. The overall momentum loss τ_w is given by

$$\tau_w^2 = \tau_{w,x}^2 + \tau_{w,z}^2. \tag{2.11}$$

We remark that surface structures that are numerically not resolvable for a given mesh may not necessarily be completely sub-grid size. In such cases, one may need to specify Δ_y to be larger than the vertical numerical grid spacing. Hence, Δ_y is considered to be a physical modeling parameter.

2.3 The integral wall model

2.3.1 Main Idea

Zonal models solve boundary layer equations such as Eq. 2.3 directly on vertically refined meshes in the vicinity of the wall in order to obtain near-wall solution. The physics encoded into terms M_i and $\partial L_i/\partial t$ $(i = x, z)$ is therefore explicitly incorporated. Conversely, equilibrium wall models equate $\tau_{w,i}$ with $\tau_{\Delta_y,i}$, i.e. they assume

$\partial L_i/\partial t + M_i = 0$. This only holds true if there is no unsteady, advective, or pressure gradient effects, or if all these effects cancel each other exactly. Here we seek an approach that includes all near wall physics represented by $\partial L_i/\partial t + M_i$, and yet retains the essential algebraic simplicity of the equilibrium wall model. The method we propose here is to condense all near-wall information in some proposed velocity profile that includes parameters describing the profile. In the proposed iWMLES method, these parameters will be solved locally to satisfy various matching and physical conditions, as well as the integral momentum equation Eq.2.6, with non-zero $\partial L_i/\partial t + M_i$. The terms L_i, M_i can be expressed analytically in terms of the assumed velocity profile and its parameters. One of the parameters characterizing the local assumed velocity profile is the wall stress τ_w, and this value is then fed back to the LES as a model for the wall stress to be used at the next time-step of the LES. This procedure provides us with a wall model that preserves the essential simplicity of the equilibrium wall model, yet includes relevant near wall physics. As mentioned before, the method is similar to the prior approach based on integrating the boundary layer equation in the vertical direction,[118] but including a more detailed description of the velocity profile between the first LES grid point and the wall.

The accuracy of the iWMLES method largely depends on an appropriate test function for the assumed velocity profile. In the case of laminar flows, a fourth order polynomial with coefficients determined from appropriately chosen boundary conditions proves to be sufficient and yields quite accurate results.[122] This simple

ansatz, however, cannot be adopted for turbulent boundary layers since these require multiple length-scales and various sublayers. In the subsequent sections, we describe the simple functional forms for turbulent boundary layer profiles we propose to use in the context of iWMLES.

2.3.2 Assumed velocity profile

Many theories and models for the near-wall profile in turbulent boundary layer have been developed and studied over the years.[126] Judicious choices have to be made based on accumulated knowledge. Here we choose to decompose the region $0 \leq y \leq \Delta_y$ into two sub-layers. The first is the viscous or roughness sub-layer that is directly affected either by viscosity, the immersed boundary drag forces f_x, f_z, or both. This sub-layer extends between $0 \leq y \leq \delta_i$. We assume that this sub-layer is characterized simply by a linear velocity profile. Linear behavior is well known to hold for the case of the smooth wall viscous sublayer, but we assume that the same is a good approximation for the averaged velocity within a roughness sublayer in the case of rough (transitional or fully rough) walls when modeled according to distributed forces. We provide supporting evidence for this approach in Appendix B by explicitly integrating the boundary layer equations in such layers with different properties. The second range between $\delta_i < y \leq \Delta_y$ is a "meso-layer" that connects with the LES-resolved flow conditions at $y = \Delta_y$. In this layer we assume that the mean velocity has an equilibrium logarithmic velocity distribution as baseline,[127,128]

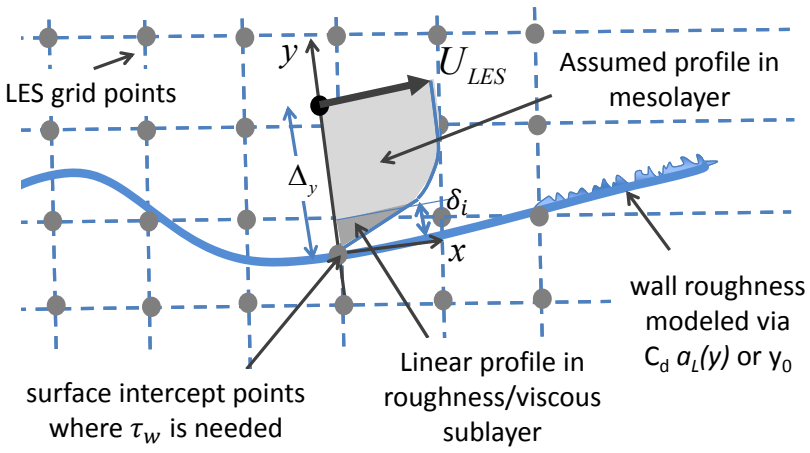

Figure 2.1: Schematic diagram explaining iWMLES. The thick blue line represents the wall. A sample assumed velocity profile above a point where the wall stress must be specified is shown. The assumed profile has a linear sublayer to represent viscous or roughness sublayers, and a mesolayer which can include a logarithmic layer modified by pressure gradient and insteady/advective effects. The LES data (velocities U_{LES}, W_{LES} and pressure gradients) are sampled at a distance Δ_y above the grid point at which τ_w is needed. Spatial interpolations and time filtering are used to obtain these LES values to be used as matching conditions for the assumed profile.

and includes an additional linear term to account for possible additional effects from pressure gradients, accelerations, etc. When local Reynolds number is low, the height of viscous layer δ_i can exceed Δ_y. In that case, the meso-layer vanishes and merely the inner layer survives. The term "outer layer" is reserved for the bulk flow that is resolved via LES. The sketch in Fig. 2.1 presents the basic idea.

For clarity, we present a one-dimensional velocity profile formulation in this section. The more general case of 2D flow parallel to the wall is presented in Appendix C.

The proposed velocity profile has the form:

$$\begin{aligned} \langle u \rangle &= u_\nu \frac{y}{\delta_\nu}, && 0 \le y \le \delta_i, \\ \langle u \rangle &= u_\tau \left[C + \frac{1}{\kappa} \log \frac{y}{\Delta_y} \right] + u_\tau A \frac{y}{\Delta_y}, && \delta_i < y \le \Delta_y. \end{aligned} \tag{2.12}$$

The parameters have mostly their traditional meanings: u_τ is the friction velocity associated with the entire momentum flux at the surface, u_ν is the velocity associated with the viscous portion of the momentum flux (for smooth surfaces $u_\nu = u_\tau$), δ_ν is the length-scale associated with the viscous layer, the coefficient C ensures that the logarithmic law matches the viscous portion, and A represents the linear perturbation to the logarithmic law in order to represent effects of pressure gradient or advection.

2.3.3 Conditions and parameters

The 6 parameters (C, A, δ_i, δ_ν, u_ν and u_τ) must be determined from boundary conditions and other consistency relations.

1. We must match with the LES velocity, i.e. $\langle u \rangle (y = \Delta_y) = U_{\text{LES}}$, i.e.

$$u_\tau (C + A) = U_{\text{LES}}. \tag{2.13}$$

2. We impose continuity of the velocity profile at $y = \delta_i$, i.e.

$$u_\nu \frac{\delta_i}{\delta_\nu} = u_\tau \left[C + \frac{1}{\kappa} \log \frac{\delta_i}{\Delta_y} + A \frac{\delta_i}{\Delta_y} \right]. \tag{2.14}$$

3. We must specify the scale separating the two layers, δ_i. For fully rough surfaces with roughness elements protruding up to a height k, we choose $\delta_i = k$. Conversely, for smooth surface cases, δ_i represents standard separation between the viscous and the inertial layer, i.e. $\delta_i = 11\ \nu/u_\tau$, the intercept between the linear viscous profile $\langle u \rangle = y u_\tau^2/\nu$ and the standard log-law $\langle u \rangle = u_\tau/\kappa \ln(y u_\tau/\nu) + B$ with $B = 5$ and $\kappa = 0.4$. In the case of low local Reynolds numbers or, equivalently, in the case of wall-resolved LES, we may have $11\nu/u_\tau > \Delta_y$. In that case, the linear profile is assumed to extend all the way to Δ_y. Therefore, in order to include all cases, we define

$$\delta_i = \min \left[\max \left(k, 11 \frac{\nu}{u_\tau} \right), \Delta_y \right]. \tag{2.15}$$

4. The inner layer length scale is defined in terms of viscosity and near wall velocity scale:

$$\delta_\nu = \frac{1}{u_\nu} (\nu + \nu_{T,y=0}), \tag{2.16}$$

As in Eq.2.10 we here include $\nu_{T,y=0}$ as given by Eq. 2.4 because ℓ_m does not always vanish at $y = 0$, e.g. for parameterized roughness layer.

5. We define the friction velocity u_τ associated with the total wall momentum flux as the sum of the viscous drag at the surface and the form drag modeled here by a distributed body force (see Appendix A) according to $\langle f_x \rangle = -C_d a_L \langle u \rangle^2$, where C_d and $a_L(y)$ are drag coefficient and roughness area density, respectively:

$$\tau_w = u_\tau^2 = u_\nu^2 + \int_0^k C_d a_L \langle u \rangle^2 dy. \tag{2.17}$$

   u_τ is the velocity scale used in the meso-layer profile. We recall that $u_\nu = u_\tau$ for smooth walls.

6. Finally, the vertically integrated momentum equation provides a condition that closes the coupled set of 6 equations for the 6 unknown:

$$\frac{\partial L_x}{\partial t} + M_x = \tau_{\Delta_y} - \tau_w = \left(\nu + \nu_T|_{y=\Delta_y}\right) \frac{u_\tau}{\Delta_y} \left(\frac{1}{\kappa} + A\right) - u_\tau^2, \tag{2.18}$$

   when $\delta_i < \Delta_y$. (In the "wall-resolving" case $\delta_i = \Delta_y$, we obtain $\tau_{\Delta_y} = \nu U_{LES}/\Delta_y$ by solving the conditions using the linear profile.)

Therefore, knowledge of U_{LES} and $\partial\langle p \rangle/\partial x$ from the LES, together with ν and surface properties C_d and $a_L(y)$, enables us to solve for the 6 parameters if we knew the non-equilibrium, inertial terms L_x and M_x needed in step (6). Knowledge of the parameters, on the other hand, enables one to evaluate the required integrals analytical as will be detailed in §2.3.5. Once the set of equations is solved, the

parameter τ_w can be fed back to the LES. This term is typically required in the evaluation of the divergence of the stress tensor when evaluating its wall-normal component (e.g. $\partial\tau_{xy}/\partial y$ in the x-direction momentum equation).

Returning now to the assumed functional form, in Appendix B we show using several examples that the assumed profiles agree quite well with profiles that would be obtained from numerical integration of the boundary layer equation with a RANS eddy-viscosity model. Figure 2.2 shows an illustrative example of normalized velocity profiles $\hat{u} = u/U_{LES}$ for a specific case with a prescribed roughness parameter $\hat{k} = k/\Delta_y$. In this example the viscosity is very small, i.e. fully rough, and there are no pressure gradients and inertial effects ($M_x = 0$). The roughness length $k/\Delta_y = 0.1$ is used and a constant roughness area density a_L is assumed. The solid line indicates the numerical integration of the boundary layer equation while the dashed line indicates the assumed function with the parameters determined based on the conditions enumerated above. As can be seen, the numerically obtained profile is very similar to that from the assumed and properly parameterized profile. This close agreement justifies our use of assumed profiles instead of having to solve a wall-normal local ODE. More examples are provided in Appendix B.

Some limits are of interest. One is the smooth wall-resolving case in which $\delta_i = \Delta_y$ (i.e. $11\nu/u_\tau \geq \Delta_y$). In this case the entire velocity profile is linear, and the matching condition at $y = \Delta_y$ leads to $u_\nu/\delta_\nu = U_{LES}/\Delta_y$, $u_\nu\delta_\nu = \nu$, and $u_\tau = u_\nu$, so that the

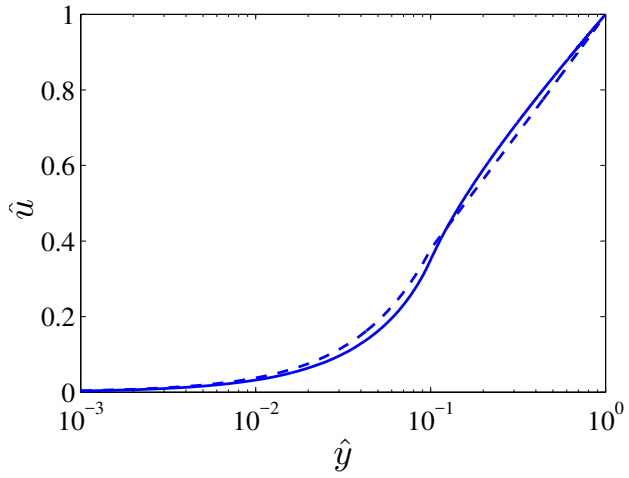

Figure 2.2: Comparison of velocity profile $\hat{u} = \langle u \rangle / U_{LES}$ solved numerically (see Appendix B for details) from the boundary layer equation (solid line) and that from the assumed profile (Eq. (2.12), dashed line) for the case $k/\Delta_y = 0.1$. Other parameters for this example are: $\partial L_x/\partial t + M_x = 0$, $Re_y = U_{LES}\Delta_y/\nu = 10^4$ and $C_d = 0.1$, with a constant $a_L = 1.0$ for $y < k$, and $a_L = 0$ above.

wall stress becomes

$$u_\tau^2 = \nu \frac{U_{LES}}{\Delta_y} \tag{2.19}$$

as expected.

The other limit of interest is very high Reynolds number cases without mean pressure gradient under equilibrium conditions. Then $\partial L_x/\partial t + M_x = 0$, and the wall stress can be obtained via a specified hydrodynamic roughness height y_0 (this length is usually called z_0 but we will use the notation y_0 to be consistent with y representing the wall-normal direction). Since y_0 is a condensed representation of the "inner layer", the "inner layer" needs not to be explicitly included in the assumed profile. Moreover, because $\partial L_x/\partial t + M_x = 0$, Eq. 2.6 is automatically satisfied, the only unknown parameter is u_τ, and the only condition to satisfy is the matching

condition at $y = \Delta_y$. The integral wall model thus reduces exactly to the equilibrium wall model.

More generally we are sometimes interested in the case when $\partial L_x/\partial t + M_x \neq 0$ but for surfaces in which the roughness length y_0 is prescribed and known. In that case the assumed profile for the "meso layer" is written as follows:

$$\langle u \rangle = \frac{u_\tau}{\kappa} \log \frac{y}{y_0} + u_\tau A \left(\frac{y}{\Delta_y} - \frac{y_0}{\Delta_y} \right) \tag{2.20}$$

The two unknown parameters A, u_τ are to be determined from the matching condition at $y = \Delta_y$:

$$\frac{u_\tau}{\kappa} \log \frac{\Delta_y}{y_0} + u_\tau A \left(1 - \frac{y_0}{\Delta_y} \right) = U_{LES} \tag{2.21}$$

and from the vertically integrated momentum equation:

$$\frac{\partial L_x}{\partial t} + M_x = \kappa u_\tau^2 A \left(\kappa A + 2 \right), \tag{2.22}$$

if we consider the fully rough and high Reynolds number case in which $\nu_{T,y=\Delta_y} >> \nu$ and $\ell_m \approx \kappa \Delta_y$ at $y = \Delta_y$. For $\partial L_x/\partial t + M_x = 0$, Eq. (2.22) implies that $A = 0$ and Eq. 2.21 again reduces to an equation to find u_τ as function of U_{LES}, i.e. the usual equilibrium wall model with prescribed roughness scale as discussed above.

We also note that if instead of y_0 one wishes to use correlations for the defect velocity ΔU^+, the usual relationship between y_0 and ΔU^+ must be used:

$$\frac{y_0 u_\tau}{\nu} = \exp\left[\kappa(\Delta U^+ - B)\right]. \tag{2.23}$$

In simulations, the LES velocity has two components U_{LES} and W_{LES}. The treatment including both directions is described in detail in Appendix C.

2.3.4 Averaging time scale T_{wall}

As mentioned in §2.2.1 the formulation of the filtered momentum equation in the wall layer involves both spatial and temporal filtering (Eq. 2.1). The temporal filtering is required conceptually because the RANS framework requires us to aim to model only the very slowest time-scales (or the temporal mean) of the flow. In fact, numerical experiments without such time filtering produced unstable results that could be traced to very large and fluctuating values of $\partial L_x/\partial t$ that dominate the entire momentum balance against which the RANS model for the wall normal diffusion cannot respond well. Physically in the integral method the *entire* velocity profile in the layer is slaved to the top velocity U_{LES}. But for fluctuations of this velocity to reach the wall requires a certain time scale, similar to the viscous Stokes 2nd problem where shear waves propagate from the wall at a time-scale dictated by diffusive rather than inertial forces. The situation near a wall is thus eminently

different from the relevant timescales in the bulk of the domain where inertial/pressure effects would help to propagate subgrid fluctuations rather quickly through the LES grid volume. But in the highly anisotropic near-wall region the physics is dictated mainly by the slower, shear diffusive (or eddy-diffusive) momentum transport of wall-parallel momentum across the wall-normal direction. Examination of instantaneous profiles of streamwise velocity profiles clearly show that temporal fluctuations of U_{LES} do not propagate instantaneously to the wall with a smooth profile slaved to it, but instead there are spatial fluctuations in the profile around the mean. The time-scale separation properties of temporal filtering allow us to link only the slow temporal fluctuations of wall stress to the slow fluctuations of U_{LES}.

In order to establish quantitatively the appropriate time-scale, we note that the characteristic diffusion time-scale for wall-normal transport is proportional to distance squared divided by viscosity. Thus the time-scale for turbulent diffusion across the meso-layer is roughly expressed as

$$T_{\text{wall}} = \theta \frac{\Delta_y}{\kappa u_\tau} \tag{2.24}$$

where θ is a dimensionless parameter that dictates over how many physical characteristic time-scales one should perform the averaging. Typically, a minimum value of $\theta = 5$ is required for an exponential correlation function to decay to less than 0.7% of its maximum value. For this work, we will use $\theta = 1$ and show that the precise value

of the averaging time-scale does not affect the results.

In order to enforce this time-scale on the wall model, the LES variables used as input to the model must be temporally averaged using this time-scale. As in prior applications of time-averaging,[129] the one-sided exponential filter that was chosen results in a first-order process in which we may write

$$U_{LES}(t) = \epsilon\ \tilde{u}_{LES}(t) + (1-\epsilon)\ U_{LES}(t-\delta t) \tag{2.25}$$

where $U_{LES}(t)$ is the time-filtered velocity from LES, $\tilde{u}_{LES}(t)$ is the instantaneous LES velocity at the particular location above the wall, and $U_{LES}(t-\delta t)$ is the time-filtered velocity at the previous time-step. The parameter ϵ is given by

$$\epsilon = \frac{\delta t}{T_{\text{wall}}}, \tag{2.26}$$

where δt is the integration time-step. Similar time averaging can be performed for the other component W_{LES} as well as the pressure gradients from LES. In this fashion, the only time-scales seen by the wall model are those for which there is sufficient time for a boundary layer-type profile to be established in the wall-normal direction.

We note that the model is Galilean invariant as long as the time-averaging is done at a spatial position attached to the wall and velocities are measured relative to the wall velocity (i.e. U_{LES} is replaced by $U_{LES} - U_w$ where U_w is the wall velocity, etc.). Thus, if the model is applied to a moving object the model must be formulated with

the wall layer moving together with the wall.

2.3.5 Non-equilibrium, inertial terms:

In this section we describe the treatment of the inertial terms $\partial L_x/\partial t$ and M_x that depend explicitly on vertical integration. Here again we restrict the presentation to the x-direction case when $W_{LES} = 0$. The general formulation including the various directions is relegated to Appendix C.

The first term in Eq.2.18 that can be computed analytically in terms of the parameters of the assumed profile is the linear momentum in the near wall region, $L_x = \int_0^{\Delta_y} \langle u \rangle dy$. The integration $\int_0^{\delta_i} \langle u \rangle \mathrm{d}y + \int_{\delta_i}^{\Delta_y} \langle u \rangle \mathrm{d}y$ results in:

$$L_x = \frac{1}{2} u_\nu \frac{\delta_i^2}{\delta_\nu} + u_\tau \Delta_y \left[\frac{1}{2} A \left(1 - \frac{\delta_i^2}{\Delta_y^2} \right) - \frac{1}{\kappa} + \left(1 - \frac{\delta_i}{\Delta_y} \right) \left(C + \frac{1}{\kappa} \log \frac{\delta_i}{\Delta_y} \right) \right] \tag{2.27}$$

The second term is the advective nonlinear term $\frac{\partial}{\partial x} L_{xx}$. The integral is evaluated as $L_{xx} = \int_0^{\Delta_y} \langle u \rangle^2 \, dy = \int_0^{\delta_i} \langle u \rangle^2 \, dy + \int_{\delta_i}^{\Delta_y} \langle u \rangle^2 \, dy$. The result is

$$\begin{aligned} L_{xx} = \frac{1}{3} u_\nu^2 \frac{\delta_i^3}{\delta_\nu^2} + u_\tau^2 \Delta_y \Bigg[& \left(C - \frac{1}{\kappa} \right)^2 - \frac{\delta_i}{\Delta_y} \left(C - \frac{1}{\kappa} + \frac{1}{\kappa} \log \frac{\delta_i}{\Delta_y} \right)^2 + \frac{1}{\kappa^2} \left(1 - \frac{\delta_i}{\Delta_y} \right) \\ & + A \left(C - \frac{1}{2\kappa} \right) \left(1 - \frac{\delta_i^2}{\Delta_y^2} \right) - \frac{A}{\kappa} \frac{\delta_i^2}{\Delta_y^2} \log \frac{\delta_i}{\Delta_y} + \frac{1}{3} A^2 \left(1 - \frac{\delta_i^3}{\Delta_y^3} \right) \Bigg] \end{aligned} \tag{2.28}$$

.

Numerically, the time-derivative of L_x is written using forward Euler differentiation, in which the parameters at the present time step n are treated as unknowns, while

those at time step $n-1$ are known:

$$\frac{L_x^n - L_x^{n-1}}{\delta t} \approx \left(\frac{\partial L_x}{\partial t}\right)^{n-1}. \tag{2.29}$$

In the analytic formulae for L_x^n the parameters u_τ, A, C, δ_i, δ_ν and u_ν are treated as unknowns at time-step n, and together with the 6 conditions mentioned above they are solved for using Newton's method. The term L_{xx} is treated fully explicitly, evaluated based on the parameters at time step $n-1$. The spatial derivative involved in the advection term is evaluated using the interpolant of bilinear interpolation among the closest four neighbouring points on the resolved surface. Because the stencil for bilinear interpolation, $f(x,z) = ax + bz + cxz + d$, has four unknowns, where x, z are the spatial coordinates on the local wall-parallel surface; a, b, c, d are the coefficients and f is the dependent variable (e.g. L_{xx}); we need four points to determine a, b, c, d. Here we have chosen the closest four points on the solid surface without including the point where the spatial derivative is to be evaluated. This reduces to standard second order central differencing if the points on the surface are structured. Note that the independent variable doesn't include y because L_x, L_{xx}, etc. are only defined on the bounding surface. The pressure gradient term is treated in the same way as the advective term. Appendix C describes the full treatment of the additional terms needed when there are contributions from the z direction as well.

Finally, it is useful to state the parameters that must be specified by the user.

They are the von Karman constant κ, the offset B, and the mixing length parameter α within the roughness layer for rough wall applications. Additional conditions based on matching with the LES or dynamic versions[27,118] could be envisioned to determine these parameters. In the current version of iWMLES, we propose to use the standard values $\kappa = 0.4$, $B = 5$ and $\alpha = 0.2$.

2.4 Applications

Four sets of tests are conducted to assess the performance of the proposed integral wall model. We begin with fully developed half-channel flow using a pseudospectral LES code.[26] Then, three sets of tests are performed using a second order finite difference solver with the sharp immersed boundary method for treating complex-geometry boundaries.[130]

2.4.1 Fully developed half-channel flow

This set of test cases are fully developed (half) channel flow driven by an imposed unit pressure gradient. The code we use is pseudo-spectral in planes parallel to the wall and second-order finite differencing (kinetic-energy conserving) in the vertical direction. This code has been used in a number of LES studies of high Reynolds number environmental flows.[27,131–134] The domain size is $2\pi L_y$ in both stream and spanwise direction and L_y in vertical direction, with $L_y = 1$. We use a very coarse

mesh, i.e. only $N_x = 32$, $N_y = 32$ and $N_z = 32$ grid points with uniform grid spacing in each direction. The specified pressure gradient is $-(1/\rho)L_y\partial p_\infty/\partial x = 1$ The nominal Reynolds number is infinite and only subgrid-scale eddy-viscosity using the scale-dependent Lagrangian dynamic model[26] is used. The code uses a staggered mesh in the finite-differencing direction, so that the first grid point is located at one half of the vertical grid spacing away from the wall. Therefore, in the wall model we set $\Delta_y = \delta_y/2$, where $\delta_y = (L_y/N_y)$ is the vertical grid spacing. Therefore, $\Delta_y = (1/64)L_y = 0.0156$. Note that the cross stream resolution of $\Delta_z \sim 0.1L_y$ is very coarse (the large-scale structures have scales on the order of 0.2-0.3 L_y) and therefore these simulations can be considered to severely test the LES and wall modeling.

We first consider a case in which we specify a hydrodynamic roughness height, $y_0 = 10^{-4}L_y$. With a prescribed roughness height y_0, there is no separate viscous or roughness sublayer, and the wall model includes only the "meso-layer". We use $T_{\text{wall}} = \theta\Delta_y/\kappa u_\tau$ with $\theta = 1$ for the running time average of the LES velocities and local pressure gradients to be input to the model. The model also includes the mean streamwise pressure gradient for consistency.

Figure 2.3 shows the mean streamwise velocity profile and the Reynolds stresses.

Figure 2.4 is a sample time history of the parameters involved in the wall model. We plot both time series of plane averaged and single point values at some arbitrary point at the wall. As expected, the average value of u_τ is equal to u_p, the velocity scale from the imposed mean pressure gradient, while the transverse direction stress

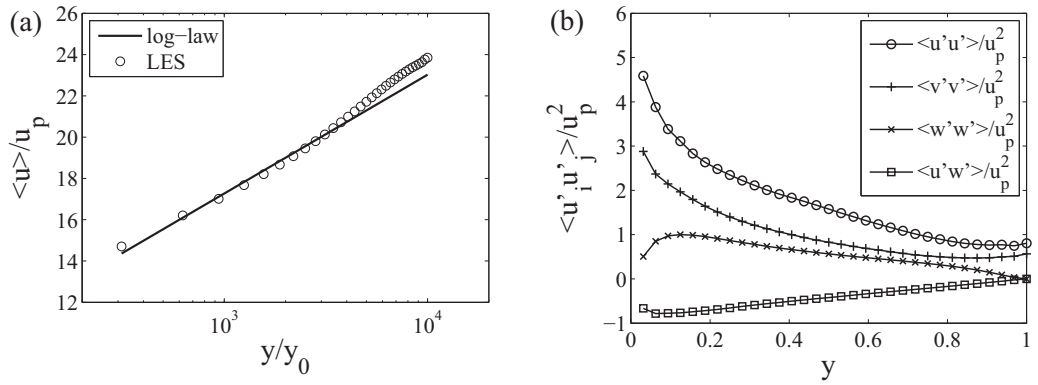

Figure 2.3: Mean streamwise velocity profile (a) and Reynolds stress (b) for half channel flow at infinite Reynolds number with hydrodynamic roughness height specified. 32 grid points are used in the vertical direction. Time filtering is applied to the LES velocity that is used in the wall model, and $T_{\text{wall}} = \Delta_y/\kappa u_\tau$. u_τ that is used in T_{wall} is determined locally and dynamically within the simulation. u_p is defined from imposed pressure gradient $u_p = \sqrt{-(\partial p_\infty/\partial x)(L_y/\rho)}$ (=1 in the units used in the simulation).

is zero. Note that the mean value of parameter A_x is non-zeros because the mean pressure gradient in included in the formulation (i.e. $M_x \neq 0$) and thus $\tau_{\Delta_y,x}$ may differ from $\tau_{w,x}$.

In order to test whether the choice of T_{wall} in the time averaging matters, several runs with different values of θ have been performed. Resulting mean velocity and variances are essentially the same (not shown). However, the fluctuations in the parameter A_x and A_z are reduced if we for instance use $\theta = 5$ instead of $\theta = 1$ (see Figure 2.5). Because of the time filtering of the LES velocity and pressure gradients used in the wall model, the wall model calculation does not have to be computed at every time step of the LES. We have tested computing and using the wall stress only at every 10 time steps of the LES (the CFL number in the LES was maintained at a fairly conservative value of 0.0625. Hence, if the LES were run with larger CFL

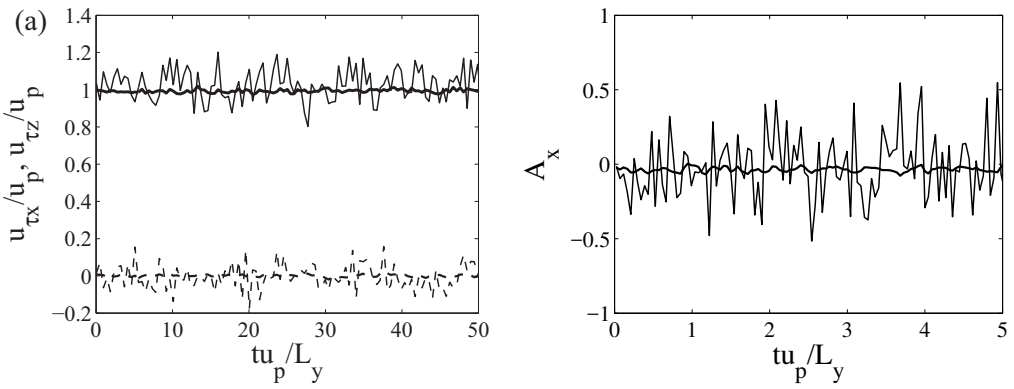

Figure 2.4: Sample time history of the parameters used in the wall model with time filtering applied to LES velocity input to the model, and $T_{\text{wall}} = \Delta_y/\kappa u_\tau$. Figure (a) plots the sample time history of $u_{\tau x}$(solid lines) and $u_{\tau z}$(dashed lines). The bold lines are plane averaged value and thin lines are single point values. Figure (b) shows A_x. The bold lines is the plane averaged value while the thin lines are taken at a single point.

values the wall model may need to be evaluated more frequently than only every 10 time-steps). The mean profile and statistics show no difference when compared with figure 2.3. As a result, in terms of CPU cost, the wall model is essentially of negligible additional computational cost when compared to cost of LES using the equilibrium model.

As a second application, we test the model in the context of a smooth-surface half channel. Now a viscous sublayer will be included in the wall model. We consider Reynolds numbers that are sufficiently high so that we do not include molecular viscosity in the LES portion of the flow. Six different Reynolds numbers are considered, ranging from $Re_\tau = u_p h/\nu = 10^5$ to 10^{10}. Figure 2.6 shows the mean velocity profile in wall units obtained in each case. The solid line is the averaged assumed profile used in the wall model for the highest Reynolds number example (others overlap as

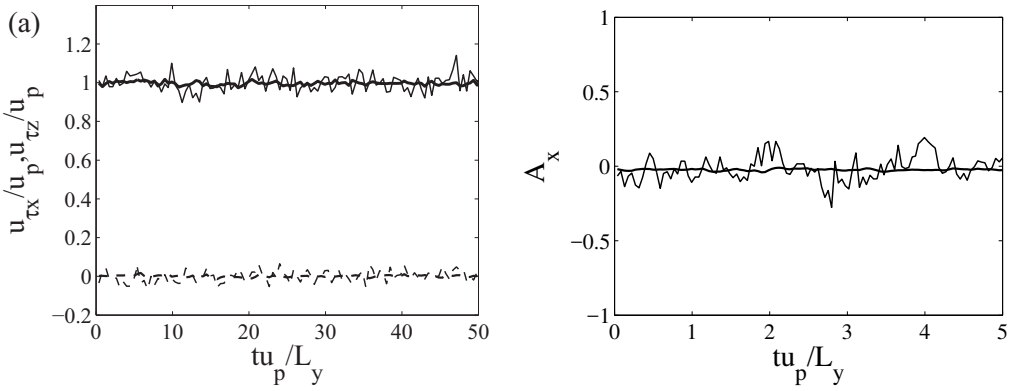

Figure 2.5: Sample time history of the parameters used in the wall model with time filtering applied to LES velocity input to the model, and $T_{\text{wall}} = 5\Delta_y/\kappa u_\tau$. Panel (a) plots the sample time history of $u_{\tau x}$(solid lines) and $u_{\tau z}$(dashed lines). The bold lines are plane averaged value and thin lines are single point values. Panel (b) shows A_x. The bold lines is the plane averaged value while the thin lines are taken at a single point.

expected).

2.4.2 Developing boundary layers

In this section we apply the iWMLES approach in the context of developing turbulent boundary layers. Applications to flow over both smooth and rough surfaces are considered. We use a finite difference solver with dynamic Vreman model for sub-grid stress[135] for the cases in this and following sections. The turbulent inflow condition is generated using the recycle-rescaling method.[2] The rescaling plane is located $6\delta_0$ downstream of the entrance plane, where δ_0 is the inlet boundary layer thickness. We define Reynolds number based on inlet boundary layer thickness and free-stream velocity, i.e. $Re_{\delta_0} = U_\infty \delta_0/\nu$. The computational domain is of size $8\delta_0$ in the streamwise direction and $4\delta_0$ in both vertical and spanwise directions. The mesh

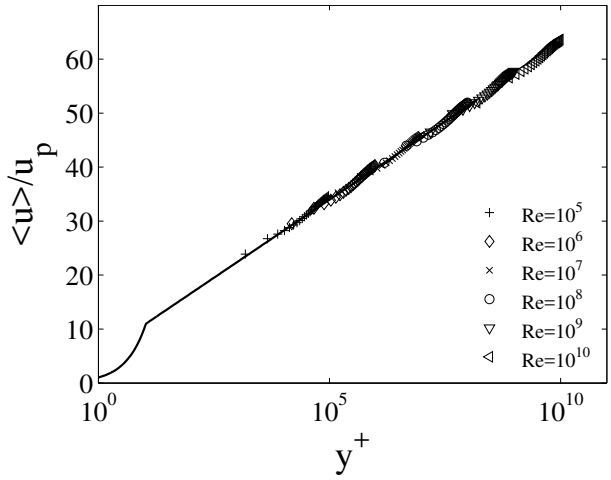

Figure 2.6: Mean streamwise velocity profile for half channel at various Reynolds number. $Re_\tau = u_p L_y/\nu$ is defined based on friction velocity(equal to u_p from imposed pressure gradient) and half channel height L_y. The solid line is averaged assumed profile from the wall model in the highest Reynolds number case.

size is $128 \times 64 \times 64$, with uniform grid spacing in every direction. The bottom wall is treated as an immersed boundary, and the wall location is at $y = 0.0625\Delta_0$. The wall model location Δ_y is taken to be $0.06\delta_0$ away from bottom wall, i.e. at $y = 0.125\delta_0$. U_{LES}, W_{LES} and the local pressure gradients at that point are obtained using trilinear interpolation from the bulk LES simulation. The wall stress is obtained from the wall model now including a near-wall sublayer.

We first present results from simulations of flow over smooth surfaces at various Reynolds numbers. Since the surfaces are smooth, we have roughness height $k = 0$, i.e. no unresolved roughness in the "inner layer". Figure 2.7 shows the mean velocity profiles of the streamwise velocity at $x = 6\delta_0$ downstream of the entrance. u_τ is obtained from spanwise averaging of the wall stress predicted by the wall model at the same x location where the profile is obtained. It is seen that the wall model can

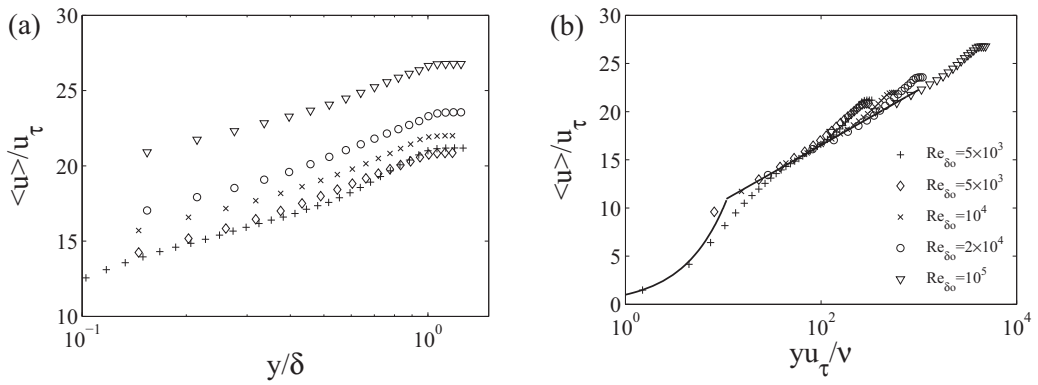

Figure 2.7: Mean profile of streamwise velocity for developing boundary layer at various Reynolds numbers in outer units (a) and inner units (b). Re_{δ_0} is defined using δ_0 at the inlet, the profile is taken $6\delta_0$ downstream, where δ_0 is the turbulent boundary layer thickness at the inlet. 16 grid points are used to resolve the δ_0 for all cases except for one case $Re_{\delta_0} = 5000$, where we have used 34 grid points. The LES velocity is taken at a distance $\Delta_y/\delta_0 = 0.06$ away from the wall except for the $Re_{\delta_0} = 5000$ case with refined mesh, where it is taken at $\Delta_y/\delta_0 = 0.0125$ away from the wall. u_τ is obtained from spanwise averaging of the wall stress predicted by the wall model.

automatically produce a linear region if the grid point is inside the viscous region. Figure 2.8 shows the Reynolds stresses for the $Re_{\delta_0} = 10^4$ case at the same location (Reynolds stresses for the other cases are very similar).

Then we test the model using a rough surface, with only unresolved roughness. We take two very high Reynolds numbers so that we are in the fully rough regime. In one case we use $k = 0.005\delta_0$, which in wall units is k^+ =52 for the $Re_{\delta_0} = 2\times10^5$ case. We also consider a case at $Re_{\delta_0} = 10^6$, in which case $k = 0.005\delta_0$ corresponds to $k^+ =$ 261. Then we consider $k = 0.01\delta_0$ with $Re_{\delta_0} = 2 \times 10^5$ and $Re_{\delta_0} = 2 \times 10^6$. These correspond to k^+ =115 and k^+ =583, respectively. We remark that in this fully-rough boundary layer, the friction velocity is not supposed to evolve downstream. Therefore, no rescaling of velocity fluctuations is needed in the recycle-rescaling method (i.e. the

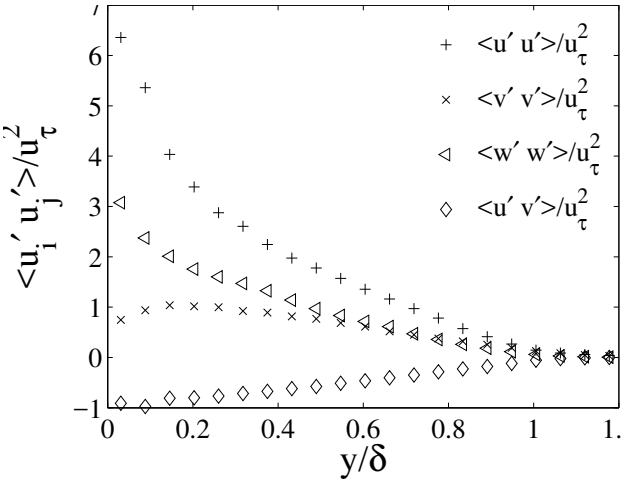

Figure 2.8: Reynolds stress profiles for the case $Re_{\delta_0} = 10^4$. u_τ is obtained from spanwise averaging of the wall stress predicted by the wall model.

rescaling parameter is set to $\lambda = 1$).

To represent surface roughness in this application, we prescribe $C_d = 0.1$ and $a_L = 7.8/\delta_0$, for $y < k$, zero otherwise. Figure 2.9 shows the mean velocity profiles. Notice that the model correctly predicts an effective hydrodynamic roughness height that is insensitive to Reynolds number, at these very high Reynolds numbers. We can "measure" the resulting effective roughness length as the intercept of the logarithmic region. We obtain $y_0 \approx 0.0016\delta_0$ for the $k = 0.01\delta_0$ case, while we obtain $y_0 \approx 0.00075\delta_0$ for the $k = 0.005\delta_0$ case. The exact value of y_0 depends on the choice of C_d and $a_L(y)$. As can be seen, y_0 scales with k (we obtain, roughly, $y_0 \approx 0.16k$).

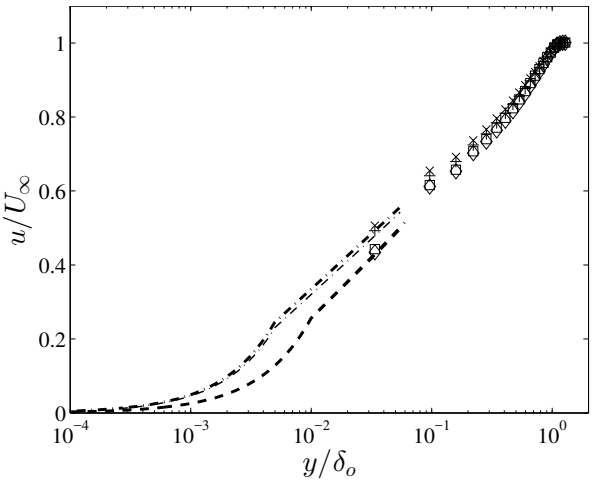

Figure 2.9: Mean profile of streamwise velocity for developing boundary layer with unresolved roughness. Length-scales are normalized by δ_0. Two Reynolds numbers are used for each specified roughness height k. $+$ represents the case $k = 0.01$, $Re_{\delta_0} = 2 \times 10^5$; $\times$ represents the case $k = 0.01$, $Re_{\delta_0} = 10^6$; $\square$ is for $k = 0.005$, $Re_{\delta_0} = 2 \times 10^5$; and $\Diamond$ is for $k = 0.005$ $Re_{\delta_0} = 10^6$. The dot dashed lines are predicted profile for $k = 0.005$, and the dashed lines are for $k = 0.01$. The bold lines are from $Re_{\delta_0} = 2 \times 10^5$, and the thin lines are from $Re_{\delta_0} = 10^6$. The roughness height measured in wall unit are 52 for $k = 0.005$, $Re_{\delta_0} = 2 \times 10^5$, 261 for $k = 0.005$, $Re_{\delta_0} = 10^6$, 115 for $k = 0.01$, $Re_{\delta_0} = 2 \times 10^5$, 583 for $k = 0.01$, $Re_{\delta_0} = 2 \times 10^6$.

2.4.3 Flow over wall-mounted cubes

The third case is a channel with the bottom wall mounted with cubes. We compare the LES results with experimental data.[1] The experiments were performed in a wind tunnel with a rectangular test section with height of 600 mm. A matrix of cubes with size $H = 15$ mm, spaced equidistantly at 45 mm (face-to-face) in both the streamwise and spanwise direction was mounted on the surface. The average velocity, which is the ratio of the mass flow rate and the integration area, is 3.86 m/s. The Reynolds number based on the bulk velocity and the cube size was $Re_H = 3,854$.

We use the in-house code Vicar3D to solve the incompressible filtered Navier-Stokes equations.[136] A second-order central finite difference scheme is used for spatial derivatives, and the projection method is employed for time discretization. The sub-grid stress tensor is modeled via the Dynamic Vreman model.[137,138] The cubic surface roughness elements are represented using the sharp immersed boundary method.[139]

In the simulation we include 2×2 cubes in the computational domain. The size of the domain is $8H \times 8H \times 3.62H$, where H is the cube height. We have used a rather coarse mesh, $64 \times 64 \times 32$, meaning that there are only 8 points across each cube and 8 to represent their height. We match the Reynolds number of the experiment. Results are shown in Fig. 2.10. The mean velocity profile from the simulation (symbols at grid points) is compared with the experimental data[1] (lines in the figure). Good agreement can be observed.

In Fig. 2.11 we present some contour plots to illustrate the resulting parameters

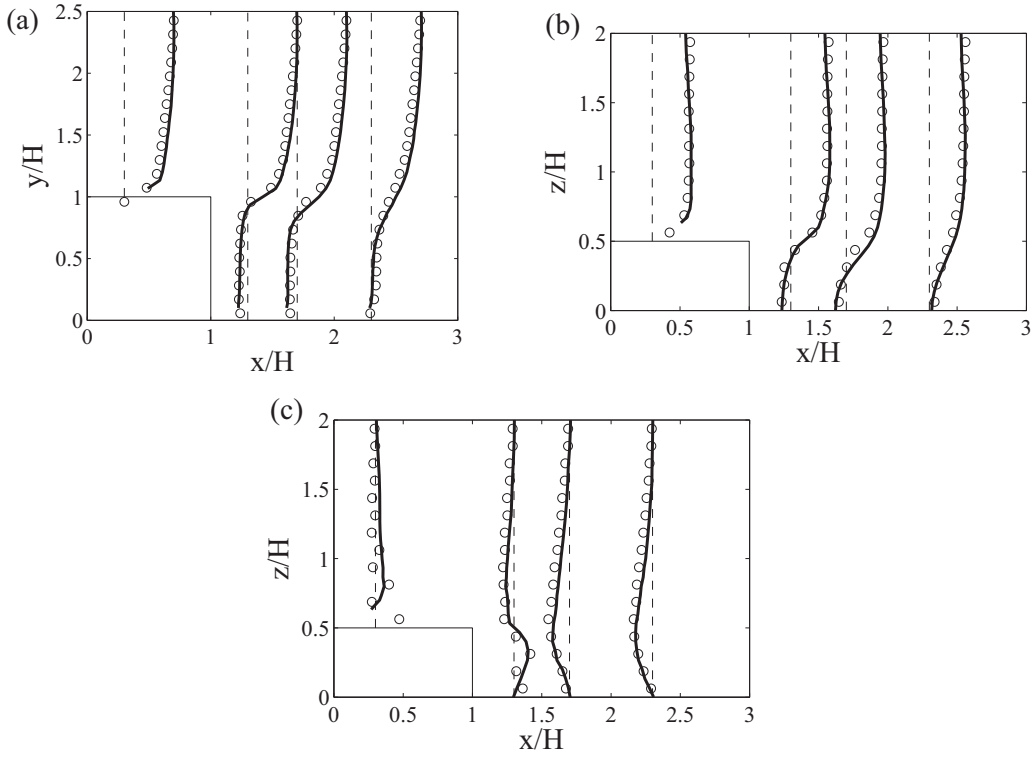

Figure 2.10: Mean streamwise velocity profiles predicted using iWMLES (open symbols) and comparisons with data from Ref. 1 (lines). The directions x, y, z are, respectively, streamwise, vertical, and spanwise direction. Panel (a) shows profiles of the $\langle u \rangle$ component at mid plane across the representative cube, at $z = 0$, as function of y at various x locations. Panel (b) shows $\langle u \rangle$ at $y = 0.5$ as function of z at various x locations while (c) shows spanwise mean velocity $\langle w \rangle$ at $y = 0.5$ as function of z at various x locations.

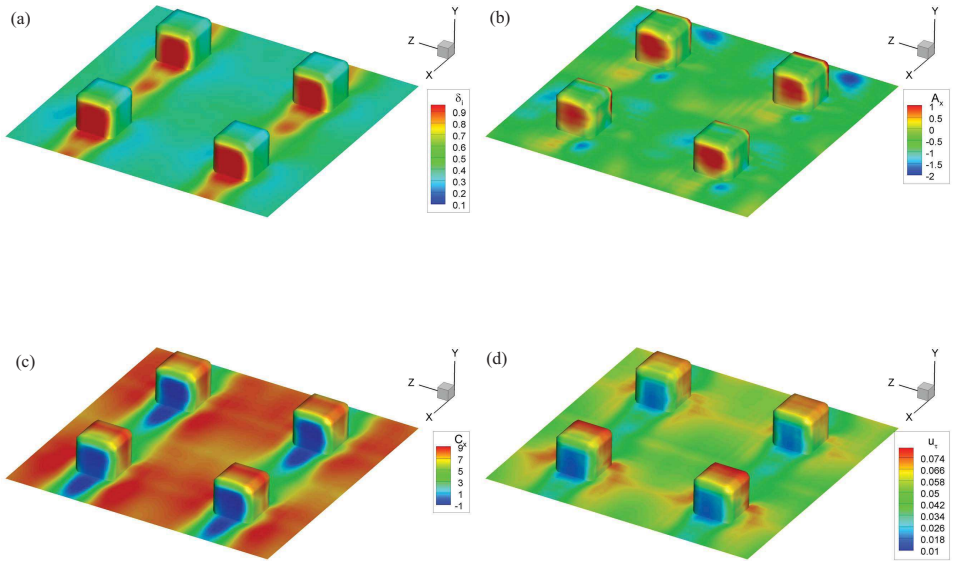

Figure 2.11: Contour plots of time-averaged surface values of the parameters δ_i/Δ_y (shown in (a)), A_x (b), C_x (c), and friction velocity u_τ (d) that result from the iWMLES model. Flow is in the positive X direction (from top right towards lower left in each panel).

from the wall model. Since all quantities and parameters fluctuate, time average results are shown. Specifically, for the parameter A_x the averaging is performed according to $\langle A_x(1-\delta_i/\Delta_y)\rangle \;/\; \langle 1-\delta_i/\Delta_y\rangle$, where $\langle\cdot\rangle$ is the time averaging operator. Similarly, the contours shown for C_x are obtained according to $\langle C_x(1-\delta_i/\Delta_y)\rangle \;/\; \langle 1-\delta_i/\Delta_y\rangle$. This particular weighting is done since A_x, C_x do not enter the model directly. Their contribution to the integral or boundary conditions is always weighted by the extent of the meso-layer, i.e. $(1-\delta_i/\Delta_y)$ (without such weighted averaging, the average values of A_x and C_x themselves can occasionally become very large but in those cases $\delta_i \to \Delta_y$ and thus they do not affect the integrations).

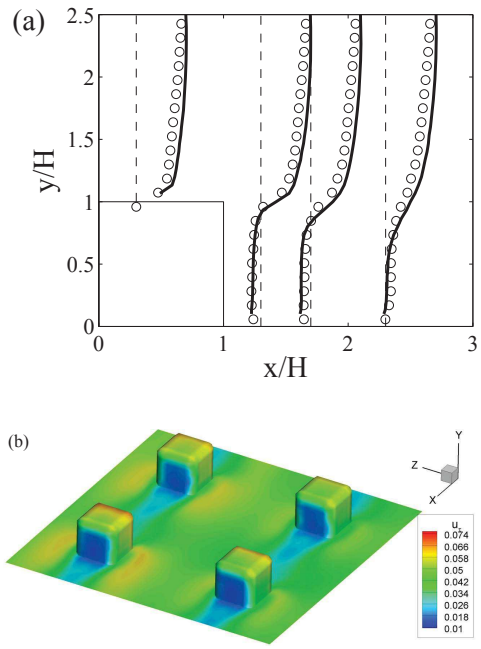

Figure 2.12: Results using equilibrium wall model. Left: Comparison of mean profiles (circles) with Ref. 1 (line), to be compared with Figure 2.10 (a) that uses iWMLES. (b): Contour plot of averaged u_τ for simulation that uses equilibrium wall model.

Figure 2.11 highlights interesting trends. In regions of very low velocity, we see that δ_i can be quite large and approaches Δ_y, i.e. the LES becomes locally wall-resolving such as in the back face of the cubes where the flow recirculates. Near the top of the cubes, large velocities yield small δ_i and large friction velocities, as well as large A_x values.

In order to highlight the effect of including the additional physics into the iWMLES approach, we have also run the same case but using an equilibrium wall model. In this case u_τ is determined iteratively at each point simply using the equilibrium law of wall $u/u_\tau = 1/\kappa \log(yu_\tau/\nu) + B$ at each time step and each surface point, i.e. assuming that the first grid point is in the logarithmic region of a smooth-wall boundary layer.

The mean streamwise profiles are shown in Fig. 2.12(a) where it is seen that the equilibrium wall model in fact yields a lower velocity above the cubes. The root-mean-square of the difference between the simulated profile and the experimental data is 0.18 for equilibrium wall model and 0.09 for the integral approach. We have tracked down this trend to the lower drag force predicted at the lower surface in between the cubes (channels) where flow is less hindered by surface drag and since the input velocity and flow rate is prescribed, slightly less flow is deflected upwards towards the center of the channel. Figure 2.12 (b) in fact shows that the predicted friction velocity is indeed lower in this case when assuming equilibrium wall model. We can see that for cases where the effects of near wall physics other than viscous and turbulent diffusion are important, the advantage of an integral wall model can already been seen in mean profile.

2.4.4 Sample application to flow over surface with truncated cones

In the applications and tests of rough surfaces presented so far, we considered either surfaces with 'subgrid roughness' (modeled using a prescribed y_0, or D_d and a_L), or smooth surfaces with numerically resolved roughness elements (i.e. wall attached cubes). It is of interest to illustrate the effect of subgrid surface roughness on the mean velocity and total surface drag force when combining both effects in

LES. Specifically we aim to show that the iWMLES approach applied to cases with resolved roughness elements can lead to differing results depending on the subgrid roughness of the surfaces on the resolved elements themselves, as well as those of the underlying surface. In order to showcase this effect, we apply the model to simulate a developing turbulent boundary layer over a rough surface that also contains with attached truncated cones whose surface is also rough. These can be thought of as idealization of bio-fouling elements such as barnacles that grow on ship hulls. The barnacles are idealized as conical frustums, whose height is $h_c = 0.25\delta_0$, where δ_0 is the height of the incoming turbulent boundary layer. The computational domain has size $16\delta_0$ in streamwise direction and $4\delta_0$ in both spanwise and vertical direction. The inlet free-stream velocity is $U_\infty = 10$ m/s. The incoming boundary layer thickness is $\delta_0 = 0.1$m and the fluid viscosity used is $\nu = 1 \times 10^{-6} m^2/s$ (i.e. $Re_{\delta_0} = 10^6$).

The cone's bottom radius is $0.25\delta_0$ and their top radius $0.125\delta_0$. These cones are resolved using the immersed boundary method. In addition, the surfaces and the underlying wall are covered with additional small-scale (unresolved) roughness elements. In order to show the effects of such roughness, two unresolved roughness height are used, $k = 0.01\delta_0 = 0.04h_c$ and $k = 0.0001\delta_0 = 0.0004h_c$). In both cases we use, as before, $C_d = 0.1$ and $a_L(y) = 1$ up to $y = k$ and zero above. Figure 2.13 shows snapshots of the flow field illustrating the streamwise velocity and pressure at a plane cutting the barnacle elements at 80% of their height. The figure also shows vortices in the boundary layer.

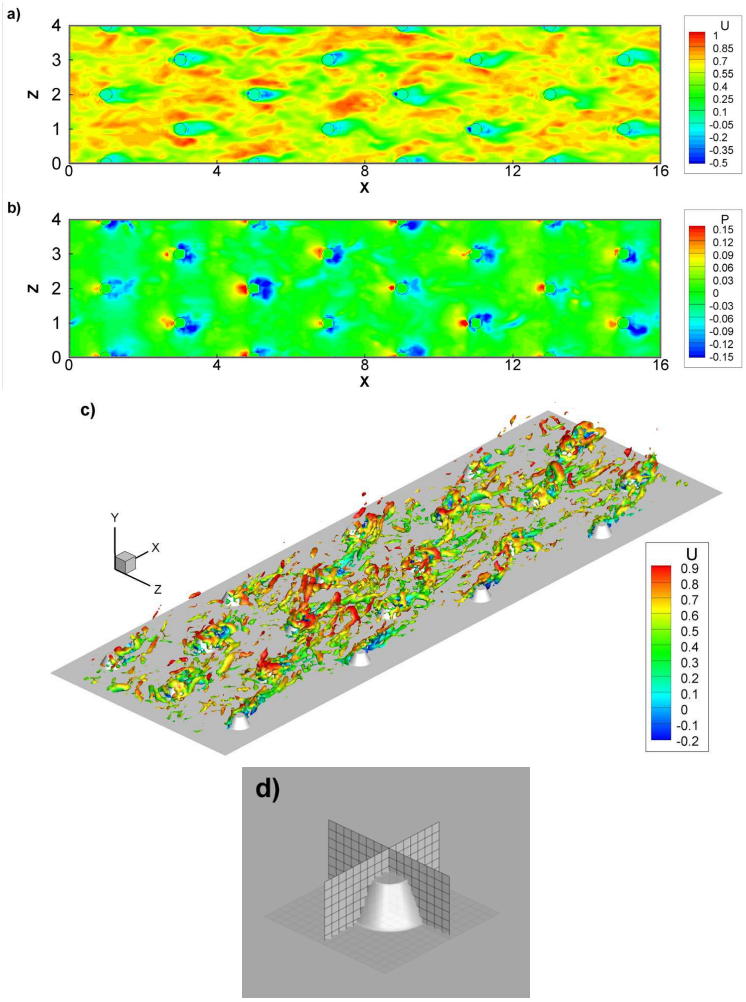

Figure 2.13: Instantaneous streamwise velocity (a) and pressure contours (b) taken at $y = 0.20\delta_0$, 80% of the resolved roughness height, for the case $k = 0.0001\delta_0$; and iso-surface of vortices using the swirling strength, colored by streamwise velocity (c). The velocity is normalized by the free stream velocity, while pressure is normalized using the free stream velocity (squared) and the boundary layer thickness at the inlet. The computational mesh around the conical frustums is shown in figure d.

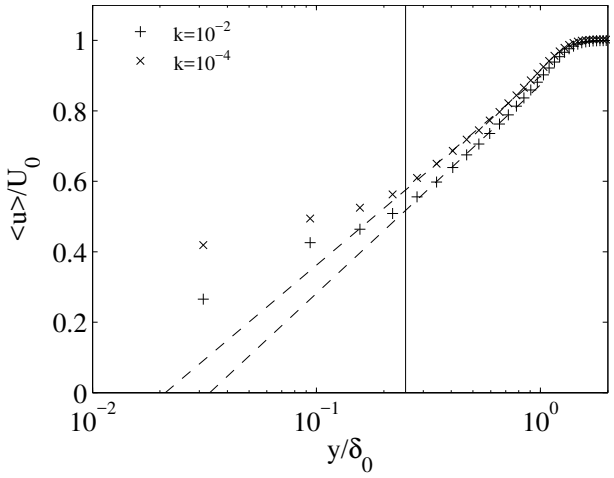

Figure 2.14: Mean velocity profile taken $12\delta_0$ downstream, where δ_0 is the boundary layer thickness at the inlet. The barnacle height is $0.25\delta_0$, and is marked by the solid line. The inferred effective roughness heights y_0 from the mean profiles are $y_0 = 0.033\delta_0$ for $k = 10^{-2}\delta_0$, and $y_0 = 0.021\delta_0$ for $k = 10^{-4}\delta_0$ respectively. The fits used to obtain these intercepts are shown as dashed lines.

Figure 2.14 shows the time and spanwise averaged profiles of streamwise velocity at $x = 12\delta_0$. These results show that while the profile is mainly determined by the resolved roughness, sub-grid roughness can play a non-negligible role in terms of the overall hydrodynamic properties of the surface and that such effects can be represented in the context of iWMLES.

2.5 Conclusions

A new approach for wall modeling in Large-Eddy-Simulations is proposed and tested in various applications. We adopt the classical integral method of von Karman and Pohlhausen (VKP) in which an assumed velocity profile with various parameters is postulated in replacement of numerical integration of the boundary layer equation

in the near-wall zone. The profile contains a viscous or roughness sublayer, and a logarithmic layer with an additional linear term accounting for inertial and pressure gradient effects. Similar to the VKP method, the assumed velocity profile coefficients are determined from appropriate boundary and matching conditions, as well as physical constraints. Similar to equilibrium wall model, the resulting integral wall model (iWMLES) is local and essentially algebraic. Thus its cost remains independent of Reynolds number and is thus significantly lower compared to standard zonal or hybrid wall models. Meanwhile, like the zonal model, iWMLES includes many near wall physics that are excluded from equilibrium wall models.

We have implemented and tested the integral wall model in the context of a pseudo-spectral code for fully developed channel flow with a dynamic Lagrangian subgrid model, as well as within a finite difference LES code including the immersed boundary method and the dynamic Vreman eddy-viscosity model. Test cases included standard turbulent fully developed half channel with unresolved roughness and over smooth surface at various Reynolds numbers, and developing boundary layer flows over smooth plates at various Reynolds numbers, over plates with unresolved roughness, and a case with resolved roughness elements consisting of an array of wall-mounted cubes for which detailed experimental data are available. A sample application to flow over a surface with truncated cones as idealized barnacle-like roughness elements is also presented.

Comparisons with canonical boundary layer behavior and with data show that the

proposed iWMLES method provides accurate predictions of mean near-wall velocity profiles in LES for both smooth and rough surfaces. Unresolved surface structures can be parameterized in this approach. Among others the results show that inferred hydrodynamic roughness heights from the mean velocity profile are essentially independent of Reynolds number for roughness elements whose local Reynolds number k^+ is sufficiently large (fully rough), as expected. An application of iWMLES to flow over wall-mounted cubes and comparisons with the use of an equilibrium wall model highlighted the effects of additional physics that can be included in the iWMLES approach. The sample application to flow over rough truncated cones shows that even when a surface contains large roughness elements, the 'subgrid roughness' of those surface elements and the bottom surface can have an appreciable effect upon the overall drag force and mean velocity profile.

Clearly, many further tests and applications to many flows should be attempted. In particular, flows in which non-equilibrium effects have major macroscopic repercussions should be considered. An example is flow in a diverging channel, where the separation point is known to be highly sensitive to near-wall physics. Also, generalizations to scalar transport, additional effects such as rotation, buoyancy, etc. can be considered. Further generalizations including dynamic formulations and additional considerations associated with the stress fluctuations could be further envisioned. As it is, however, the iWMLES approach already enables inclusion of rich boundary layer near-wall physics at a cost that scales comparably with equilibrium algebraic

wall models.

Chapter 3

Rescaling-recycling inflow generation for spatially-growing rough-wall turbulent boundary layers

3.1 Introduction

In this chapter we extend the Lund et al.[2] inflow generation technique for developing boundary layers over very rough surfaces in which surface elements are resolved on the computational grid and affect the mean velocity significantly in the vicinity of the wall. The material presented in this chapter has been published in Ref. 140. For

a comprehensive recent review of inflow generation techniques, see We (2016).[141]

3.2 Review of rescaling-recycling method for smooth surfaces

In this section, we briefly review the rescaling-recycling method of Lund et al[2] while also motivating the development of a rescaling-recycling method for rough wall boundary layer simulations. Consider simulation of the spatially developing turbulent boundary layer sketched in figure 3.1. The Cartesian coordinates x, y, z denote streamwise, wall normal, and spanwise directions, respectively. A realistic turbulent inflow condition is needed at the inlet plane. The instantaneous velocity is decomposed into mean ($\bar{u_i}$) and fluctuating (u_i') velocities. Both the mean and the fluctuating velocities sampled at the recycle plane are rescaled and recycled to the inlet plane to provide the inflow.

Consider the mean velocity profile first. It is determined by both the wall and the free stream properties. Generally, we have

$$\bar{u} = \bar{u}\left(y, l_\nu, l_\delta, u_\tau, U\right), \tag{3.1}$$

where additional dependence on (x) is assumed but not indicated explicitly. u_τ is the friction velocity, U is the free stream velocity, l_ν is an inner length scale introduced

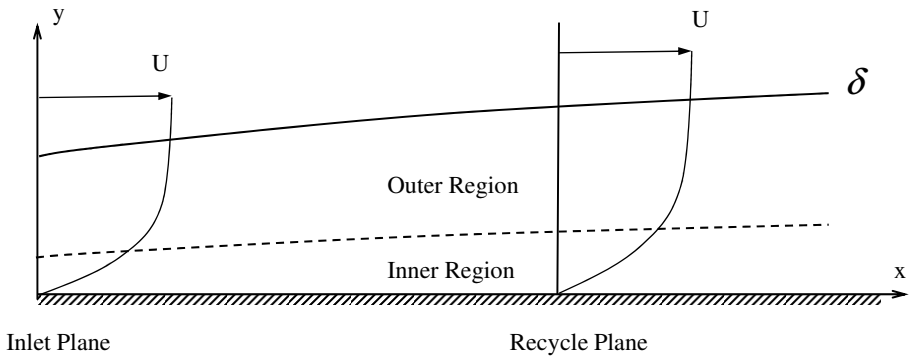

Figure 3.1: Schematic of developing turbulent boundary layer with the inlet plane and the recycle plane.

by the solid surface, and l_δ is an outer layer length scale, and is usually the boundary layer thickness δ. Lund et al[2] considered the case of a hydrodynamic smooth surface, in which case, $l_\nu = \nu/u_\tau$. Then $\bar{u}(y, l_\nu, l_\delta, u_\tau, U)$ can be written as $\bar{u}(y, \nu, u_\tau, U, \delta)$.

The inner region is mainly affected by the wall while the outer region is mainly affected by the free stream. Hence, Eq. 3.1 can be rewritten as follows[2]

$$\frac{\bar{u}}{u_\tau} = F_\nu\left(\frac{y}{l_\nu}\right)[1 - W(y, l_\nu, l_\delta)] + F_\delta\left(\frac{y}{l_\delta}, \frac{U}{u_\tau}\right)W(y, l_\nu, l_\delta), \tag{3.2}$$

where F_ν is the law of wall, F_δ is the defect law, and $W(y, l_\nu, l_\delta)$ is a weight function. Similar arguments apply to the fluctuations, i.e.:

$$\frac{u'}{u_\tau} = f_\nu\left(\frac{y}{l_\nu}\right)[1 - W] + f_\delta\left(\frac{y}{l_\delta}, \frac{U}{u_\tau}\right)W, \tag{3.3}$$

where f_ν, f_δ are the counterparts of F_ν, F_δ for the fluctuations and additional dependence on the other directions (x, z) is assumed but not written out. A weight function

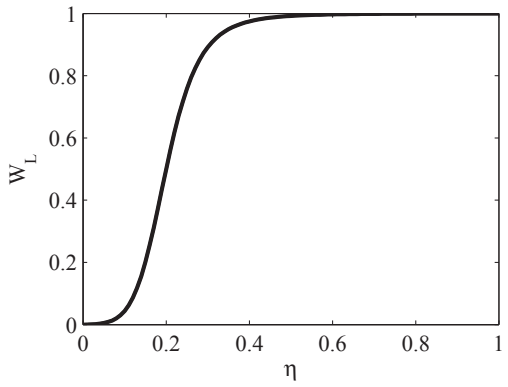

Figure 3.2: The weight function $W(\eta)$ proposed by Lund et al.[2]

was chosen for applications to smooth surface simulations in Lund et al[2] according to:

$$W_L(\eta) = \frac{1}{2}\left\{1 + \tanh\left[\frac{\alpha(\eta - b)}{(1-2b)\eta + b}\right] \Big/ \tanh(\alpha)\right\}, \tag{3.4}$$

where $\eta = y/\delta$, and $\alpha = 4$, $b = 0.2$. The weight function vanishes at $\eta = 0$ and is $W = 0.5$ at $\eta = b$. The parameter α controls the width of the region over which the function transitions from 0 to 1.

By using Eqs. 3.2 and 3.3, the velocity at the recycle plane is rescaled and recycled to the inlet. Since velocity scales with u_τ locally, the friction velocity ratio at the inlet and recycle planes, $\lambda = u_{\tau,\mathrm{inl}}/u_{\tau,\mathrm{rec}}$, must be known to perform the rescaling. Here the subscripts rec, inl denote the recycle and the inlet planes, respectively. Lund et al[2] invoked an empirical relation $\lambda = (\theta_{\mathrm{resc}}/\theta_{\mathrm{inlt}})^{1/2(n-1)}$, where θ is the momentum thickness. An empirical value is used for n, typically $n = 5$ (but this exponent is expected to be Reynolds number dependent). This relation is valid only for smooth-surfaces boundary layers with zero pressure gradient. For the case of moderate roughness

lengths, a different relation can be used,[68] that is, the resistance formula of sand-roughened plate by Prandtl.[142] The friction velocity ratio λ is expressed in terms of the ratio of the momentum thickness $\beta = \theta_{\text{inl}}/\theta_{\text{rec}}$:

$$\beta^{-1} - 1 = \frac{c'_f}{2}\left(\frac{x}{\theta_{\text{inl}}}\right)\frac{1}{1-r}\left(\lambda^{2r-2/r} - 1\right), \tag{3.5}$$

where $r = 3.95/(2.87 + 1.58\log(x/k_s))$, c'_f is the local skin friction coefficient, k_s is the equivalent sand-grain roughness and x is the distance from the leading edge of the surface. The latter is determined from θ at the inlet using the resistance formula. For wider general applicability, e.g. to include effects of pressure gradients and Reynolds number, Araya et al.[143] proposed a dynamic approach to compute λ by using a secondary sampling (test) plane.

Having summarized the various existing recycle methods based on Ref. 2 for smooth surfaces, we proceed to consider the case of rough wall boundary layers in which surface elements are resolved on the computational grid, i.e. their effects are not being modeled by an equivalent sand-grain roughness. In the fully rough regime, the viscous length scale ν/u_τ becomes irrelevant. Another appropriate inner sublayer length scale l_d that characterizes the inner layer is needed. Possible candidates for this inner length scale can be the roughness height k, which is only well defined for regular roughness with fixed height, or the hydrodynamic roughness length y_o. The latter is difficult to obtain dynamically within a simulation (except for some cases where the

surface has scale-invariant properties, see[144]). Here we propose to diagnose vertical distributions of the dispersive stress, as explained in more detail in the next section, §3.3. There the use of this length scale is compared to other possible candidates. Another aspect in which the presently proposed approach differs from the original Lund et al[2] method concerns the weight function $W(\eta)$. For the rough surfaces envisioned in the present work, the region in which the weight function is 0, i.e. the region in which the flow configuration is dominated by the surface roughness, must be dependent on the surface roughness properties, suggesting explicit dependency of W on the inner scale, not just $\eta = y/\delta$. A different weight function therefore has to be employed for rough wall boundary layer simulations.

Finally, in the fully rough regime, there is some evidence[145–148] that the friction velocity becomes independent of Reynolds number, which would imply $\lambda = 1$. However, for the most general case involving a finite ratio between the roughness scale and δ, the friction factor can still depend on the ratio of the roughness height to δ and since δ depends on x, possible dependencies on downstream distance are possible.[149] Recent work[150] has observed a mild decrease in friction velocity with downstream distance, even in the fully rough regime. Since no universal empirical law exist for λ for general rough surfaces, these findings suggest that a dynamic approach[143] is desirable. In this work we will test both the dynamic approach and setting $\lambda = 1$ in simulations to be presented in §3.5. As will be seen, for the cases to be considered there is very little difference between the dynamic approach and $\lambda = 1$. It is noted

that the dynamic approach should be used if the streamwise distance between the rescaling plane and the inlet is large and appreciable decrease in the friction velocity is expected from the inlet to the rescaling plane. In the next section, methods to specifying the weight function and determining the appropriate roughness scale for simulations of flow over very rough surfaces are presented.

3.3 Inner scale and weight function for rough surfaces

Eq. 3.4 was developed for flow over smooth surfaces. Employing this weight function for rough-surface boundary layer simulations can be problematic if the surface under consideration has roughness elements of a size k that is not negligible compared to the boundary layer thickness, e.g. with $k > 0.2\delta$ as illustrated in figure 3.3. If the weight function in Eq. 3.4 is to be used, the rescaled velocity profile would lead to an erroneous inflow (denoted by the dashed line). The cause for this erroneously rescaled profile is an underestimation of the penetration depth of the surface heterogeneity into the bulk of the flow.

For general applicability, we require a surface length-scale that characterizes the mean flow heterogeneity due to the roughness elements in the surface layer. We denote this "penetration depth" of the surface heterogeneity as l_d. Below l_d, the flow is dominated by the surface roughness while above l_d, the mean velocity is horizontally

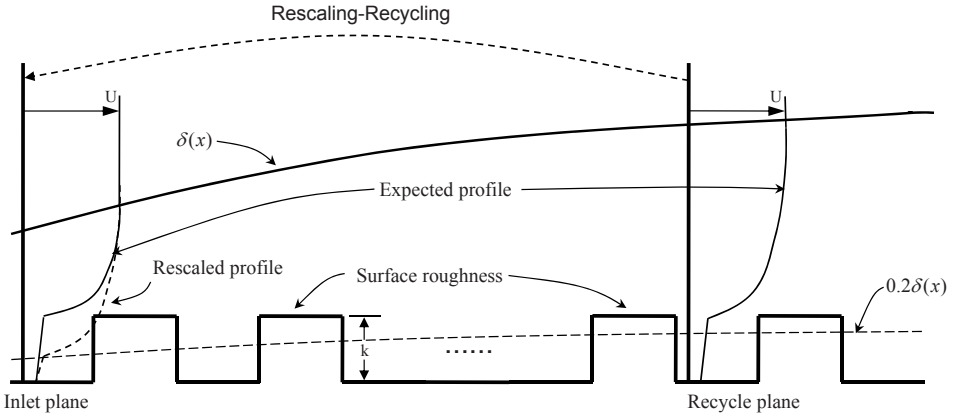

Figure 3.3: Sketch of recycle-rescaling method with the traditional weight function when applied to a case in which the roughness height k is $k > 0.2\delta$. The method causes an erroneous inlet mean velocity profile (dashed line).

approximately homogeneous. We seek to impose the requirement that the weight function must be 0 for $y < l_d$ (i.e. the rescaling is entirely dominated by inner scales there). If l_d is known, the traditional weight function can thus be modified to the new 'rough-wall' weight function W_R defined according to:

$$W_R\left(y;\delta,l_d\right) = \begin{cases} 0 & y < l_d, \\ W\left(\frac{y-l_d}{\delta-l_d}\right) & l_d \leq y < \delta, \end{cases} \tag{3.6}$$

where W is the traditional weight function by Lund et al[2] (defined in Eq. 3.4). W_R reduces to W if $l_d = 0$. Typically, W_R would have an extended inner region compared to W_L.

As a next step, we need to determine the inner scale l_d. An apparent candidate for l_d could be the roughness height k, but to set $l_d = k$ is in fact unphysical because, among others, k is unchanged when the coverage density is changed. For instance,

if very sparsely distributed elements are used, the roughness height k can be an overestimate of the actual average penetration depth of the inner region. Also, k is difficult to define for the case of multi-scale roughness e.g. roughness elements of different heights.

Instead of defining l_d based on geometric surface properties, which often do not correlate easily to hydrodynamic properties, we propose to use properties of the mean flow itself to diagnose the flow heterogeneity. Specifically, we propose to define the surface heterogeneity penetration depth in terms of stream-wise dispersive stress[151,152] T_{xx}, where T_{xx} is defined according to:

$$T_{xx}(x,y) = \langle \bar{u}\bar{u} \rangle_z - \langle \bar{u} \rangle_z^2 , \tag{3.7}$$

and where $\langle \cdot \rangle_z$ is the spanwise averaging operator. If no surface heterogeneity is present in the spanwise direction, $\langle \bar{u}\bar{u} \rangle_z$ is equal to $\langle \bar{u} \rangle_z^2$ and T_{xx} vanishes. It is helpful to illustrate typical profiles of dispersive stresses by means of an application. We use large eddy simulation of flow over wall mounded cubes in an aligned configuration. We have used the in-house code Vicar3D to conduct this LES (see sect. 2.4.3 for details of the code). The roughness element height, k compared to the inlet boundary layer thickness, δ_0, is $k = 0.25\delta_0$. The solidity is 0.25. In units normalized by δ_0, the local boundary layer thickness is 1.18 at $x = 5$ and 1.39 at $x = 9$. Additional details about the simulation and this data set are provided in the section below (§3.5).

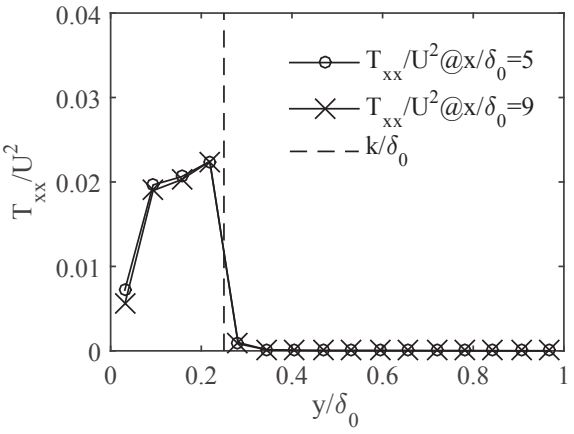

Figure 3.4: Profiles of dispersive stress T_{xx} for LES case a described in §3.5 at two streamwise locations where the flow is developed.

A typical profile of dispersive stress is plotted in figure 3.4, from which we can make two observations. First, T_{xx} drops dramatically for $y > k$. Similar results have been reported before, see.[153–155] Second, the dispersive stress profile does not depend on the boundary layer thickness. The first observation suggests a definition of l_d as the vertical distance where T_{xx} drops to a certain threshold of its maximal value. Potentially l_d according to this definition can be a function both of the surface roughness and boundary layer thickness. The second observation, however, suggests that l_d scales only with the surface roughness. This is further supported by figure 3.5, where we have plotted the boundary layer thickness and the distance by which T_{xx} drops to 3% and 10% of its local maximum value. We can see from figure 3.5 that while considerable increase is observed in the boundary layer thickness, no observable increase or decrease can be seen in l_d based on the 3% or 10% threshold criteria. Considering the fact that W_R involves a transitional region from being $y = l_d$ to

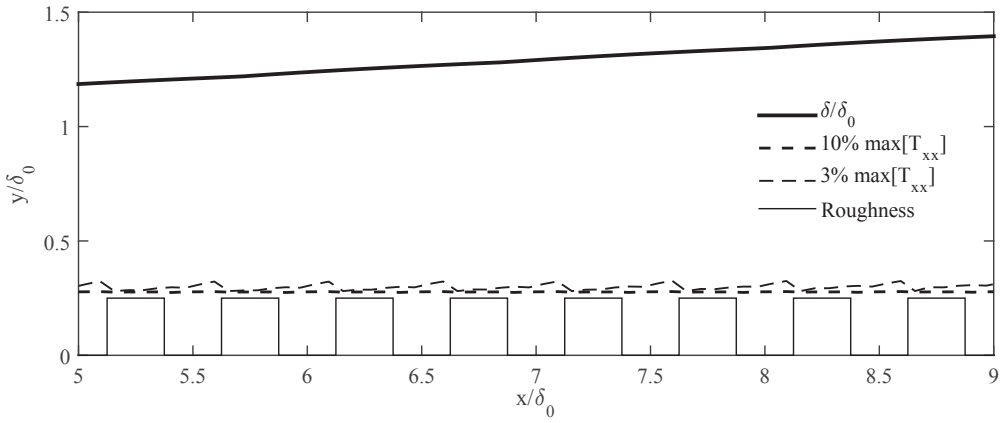

Figure 3.5: Various length scales in the developing boundary layer. The surface roughness is perfectly aligned cubes with surface solidity being 0.25. The cube height k is 0.25 and the roughness is plotted by thin solid line. The distance where T_{xx} drops to 3% and 10% of its local maximum value is marked by thin dashed line and thick dashed line, respectively. The boundary layer thickness based on $99\%U$ is marked by thick solid line. Details on this simulation and data set is presented in §3.5.

$y = \delta$, we define l_d to be the vertical distance at which T_{xx} drops to 10% of its local maximum value. The behavior of l_d defined based the 3% or 10% threshold criteria is further examined in §3.5, where for hemispherical roughness elements one can observe significant streamwise variations and differences to k, thus justifying the use of T_{xx} instead of k as a criterion to determine l_d. We note here that while it is known that some effect of surface roughness can still be seen further into the core region (up to $2 - 5k$, where k is the roughness height[41,156]), the length scale l_d denotes only the region within which the effect of roughness dominates the mean flow.

3.4 Rescaling-recycling method for rough surface boundary layers

In this section we summarize the rescaling-recycling method for spatially evolving rough wall boundary layers. We use l_d to be the inner length scale instead of l_ν, and the boundary layer thickness $\delta(x)$ as the outer length scale. Since l_d depends only on the surface roughness, we have $l_{d,\text{inl}} = l_{d,\text{rec}}$ for streamwise homogeneous roughness distributions. Thus we will drop the subscript "inl" and "rec" for l_d for convenience.

At any downstream position x we decompose the velocity into a spanwise mean and deviations according to:

$$u_i = \langle \bar{u}_i \rangle_z + u_i''. \tag{3.8}$$

As a result, the velocity fluctuations u_i'' include both fluctuations from the turbulence unsteadiness and the span-wise spatial heterogeneity of the mean velocity due to the

surface roughness. The rescaling is performed according to Eqs. 3.2 and 3.3:

$$\begin{aligned}
(\langle\bar{u}\rangle_z)^{\text{inner}}_{\text{inl}}(y/l_d) &= \lambda\ (\langle\bar{u}\rangle_z)_{\text{rec}}(y/l_d),\\
(\langle\bar{u}\rangle_z)^{\text{outer}}_{\text{inl}}(y/l_{\delta,\text{inl}}) &= \lambda\ (\langle\bar{u}\rangle_z)_{\text{rec}}(y/l_{\delta,\text{rec}}) + (1-\lambda)U,\\
(\langle\bar{v}\rangle_z)^{\text{inner}}_{\text{inl}}(y/l_d) &= \lambda\ (\langle\bar{v}\rangle_z)_{\text{rec}}(y/l_d),\\
(\langle\bar{v}\rangle_z)^{\text{outer}}_{\text{inl}}(y/l_{\delta,\text{inl}}) &= \lambda\ (\langle\bar{v}\rangle_z)_{\text{rec}}(y/l_{\delta,\text{rec}}),\\
(\langle\bar{w}\rangle_z)^{\text{inner}}_{\text{inl}}(y/l_d) &= 0,\\
(\langle\bar{w}\rangle_z)^{\text{outer}}_{\text{inl}}(y/l_{\delta,\text{inl}}) &= 0,\\
\left(u_i''\right)^{\text{inner}}_{\text{inl}}(y/l_d) &= \lambda\ \left(u_i''\right)_{\text{rec}}(y/l_d),\quad i=1,2,3,\\
\left(u_i''\right)^{\text{outer}}_{\text{inl}}(y/l_{\delta,\text{inl}}) &= \lambda\ \left(u_i''\right)_{\text{rec}}(y/l_{\delta,\text{rec}}),\quad i=1,2,3.
\end{aligned} \tag{3.9}$$

The rescaled velocity components ($i = 1, 2, 3$) are:

$$(u_i)_{\text{inl}} = \left[(\langle\bar{u}_i\rangle_z)^{\text{outer}}_{\text{inl}} + (u_i'')^{\text{outer}}_{\text{inl}}\right] W_R(y/l_{\delta,\text{inl}}) + \left[(\langle\bar{u}_i\rangle_z)^{\text{inner}}_{\text{inl}} + (u_i'')^{\text{inner}}_{\text{inl}}\right] \left[1 - W_R(y/l_{\delta,\text{inl}})\right], \tag{3.10}$$

where W_R is defined in Eq. 3.6, $\lambda = u_{\tau,\text{inl}}/u_{\tau,\text{rec}}$ is obtained dynamically (see appendix 8.2.1). It has been found, however, that there is barely any difference if λ is set to be 1 or determined dynamically, in the cases considered here. The scale l_d is obtained dynamically from the profile of dispersive stresses as explained in the previous section. The profiles of $T_{xx}(y)$ can in turn be obtained from the mean velocity distributions during the simulation provided an appropriate time-averaging procedure is used. Here temporal averages of any quantity ϕ are computed using a exponentially weighted time

averaging:[157]

$$\bar{\phi}^n = \bar{\phi}^{n-1}\left(1 - \frac{\Delta t}{T}\right) + \phi^n \frac{\Delta t}{T}, \tag{3.11}$$

where Δt is the simulation time step size, T is the prescribed averaging time scale. We use $T = \delta_0/\kappa u_\tau$, where δ_0 is the inlet boundary layer thickness, κ is the Karman constant and u_τ is the estimated friction velocity.[124]

For self-consistency, the proposed method requires the roughness elements and configuration downstream of the rescaling plane to be the same as the roughness elements downstream of the inlet. Still the method is applicable to situations in which several boundary layer thicknesses downstream of the rescaling plane, where the roughness does not have direct influence on the flow field at the rescaling plane, the roughness is arbitrary. For example, using "|" to denote symbolically the locations of inlet and rescaling planes, assuming the flow goes from left to right, and denoting different roughness element types with different letters, this inflow generation technique could handle roughness represented by the sequence: |ABAB|ABCDEF$\cdots$.

3.5 Applications in large eddy simulations

All three cases in this section use a computational domain of size $16\delta_0 \times 4\delta_0 \times 4\delta_0$ in the x, y, z directions, respectively, where δ_0 is the boundary layer thickness at the inlet. The number of grid points (equally spaced) is $256 \times 64 \times 64$. On all surfaces, we use the equilibrium wall model with a prescribed roughness length set at $y_0 = 10^{-4}\delta_0$

Table 3.1: Details of the surface roughness. The parameter λ_f is the solidity, defined to be the total projected frontal roughness area per unit of wall-parallel projected area. λ_p is defined to be the percentage of the wall-parallel area covered by roughness elements. k is the roughness height, defined to be the distance between the wall and the highest point of the roughness.

surface	λ_f	λ_p	k/δ_0	roughness geometry
a	0.25	0.25	0.25	cube(aligned)
b	0.10	0.20	0.25	hemisphere(aligned)
c	0.13	1.00	0.25	$\lvert\sin(2\pi z)\rvert \times (\lvert\sin(2\pi x)\rvert + \lvert\sin(\pi x)\rvert)$

(i.e. much smaller than the roughness elements such that the subgrid roughness does not contribute significantly to the momentum balance). Periodic boundary conditions are used in the spanwise (z) direction. The top boundary condition is a zero gradient condition. A standard zero-diffusion condition is employed at the outlet. The code has been extensively validated.[136] A validation case that is particularly relevant is provided in Appendix 8.2.2. The free stream velocity U is used as a velocity scale and the boundary layer thickness δ_0 at the inlet is used as a length scale to normalize all results shown. The inflow velocity is prescribed via the extended rescaling-recycling method described in section 3.4.

We present results from three cases of developing boundary layers over surfaces with various roughness solidities and shapes (table 3.1) using the extended rescaling-recycling method. Roughness elements of a single size are used in cases a and b, while the roughness in case c is multi-scale. When showing results, we omit the mean overbar ($\bar{\cdot}$) for convenience. In figure 3.6, a sample horizontal instantaneous streamwise velocity contour at $y/k = 0.5$ is shown along with the time averaged

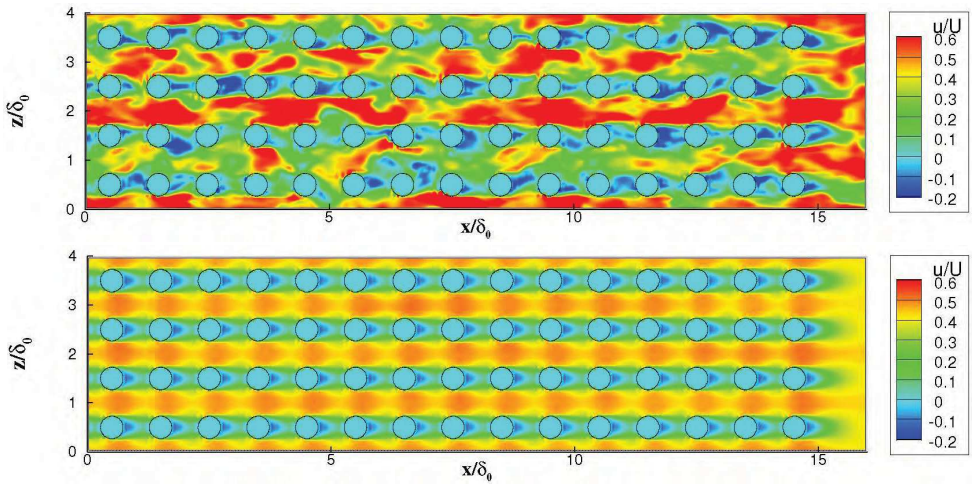

Figure 3.6: A sample horizontal instantaneous streamwise velocity contour (top) and the averaged velocity (bottom) at $y/k = 0.5$ for case b.

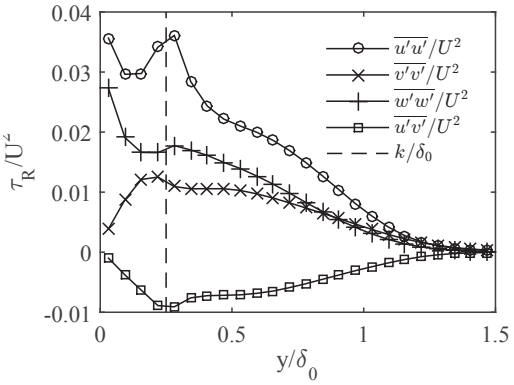

Figure 3.7: The Reynolds stresses at $x/\delta_0 = 5$ for case b.

velocity for case b. The normal Reynolds stresses and the Reynolds shear stress for case b at $x/\delta_0 = 5$ are plotted in figure 3.7.

The downstream evolution of various length scales for the three cases is plotted in Figs. 3.5 and 3.8. The recycle plane is located at $x/\delta_0 = 8$. We make three observations. First, the growth of the boundary layer thickness is nearly linear. A linear growth in boundary layer thickness is considered to be one condition of self-

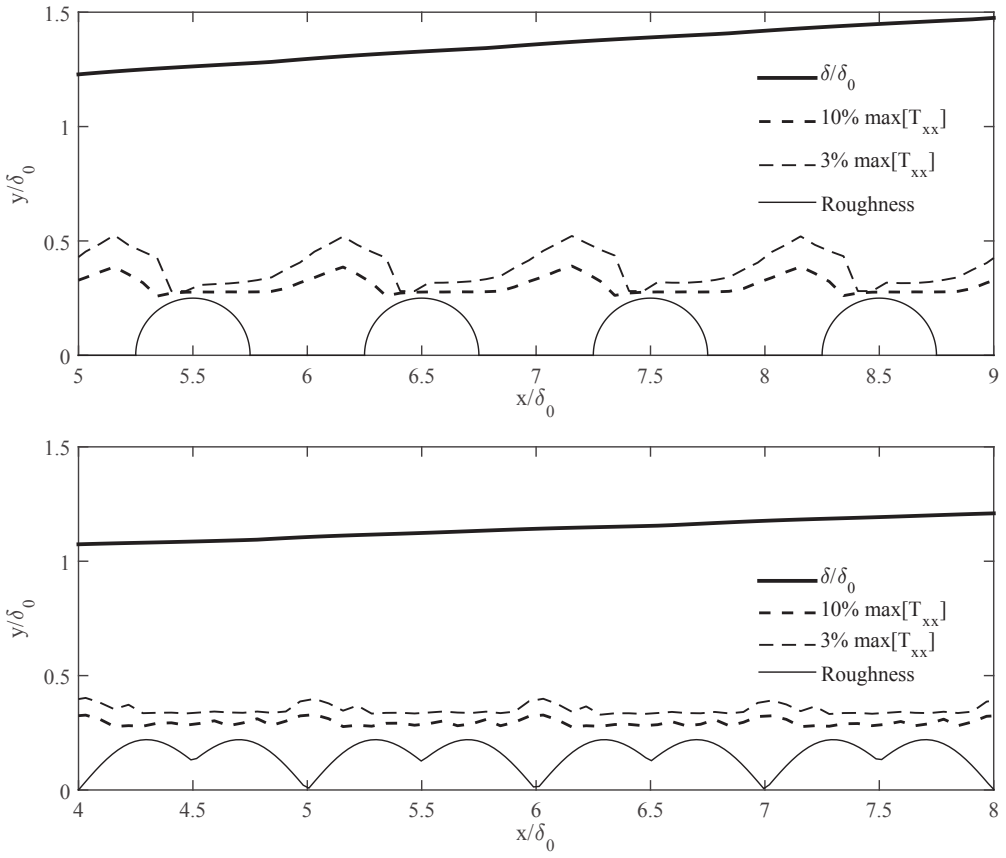

Figure 3.8: Outer and inner length scales in the developing boundary layer for case b, and c.

preservation.[158] Similar results have been reported both in experiments and numerical computations,[158].[147] Second, the length scale l_d, defined to be the vertical position at which the dispersive stress drops to 10% of its local maximum, is responsive to the near wall flow configuration – the roughness height k (maximum element height) is the same for all three cases, but l_d differs from case to case. Third, as we have mentioned in section 3.3, l_d is rather independent of the boundary layer thickness. Even as $\delta(x)$ grows nearly linearly, l_d remains constant.

At the inlet plane, l_d is 0.27 δ_0, 0.31 δ_0, 0.32 δ_0 respectively for cases a, b, and c.

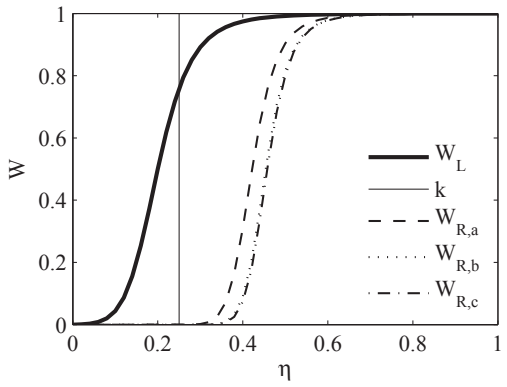

Figure 3.9: Weight function at the inlet plane for three cases. The weight function by Lund et al[2] is also plotted. The roughness height is marked with a thin solid line. At the inlet plane $\eta = y/\delta = y/\delta_0$

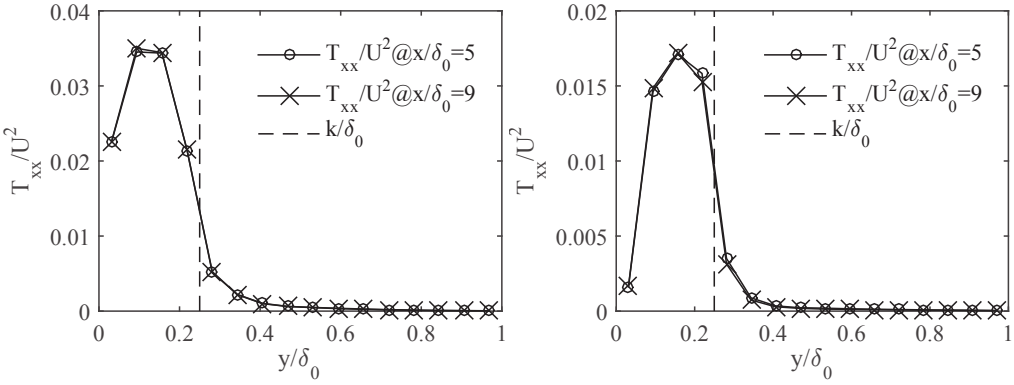

Figure 3.10: Profile of the dispersive stress at two different streamwise locations. The left figure is for case b and the right figure for case c.

The presently used weight function W_R is compared with W_L in figure 3.9. An inner region that has zero weight is present in W_R for all three cases.

The profiles of the dispersive stress at two different streamwise locations are plotted in figure 3.4 and figure 3.10. Two observations can be made that confirm previous observations: the dispersive stress drops rapidly beyond the roughness height and there is little difference both in the shape of the profile and strength downstream.

A self-consistency check for the proposed rescaling-recycling method is to examine

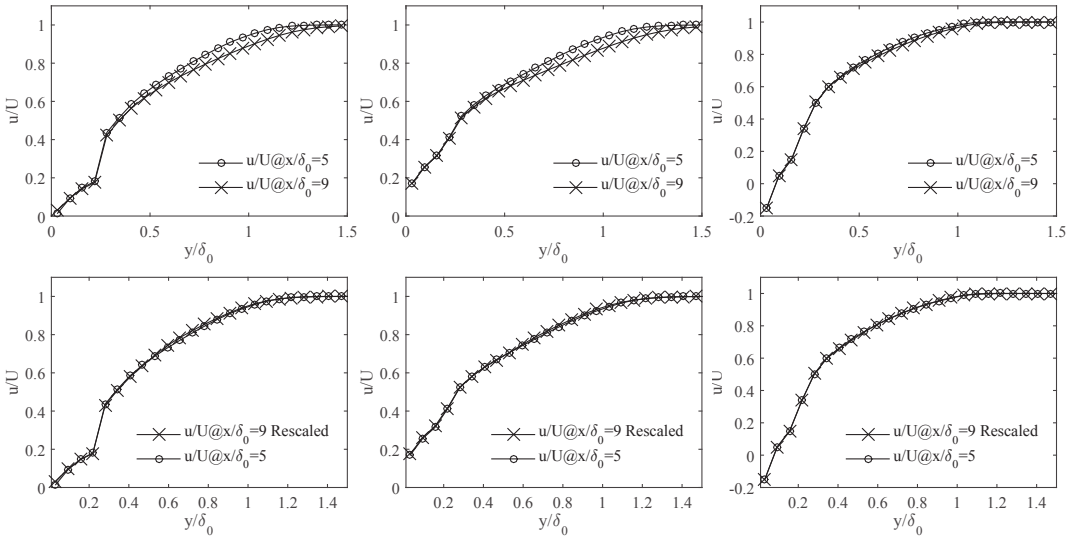

Figure 3.11: Velocity profiles at two different streamwise locations, from left to right for cases a-c, respectively. The top row is the raw velocity while the bottom row compares the mean velocity profile at the plane $x/\delta_0 = 9$ after rescaling according to Eq. 3.10 and the mean velocity upstream at $x/\delta_0 = 5$.

whether the rescaled velocity downstream collapses with the mean profile upstream. A good test is to perform this check between two planes different from the recycle and inlet planes. The un-rescaled and rescaled profiles are compared in figure 3.11.Indeed, a very good collapse of the rescaled downstream velocity profile and the upstream velocity profile can be observed. Also, one may observe an inner layer that is quite independent of the bulk flow. We also include a sample comparison of the rescaled and unrescaled Reynolds stress $\overline{u'u'}$ with $\overline{u'u'}$ upstream in figure 3.12 for case b. A good collapse is again observed.

We then plot the velocity profiles in log-linear scale in figure 3.13. Above the surface roughness elements there is some indication of a logarithmic region whose extent appears to grow slightly with downstream distance. Also, an indication that

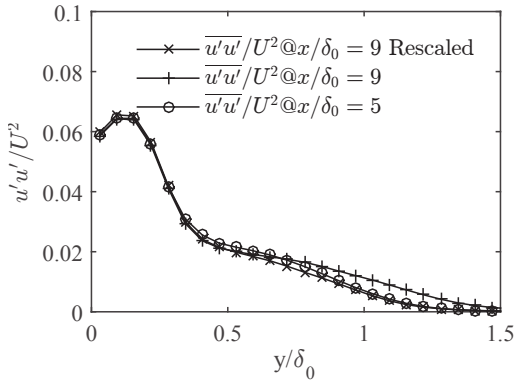

Figure 3.12: A sample comparison of the rescaled Reynolds stress with the Reynolds stress upstream in figure 3.12 for case b.

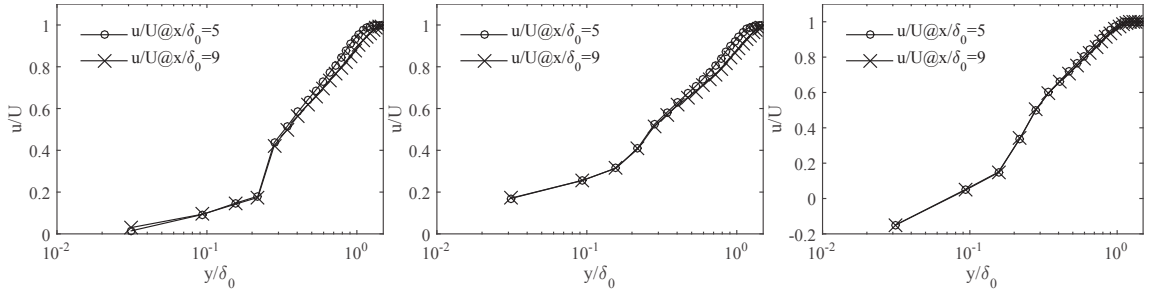

Figure 3.13: Mean velocity profiles at two different streamwise locations for cases a-c plotted in a log-linear scale.

its slope slightly decreases with downstream distance is consistent with an increase in the length-scale ratio $\delta(x)/k$.

Lastly we examine the periodicity introduced to the signal by rescaling-recycling. In figure 3.14, we plot the frequency spectrum of the streamwise velocity at $y = k$ and $y = \delta_0$ at the rescaling plane (located at $x = 8\delta_0$). It is observed that the periodicity brought in by recycling the fluctuating velocity to the inlet does not contribute significantly to the energy spectrum, i.e. no artificial peak is observed at $f\ 8\delta_0/U_C = 1$.

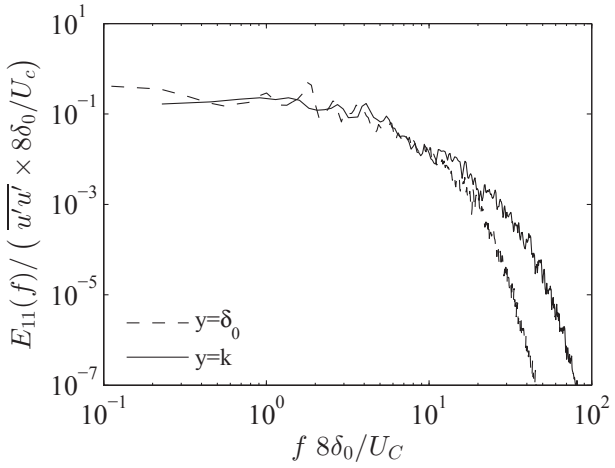

Figure 3.14: Frequency spectrum of the streamwist velocity at $y = k$ and $y = \delta_0$ at the rescaling plane. The frequency is normalized by $8\delta_0/U_C$, where U_c is the convective velocity, i.e. the mean velocity at $y = k$ and $y = \delta_0$.

3.6 Conclusions

The rescaling-recycling method of Ref.[2] has been extended to spatially evolving boundary layers over very rough walls. For the inner roughness region where the flow configuration is dominated by the surface roughness a length scale, l_d can be defined in terms of profiles of the streamwise component dispersive stress tensor. This length scale is used for inner layer velocity rescaling as well as to specify the inner region depth for the weight function. The extended rescaling-recycling method has been applied for inflow specification for LES of boundary layer flow over walls with various surface roughness characteristics. Rescaled downstream velocity profiles were shown to collapse with the velocity profile upstream. It was shown that the newly defined inner layer length scale is responsive to roughness properties of the surface while being nearly independent of the boundary layer thickness as it evolves downstream.

The general rescaling-recycling method therefore enables one to simulate developing boundary layer flows over surfaces with large resolved roughness elements.

We close with a final comment on the inner layer length scale and its relationship to the mean and fluctuating velocities. In Lund et al,[2] the same inner layer length scale ν/u_τ is used for both the velocity fluctuations and mean velocity. Recent experiments[90,92–94] and numerical simulations[159] have reported a generalized log-law for the variance of streamwise velocity fluctuations for turbulent boundary layers. The results show a relationship of the form $\left\langle (u'^+)^{2p} \right\rangle^{1/p} = B_p - A_p \ln(y/\delta)$, where $'$ denotes fluctuations, $+$ denotes normalization by u_τ, p is an integer, and A_p, B_p are universal constants. Different from the log-law of mean velocity profile, where the wall distance is normalized by ν/u_τ, this generalized log law for velocity fluctuations suggests that the appropriate length scale for velocity fluctuations in the log-region (i.e. still within the inner region) is the boundary layer thickness, δ. This represents a possible conflict between the rescaling-recycling method for the smooth surface[2] and present rough-wall implementation and the observations of generalized logarithmic laws for the fluctuations. A simple generalization to resolve this inconsistency is to adopt a different weighting function for velocity fluctuations. Such generalizations are left to be explored in further work.

Chapter 4

LES of flow over rough walls and an analytical rough wall model

4.1 Introduction

In this study we aim to provide an analytical description of rough wall boundary layers by adopting the von-Karman Pohlhausen integral approach,[160] in which a functional form for the mean velocity is assumed, including parameters that must be obtained from physical constraints. At the simplest level, there have been expectations that an exponential profile occurs within the roughness layer. This expectation can be motivated[8,9,161] by writing the Reynolds-averaged streamwise momentum equation in which the vertical (direction z) gradient of momentum flux (modeled using a constant mixing-length eddy viscosity) balances the distributed drag from roughness

elements:

$$\frac{d}{dz}\left[l_m^2\left|\frac{dU(z)}{dz}\right|\frac{dU(z)}{dz}\right] = C_d U(z)^2 \frac{dA_f}{dV}. \tag{4.1}$$

Here dA_f/dV is the projected frontal area per unit volume, and l_m and C_d are the mixing length and drag coefficient, respectively. These quantities can in principle be z-dependent, but at this stage they are assumed to be constant in order to obtain a simple solution, whose validity must then be tested empirically. It can be readily seen that an exponential function of z, $U(z) \sim \exp(z)$, solves Eq. 4.1:

$$U/U_h = \exp\left[a(z/h - 1)\right] \tag{4.2}$$

where h represents the height of the roughness elements, U_h is the velocity at $z = h$, and a is an attenuation factor (that depends upon the parameters in Eq. 4.1).

Our first goal is to establish additional empirical evidence to confirm or refute the expectation of an exponential velocity profile under more realistic conditions in which some of the underlying assumptions used in Eq. 4.1 may not hold exactly. Therefore, as a first step we determine the mean flow behavior within the roughness layer via a series of Large-Eddy-Simulations (LES) of turbulent boundary layers over arrays of wall-attached rectangular prism roughness elements. Various height distributions, arrangements and surface coverage densities are considered. The results will be shown to support a generic form for the velocity profile within the roughness layer with exponential behavior, Eq. 4.2. This observation motivates us to employ an exponential

shape function for the velocity profile with free parameters (a, U_h, ..) that depend on the local surface morphometric properties and flow configurations in the roughness sublayer. Since we have used the shape function in place of the momentum equation within the roughness sublayer, the model is algebraic rather than differential. A similar approach has been used recently to develop a new wall model for Large-Eddy-Simulations.[124] In order to determine the most important profile parameter, namely the attenuation coefficient a in the exponential function, an additional model for mutual sheltering effects among roughness elements must be included. While the model is developed for possibly more general rough surfaces, it is motivated, validated and applied here only for the specific, but important, case of 3D and 2D rectangular roughness elements with uniform and non-uniform height distributions. As mentioned before such surfaces are commonly found in urban canopies but also in flow over engineered surfaces such as electronic circuit boards, etc. In developing an analytically tractable model for hydrodynamic roughness, we are motivated by the continued relevance of such models when computational flow predictions spanning multiple scales and levels are required. For example, in the newly introduced integral wall model for LES,[124] for high Reynolds number flow over rough surfaces in which the roughness falls much below the first grid-point affordable via LES near the surface, an analytical model for the roughness length z_0 must still be provided to the (non-equilibrium) wall model. Modeling of geophysical flows also require such parameterizations, while engineering design tools require the ability to cover many

cases rapidly often precluding numerical simulations.

The remainder of the chapter is organized as follows: Numerical simulations (LES) that resolve the roughness elements within the roughness layer are used to determine the mean velocity profile in the roughness layer in §4.2. Motivated by the simulation results, the assumed shape function for the velocity profile is briefly described in §4.3 with various constraints that must be satisfied in order to build an analytical model. The shape function provides a horizontally averaged description of the flow field, yet some additional details about flow within the roughness sublayer in between roughness elements must also be taken into account to build the model. The flow within the roughness sublayer is examined and modelled in §4.3.2 where a geometry-based sheltering model is proposed. Detailed comparisons of the model predictions with experimental and numerical data for 3D cubic roughness elements and 2-dimensional elements (bars) are presented in §4.4. The model predictions for roughness with a non-uniform height distribution are compared with LES results in §4.4.3, 4.4.4. In order for the model to display the correct asymptotic behavior at low surface coverage, a correction for drag partitioning is included in appendix 8.3.2. Conclusions are given in §4.5. This work has been published in Ref. 162

4.2 Mean flow profiles within the roughness layer from LES

4.2.1 Simulation setup

We use the in-house finite-difference code Vicar3D to solve the incompressible filtered Navier-Stokes equations including the Vreman subgrid-scale model[138,163] and the iWMLES model for the near-wall closure.[124] Details of the code and the LES setup can be found in sect. 2.4.3. A validation of particular interest can be found in Ref. 124, where simulation results for channel flow with the bottom wall mounted with cubes has been compared with experimental measurements, showing good agreement in the predicted mean velocity distribution between the cubes. Considering the fact that in LES the sub-grid scale turbulence is not explicitly computed, we restrict the current analysis to the spatially/temporally averaged velocity profiles, which are expected to be less sensitive to SGS modeling than, say, second order statistics, and have been shown to be reproduced accurately by the code.

The roughness elements considered have the shape of rectangular prisms. The simulated flow is a spatially-growing boundary layer, for which the boundary layer height grows downstream. This enables us to sample results at various downstream distances, and thus test that the roughness parameters to be obtained (i.e. z_o, d) are independent of outer boundary layer conditions and Reynolds number that vary

slowly as function of x. The inflow is generated via an extended rough wall rescaling-recycling technique.[140] The boundary layer thickness at the inflow δ_0 is $4h_m$ (for single-height roughness cases) to $6h_m$ (for varying-height roughness cases), where h_m is the averaged roughness height. Length-scales are expressed in terms of the incoming boundary layer thickness (i.e. $\delta_0 = 1$) used for the reference case (simulations with single-height roughness). In these units, the value of the mean height of roughness elements is always $h_m = 0.25$, while the computational domain size is $16 \times 6 \times 6$ in the streamwise, spanwise, wall normal directions, respectively. The Cartesian mesh size for LES is $256 \times 96 \times 96$. The average roughness height h_m is resolved by 8 grid points in the vertical direction. For the cases with varying height, the inflow boundary layer is increased to $\delta_0' = 1.5$ (to keep the largest height from approaching the height of the incoming boundary layer thickness). The Reynolds number based on the inlet boundary layer thickness and freestream velocity is $Re_{\delta_0} = \delta_0 U_0/\nu = 10^6$, i.e. sufficiently high for the flow to be in the fully rough regime (U_0 is the free stream velocity and ν the kinematic viscosity). The surfaces of roughness elements themselves, as well as the bottom wall are assumed to be smooth with no subgrid-scale roughness. A total simulation time of 100 flow-through times is computed, using a time step $dt = 0.33dx/U_0$, where dx is the grid spacing in the streamwise direction. The flow-through time is defined as $T_0 = L_x/U_0$, where $L_x = 16$ is the computational domain size. The code is massively parallelizeable and MPI is used for inter-processor communication.

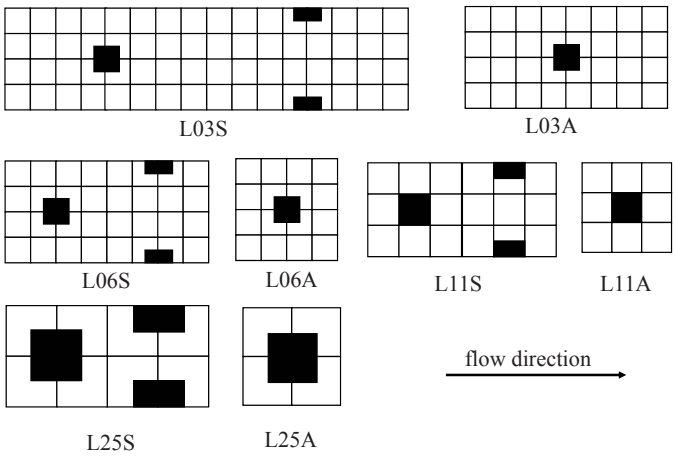

Figure 4.1: Repeating tiles for the first set of simulations denoted by 'I'. The roughness elements are cubic and are colored black. Each case in this set is denoted with LXXS/A, where L stands for λ_f, the number following L is $100\lambda_f$, S stands for "staggered" and "A" stands for "aligned". The surface coverage density is systematically varied within this set of rough walls for both perfectly aligned and staggered roughness arrangements.

4.2.2 Roughness geometries considered

LES of developing turbulent boundary layer flow over 3 sets of rough walls are conducted, for various roughness configurations. For Set I, the solidity is systematically varied for both aligned and staggered arrangements of cubic roughness elements. Figure 4.1 shows the repeating tiles for this set of rough walls. Set II consists of aligned rectangular roughness with 11% surface coverage and non-uniform roughness heights. The roughness height is selected from a Gaussian distribution with several values of standard deviation; $\sigma_h = 0.24h_m$, $0.35h_m$, $0.5h_m$. The probability-density-function of the roughness heights used in the LES is compared with the Gaussian distribution in figure 4.2. For each σ_h, four realizations of rough walls are randomly generated, thus resulting in 12 rough walls in total in this set. Each case in this set is denoted

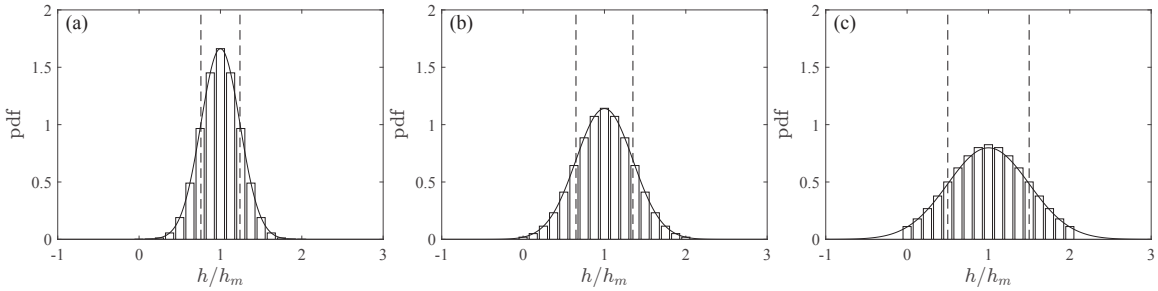

Figure 4.2: The discretized roughness height PDF compared with the Gaussian PDF. The standard deviation in roughness height is (from left to right) $0.24h_m$, $0.35h_m$, $0.5h_m$. $h_m \pm \mathrm{std}(h)$ are marked with dashed lines.

with LXXStdXXA/S-X, where the two digits following L denotes the value equal to $100\lambda_f$, the digits following Std represents $100\sigma_h/h_m$, "A" and "S" stand for aligned and staggered arrangement respectively, and the last digit is the simulation index associated with the same σ_h. Figure 4.3 shows a visualization of the surface for case L11Std50A-1 (Fig. 4.3(a)), and instantaneous and averaged streamwise velocities on a plane at height $z = h_m$ (Figs. 4.3(b,c)), for flow case L11Std50-1 in rough wall set II.

Using set III, the hydrodynamic response to lateral displacement of roughness elements is examined. In Set III, we systematically vary the staggering at two roughness solidities, $\lambda_f = 0.06, 0.11$. The repeating tiles for this set of rough walls are shown in figure 4.4.

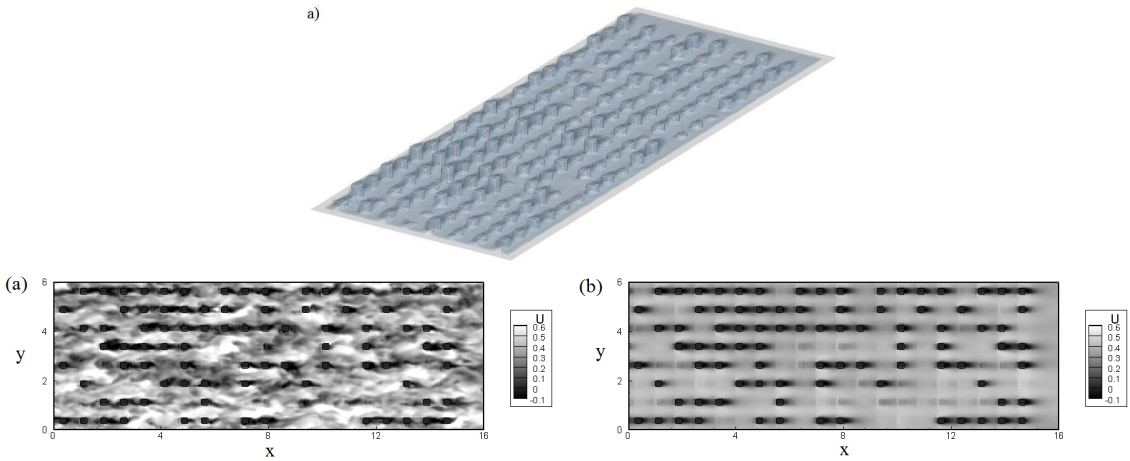

Figure 4.3: Flow visualization from LES of flow over array of wall attached rectangular prisms, for case L11Std50A-1. (a) Bottom surface geometry and transparent iso-velocity surface, (b) instantaneous and (c) averaged streamwise velocities on a plane at height $z = h_m$, for cubic roughness L11Std50A-1. Here h_m is the roughness element's mean height. The velocity is normalized with the free stream velocity U_0, and the length is normalized with $\delta_0 = 4h_m = 4h$.

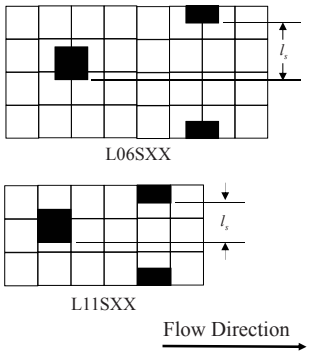

Figure 4.4: Repeating tiles for Set III. Roughness elements are cubic and are colored black. Each case in this set is denoted as LXXSXX, where L stands for λ_f, S stands for percentage of staggering. Percentage of staggering is defined as $200 l_s \sqrt{\lambda_f}/h$, where h is the cube height and l_s is the roughness displacement in the spanwise direction. Perfectly aligned arrangement is 0% staggering and perfectly staggered arrangement is 100% staggering. The number following L is $100\lambda_f$ and the number following S is the percentage of staggering. For $\lambda_f = 0.06$, 6 different percentages of staggering, spaced equally between 0% to 100% are considered and for $\lambda_f = 0.11$, 7 different cases of staggering are considered. Hence this set includes 13 separate cases.

4.2.3 Mean Velocity Profile within the Roughness Layer

The velocity profile is examined in detail within the roughness layer, i.e. below $z = H$, where $H = h_m + \sigma_h$ and σ_h is the standard deviation in roughness height. H is referred to as the generalized roughness layer height, which for the case of uniform roughness height is simply $H = h = h_m$. For the general cases, the choice of $H = h_m + \sigma_h$ is guided by examination of the data and by practicality. First, the results for the case of a bimodal distribution of heights will clearly show that the break between the logarithmic and the exponential behaviors occurs at the height of the larger roughness elements. This has also been observed in Refs. 3, 164. Since for a bimodal distribution with equal probabilities the standard deviation is equal to the difference between the mean and the maximum (or minimum) height, the larger element's height equals $h_m + \sigma_h$. Mean velocity profiles for the case with Gaussian height distributions further confirm that this is a good approximation of where the mean velocity profile transition takes place.

The velocity profile within the roughness layer is obtained via spatially averaging the temporally averaged velocity field for 2 (for perfectly aligned arrangements) or 1 (for all other arrangements) repeating tiles in the streamwise direction at the middle of the computational domain. Figures 4.5, 4.6, 4.7 show the LES computed profiles within the roughness layer for all three sets of rough walls. In each of the individual

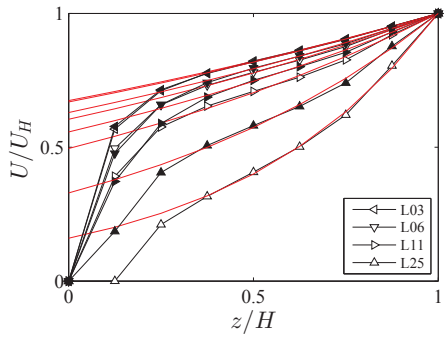

Figure 4.5: Comparison of simulated velocity profiles within the roughness layer and the exponential fit (thin red lines), for Set I. The hollow symbols are for the staggered arrangement and the filled symbols are for the aligned arrangement.

plots, an exponential has been fitted in a range of z between $H/2$ and H. Fits are constrained to pass through $(U/U_H = 1, z/H = 1)$, thus, the parameter fitted is the attenuation coefficient a for each case.

In figure 4.8, we summarize all cases simulated by plotting $\ln(U/U_H)/a$ against the wall normal distance, using the fitted value of a. The linear behavior indicates that for all rough walls considered in our LES, except for the near-wall region, an exponential profile is a very good representation of the velocity profile within the roughness layer (the collapse among the cases is due to the fitting and thus not surprising in this plot).

These observations provide good support for the generality of the exponential mean velocity profile within a roughness layer, at least for the specific class of roughness elements that have a well-defined length-scale, each with reasonably uniform cross-sectional area, and well-defined flow separation points.

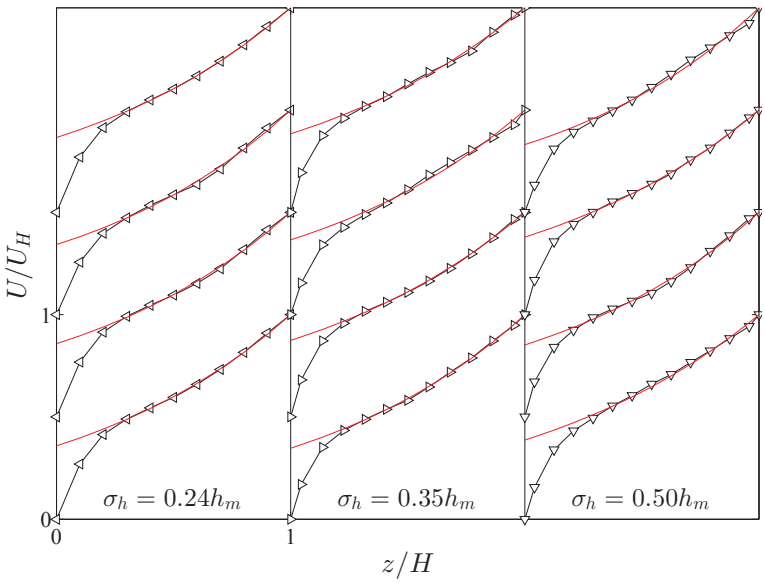

Figure 4.6: Comparison of simulated velocity profiles within the roughness layer and the exponential fit (thin red lines) for Set II. Cases corresponding to different σ_h are displaced horizontally, while four random generated rough walls with the same σ_h (from bottom to top: cases L11StdXXA-1/2/3/4) are displaced vertically for clarity of presentation.

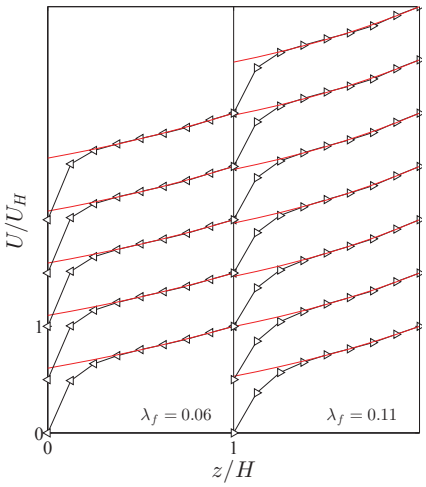

Figure 4.7: Comparison of the simulated velocity profiles within roughness layer and the exponential fit (thin red line), for Set III. The cases with two different solidities are displaced horizontally. Within each panel, the percentage of staggering increases from bottom to top (from bottom to top: cases L06S00/25/50/75/100 (left), L11S00/17/33/50/67/83/100 (right)).

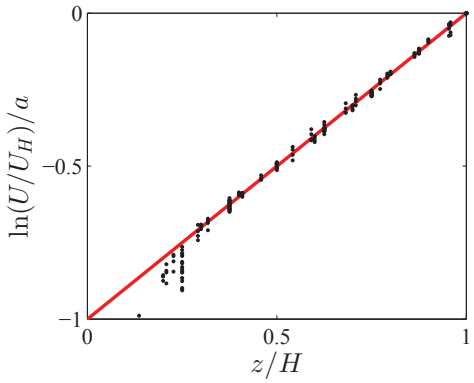

Figure 4.8: Velocity profiles for all LES cases plotted together within the roughness layer, in linear-log scale. The collapse onto a line confirms exponential behavior, although each case is characterized by a different (fitted) parameter a.

4.3 An analytical rough-wall flow model

4.3.1 Assumed shape function for mean velocity profile

The proposed approach is inspired by the von-Karman Polhausen method[160] and begins by postulating a shape function for the vertical distribution of the horizontally averaged velocity profile $U(z)$. We divide the height into two layers: (1) the roughness layer for heights below the roughness elements (for now we use the symbol h, but for cases with varying heights, this can be replaced by H that includes the mean and standard deviation of the element heights). Based on the results presented in §4.2, for the first layer we use an exponential profile. (2) Above $z = h$ (or H), we assume a standard logarithmic law[41,42] arising from a constant stress layer in which turbulence alone conveys momentum in the vertical direction. In sum, the following

shape function is assumed in replacement of the integration of the RANS equations:

$$\begin{cases} U(z) = U_h \exp\left[a(z-h)/h\right], & 0 < z < h; \\ U(z) = u_\tau/\kappa \left[\log\left[(z-d)/z_o\right] + \Pi\ W(z/\delta)\right], & h \leq z < \delta; \end{cases} \tag{4.3}$$

where κ is the von-Karman constant, δ is the boundary layer thickness, and $\Pi\ W(z/\delta)$ is a wake function[165] with the parameter Π typically of order unity (we take $\Pi = 0.2$ in this study) and $W(1) = 2$.[42] The parameter U_h is the mean velocity at roughness element height. Above $z = \delta$, we take $U = U_0$, the free stream velocity. Figure 4.9 illustrates the various layers. Note that the profile does not vanish at $z = 0$ but for now we are not interested in an additional, possibly very thin, further layer in which the velocity decreases rapidly from $\exp(-a)U_h$ down to zero. While the numerical results shown in Figs. 4.5-4.7 show that the exponential fit deviates from the data in the bottom 20-25% of the roughness layer, experimental and DNS data typically show a more sudden drop closer to the surface (a thinner near-wall layer, see e.g. Fig. 4 in Ref. 9 and Fig. 4 in Ref. 6). In our simulations the deviations from the exponential layer only occur for the 1-2 grid points nearest to the bottom surface, where the LES results can be affected by the wall model and numerical errors. Hence, we take the view that the validity of the exponential profile extends even closer to the surface than our LES results show.

Note that at $z = h$, Eq. 4.3 implies a sign change in the curvature of the assumed velocity profile. An inflection point near the roughness layer top is typically observed

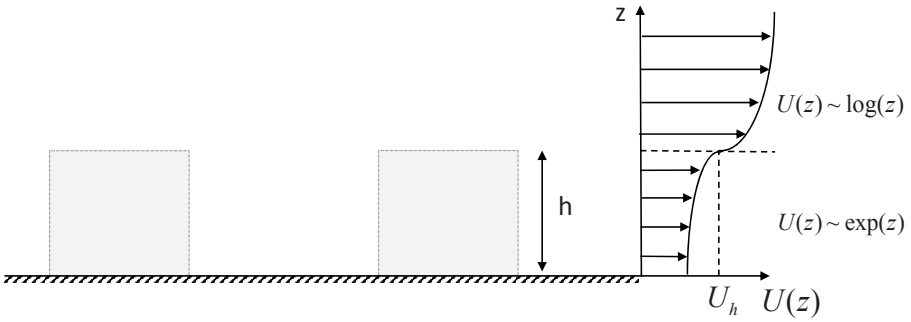

Figure 4.9: Sketch of layers of the assumed mean velocity profile representing the horizontally averaged velocity of the fluid in the flow domain (excluding the roughness elements). From top to bottom a standard logarithmic layer characterized by roughness & displacement lengths and friction velocity (and further above possibly a wake), and an exponential layer characterized by the roughness element height and an attenuation coefficient.

in rough wall boundary layers and canopy flows (see e.g. Refs. 166) and is the cause of the instability that in turn leads to mixing among the roughness layer and the inertial layer. Often, hyperbolic tangent-like profiles are used to model this mixing-layer type profile and one could imagine introducing a third intermediate layer in the present model. Here, for simplicity, connecting an exponential and a logarithmic profiles on both sides serves a similar purpose and provides a good approximation to the mixing-layer type profile for present purposes.

Note that there are 5 unknown parameters in Eq. 4.3, i.e. U_h, u_τ, d, z_o, and a. It will be assumed that we know the velocity outside the boundary layer, U_0, the boundary layer height δ, the element height h (or H) and the element's geometrical distribution on the surface. Using this information as input, we require 5 constraints to express the 5 unknown parameters U_h, u_τ, d, z_o, and a as function of U_0, δ, h, and knowledge about the spatial distribution of the roughness elements, including the

parameter λ_f.

Three fundamental constraints can be found, one based on the basic principle of momentum balance and two from continuity of the velocity profile. A fourth constraint is based on relating the displacement height d to the center of force, the height at which one may consider the effective wall stress to be applied by the roughness elements onto the flow.[167] The fifth constraint determines the exponential attenuation coefficient a and is discussed separately in §4.3.2, based on considerations of flow sheltering.

Firstly, we take the control volume that contains vertically the whole roughness layer and part of the inertial layer. The downward momentum flux within the inertial layer is balanced by the form drag due to the wall roughness. This leads to the vertically integrated momentum equation:

$$A_T u_\tau^2 = \int_{A_f} C_d \, U(z)^2 dA_f, \tag{4.4}$$

where the integration is performed on the projected frontal area A_f within the lot area A_T. For the right hand side we have employed the quadratic law for the form drag, i.e. $dF = C_d U(z)^2 dA_f$. C_d is the drag coefficient for which a typical value $C_d = 1$ is used.[8] The drag coefficient can depend on the vertical distance, the detailed distribution of the ground roughness, the details of the local flow, etc.[168] The simplification of employing a constant drag coefficient is made here, following common practice in

rough-wall modeling.[8,9,86,87] The viscous skin friction is not considered in the r.h.s of Eq. 4.4, based on the assumption of 'fully rough' regime (transitional roughness will be considered in appendix 8.3.2 based on partitioning the drag to include viscous skin friction). For rectangular-prism roughness elements, integrating the exponential velocity profile between $z = 0$ and $z = h$, Eq. 4.4 leads to:

$$u_\tau^2 = \frac{1 - \exp(-2a)}{2a} \lambda_f C_d U_h^2. \tag{4.5}$$

Commenting on the accuracy of the exponential fit near the bottom surface, if the integration were done between $z = 0.2h$ to h (the typically observed range of validity of the exponential fit in our LES) instead of between 0 and h, for a representative value of $a = 1$,the resulting drag force from the integration leads to a difference of u_τ of only $\sim 4\%$ because the integral is dominated by the profile near $z \sim h$.

The second condition related to velocity profile continuity imposed at $z = h$ leads to:

$$\frac{U_h}{u_\tau} = \frac{1}{\kappa} \log\left(\frac{h - d}{z_o}\right), \tag{4.6}$$

where we have assumed $W(h/\delta) \approx 0$ (an assumption that requires $h/\delta << 1$ but that will be checked based on data in §4.4 to hold even in cases where $h/\delta \sim 0.2$). Continuity of total stress at $z = h$ is usually used in rough wall models to constrain the mixing length (see e.g. Ref. 8). Because we do not invoke the mixing length in the formulation, continuity in total stress is not explicitly used (although it could be

used to derive the implied mixing length from the roughness layer at $z = h$).

Thirdly we require the velocity at $z = \delta$ to be the free stream velocity U_0:

$$\frac{U_0}{u_\tau} = \frac{1}{\kappa}\left[\log\left(\frac{\delta - d}{z_0}\right) + 2\ \Pi\right]. \tag{4.7}$$

And fourth, we use the viewpoint proposed in Ref. 167 that the displacement height d can be set equal to the centroid height of the distributed drag force, namely

$$d = \frac{\int_{A_f} C_d\ U(z)^2\ z\ dA_f}{\int_{A_f} C_d\ U(z)^2 dA_f}. \tag{4.8}$$

For single-height rectangular prism roughness after integration of the exponential profile between $z = 0$ and $z = h$, Eq. 4.8 simply leads to:

$$\frac{d}{h} = \frac{1}{1 - \exp(-2a)} - \frac{1}{2a}. \tag{4.9}$$

Combining Eqs. 4.5, 4.6, and 4.9, z_o for single-height rectangular prism roughness can be expressed as:

$$\frac{z_o}{h} = \left(1 - \frac{d}{h}\right)\ \exp\left[-\kappa\Big/\sqrt{\frac{1}{2a}C_d\lambda_f\left(1 - e^{-2a}\right)}\right]. \tag{4.10}$$

Replacing Eq. 4.10 into Eqs. 4.6, 4.7, we obtain the expression for u_τ

$$\frac{u_\tau}{U_0} = \left[\frac{1}{\kappa}\log\frac{\delta - d}{h - d} + \sqrt{\frac{2a}{1 - \exp(-2a)}}\frac{1}{\sqrt{C_d\lambda_f}} + \frac{2\Pi}{\kappa}\right]^{-1}, \tag{4.11}$$

and

$$\frac{U_h}{U_0} = \left[1 + \frac{1}{\kappa} \left(\log \frac{\delta - d}{h - d} + 2\Pi \right) \sqrt{C_d \lambda_f \frac{1 - \exp(-2a)}{2a}} \right]^{-1}, \tag{4.12}$$

where d is obtained from Eq. 4.9. Again, note that Eqs. 4.9, 4.10, 4.11, 4.12 are valid only for single-height rectangular prism roughness elements. Eqs. 4.4, 4.6, 4.7, and 4.8 can be used for general rectangular roughness. The fifth condition to determine a incorporates the effects from mutual sheltering among the roughness elements and is discussed in the next section.

4.3.2 Volumetric Sheltering

In this section, we model the reduction in the momentum in the wakes of rectangular prism roughness elements and its effects upon the drag on neighboring roughness elements. This reduction is denoted as volumetric sheltering and has been considered in various prior studies (see e.g.[7,169,170]). Qualitatively the extremes have been denoted as 'd-type' and 'k-type' roughness where in the first case much sheltering occurs and the flow can 'skim over' the elements, whereas in 'k-type' roughness each element produces considerable drag.[171]

Consider the situation as sketched in figure 4.10 (a). In the wake of rectangular-prism roughness elements there is a sheltered region in which the velocity is lower than in the unsheltered region. Depending on the spacing between the roughness elements, one may be in a sheltered, unsheltered, or 'just sheltered' condition (the latter is defined as when the sheltering region 'just' begins to intersect the downstream

element, i.e. when h_s changes from $h_s = 0$ to $h_s > 0$). We consider the case of 'just sheltered' and determine the attenuation parameter in the mean velocity profile based on momentum balance, namely that the integrated distributed drag equal the drag on the fully exposed frontal area of an individual roughness element (here we take $A_f = wh$, where w is the element width). We assume the latter to be $\frac{1}{2}C_{DH}\ U_h^2\ wh$, where C_{DH} is the drag coefficient (assumed to be known) that expresses the total drag on the element when using the tip velocity U_h as velocity scale. In other words, for a rectangular prism we can write

$$\int_{A_f} C_d\ U(z)^2\ dA_f = C_d\ U_h^2\ wh\ \frac{1}{2a}[1 - \exp(-2a)]\ =\ \frac{1}{2}C_{DH}\ U_h^2\ wh, \tag{4.13}$$

where for C_{DH} we use the drag coefficient for a surface mounted cube for which data exists, and (again) C_d is assumed to be constant. It is known that approximately $C_{DH} \approx 1.4$.[172–174] Essentially we are assuming that the drag coefficient C_{DH} appropriate for an unsheltered or 'just sheltered' cuboid in the array is equal to that of an isolated element. Since we are using $C_d = 1$, from this equality we can find the attenuation of the velocity profile. The condition for a for the 'just sheltered' condition is given by

$$\frac{1}{2a}[1 - \exp(-2a)] = \frac{C_{DH}}{2C_d}\ \approx\ 0.7. \tag{4.14}$$

The solution is $a \approx 0.4$. As roughness elements are placed further apart distances (even lower λ_f), momentum balance (for fully rough conditions) implies that a is

unchanged and remains at 0.4. Thus we refer to this value as $a_{\min} = 0.4$. Direct measurements of the attenuation coefficient a characterizing the nearly exponential velocity profile are presented in §4.4, and the measurements confirm the numerical value $a_{\min} \approx 0.4$ characterizing the limiting attenuation in the limit of small λ_f. As elements are placed closer together leading to sheltering effect, we expect a to increase above 0.4, since the velocity profile will be increasingly attenuated to values smaller than U_h as z decreases from $z = h$ down towards the wall.

In order to determine the value of a that depends on the degree of sheltering, we employ again the momentum balance as before. However, because C_{DH} is measured for unsheltered cubes, the momentum balance is only applied for the top portion above the sheltered region for $z > h_s$ as if the element only protrudes a height h_s above the surface, thus neglecting the sheltered region's contribution to drag. The sheltering height h_s depends on the expansion rate of the wake as shown in figure 4.10 (b) and will be modeled later. For the momentum balance with sheltering we obtain the condition

$$\int_{h_s}^{h} C_d\, U(z)^2\, w\, dz \;= \frac{1}{2a}\left(1 - \exp\left[-2a\left(1 - h_s/h\right)\right]\right)\; wh\; C_d\, U_h^2 \;=\; \frac{1}{2} C_{DH} U_h^2 w (h - h_s), \tag{4.15}$$

leading to

$$\frac{1}{2a\left(1 - h_s/h\right)}\left(1 - \exp\left[-2a\left(1 - h_s/h\right)\right]\right) \;=\; \frac{1}{2a_{\min}}[1 - \exp(-2a_{\min})]. \tag{4.16}$$

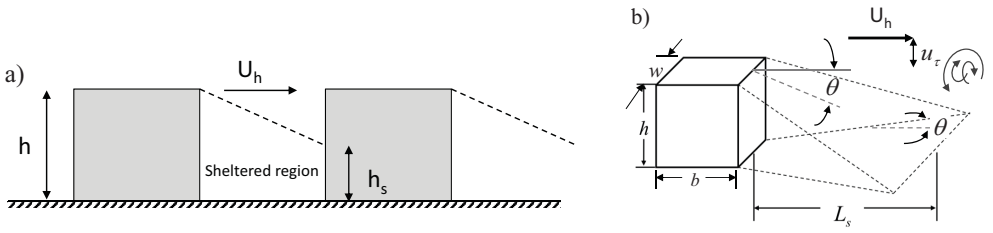

Figure 4.10: (a) Sketch of the sheltering effect and simplified model in which the complicated flow between roughness elements is assumed to consist of two regions with characteristic velocities U_h (unsheltered region) and small velocity in the sheltered region. The case shown is for when the downstream element overlaps with the sheltered region, i.e. when $h_s > 0$. (b) A sketch of the volume within the wake of a rectangular prism roughness that has reduced momentum. The roughness is h in height, w in width, and b in streamwise length. The streamwise length of the sheltered region is L_s and based on the linear expansion model is given by $L_s = h/\tan\theta$.

The solution is simply

$$a = \frac{a_{\min}}{1 - h_s/h}. \tag{4.17}$$

Hence, knowing h_s/h allows us to determine a. For unsheltered cases ($h_s = 0$), we use $a = a_{\min} = 0.4$.

Next, we discuss the determination of h_s. Figure 4.10(b) sketches the volume within the wake of a rectangular prism element that has reduced momentum fluid. Wake expansion in the vertical direction can bring in fluid with high momentum, a reduction in the volume of low momentum fluid would thus be expected. Wake expansion in the spanwise direction, on the other hand, expands the volume of low momentum fluid. This configuration is physical for near wall roughness with aspect ratio h/w not large. Naturally, we expect the wake be eaten up from the side if the roughness geometry is 'stick-like', which is not captured by the configuration in 4.10 (b). The horizontal convective velocity in the roughness sublayer is on the order of

U_h, while the turbulent transport velocity scale in the vertical and spanwise directions is on the order of the friction velocity u_τ. As a result, we estimate the wake expansion rate as

$$\tan\theta = C_\theta \, \frac{u_\tau}{U_h}, \tag{4.18}$$

where C_θ is a coefficient of order unity that may depend upon element geometry (and in the case of rectangular prisms, the aspect ratio). Any portion of a downstream roughness element that falls in this region of reduced momentum is considered to be sheltered. Determination of h_s thus proceeds by calculating the expansion rate using Eq.4.18, and using it to evaluate the area of sheltered region A_s as the frontal area of the closest downstream rectangular prism roughness elements. For cases in which sideways growth of the wake causes partial sheltering of the width, the momentum argument presented above is equivalent to setting $h_s = A_s/w$ in Eq. 4.15 and thus of Eq. 4.17 (a more precise definition is given in Eq. 4.23).

Depending on roughness element placement on the surface, the calculation of the sheltered area can be more or less involved. The most general procedure is to, first, find all upstream roughness elements that could shelter the roughness under consideration; second, calculate the sheltered frontal area due to each roughness elements found in the first step. To ensure that no roughness interactions are missed, a large enough upstream search domain of size $\ell \times (2\ell + w)$ is used, with $\ell = 3h_{\max}U_h/u_\tau$, as shown in Fig. 4.11(a). Multiple roughness elements could shelter the roughness element under consideration, e.g. in Fig. 4.11(b), the roughness element under con-

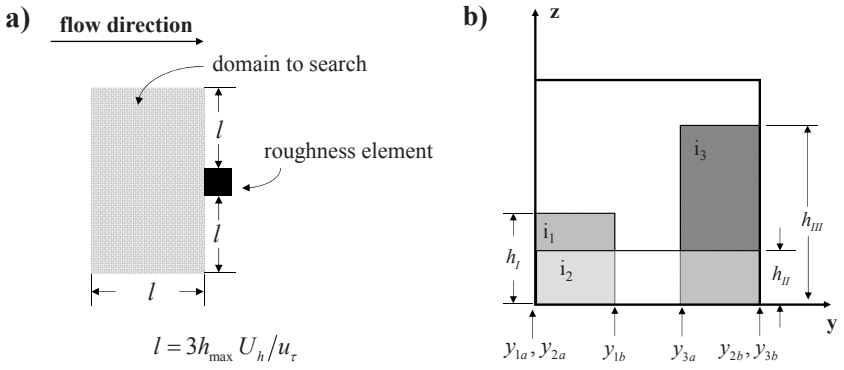

Figure 4.11: a) Sketch of the upstream search domain of size for roughness elements that could shelter the roughness under consideration (black cube). To determine ℓ, $h_{\max}$ is the maximum height of all roughness on the wall, U_h/u_τ is iterated. (b) Sketch of the frontal area of the roughness under consideration. The rectangles $i = 1$, 2, 3 are sheltering areas caused by 3 upstream roughness elements.

sideration is sheltered by 3 upstream roughness elements. In general, if n roughness elements upstream leave sheltering imprints on the roughness under consideration, we denote each of the sheltering area by $S_i(y)$ $(i = 1, 2, 3..n)$. For example, in figure 4.11 (b), $S_1(y) = h_1[\mathcal{H}(y - y_{1a}) - \mathcal{H}(y - y_{1b})]$, where $\mathcal{H}(\cdot)$ is the Heaviside function and y_{1a} and y_{1b} are the beginning and end location for the $i = 1$ element's sheltering area. The combined sheltered area of the roughness element under consideration is $\Delta A_s = \int_0^w \max[S_1(y), S_2(y), ...]dy$. Notice that in this way we do not double count the sheltering areas.

For simple cases, this procedure can be done analytically. For example, the aligned cubes arrays, in which the interaction is limited to the roughness element under consideration and its nearest roughness element upstream (no need to search for a large area), the entire width of the element under consideration is in the sheltered

region if sheltering occurs. Then h_s is simply given by

$$h_s = \max[h - C_\theta(u_\tau/U_h)L_x, 0] \tag{4.19}$$

where L_x is the horizontal distance between roughness elements. Substituting Eq. 4.19 into Eq. 4.17 leads to

$$a = 0.4 \max\left[1, C_\theta^{-1}\frac{h}{L_x}\frac{U_h}{u_\tau}\right] \tag{4.20}$$

which, together with Eqs. 4.9, 4.10, 4.11 and 4.12, determines the model. More generally this procedure of calculating the sheltering can be done numerically (see appendix 8.3.1).

Once h_s is determined from such geometrical arguments, Eq. 4.17 provides the final condition to determine the unknowns in Eq. 4.3. In the appendix, some other evaluations of h_s and a appropriate for some sample geometries considered later in this chapter are also provided (e.g. staggered cubes, non-uniform heights, etc.). These evaluations of h_s are only relevant for cases in which the spacing between elements is smaller than L_s and thus $a > a_{\min}$. We still have as of yet undetermined parameter, C_θ.

4.3.3 The wake expansion rate

The wake expansion rate is expressed as $\tan\theta = C_\theta\ u_\tau/U_h$. We consider here rectangular-prism roughness elements, allowing for different height/side/width ratios. We recognize that the expansion rate can be different for different ratios. Consider cubes and 2D transverse ribs as examples to be contrasted. Most data available on rectangular roughness suggests that the region affected by sheltering is shorter for 3D cubes than for 2D ribs. A similar trend is known to exist for recirculation regions which are typically shorter for 3D objects compared to 2D obstructions (although we clarify that sheltering region is different from recirculation regions). Thus we expect stronger volumetric sheltering effects for 2D roughness compared to 3D roughness elements, which is related to the relatively weaker spreading rate of the sheltering region for 2D roughness elements.

To estimate the differing expansion rates $\tan\theta$ for objects of different aspect ratios, we consider the momentum balance for the case of 'just sheltered' but for various aspect ratios w/h, as is sketched in figure 4.12. The total drag on the element, $\frac{1}{2}C_{DH}\ U_h^2\ hw$ is equated to the vertical momentum flux in the rectangular area of length $h/\tan\theta$ and width $w + 2h$ that is physically associated with wake expansion before the sheltering region has been reduced vertically such that the wake 'touches' the ground (dashed line in Fig. 4.12). The width $2h + w$ comes from the fact that rate of the wake being 'eaten up' from the top equals to the rate the wake expands sideways, and by the time the entire wake is 'eaten away' from the top (i.e. by a

distance h), the side expansion is then also h, on both sides. The vertical flux of momentum per unit area is u_τ^2. Thus the balance can be written as:

$$\frac{h}{\tan\theta}\,(2h+w)\,u_\tau^2 = \frac{1}{2}C_{DH}\;hw\;U_h^2. \tag{4.21}$$

We replace $\tan\theta = C_\theta(u_\tau/U_h)$ and solve for C_θ to obtain

$$C_\theta = \left(\frac{6}{C_{DH}}\frac{u_\tau}{U_h}\right)\left(\frac{1}{3}+\frac{2h}{3w}\right) \approx O(1)\times\left(\frac{1}{3}+\frac{2h}{3w}\right) = 1-\frac{2}{3}\left(1-\frac{h}{w}\right), \tag{4.22}$$

where the prefactor $O(1)$ arises because $C_{DH} = 0.7$ and while the ratio (u_τ/U_h) depends on details of the flow and roughness configurations, in most cases it is on the order of $\sim O(10^{-1})$. Therefore, as a model for C_θ, we simply take $C_\theta = \frac{1}{3}+\frac{2h}{3w}$. As a result, for a given ratio u_τ/U_h the expansion rate for 2D bar roughness elements ($h << w$) is predicted to be one-third of that of cubic roughness elements ($h = w$). The validity of Eq. 4.22 is associated with the validity of the assumed sheltering region shape in figure 4.10 (b). Because such a shape is not physically reasonable for slender, 'stick-like' roughness elements (e.g. a canopy of long wall attached vertical cylinders or tall buildings for which the sideways expansion should transition into an inward reduction at some distance downstream), the use of Eq. 4.22 should be limited to roughness elements of an aspect ratio h/w that do not exceed an upper threshold (here we typically have $h/w \lesssim 2$). For a generalization to $h/w > 2$ see Ref. 175.

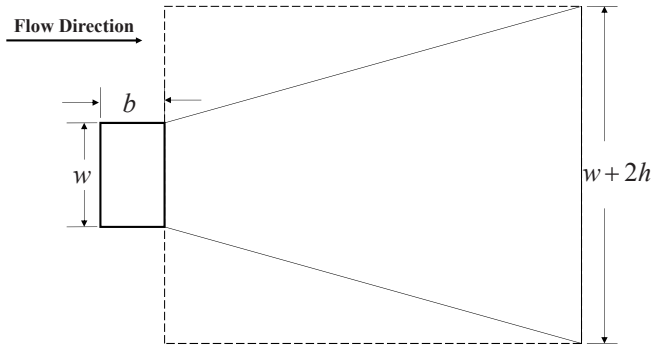

Figure 4.12: Top view of the rough wall. Consider the case of 'just touching'. The roughness is shown by thick solid line. The roughness width is w, its length is b, and its height is h. The rectangular region enclosed by the dashed line is argued to carry the vertical flux of momentum associated with the wake growth and vertical reduction of the sheltered region.

This completes the description of the analytical roughness model for rectangular prisms since based solely on geometric considerations one may find C_θ, $\tan\theta$, h_s and thus a, followed by the roughness parameters z_0, d, U_h and u_τ.

4.3.4 Summary of wall and sheltering model

We briefly summarize the rough wall model and outline how it can be applied to rough walls mounted with rectangular-prism roughness elements. At first, an initial guess for the attenuation coefficient a is made, e.g. $a = a_{\min} = 0.4$. Then the four unknowns U_h, friction velocity u_τ, effective roughness height z_o, zero-plane displacement d are obtained from solving the constraints Eqs. 4.4, 4.6, 4.7 and 4.8. With u_τ and U_h known, their ratio is used to determine the angle $\tan(\theta)$ by means of Eqs. 4.18, 4.22.

The next iteration of the attenuation coefficient a is determined using Eq. 4.17 but this expression requires the equivalent sheltered layer height, h_s. A condition to find h_s that can be applied in general configurations of rectangular-prism roughness element can be written as

$$\int_0^{h_s} w_t(z)dz = A_s, \tag{4.23}$$

where $A_s = \sum \Delta A_s$ is the total sheltered frontal area in a given region of interest and $w_t(z)$ is the total flow direction projected width of roughness elements at height z, also over the same area of interest. Eq. 4.23 reduces to $h_s = \Delta A_s/w$ for single-height, single aspect-ratio roughness. We need Eq. 4.23 mainly to account for roughness elements with non-uniform height distribution. In such a case, in fact h_s could be larger than the height of some roughness elements.

The sheltered frontal area A_s needs to be calculated geometrically using the sheltering model. The volumetric sheltering behind a cube was sketched in figure 4.10 and the wake expansion rate is given by Eqs. 4.18, 4.22, i.e $\tan(\theta) = [1/3 + 2h/3w]\,(u_\tau/U_h)$, where h is the height of the rectangular roughness, and w is its width. When the surface contains elements with different aspect ratios $\tan(\theta)$ is calculated for each roughness element aspect ratio. That is to say, while the ratio (u_τ/U_h) is an averaged quantity, $\tan(\theta)$ is dependent on each individual element.

The steps to implement the sheltering model are:

1. Begin with an initial guess for u_τ/U_h (e.g. 0.1) and use it as initial guess of

$\tan(\theta)$.

2. For every roughness element under consideration, identify all upstream roughness elements that could shelter it.

3. Calculate the sheltered area by each element identified in step (ii) and for all elements under consideration to obtain A_s.

4. Calculate the sheltering height h_s with Eq. 4.23.

5. Use Eq. 4.23, Eq. 4.17 to obtain a. (Note $a > a_{\min} = 0.4$)

6. Solve for U_h, u_τ, d, z_o using Eqs. 4.4, 4.6, 4.7, and 4.8.

7. Obtain corrected u_τ/U_h and repeat previous steps until convergence.

Typically this procedure leads to convergence in just a few iterations.

The model parameters are the von Karman constant $\kappa = 0.4$, the sectional drag coefficient $C_d = 1$ (for rectangular prisms), the outer wake correction strength $\Pi = 0.2$, and the minimum attenuation coefficient $a_{\min} = 0.4$. The model inputs include the boundary layer height δ, the free stream velocity U_0, and the geometric information about the surface roughness elements and their positioning. As it turns out, the predictions on z_o and d are independent of δ and U_0, while u_τ, and U_h do depend on these outer flow conditions.

4.4 Applications

In this section, we report results of LES of flow over 1) aligned and staggered cube arrays; 2) 2D transverse ribs; 3) rectangular roughness with bi-modal height distribution; 4) rectangular roughness with Gaussian height distribution. The purposes of this section are two-folds, first, we provide data on roughness distributions that have not been fully studied; second, we compare measurements of z_o, d, u_τ, U_h from LES with the predictions from the sheltering model.

4.4.1 Aligned and staggered cubic arrays

In this subsection the model predictions are compared with relatively recent experimental and numerical datasets from Refs. 3–6 as well as the results from current LES. The LES code has already been described in §4.2. The roughness considered in this section are the aligned/staggered arranged cubic roughness elements with various surface coverage densities (see §4.2, Set I).

The mean velocity profile within and above the roughness canopy is obtained by averaging over one repeating tile (for staggered arrays) or two repeating tiles (for aligned arrays) centered around $x = 9\delta_0$ for all cases ($x = 0$ corresponds to the inlet location). The form drag leading to the wall stress from the roughness elements (denoted as τ_w) is measured within the simulation at each time-step by integrating the pressure over the immersed boundary. The friction velocity is $u_\tau = \sqrt{\tau_w/\rho}$. We

have neglected the contribution from viscous skin friction, which in all simulated cases is very small. We have checked from the integral wall model (which includes viscous wall stress at the wall as part of the model) that the contributions are in all cases less than 2% of the form drag on the roughness elements.

Having available the friction velocity u_τ, we take the mean velocity profiles above the roughness elements and fit a logarithmic law determining the hydrodynamic roughness height z_o and displacement d from the regression, as done also in Refs. 16, 176. Note that in Fig. 4.13 the logarithmic scaling extends down to almost $z = h$ (the first points shown in the plots correspond to the height of the first LES grid points above $z = h$). In order to provide fits that are least affected by possible deviations from logarithmic scaling near the roughness elements, the log laws are fitted between $z = 1.5h$ to $z = 2.5h$. A value $\kappa = 0.4$ is used in this procedure. Comparisons between the simulated mean profile above the cubic roughness ($z/h > 1$) and the resulting logarithmic fits (dashed lines) are shown in Fig. 4.13. As can be seen, the profiles obtained from the LES follow the log law quite well. We also observe that close to the roughness height any wake correction is negligible and it is therefore valid to neglect the wake term in Eq. 4.6. Finally, we recall that the attenuation coefficient a has been obtained by performing an exponential profile regression on the measured mean velocity profile between the heights $0.5 < z/h < 1$.

Table 4.1 lists the relevant quantities determined for each case. The attenuation parameters a for all cases are plotted against λ_f in figure 4.14. It is observed that

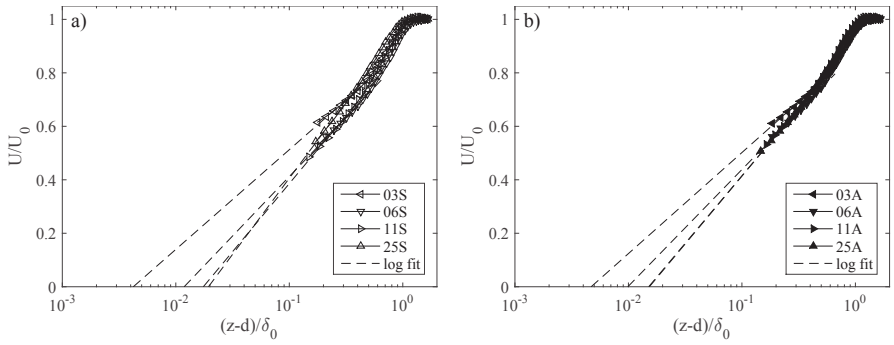

Figure 4.13: Mean velocity profile above the roughness elements ($z/h > 1$) from LES, and the log law fits. The measured friction velocity u_τ, displacement height d, and the hydrodynamic roughness height z_o are listed in table 4.1.

Table 4.1: List of the relevant quantities for each case for cubic roughness of staggered or aligned arrangements. Normalization is via the boundary layer thickness at the inlet and free stream velocity. The friction velocity u_τ is obtained directly in the simulations. The roughness height is $h = 0.25\delta_0$. The boundary layer thickness δ is measured at $x = 9\delta_0$ downstream of the simulation inlet.

Case	a	δ/δ_0	u_τ/U_0	U_h/U_0	z_o/δ_0	d/δ_0
L03A	0.40	1.31	0.066	0.54	0.0047	0.14
L03S	0.40	1.30	0.065	0.54	0.0042	0.15
L06A	0.47	1.34	0.076	0.47	0.0099	0.14
L06S	0.50	1.38	0.076	0.43	0.0113	0.16
L11A	0.58	1.19	0.088	0.41	0.0153	0.17
L11S	0.70	1.23	0.089	0.36	0.0175	0.18
L25A	1.11	1.26	0.088	0.30	0.0151	0.18
L25S	1.83	1.15	0.099	0.31	0.0194	0.16

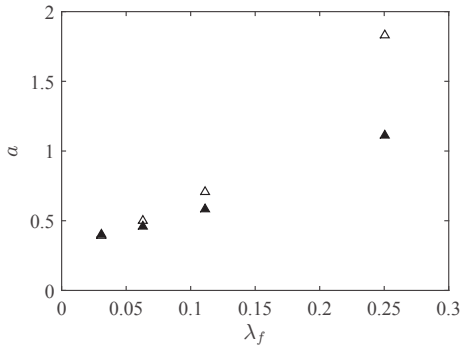

Figure 4.14: Measured attenuation coefficient from fits to the LES results plotted against packing density for all cases. Solid symbols are for aligned cases and hollow symbols are for staggered cases.

$a \to 0.4$ for $\lambda_f \to 0$, providing empirical evidence for the result presented in the previous section that for unsheltered conditions $a_{\min} \approx 0.4$.

Next, the analytical model is applied to these cases. We mainly study the dependency of various quantities on the solidity λ_f. The boundary layer thickness is kept constant in the model $\delta/\delta_0 = 1.3$ (a typical value for the boundary thickness listed table 4.1) and $h = 0.25$. A moderate wake correction of $\Pi = 0.2$ is added.[149] The von Karman constant κ is set to $\kappa = 0.4$, and $C_d = 1$ throughout. A comparison of the model predicted z_o and d with the experimental and numerical data is shown in figures 4.15 and 4.16. It is noted that the data in the literature exhibits high scatter. Compared to relatively early experiments, for example, Ref. 5 (which Refs 8, 9 have used for model calibration), the hydrodynamic roughness lengths reported by more recent experiments and simulations[4,164] tend to be smaller. We follow the usual convention and examine the behavior of z_o and d as function of packing density and compare with the data available from the prior studies. Moreover, model predictions

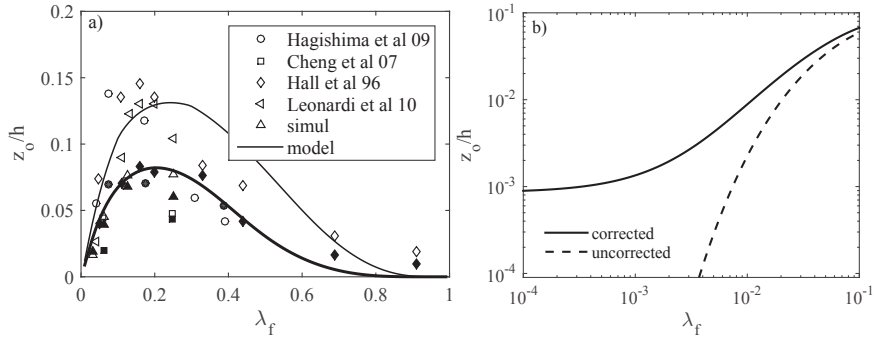

Figure 4.15: (a) Comparison of hydrodynamic roughness length z_o predicted by the new model with experimental and simulation data from Refs 3–6, and with LES data from this study (upright triangles), for cubic roughness. Solid symbols: aligned arrangement; empty symbols: staggered arrangement. Thick and thin lines are the model predictions for the aligned and staggered arrangements, respectively. (b) Comparison of the model prediction for z_o with (solid line) and without (dashed line) the correction based on the drag partition by Ref. 7 for the aligned arrangement (see appendix 8.3.2).

for U_h and u_τ are compared with LES data in figure 4.17. Since they are typically not reported in the literature, only data from the present LES study are included. The model predictions and overall trends agree well with the experimental and simulation data, considering the scatter in the data. Model predicted z_o and d are independent of the boundary layer thickness, following the "fully rough" assumption, yet u_τ, U_h depend on δ. The dominant dependency is on the solidity and dependency on δ is very weak.

Figure 4.18 compares the present model with the roughness wall models of Ref. 8 and Ref. 9. Because these prior models are insensitive to the relative arrangements of roughness elements, and the parameters were chosen to fit the data for staggered cube arrays, we compare only the predictions for staggered arrays. The comparison shows that all models give quite similar predictions, but comparison with Fig. 4.15

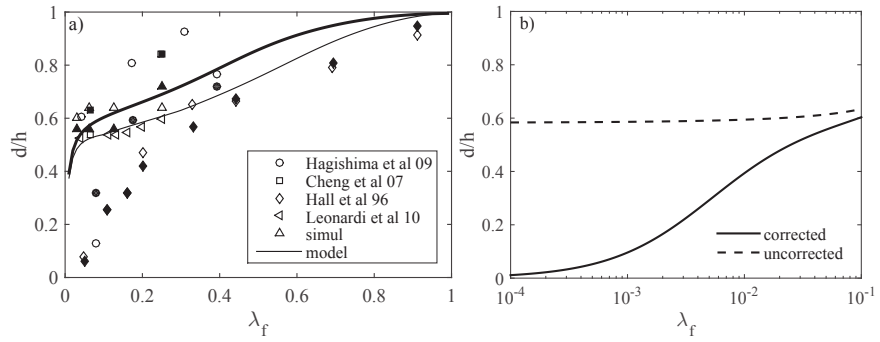

Figure 4.16: Same as figure 4.15 but for the zero-plane displacement d.

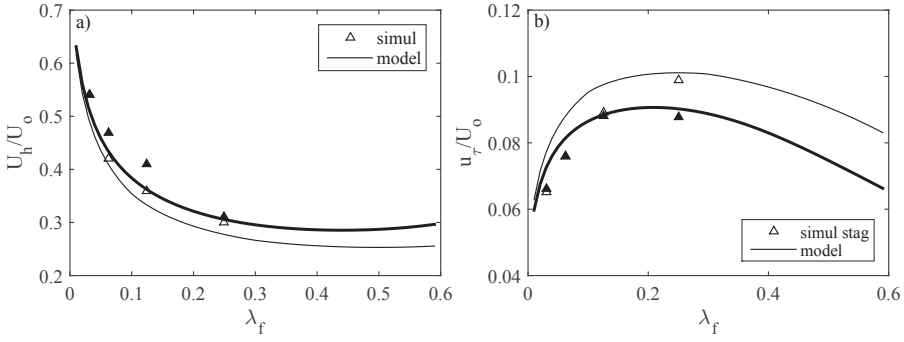

Figure 4.17: (a) Comparison between model predicted velocity U_h at the top of the cubic roughness, and (b) friction velocity u_τ with LES data. Solid symbols: aligned arrangement; empty symbols: staggered arrangement. Thick and thin lines are the model predictions for the aligned and staggered arrangements, respectively.

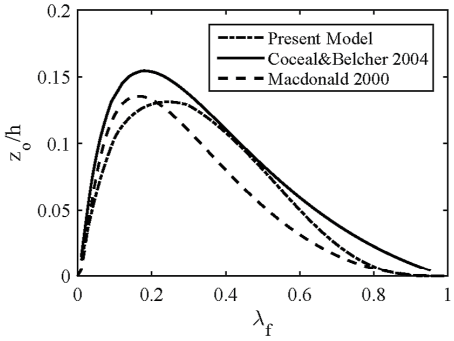

Figure 4.18: A comparison of various model predictions for z_o, for the case of staggered arrays at different λ_f. Note that the models of Ref. 8 and Ref. 9 do not depend on the relative arrangements of roughness elements, only on λ_f.

shows that the present model yields significantly smaller values of z_0 for the aligned cases, consistent with the data (solid symbols in Fig. 4.15).

Finding experimental and simulation data for $\lambda_f > 0.4$ is challenging, but the model prediction in densely packed region can be assessed via asymptotic behaviors. It is expected that when $\lambda_f \to 1$, the flow becomes entirely skimming over the roughness elements, approaching an elevated flat plate turbulent boundary layer. Hence, z_o must reduce to 0 while the displacement height $d \to h$. Those behaviors can indeed be observed in figure 4.16. The expected independence of z_o and d with respect to δ and U_o is also satisfied.

4.4.2 Transverse 2D ribs

In this subsection, the model is applied to transverse (2D) ribs, which, as is well known, can exhibit very different behavior from 3D roughness elements. The height of the ribs is $0.25\delta_0$. The roughness solidity studied includes $\lambda_f = 0.125, 0.25$. The

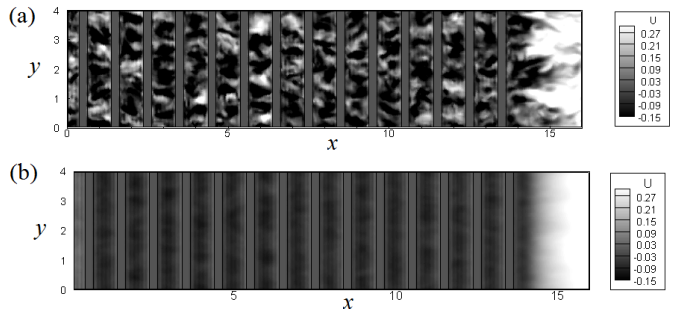

Figure 4.19: Sample instantaneous (top) and mean (bottom) streamwise velocity field at $z/h = 0.5$ for boundary layer flow over transverse square ribs. The velocity is normalized with the free stream velocity. This case corresponds to $\lambda_f = 0.25$.

computational domain is of size $16\delta_0 \times 4\delta_0 \times 4\delta_0$ and the mesh size is $256 \times 64 \times 64$. The velocity profile averaged over one repeating tile centered around $8\delta_0$ downstream the inlet. Drag is measured within the simulation and z_o and d are fitted from the measured profile.

One sample instantaneous and mean streamwise velocity field is shown in figure 4.19. A comparison between the simulated mean profile above the cubic roughness ($z/h > 1$) and the log fit is shown in figure 4.20. Qualitatively, it can be seen that the vertical rate at which the sheltered region is decreasing downstream between the 2D bars appears slower than downstream of 3D cubic objects (comparing e.g. with Fig. 4.3). This trend is consistent with the discussion of expansion rates as function of roughness element aspect ratio in §4.3.3.

Following prior practice, results are first compared as function of the distance between the center of two transverse square ribs $\lambda = L_x/h + 1$. Results are shown as function of the additive constant B in the expression $U(z)/u_\tau = 1/\kappa \log[(z-d)/h] + B$.

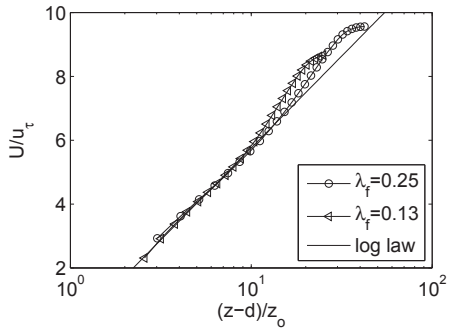

Figure 4.20: Symbols: mean velocity profile above ($z/h > 1$) the transverse ribs roughness elements from LES. Lines: log law fit plotted with fitted displacement heights and roughness lengths. The displacement heights are $0.13\delta_0$, $0.17\delta_0$, the friction velocities are $0.12, 0.11$ (normalized by free-stream velocity), and the hydrodynamic roughness lengths are $0.053\delta_0$, $0.030\delta_0$, for the $\lambda = 0.125$ and 0.25 cases, respectively. The rib height is $0.25\delta_0$.

Figure 4.21 shows the comparison between the model with extensive data sets.

In order to provide a comparison with the results for cubic roughness elements, in Fig. 4.22 the model prediction for 2D ribs are compared with the model predictions for cubic aligned and staggered cubes, shown before in figure 4.15. Overall the shape and order-of-magnitude of the results is comparable, although the peak occurs at lower λ_f for the 2D ribs (sheltering effects still occur at larger distances between the elements, i.e. smaller λ_f, due to the decreased spreading rate in the 2D case).

4.4.3 Rectangular roughness with non-uniform, bi-modal height distributions

The cases presented in previous sections considered roughness elements of uniform height. The next level of complexity is to consider roughness elements with

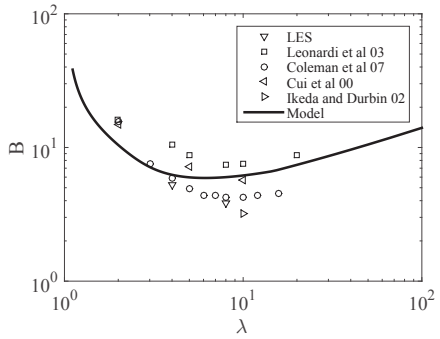

Figure 4.21: Comparison of the additive constant B from the model prediction ($B = \kappa^{-1}\ln(h/z_o)$) and from experiments and numerical simulations[10–13] for transverse ribs. Two points are from this study's LES . The height of the transverse square rib is $\approx 1/5$ of the boundary layer height.

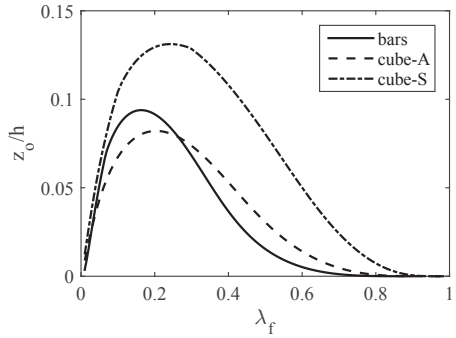

Figure 4.22: Comparison of the roughness length z_0 from the model prediction for aligned and staggered cubes, as well as 2D ribs.

non-uniform height distributions. Varying height distributions was studied in experiments as described in Refs. 3, 16, 177. Ref. 164 studied the behavior hydrodynamic roughness length z_o by systematically varying the degree of roughness height non-uniformity while keeping the solidity $\lambda_f = 0.11$. The results showed that z_o increases monotonically with the standard deviation of the roughness height distribution, although it is not known whether this trend would hold for roughness at a different solidity, or with different roughness arrangements.

The goals of this subsection are twofold. First, to provide LES data on rectangular prism roughness with non-uniform heights for various solidities and different arrangements (staggered and aligned). For each case the hydrodynamic roughness length z_o and friction velocity u_τ are measured from the LES. Second, we aim to compare the measured values with the predictions from the analytical model described in §4.3. As a first step considering non-uniform heights, we consider the bi-modal height distributions in which the mean height h_m of the elements is kept constant but the spread around it, quantified using the standard deviation of the element's height, was varied. Note the roughness height is either $h_h = h_m + \sigma_h$, or $h_l = h_m - \sigma_h$. The results of roughness with Gaussian height distribution is presented in §4.4.4. The setup for these cases (denoted as LXXS/A-StdXX) was already described in §4.2. The repeating tiles for the rough walls are presented in figure 4.23.

The mean velocity profile above the roughness is obtained via averaging the temporally averaged flow field in the spanwise y direction, and in the streamwise direction

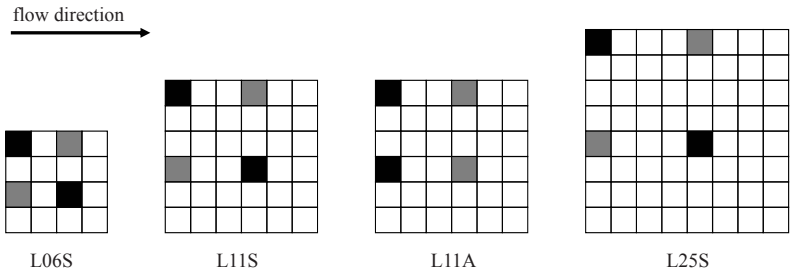

Figure 4.23: Repeating tiles for the cases considered. L stands for λ_f, the two digits behind is $100\lambda_f$, the last letter S is for 'staggered' and A is for 'aligned'. The roughness is colored with black/gray. Black is for elements of height $h_h = h_m + \sigma_h$, and gray is for height $h_l = h_m - \sigma_h$. The subscript 'h' stands for 'high', and 'l' stands for 'low' and the mean height is $h_m = (h_h + h_l)/2$.

x between 2 repetitive tiles starting from $x = 4\delta_0$. Figure 4.24 shows the resulting set of velocity profiles for all cases. The log-law is fitted between $z = h_h + 0.5h_m$ to $z = h_h + 2h_m$. To reduce the uncertainty in the log law fitting, we use the displacement height determined from the rough wall model (Eq.4.8, and note that in this case A_f is not a constant but a function of the wall normal distance). The values obtained from the model are tabulated in tables 4.2, 4.3, 4.4, 4.5. Figure 4.25 shows the velocity profiles in a log-linear scale. The measured (fitted) values for the hydrodynamic roughness length z_o, friction velocity u_τ and velocity at the top of the roughness canopy $U_h = U(z = h_h)$ are tabulated in tables 4.2, 4.3, 4.4, 4.5.

We then compare the LES results with the model prediction. The analytical model requires careful evaluation of h_s (to obtain a, etc.) and some intermediate results of the geometric calculations are shown in Appendix 8.3.1. Figure 4.26 shows a comparison of the values of z_o, U_h, and u_τ predicted by the analytical model with those measured from LES. We observe that the analytical model captures the measured

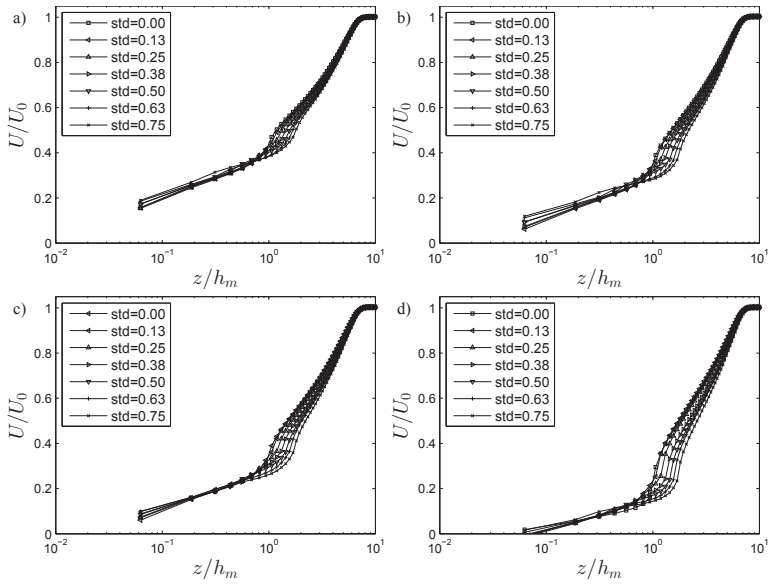

Figure 4.24: The mean velocity profiles for all the cases. a) Lf06S, b) Lf11S, c) Lf11A, d) Lf25S. The indicated standard deviation of the roughness elements is normalized with the mean roughness height.

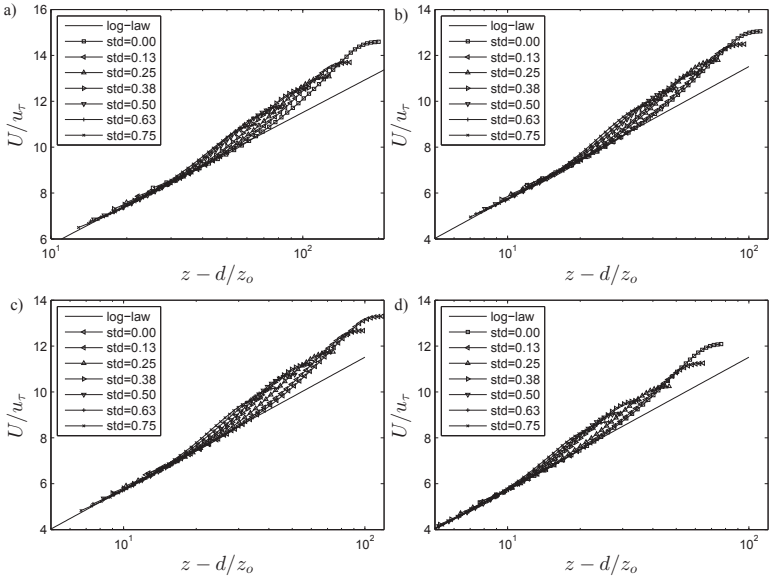

Figure 4.25: The log law fitted velocity profile for all the cases: a) Lf06S, b) Lf11S, c) Lf11A, d) Lf25S. Only data above $z > h_h + 0.5h_m$ are shown. The standard deviation of the roughness elements is normalized with the mean roughness height.

Table 4.2: Displacement height d (from model), hydrodynamic roughness length z_o, friction velocity u_τ and velocity at the top of the roughness canopy $U(z = h_h)$ for case Lf06S. Std stands for the standard deviation. Length is normalized with h_m and velocity is normalized with the freestream velocity U_0.

Std	0.00	0.125	0.250	0.375	0.500	0.625	0.750
d	0.619	0.619	0.652	0.701	0.760	0.834	0.923
z_o	0.037	0.048	0.058	0.070	0.088	0.096	0.109
u_τ	0.069	0.073	0.077	0.079	0.085	0.087	0.091
U_h	0.427	0.463	0.471	0.474	0.475	0.478	0.483

Table 4.3: Same as table 4.2 for case Lf11S.

Std	0.00	0.125	0.250	0.375	0.500	0.625	0.750
d	0.638	0.633	0.664	0.705	0.763	0.836	0.924
z_o	0.066	0.077	0.099	0.118	0.146	0.157	0.181
u_τ	0.077	0.080	0.085	0.089	0.095	0.099	0.102
U_h	0.348	0.394	0.398	0.403	0.3960	0.393	0.393

Table 4.4: Same as table 4.2 for case Lf11A.

Std	0.00	0.125	0.250	0.375	0.500	0.625	0.750
d	0.638	0.633	0.664	0.705	0.763	0.836	0.924
z_o	0.066	0.075	0.100	0.123	0.142	0.164	0.190
u_τ	0.077	0.079	0.085	0.089	0.093	0.098	0.103
U_h	0.348	0.392	0.393	0.392	0.388	0.392	0.385

Table 4.5: Same as table 4.2 for case Lf25S.

Std	0.00	0.125	0.250	0.375	0.500	0.625	0.750
d	0.704	0.675	0.680	0.712	0.768	0.840	0.925
z_o	0.096	0.114	0.158	0.210	0.249	0.275	0.311
u_τ	0.083	0.089	0.098	0.104	0.110	0.115	0.119
U_h	0.227	0.304	0.304	0.287	0.283	0.283	0.275

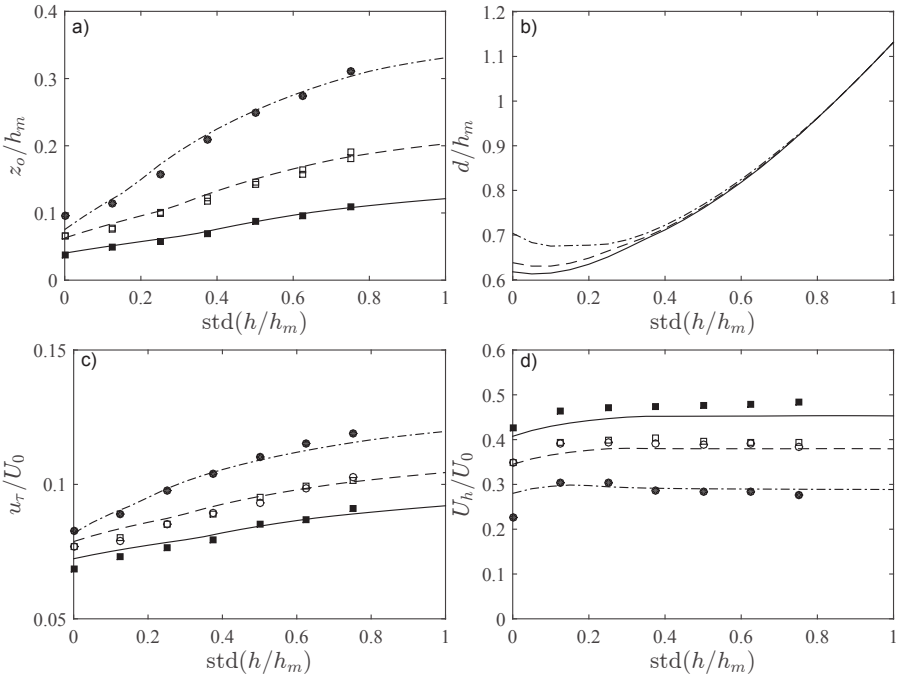

Figure 4.26: Comparison of the analytical model predictions of z_o, d, U_h, u_τ as function of the height standard deviation (line) with the LES measurements (symbols). LES measurements are denoted with symbols. L06S: solid square, L11S: empty square, L11A: empty circle, L25S: solid circle. The lines are model predictions. L06S: solid line, L11S/A: dashed line (no difference is observed for model prediction for L11S and L11A for this roughness configuration), L25S: dot-dashed line.

results quite well over a significant range of parameters.

Several observations can be made about the model. First, both z_o and u_τ increase with the standard deviation of the roughness height. An up to threefold increase in z_o can be observed for Lf25S from std(h/h$_\mathrm{m}$) = 0 to std(h/h$_\mathrm{m}$) = 1. Second, while z_o, u_τ increase steadily for Lf06S and Lf11S as std(h/h$_\mathrm{m}$) increases, for Lf25S a faster increase in z_o and u_τ is observed at low std(h/h$_\mathrm{m}$). A similar rate of increase with the standard deviation is observed at high standard roughness deviation for all three sets of cases considered. Third, an increase in U_h is observed at low standard deviation of

roughness height, and then the value stays almost constant, although the exact value varies from case to case. The increase in U_h at low std($\mathrm{h/h_m}$) could due to the fact that we have defined U_h at $U(z = h)$. Because of height non-uniformity, at h_h the planar area density λ_p is only half of that for the case when roughness has uniform height.

Next, a qualitative explanation is attempted to elucidate the trends in the changing slopes of z_0 and d as function of std(h/h_m). It is postulated that the change in behavior indicates a change in roughness regime, changing from '$d'-$type of roughness to '$k'-$type of roughness at larger std(h/h_m). Consider figure 4.27, which shows several vertical plane cuts from cases L06S-Std00, L06S-Std50, L25S-Std00, L25S-Std50. A d-type roughness behavior is observed in L25S-Std00. For 'd'-type of roughness, the flow above the roughness skims over the roughness elements and as a result less drag is generated. As the standard deviation in the roughness height increases, the roughness for $L25S$ clearly changes from 'd'-type roughness to 'k'-type roughness (figure 4.27,d)), allowing the flow above to impinge some of the roughness elements. This transition in flow regime is consistent with a more rapid increase in u_τ, and z_o at low std(h/h_m). Once std(h/h_m) is above some value (for the cases studied here it seems to be around std(h/h_m) ~ 0.3), the increase is less rapid since the entire behavior follows 'k'-type behavior without the rapid increase in drag associated with the transition from '$d'-$type to '$k'-$type roughness. For low initial solidities, even the cases with uniform roughness height are already in the '$k'-$type regime and thus

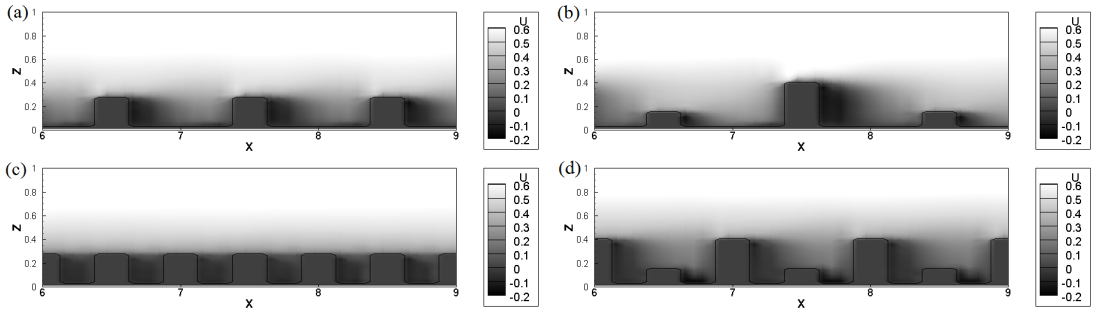

Figure 4.27: Vertical plane cuts of the averaged streamwise velocity from a) L06S-Std00, b) L06S-Std50, c) L25S-Std00, d) L25S-Std50 through the middle plane of the roughness.

display a more uniform increase with standard deviation.

4.4.4 Rectangular roughness with Gaussian distribution

In this subsection, the model predictions are compared with the LES measurements of rectangular roughness with Gaussian distribution (set II in §4.2.2). Both the mean roughness height and surface coverage (11%) are kept constant. The standard deviation in roughness height is varied according to values $\sigma_h/h = 0.24, 0.35, 0.50$. For each σ_h, four realizations of rough walls are randomly generated for the LES runs. The LES setup has been described in §4.2.1.

The temporally averaged velocity is further averaged within a streamwise section of length $6h_m$ centered at $x = 24h_m$ to obtain the mean velocity profile. Figure 4.28 shows the mean profiles for all the cases considered in this subsection. Very little differences are observed between cases with the same roughness height distribution.

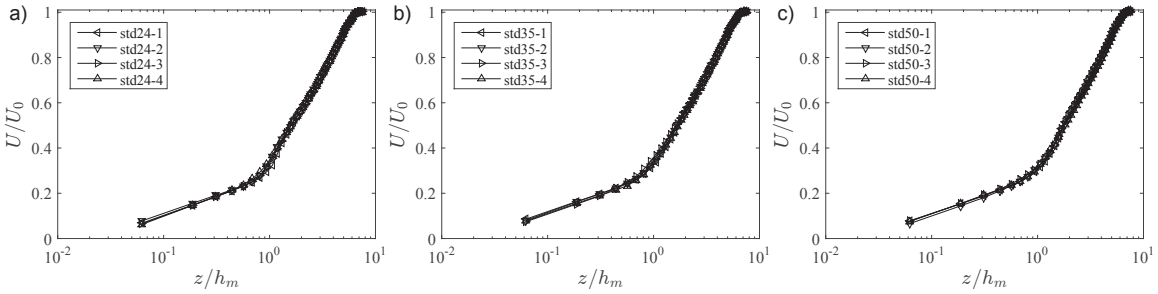

Figure 4.28: The mean streamwise velocity profile for $\text{std}(h/h_m) = 0.24, 0.35, 0.50$ (from left to right). For each σ_h, four LES cases consisting of four realizations of randomly generated surfaces are conducted.

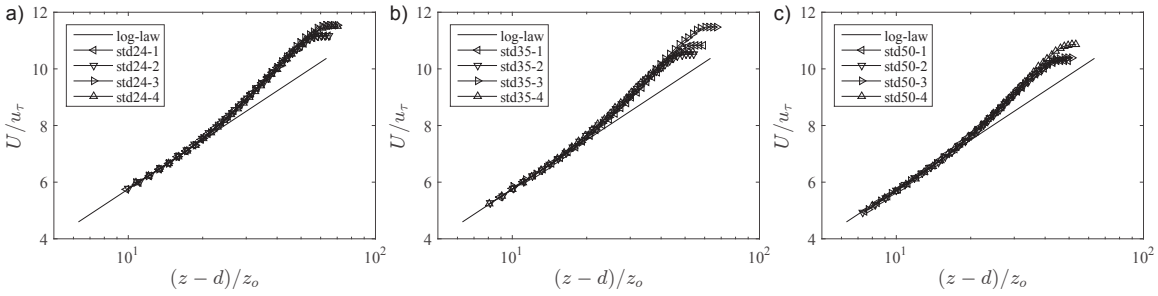

Figure 4.29: A comparison of the log law and the fitted mean streamwise velocity profile for all cases. From left to right $\text{std}(h/h_m) = 0.24, 0.35, 0.50$.

The log law is fitted between $z = 1.5h_m + \sigma_h$ and $z = 2.5h_m + \sigma_h$ using the displacement d from the rough wall model (see below) and the von Karman constant $\kappa = 0.4$. The measured values of z_o, u_τ, and the boundary layer thickness δ are tabulated in table 4.6. Figure 4.29 compares the log law and the fitted profiles.

Next, to obtain the model predictions for z_o, d, u_τ and U_h, we generate 512 realizations (sufficiently many to obtain converged statistics) of rough surfaces for a large range of roughness height variances $std(h/h_m)$ between 0 and 0.5. We apply the sheltering model to each surface. Geometrically computing the sheltered frontal area is non-trivial for such complex surfaces, and therefore in this case we must use a

Table 4.6: Hydrodynamic roughness height z_o, displacement height d, friction velocity u_τ, and 99% boundary layer thickness δ for roughness with different height variation. z_o, d, δ are normalized by the mean roughness height h_m and the friction velocity is normalized with the free stream velocity U_0.

	std24-1	std24-2	std24-3	std24-4	std35-1	std35-2	std35-3	std35-4
$z_o(h_m)$	0.108	0.106	0.098	0.098	0.116	0.128	0.103	0.129
$d(h_m)$	0.630	0.629	0.630	0.629	0.651	0.650	0.650	0.648
$u_\tau(U_0)$	0.090	0.090	0.087	0.087	0.093	0.095	0.087	0.950
$\delta(h_m)$	6.31	6.35	6.34	6.37	6.34	6.36	6.44	6.36

	std50-1	std50-2	std50-3	std50-4
$z_o(h_m)$	0.139	0.142	0.135	0.130
$d(h_m)$	0.681	0.680	0.680	0.679
$u_\tau(U_0)$	0.098	0.097	0.097	0.093
$\delta(h_m)$	6.35	6.56	6.38	6.50

numerical code to obtain A_s. The method is as described in more detail in Appendix A. Figure 4.30 is a graphical visualization of the modeled sheltering regions for one particular realization with $\sigma_h = 0.5h$. We then average the model predictions for z_o, d, u_τ and U_h and plot the results as solid lines in Fig. 4.31.

Figure 4.31 compares the model predictions and the mean values from the four LES realizations for each value of std(h). The boundary layer thickness is set to be $\delta = 6.4h_m$ in the model and a mild wake correction $\Pi = 0.5$ is used. As can be seen, the model predictions agree well with the LES data. The uncertainty in z_o, u_s due to the randomness in the roughness height distribution is not strong. We observe that with an increase in the roughness height variation, z_o increases considerably, while u_τ and U_h increase but only by a small amount.

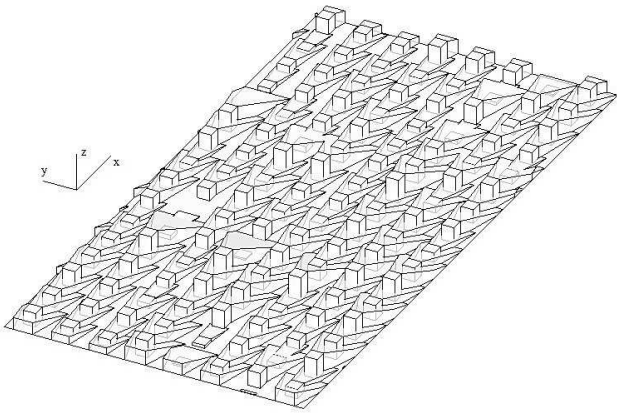

Figure 4.30: Visualization of the sheltering regions among the roughness elements with Gaussian height distribution in a realization, with $\sigma_h = 0.5h_m$. Periodicity is assumed in the spanwise (y) and streamwise (x) directions.

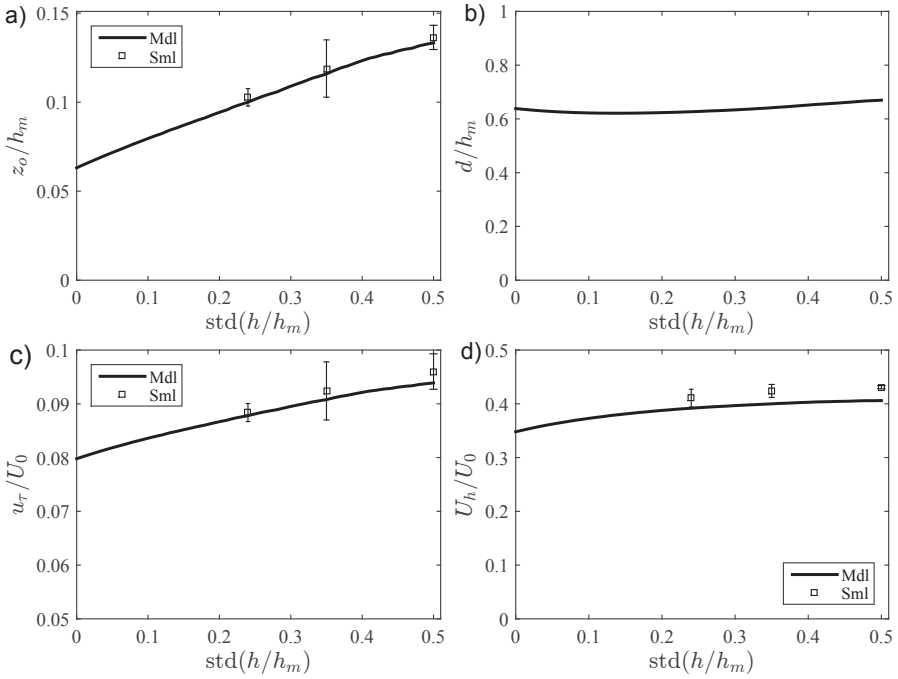

Figure 4.31: A comparison of the model predictions and the LES measurements. Mdl stands for model and the symbols stand for LES results. For each symbol, the largest deviation from the mean value observed in the 4 LES with the same std(h/h_m) is shown as the extend of either side of the error bar.

4.5 Conclusions

In this study, the mean velocity distribution within the roughness layer of turbulent boundary layer flow over arrays of rectangular-prisms is examined. It is found that for a wide range of element placement morphologies, a generic exponential velocity profile with respect to the wall normal distance is a very good description of the mean velocity within the upper 70-80% portion of the roughness layer. To model the hydrodynamic effects of rough walls, a shape function for the velocity profile is proposed in replacement of a mixing length closure and integration of the temporally/spatially averaged momentum equation. There are five unknowns in the shape function: the hydrodynamic roughness length z_o, displacement height d, friction velocity u_τ, velocity at the top of the canopy U_h, and an attenuation coefficient a. Four constraints, including the momentum balance, are available from the first principles. In addition, a geometric sheltering model is developed to provide the fifth condition. Moreover, a drag coefficient C_d is set to unity, and the sheltering expansion rate is set to $C_\theta u_\tau/U_h$ with a coefficient C_θ that is dependent on roughness element aspect ratio. Different from earlier analytical roughness models, the model developed in this study is responsive to the roughness distribution because the model is coupled with a geometric sheltering model. The model is applied to cubic roughness distributions of various solidities, to the case of arrays of transverse 2D square ribs, and to roughnesses with non-uniform height distributions. The model predictions compare well with experimental and numerical datasets from other authors, and with the LES

results from this study. Correct asymptotic behaviors are obtained both at $\lambda_f \to 1$ and $\lambda_f \to 0$ (in the latter case including a correction via drag partition described in appendix 8.3.2). The sheltering model developed here can also be responsive to additional variations in the spatial roughness distribution. Comparisons of the model predicitions with rectangular roughnesses oriented at angles (i.e. non-frontal) with the flow, or different incident flow directions, and arrays with elements displaced in the spanwise direction for arbitrary distances, will be presented in a separate report.

The analytical model is, for now, restricted to roughness with rectangular-prism shape, since the sheltering region within the wake of such objects can be clearly related to the frontal cross section of the object. For more general shapes, such as surfaces covered with Lego blocks,[178,179] as well as with as cones, semi- hemispheres, frustums, etc., where the flow separation point may not be easily identified, further generalizations and detailed comparisons with data are required to establish wider generality and applicability of the model's basic ingredients. Also, inclusion of spatially changing roughness configuration and effects of non-equilibrium conditions[180] would be of considerable interest.

Chapter 5

A hierarchical-random-additive model for wall-bounded flows at high Reynolds number

5.1 Introduction

A robust feature of high Reynolds number turbulent boundary layer flows over walls is the presence of the logarithmic region, a region where neither the viscosity nor the bulk flow appears to be dynamically dominant.[89,181,182] One particularly effective conceptual model of wall turbulence dates back to Townsend,[15] who hypothesized that the logarithmic region consists of space-filling, self-similar eddies as shown schematically in figure 5.1(a), whose sizes scale with their distance from the wall. This

attached eddy hypothesis has proven to be quite useful in providing (non-trivial) estimates on the scalings in various turbulence quantities including turbulence intensity, Reynolds stress, single-point moments, two-point statistics, pressure fluctuations etc. in wall-bounded flows at high Reynolds number.[14,15,91,94–98] The hypothesis has also guided studies of flow structures,[99,100] including near-wall hairpins,[101–105] coherent vortex packets/clusters;[106–112] and has provided insights into modelling of flow spectra.[113–115]

Therefore it is not surprising that many efforts have been devoted to various formal mathematical formulations of the Townsend attached eddy hypothesis.[14,15,96,116,117] While details might vary among the various formalisms, all attached eddy models are based on an eddy population density that is inversely proportional to the wall distance, i.e. $P(z) \sim 1/z$, which is a direct consequence of the space-filling property of the hierarchical attached eddies.[14] Note that to be consistent with the high Reynolds number boundary layer literature, in this chapter, we use z instead of y used in chapters 2-4 to denote wall distance.

A particularly simple version of the attached eddy hypothesis was invoked in Ref. 94 to make predictions of logarithmic scaling in single-point high-order moments. Discretizing the wall normal distance logarithmically and counting the number of attached eddies that affect a generic point at height z, namely adding the contributions from the eddies at all heights above z up to the largest at the top of the boundary

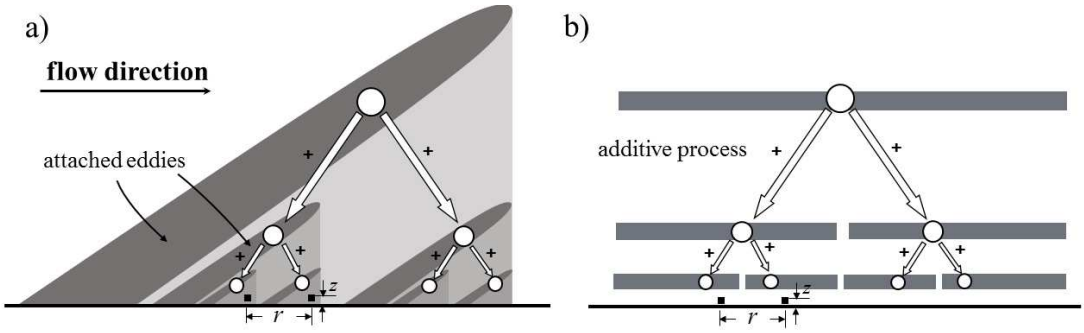

Figure 5.1: Sketch of hypothesized structure of attached eddies in wall bounded flows (a). The eddy population density is inversely proportional to the wall distance. On a 2D plane cut as shown here, on average, the number of visible eddies doubles as the size halves. (b) is a more explicit representation of the additive process.

layer (at $z \sim \delta$), one obtains:

$$N_z \sim \int_z^\delta P(z)\, dz \sim \log\left(\delta/z\right). \tag{5.1}$$

The velocity at a point at height z is assumed to be an additive superposition of the velocity induced by each attached eddy that overlaps the particular point of interest. Taking into consideration the self-similar property of the assumed attached eddies and assuming that they are non-interacting, the instantaneous velocity at this generic point is simply modeled as a sum of identically, independently distributed (i.i.d.) random additives a_i with $\langle a_i \rangle = 0$. Denoting the instantaneous streamwise velocity normalized by friction velocity (or velocity fluctuation if its time mean is subtracted) at height z as u_z^+, a "poor man's" attached eddy model can be written as:

$$u_z^+ = \sum_{i=1}^{N_z} a_i. \tag{5.2}$$

The various a's are organized hierarchically on a tree-like structure as depicted in figure 5.1(b), with a_1 corresponding to the largest eddy that overlaps the entire hierarchy, a_2 taking on different values at each of the smaller eddies (two shown, but four on the plane), and so forth. Besides Ref. 94, this hierarchical additive model has been recently used in Ref. 183 to provide quantitative estimates on the scalings of single-point, two-point moment-generating-functions in high Reynolds number boundary layers. The predicted power-law behaviors in the single-point $\langle \exp(qu) \rangle$ and two-point $\langle \exp(qu + q'u(x+r)) \rangle$ moment generating functions with respect to the wall normal distance z/δ and two-point displacement r/δ were confirmed in experimental measurements in Ref. 183. Here we apply the formalism to elucidate logarithmic scaling laws of particular two-point moments that scale with $\log(\delta/r)$.

One of the major results Townsend arrived at is the logarithmic scaling in the variance of streamwise velocity fluctuation:

$$\left\langle u_z^2 \right\rangle = A_1 \log\left(\delta/z\right) + B_1, \tag{5.3}$$

where $A_1 \approx 1.26$ is the Townsend-Perry constant,[89,90,92,93,184] B_1 is a (flow-dependent) constant, $\langle \cdot \rangle$ indicates ensemble averaging and we have dropped henceforth the superscript + (conventionally used to indicate normalization by wall units). A considerable amount of empirical evidence both from laboratory experiments and numerical simulations has been reported recently in support of the logarithmic scaling shown in Eq.

5.3.[90,185]

As an example of the application of the HRAP based attached eddy model, the basic scaling of Eq. 5.3 using Eqs. 5.1, 5.2 can be derived simply as follows: given that a_i's are i.i.d.'s, squaring both sides of Eq. 5.2 leads to

$$\left\langle u_z^2 \right\rangle = N_z \left\langle a^2 \right\rangle \sim \log(\delta/z) \tag{5.4}$$

thus recovering the logarithmic scaling in $\langle u_z^2 \rangle$.

While the HRAP enables us to obtain very rapidly scaling behavior (functional forms), evaluating pre-factors and additive coefficients requires more detailed modeling assumptions and more extensive calculations. For instance in the formalism developed in Refs. 14, 95, where the arrival of an attached eddy at a generic point in the flow field is assumed to be described by a Poisson process, rigorous, step-by-step derivations can be carried out to derive generalized log laws in even-order-moments of single-point velocity fluctuations and even-order-moments of structure-functions, i.e.

$$\begin{aligned} \left\langle (u_z)^{2p} \right\rangle^{1/p} &= A_p \log(\delta/z) + B_p, \\ \left\langle (u_z(x+r) - u_z(x))^{2p} \right\rangle^{1/p} &= D_p \log(r/z) + E_p, \end{aligned} \tag{5.5}$$

where A_p, B_p, D_p, E_p are coefficients. Empirical evidence for the logarithmic laws shown in Eq. 5.5 has been reported in Refs. 94, 95, 159. Hereafter we focus mainly on the scaling behavior and will not emphasize the typically flow-dependent coefficients B_p, E_p.

We show that predictions of the generalized logarithmic laws in Eq. 5.5, as well as for the standard two-point correlation function $S_1 = \langle u_z(x)u_z(x+r)\rangle = A_1 \log(\delta/r) + B_1'$ can be made quite easily using Eqs. 5.1, 5.2. Moreover, the HRAP model will be used in this section to predict the existence of a new family of logarithmic laws such as

$$\begin{aligned} S_2 &= \left[\frac{3}{2}\left\langle u_z^2(x)u_z^2(x+r)\right\rangle - \frac{1}{2}\left\langle u_z^4(x)\right\rangle\right]^{1/2} \\ &= A_2 \log\left(\frac{\delta}{r}\right) + B_2', \end{aligned} \tag{5.6}$$

$$\begin{aligned} S_3 &= \left[\frac{5}{2}\left\langle u_z^3(x)u_z^3(x+r)\right\rangle - \frac{3}{2}\left\langle u_z(x)u_z^5(x+r)\right\rangle\right]^{1/3} \\ &= A_3 \log\left(\frac{\delta}{r}\right) + B_3', \end{aligned} \tag{5.7}$$

$$\begin{aligned} S_4 = \Bigg[& \frac{1}{10}\left\langle u_z^8(x)\right\rangle + \frac{9}{10}\left\langle u_z(x)u_z^7(x+r)\right\rangle \\ & -\frac{49}{10}\left\langle u_z^2(x)u_z^6(x+r)\right\rangle - \frac{21}{10}\left\langle u_z^3(x)u_z^5(x+r)\right\rangle \\ & +\frac{70}{10}\left\langle u_z^4(x)u_z^4(x+r)\right\rangle\Bigg]^{1/4} = A_4 \log\left(\frac{\delta}{r}\right) + B_4'. \end{aligned} \tag{5.8}$$

Note that the two-point structure functions studied in Ref. 95 depend on $\log(r/z)$. It will be shown that the new generalized two-point correlations depend on $\log(\delta/r)$ instead, i.e. scaling with the boundary layer thickness rather than the local scale z. Invoking the Taylor's frozen turbulence hypothesis,[186] experimental hot-wire turbulence measurements from the Melbourne High-Reynolds-Number-Boundary-Layer-Wind-Tunnel (HRNBLWT)[187] are analyzed to test the existence of such new logarithmic laws.

The rest of the chapter is organized as follows: in section 5.2, the HRAP model is

used to derive various generalized logarithmic laws. Empirical evidence for the new laws is presented in section 5.3. In section 5.4 it is shown that similar scaling can be recovered more rigorously using the formalism developed in Ref. 14. Conclusions are given in section 5.5.

5.2 Hierarchical Random Additive Process (HRAP)

In this section, HRAP is used to predict the scalings of various turbulence quantities in the logarithmic region. We assume the flow is at high Reynolds number and we consider only streamwise velocity fluctuations. Unless stated otherwise, wall units are used for normalization.

In the limit of high Reynolds number, $N_z \sim \log(\delta/z)$ tends to large values and the central limit theorem applied to the sum in Eq. 5.2 leads to

$$u_z = \mathcal{N}(\mu = 0, \sigma^2 = N_z \left\langle a^2 \right\rangle), \tag{5.9}$$

where $\mathcal{N}(\mu, \sigma^2)$ is a Gaussian random variable with mean μ and variance σ^2. As argued in Ref. 94, Eq. 5.9 directly leads to

$$\left\langle u_z^{2p} \right\rangle = (2p-1)!! A_1^p \log^p(\delta/z), \tag{5.10}$$

where A_1 is the Townsend-Perry constant mentioned before. Comparing with Eq. 5.5 leads to

$$A_p^p = (2p-1)!!A_1^p. \tag{5.11}$$

As shown in Ref. 94, data support the logarithmic scaling of Eq. 5.10 but show that A_p is smaller than the Gaussian prediction of Eq. 5.11.

Next we consider the velocity at a point P' above P and at a distance z_1 from the wall, $z_1 > z$. Because an attached eddy that contributes to the velocity at point P' also affects point P, Eq. 5.2 directly leads to

$$\begin{aligned} u_z - u_{z_1} &= \sum_{i=1}^{N_z} a_i - \sum_{i=1}^{N_{z_1}} a_i = \sum_{i=N_{z_1}}^{N_z} a_i, \\ N_z - N_{z_1} &\sim \log(\delta/z) - \log(\delta/z_1) = \log(z_1/z). \end{aligned} \tag{5.12}$$

Following the same arguments that lead to Eq. 5.10, Eq. 5.12 directly leads to

$$\left\langle (u_z(x) - u_{z_1}(x))^{2p} \right\rangle = (2p-1)!!A_1^p \log^p(z_1/z). \tag{5.13}$$

Now we consider the velocity at P and a point P'' which is at a distance r downstream of P (as shown in Fig. 5.1). For small r compared to z, all eddies that affect P similarly affect P''. At a distance $r = z/\tan\theta$, where θ is the inclination angle of a typical attached eddy, P, P'' are different by at most about one eddy (one additive term) and share all eddies above z. As a result, $u_z(x)$ and $u_z(x + z/\tan\theta)$, differing

by one random additive (the random additive that is associated with eddies of size z), are approximately equal because $N_z = \log(\delta/z)$ is assumed to be large (see similar argument in Refs. 188, 189). As r further increases P, P'' share fewer and fewer common eddies.

Now let us consider the general case for arbitrary, large r in the context of two-point moments of the form $\langle u_z^n(x) u_z^{2p-n}(x+r)\rangle$. We decompose the velocity fluctuation at a point into contributions from eddies of size smaller than r (height smaller than $r\tan\theta$) and greater than r (height larger than $r\tan\theta$). Let

$$z_r = r\tan\theta \tag{5.14}$$

and define $u_{z\setminus z_r}(x) = u_z - u_{z_r}$, which within the additive model can be regarded as the contribution to the velocity fluctuation only from those eddies whose size is smaller than r. Then we have:

$$\begin{aligned}\left\langle u_z^n(x) u_z^{2p-n}(x+r)\right\rangle = \left\langle [u_{z\setminus z_r}(x) + u_{z_r}(x)]^n \times \right. \\ \left. [u_{z\setminus z_r}(x+r) + u_{z_r}(x+r)]^{2p-n}\right\rangle .\end{aligned} \tag{5.15}$$

In the HRAP model, $u_{z\setminus z_r}(x)$ and $u_{z\setminus z_r}(x+r)$ can be considered statistically independent because eddies of size smaller than z_r cannot affect two points that are separated by a distance r. Moreover, $u_{z\setminus z_r}(x)$ and $u_{z_r}(x)$ are statistically independent (so are $u_{z\setminus z_r}(x+r)$ and $u_{z_r}(x+r)$) because eddies of different sizes are not correlated

in the current version of the model since all a's are assumed independent. Combining these observations and the approximation $u_{z_r}(x) \approx u_{z_r}(x+r)$, the moments $\langle u_z^n(x) u_z^{2p-n}(x+r)\rangle$ can be evaluated.

When evaluating the products and separating them accordingly at various orders, there seems to be no compact expression for $\langle u_z^n(x) u_z^{2p-n}(x+r)\rangle$. However, since it is unlikely that there would be much interest in much higher order statistics than the 8th order moments, we can explicitly evaluate each combination of p and n for $p < 5$. As an initial example, we evaluate the standard two-point correlation function $\langle u_z(x) u_z(x+r)\rangle$ as follows:

$$\begin{aligned} & \langle u_z(x) u_z(x+r)\rangle \\ = \;& \left\langle \left(u_{z\setminus z_r}(x) + u_{z_r}(x)\right)\left(u_{z\setminus z_r}(x+r) + u_{z_r}(x+r)\right)\right\rangle \\ = \;& \left\langle u_{z\setminus z_r}(x)\right\rangle \left\langle u_{z\setminus z_r}(x+r)\right\rangle + 2\left\langle u_{z\setminus z_r}(x)\right\rangle \langle u_{z_r}(x)\rangle \\ & + \langle u_{z_r}(x) u_{z_r}(x)\rangle \,. \end{aligned} \tag{5.16}$$

Since the the velocity fluctuation u has zero mean, we obtain

$$\begin{aligned} \langle u_z(x) u_z(x+r)\rangle = \langle u_{z_r}(x) u_{z_r}(x)\rangle &= A_1 \log(\delta/z_r) \\ &= A_1 \log(\delta/r) + B_1', \end{aligned} \tag{5.17}$$

where the last equality holds up to an additive coefficient B_1' that can depend on, for instance, $\tan\theta$.

Defining

$$L_{p,n} = \log^{p-n}(\delta/z_r) \log^n(z_r/z)\,, \tag{5.18}$$

and following the same procedure used to obtain Eq. 5.17, and using Eq. 5.10, Eq. 5.13, we have

$$\begin{aligned}
\left\langle u_z^0(x)u_z^4(x+r)\right\rangle &= A_2^2L_{2,2}+6A_1^2L_{2,1}+A_2^2L_{2,0};\\
\left\langle u_z^1(x)u_z^3(x+r)\right\rangle &= 0 \qquad +A_1^2L_{2,1} \ +A_2^2L_{2,0};\\
\left\langle u_z^2(x)u_z^2(x+r)\right\rangle &= A_1^2L_{2,2}+A_1^2L_{2,1} \ +A_2^2L_{2,0};
\end{aligned} \tag{5.19}$$

$$\begin{aligned}
\left\langle u_z^0(x)u_z^6(x+r)\right\rangle &= A_3^3L_{3,3} \quad +15A_2^2A_1L_{3,2} \qquad +15A_1A_2^2L_{3,1}+A_3^3L_{3,0};\\
\left\langle u_z^1(x)u_z^5(x+r)\right\rangle &= 0 \qquad +5A_2^2A_1L_{3,2} \qquad +10A_1A_2^2L_{3,1}+A_3^3L_{3,0};\\
\left\langle u_z^2(x)u_z^4(x+r)\right\rangle &= A_2^2A_1L_{3,3}+\left(6A_1^3+A_2^2A_1\right)L_{3,2}+7A_1A_2^2L_{3,1} \ +A_3^3L_{3,0};\\
\left\langle u_z^3(x)u_z^3(x+r)\right\rangle &= 0 \qquad +9A_1^3L_{3,2} \qquad +6A_1A_2^2L_{3,1} \ +A_3^3L_{3,0};
\end{aligned} \tag{5.20}$$

$$\begin{aligned}
\left\langle u_z^0(x)u_z^8(x+r)\right\rangle &= A_4^4L_{4,4} \quad +28A_3^3A_1L_{4,3} \qquad +70A_2^4L_{4,2} \qquad +28A_1A_3^3L_{4,1}+A_4^4L_{4,0};\\
\left\langle u_z^1(x)u_z^7(x+r)\right\rangle &= 0 \qquad +7A_3^3A_1L_{4,3} \qquad +35A_2^4L_{4,2} \qquad +21A_1A_3^3L_{4,3}+A_4^4L_{4,0};\\
\left\langle u_z^2(x)u_z^6(x+r)\right\rangle &= A_3^3A_1L_{4,4}+\left(15A_1^2A_2^2+A_3^3A_1\right)L_{4,3}+\left(15A_1^2A_2^2+15A_2^4\right)L_{4,2}+16A_1A_3^3L_{4,1}+A_4^4L_{4,0};\\
\left\langle u_z^3(x)u_z^5(x+r)\right\rangle &= 0 \qquad +15A_1^2A_2^2L_{4,3} \qquad +\left(30A_1^2A_2^2+5A_2^4\right)L_{4,2} \ +13A_1A_3^3L_{4,1}+A_4^4L_{4,0};\\
\left\langle u_z^4(x)u_z^4(x+r)\right\rangle &= A_2^4L_{4,4} \quad +12A_1^2A_2^2L_{4,3} \qquad +\left(36A_1^2A_2^2+2A_2^4\right)L_{4,2} \ +12A_1A_3^3L_{4,1}+A_4^4L_{4,0};
\end{aligned} \tag{5.21}$$

The A_p's in Eq. 5.19, Eq. 5.20, Eq. 5.21 can be replaced with $[(2p-1)!!]^{1/p}A_1$ to further simplify the expressions (not shown here).

We make three observations. First, except for $n=0$ and $n=p$, all $L_{p,n}$'s are mixed logarithmic scalings involving different powers of $\log(\delta/z_r)$ and $\log(z_r/z)$. At high Reynolds number, as $r/z\to\infty$ (and $z_r/z\to\infty$), for $\delta/z_r\sim O(1)$ $L_{p,p}$ becomes the dominant term; as $r/z\sim O(1)$, $\delta/r\to\infty$, $L_{p,0}$ becomes the dominant term. As a result, in those limits logarithmic scaling can be observed in quantities such as $\left\langle u_z^n(x)u_z^{2p-n}(x+r)\right\rangle^{1/p}$. This aspect is, however, not further explored here. Second,

for a fixed p, the coefficient in front of the term $L_{p,0}$ is A_p^p and is not dependent on n.

Third, the traditionally defined two-point structure functions $\langle [u_z(x) - u_z(x+r)]^{2p} \rangle$ (in Eq. 5.5), being combinations of $\langle u_z^n(x) u_z^{2p-n}(x+r) \rangle$, i.e.

$$\begin{aligned} &\left\langle (u_z(x) - u_z(x+r))^{2p} \right\rangle^{1/p} \\ &= \left[\sum_{n=0}^{2p} C_{2p}^n \left\langle u_z^n(x) u_z^{2p-n}(x+r) \right\rangle \right]^{1/p}, \end{aligned} \tag{5.22}$$

where $C_{2p}^n = (2p)!/[n!(2p-n)!]$, can be shown to depend only on the term $L_{p,p}$. In order to verify this, we compute, for example, $\langle (u_z(x) - u_z(x+r))^6 \rangle$:

$$\begin{aligned} &\left\langle (u_z(x) - u_z(x+r))^6 \right\rangle \\ = \quad & 2 \left\langle u_z^0(x) u_z^6(x+r) \right\rangle - 12 \left\langle u_z^1(x) u_z^5(x+r) \right\rangle \\ & +30 \left\langle u_z^2(x) u_z^4(x+r) \right\rangle - 20 \left\langle u_z^3(x) u_z^3(x+r) \right\rangle . \end{aligned} \tag{5.23}$$

Substituting Eq. 5.20 into Eq. 5.23 indeed leads to

$$\begin{aligned} &\left\langle (u_z(x) - u_z(x+r))^6 \right\rangle \\ =&(2A_3^3 + 30A_2^2 A_1) L_{3,3} \\ =&(2A_3^3 + 30A_2^2 A_1) \log(z_r/z) \sim \log(r/z), \end{aligned} \tag{5.24}$$

i.e. one obtains an exact cancellation of all $L_{p,n}$'s for $n < p$. The same cancellations are found for structure functions of second, fourth, eighth orders, etc. (not shown here). Hence we recover the logarithmic scaling in structure functions (such scaling

has been explored based on experimental data in Ref. 95).

Structure functions thus pick up the logarithmic scaling $\log(r/z)$, i.e the term $L_{p,p}$. The other term that does not contain mixed logarithmic scalings is $L_{p,0}$. We attempt to find combinations of $\langle u_z^n(x) u_z^{2p-n}(x+r)\rangle$ such that all $L_{p,n}$ $n>0$ cancel except for $L_{p,0}$. Formally, for a fixed p, we attempt to find c_n's such that

$$\sum_{n=0}^{p} c_n \langle u_z^n(x) u_z^{2p-n}(x+r)\rangle = A_p^p L_{p,0}. \tag{5.25}$$

The new logarithmic laws in Eqs. 5.6-5.8 are obtained by solving Eq. 5.25 for the c_n's. Here, as an example, we verify S_3:

$$\begin{aligned} &\left[\frac{5}{2}\left\langle u_z^3(x) u_z^3(x+r)\right\rangle - \frac{3}{2}\left\langle u_z(x) u_z^5(x+r)\right\rangle\right]^{1/3} \\ &= \left[A_3^3 L_{3,0} + \left(\frac{45}{2}A_1^3 - \frac{15}{2}A_2^2 A_1\right) L_{3,2}\right]^{1/3}. \end{aligned} \tag{5.26}$$

Using Eq. 5.10 (i.e. $A_2^2 = 3A_1^2$), Eq. 5.26 leads to

$$\begin{aligned} &\left[\frac{5}{2}\left\langle u_z^3(x) u_z^3(x+r)\right\rangle - \frac{3}{2}\left\langle u_z(x) u_z^5(x+r)\right\rangle\right]^{1/3} \\ &= A_3 L_{3,0}^{1/3} \;=\; A_3 \log(\delta/r) + B_3'. \end{aligned} \tag{5.27}$$

S_2, S_4 can be verified in the same manner and again the relation $A_p^p = (2p-1)!! A_1^p$ needs to be used to ensure exact cancellation of $L_{p,n}$, $n>0$. Notice that the term that remains when evaluating S_i, $i=1,2,3,4$ comes from $\langle (u_z - u_{z_r})^{2p}\rangle = A_p^p \log^p(z/r)$, and the predicted slopes in those logarithmic laws are directly expressed in terms of A_p ($p=1,2,3,4$) and not as $(2p-1)!!A_p^p$. As a result, for a comparison of the slopes predicted in those logarithmic scaling (in section 5.3), we use the measured A_p's instead of the Gaussian predictions $A_p = [(2p-1)!!]^{1/p} A_1$.

Up to here we have derived, using the HRAP model, the previously known logarithmic laws (Eq. 5.5) and new ones (Eqs. 5.6-5.8). Supporting empirical evidence for the new logarithmic laws in Eqs. 5.6-5.8 is presented below in section 5.3.

5.3 Experimental Data Analysis

In this section, the logarithmic scalings in Eqs. 5.6-5.8 are examined using the Melbourne wind tunnel measurements. The Reynolds number based on boundary layer height and friction velocity is $Re_\tau = 19030$ (see Ref. 187 for more details of the dataset). The analysis focuses on the scaling in r in the inertial region. The Taylor's frozen turbulence hypothesis is invoked to convert the temporal data from hot-wire measurements to spatial data.[186,190]

Statistical two-point moments as defined in Eqs. 5.6-5.8 are plotted against r^+ and r/z at various heights, namely at $z^+ \approx 3Re_\tau^{0.5}$, 700, 1200 and $z = 0.10\delta$ in figures 5.2, 5.3, 5.4, 5.5. Solid lines show fitted slopes, 1.1, 1.5, 2.0, 1.8 respectively for S_1, S_2, S_3, S_4. Compared with the measured A_p values from Ref. 94, i.e. $A_1 \approx 1.2$, $A_2 \approx 1.8$, $A_3 \approx 2.4$, $A_4 \approx 3.00$, given the uncertainty in the measurements both here and in Ref. 94, the agreement is reasonably well, except for S_4. The fit is conducted within the log region and averaged over the four wall normal locations. The start of the logarithmic region is at around $z^+ = 3Re_\tau^{0.5}$. No logarithmic scaling as indicated in Eqs. 5.6-5.8 is expected $z^+ < 3Re_\tau^{0.5}$, nor above $z^+ = 0.15\delta$, which is the end

of the logarithmic region.[90] At a specific wall normal location in the log region, i.e. following Ref.90, in $3Re_\tau^{0.5} < z^+$, $z < 0.15\delta$, one expects to observe the logarithmic scalings in Eqs. 5.6-5.8 in a range of two-point displacement r that corresponds to flow structures whose elongation is associated with wall distances z belonging to the log region. To obtain a crude estimate of this range, we note that an attached eddy of size h in the vertical direction can affect a distance of $h/\tan(\theta)$ in the flow direction, where θ is the inclination angle of an attached eddy. At a height z, an attached eddy of height $h < z$ is not relevant and therefore, the relevant r range is expected to begin at $r > z/\tan(\theta)$. At large displacements, by this argument, the end of the logarithmic scaling occurs at $r = 0.15\delta/\tan(\theta)$. The typically observed inclination angle of an attached eddy is $\theta \approx 11^\circ - 16^\circ$.[191–194] This leads to an expected range of logarithmic scaling $z/\tan\theta < r < 0.15\delta/\tan\theta$, which is approximately $4z < r < 0.6\delta$. Practically, the relevant range of r, within which logarithmic scaling can be observed, can differ from this estimate and can vary depending on the specific statistical quantity under consideration. However, this estimate is instructive as it correctly points out that the start of the logarithmic scaling in r depends on z and the end on the boundary layer height. With this understanding, we examine figures 5.2-5.5 in detail. First, by plotting against r/z, the starting point of the log region can be determined. At $z^+ = 3Re_\tau^0.5$, slight deviations from logarithmic scaling can be observed for S_1, S_2 from $r/z \approx 2$ to the left. For S_3, S_4 at $z^+ = 3Re_\tau^{0.5}$ and for all S_i, $i = 1, 2, 3, 4$ at $z^+ = 700, 1200, 1900$ ($z = 0.1\delta$), logarithmic scalings start at $r = z$. Hence, $r = z$ is

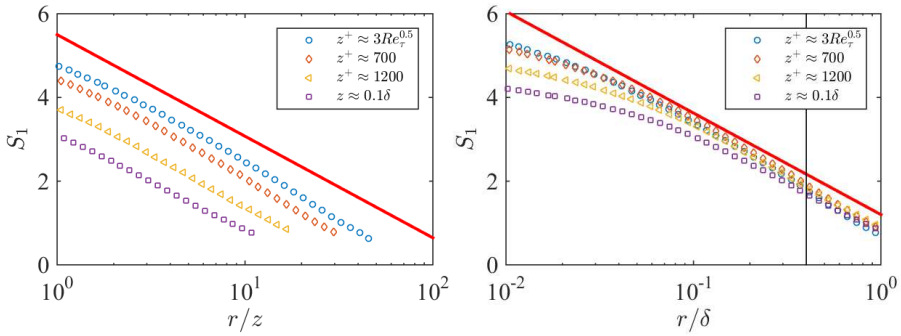

Figure 5.2: S_1 against r/z(top), r^+(bottom) at $z^+ \approx 3Re_\tau^{0.5}$, 700, 1200, and $z = 0.10\delta$. The solid line indicates the fitted slope. $r/\delta = 0.4$ is indicated with a vertical line.

probably a safe estimate for the start point of the logarithmic scalings. The end of the log scaling is better determined by plotting the two-point moments against r/δ. For $S_1 = \langle u_z(x)u_z(x+r)\rangle$, the logarithmic scaling is found to extend at least up to $r = \delta$(and even beyond). For S_2, S_3, flattening of the scaling (decrease in the slope) is found at around $r^+ = 8000$ ($r = 0.4\delta$). The end point of the log scalings is therefore around $r = 0.4\delta$ for S_2, S_3. A lack of data convergence for S_4 makes determining the end point of log scaling of S_4 difficult, but the data is not inconsistent with the estimate $r = 0.4\delta$. In sum, empirically, the logarithmic scaling can be observed in $z < r < 0.4\delta$. To ensure the existence of such a region and at the same time ensuring that the measurement remain in the log region, the analysis must be restricted to heights such that $3Re_\tau^0.5 < z^+$, $z < 0.15\delta$.

The undulations seen in figure 5.5 at large r are due to a lack of full statistical convergence. Limited by the size of the data, we therefore do not consider statistics of higher order. As can be seen, the statistics in Eqs. 5.6-5.8 follow the predicted

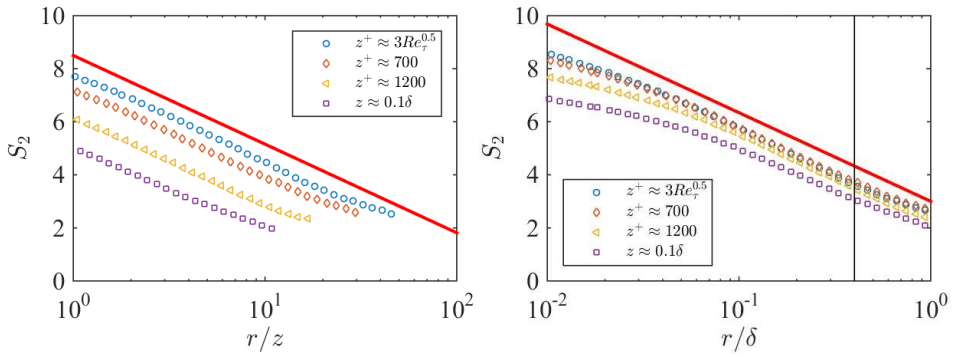

Figure 5.3: Same as figure 5.2, but for S_p ($p = 2$).

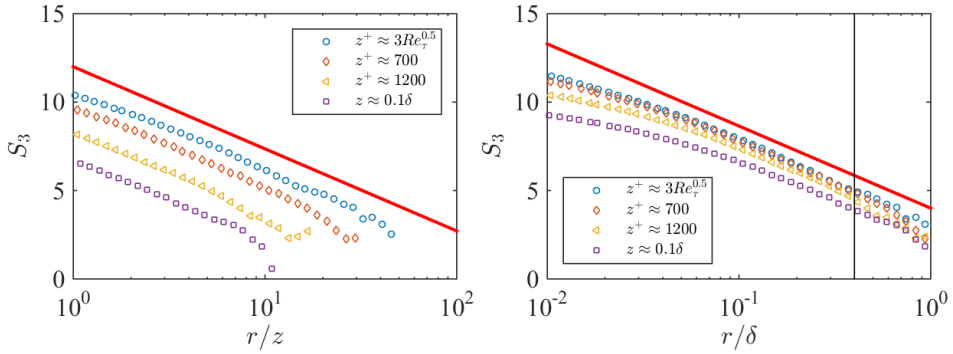

Figure 5.4: Same as figure 5.2, but for S_3.

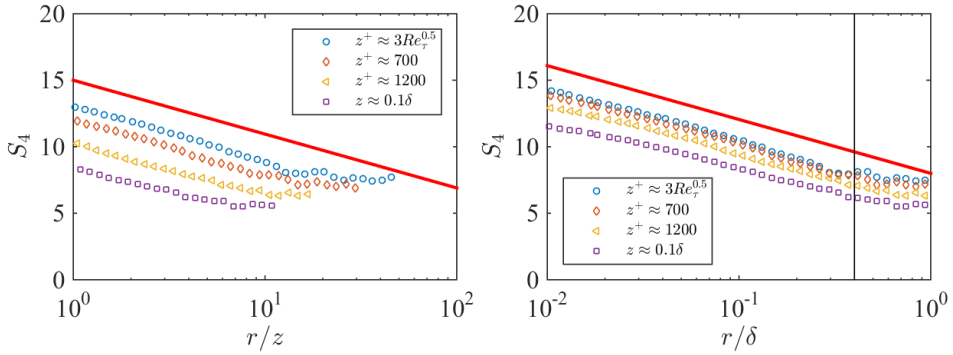

Figure 5.5: Same as figure 5.2, but for S_4.

logarithmic scaling rather closely, at least within the expected range of r. In contrast to $\langle (u_z^+(x+r) - u_z^+(x))^{2p} \rangle^{1/p}$, plotting against r/z does not collapse the data, instead, plotting against r^+ (or against r/δ) a better collapse is obtained (although evidently not a full collapse). In Eqs. 5.19-5.21, neglecting additive constants and equating $\langle u^{2p} \rangle^{1/p}$ to $\log(\delta/z)$ is unlikely to cause this lack of collapse because the additive constants can be absorbed as a single multiplying factor of the outer length scale δ. The lack of full collapse is possibly due to a lack of exact cancellation of $L_{p,n}$ $n > 0$. Exact cancellation of $L_{p,n}$, $n > 0$ in the framework of HRAP depends, for the logarithmic scalings in Eqs. 5.6-5.8, critically on $A_p = [(2p-1)!!]^{1/p} A_1$ (see. Eqs. 5.26, 5.27), i.e. on wall eddies being non-interacting, equivalently, on a_i in Eq. 5.2 being i.i.d.. In reality, eddies clustering can lead to significant correlations among the attached eddies.[110] A_p can then differ from $[(2p-1)!!]^{1/p} A_1$, leading to the lack of complete collapse of the logarithmic scalings at different wall normal heights. Observed slopes in the logarithmic laws agrees reasonably well with the model predictions (considering the uncertainty in the measurements), which indirectly confirms Eq. 5.13 (notice $L_{p,0} = \log(\delta/r)$ is based on Eq. 5.13), although some deviations are observed, especially for high order statistics.

Next we verify the statistical convergence of the moments shown in figures 5.2 - 5.5. To achieve statistical convergence of higher order statistics (6th and 8th order statistics) one requires larger amounts of data and it is more challenging as compared the convergence in lower order statistics (2nd and 4th order). Here we examine the

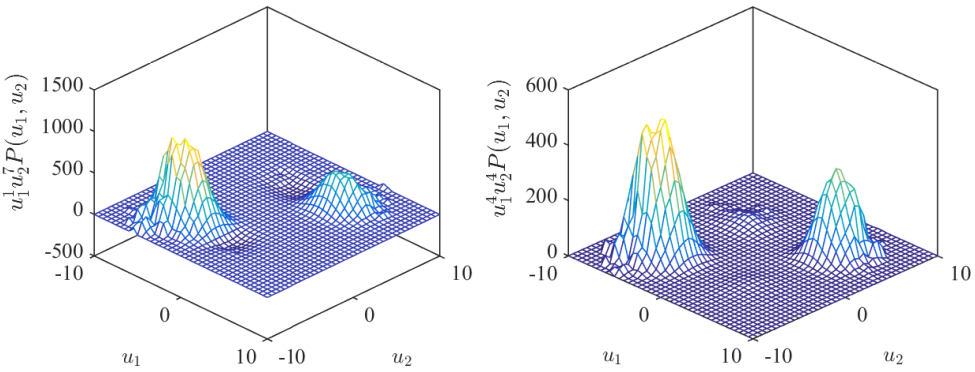

Figure 5.6: Premultiplied p.d.f for $u_z(x)u_z^7(x+r)$ and $u_z^4(x)u_z^4(x+r)$ at a vertical height $z^+ = 1400$ and a streamwise separation $r = 0.3\delta$. $u_1 = u_z(x)$ and $u_2 = u_z(x+r)$. The two-point p.d.f. $P(u_1, u_2)$ corresponds to the two points $u_1 = u_z(x)$ and $u_2 = u_z(x+r)$.

pre-multiplied joint probability density function (p.d.f) of $u_z(x)$ and $u_z(x+r)$. The two plots are relevant for the evaluation of $\langle u_z(x)u_z^7(x+r)\rangle$ and $\langle u_z^4(x)u_z^4(x+r)\rangle$. A representative wall distance $z^+ = 1400$ and a relatively large streamwise separation $r = 0.3\delta$ (which is a more challenging case compared to small streamwise separations) is considered. Figure 5.6 shows the premultiplied joint p.d.f. As can be seen from figure 5.6, the two-point moments under consideration, which is essentially the area (volume) under the surface, can be reasonably captured by the amount of data available as the probability density goes to zero at the high values.

5.4 A more rigorous derivation of the new logarithmic laws

In this section, we derive the logarithmic scalings in Eqs. 5.6-5.8 in a more rigorous manner using the formalism developed in Ref. 14. The goal here is to show that the new logarithmic laws are not dependent on the exact details of the attached eddy formulation but depend on the essential structure of the model. We only need to show that the attached eddy formulation used in Ref. 14 gives the same prediction for the two-point velocity fluctuation correlations raised to arbitrary powers (i.e. $\langle u_z^n(x) u_z^{2p-n}(x+r)\rangle$).

Following Ref. 14, the streamwise velocity fluctuation at a point is expressed as

$$u(\mathbf{x}) = \sum_k Q_x\left(\frac{\mathbf{x}-\mathbf{x}_{e_k}}{h_k}\right), \tag{5.28}$$

where $Q_x((\mathbf{x}-\mathbf{x}_{e_k})/h_k)$ is the streamwise velocity fluctuation at a point $\mathbf{x}$ induced by a typical attached eddy of size h_k located at $\mathbf{x}_{e_k}$ and the sum is over all eddies in the domain. The inclination angle of a typical eddy is θ and it follows that the extent of a typical eddy at height z_r covers a streamwise distance $r = z_r/\tan\theta$.

Decomposing the right hand side of Eq. 5.28 into contributions from eddies of

size smaller than z_r and eddies of size larger than z_r leads to:

$$\begin{aligned} u(\mathbf{x}) = & \sum_{h_k<z_r} Q_x\left(\frac{\mathbf{x}-\mathbf{x}_{e_k}}{h_k}\right) \\ & + \sum_{h_k>z_r} Q_x\left(\frac{\mathbf{x}-\mathbf{x}_{e_k}}{h_k}\right) \end{aligned} \tag{5.29}$$

Performing the same decomposition to the velocity fluctuation at $\mathbf{x}+\mathbf{i}r$, where $\mathbf{i}$ is the unit vector in the streamwise direction leads to:

$$\begin{aligned} u(\mathbf{x}+\mathbf{i}r) = & \sum_{h_k<z_r} Q_x\left(\frac{\mathbf{x}+\mathbf{i}r-\mathbf{x}_{e_k}}{h_k}\right) \\ & + \sum_{h_k>z_r} Q_x\left(\frac{\mathbf{x}+\mathbf{i}r-\mathbf{x}_{e_k}}{h_k}\right). \end{aligned} \tag{5.30}$$

Following the same arguments that lead to $u_z(x) \approx u_z(x+r)$, we have

$$\sum_{h_k>z_r} Q_x\left(\frac{\mathbf{x}+\mathbf{i}r-\mathbf{x}_{e_k}}{h_k}\right) \approx \sum_{h_k>z_r} Q_x\left(\frac{\mathbf{x}-\mathbf{x}_{e_k}}{h_k}\right). \tag{5.31}$$

Eq. 5.29, Eq. 5.30 and Eq. 5.31 lead to

$$\begin{aligned} & \left\langle u^n(\mathbf{x}) u^{2p-n}(\mathbf{x}+\mathbf{i}r)\right\rangle = \\ & \left\langle \left[\sum_{h_k<z_r} Q_x\left(\frac{\mathbf{x}-\mathbf{x}_{e_k}}{h_k}\right) + \sum_{h_k>z_r} Q_x\left(\frac{\mathbf{x}-\mathbf{x}_{e_k}}{h_k}\right)\right]^n \times \right. \\ & \left. \left[\sum_{h_k<z_r} Q_x\left(\frac{\mathbf{x}+\mathbf{i}r-\mathbf{x}_{e_k}}{h_k}\right) + \sum_{h_k>z_r} Q_x\left(\frac{\mathbf{x}-\mathbf{x}_{e_k}}{h_k}\right)\right]^{2p-n} \right\rangle \end{aligned} \tag{5.32}$$

Expanding the right hand side of Eq. 5.32 gives raise to terms like

$$\left\langle \left[\sum_{h_k<z_r} Q_x\left(\frac{\mathbf{x}-\mathbf{x}_{e_k}}{h_k}\right)\right]^{p_1}\right\rangle \times \left\langle \left[\sum_{h_k<z_r} Q_x\left(\frac{\mathbf{x}+\mathbf{i}r-\mathbf{x}_{e_k}}{h_k}\right)\right]^{p_2}\right\rangle \times \left\langle \left[\sum_{h_k>z_r} Q_x\left(\frac{\mathbf{x}-\mathbf{x}_{e_k}}{h_k}\right)\right]^{p_3}\right\rangle$$

We now recall that Ref. 14 (their Eqs. 18, 23) prove that

$$\begin{aligned} &\left\langle \left[\sum_{k,h_1<h_k<h_2} Q_x\left(\frac{\mathbf{x}-\mathbf{x}_{e_k}}{h_k}\right)\right]^{2p'}\right\rangle \\ &= A_{p'}^{p'} \log^{p'}\left(\frac{h_2}{\max(z,h_1)}\right), \end{aligned} \tag{5.33}$$

by considering the size of the smallest eddy being h_1 and the size of the largest eddy being h_2. Then, by using Eqs. 5.32, 5.33, we can recover the predictions for $\langle u_z^n(x) u_z^{2p-n}(x+r)\rangle$ made using the HRAP formalism (i.e. Eqs. 5.19, 5.20, 5.21) and with Eqs. 5.19, 5.20, 5.21 the new logarithmic laws in Eqs. 5.6-5.8 can be verified. This completes the proof of the new logarithmic laws (in Eq. Eqs. 5.6-5.8) using the formalism developed in Ref. 14.

5.5 Conclusions

New logarithmic laws (Eqs. 5.6-5.8) for wall bounded flows can be predicted if one follows the HRAP formalism to its logical conclusion. The HRAP model enables us

to easily make predictions about scaling behaviors in turbulence statistics (including conventional moments and moment-generating function[183]) in the logarithmic region at high Reynolds numbers. Empirical evidence supporting the newly predicted logarithmic laws are presented by analyzing the $Re_\tau = 19030$ dataset.[187] We also arrive at the logarithmic laws in Eqs. 5.6-5.8 using the formulation developed in Ref. 14 in a more rigorous manner. Those newly found logarithmic laws provide additional support to the basic hierarchical structure of wall bounded eddies hypothesized in Townsend's hypothesis and can be used for model and code validation as well as for discriminating among different simplified models of wall eddies.

We recognize also that not all flow statistics can be correctly predicted within the present HRAP framework, even when restricting attention in the logarithmic inertial region. For instance, both the attached model developed in Ref. 14 and the HRAP used in this work predict a collapse of the new logarithmic scalings using $\log(\delta/r)$ at different wall normal distances at high Reynolds number. However the experimental data does not show a full collapse using $\log(\delta/r)$ (although the collapse is appreciably better using $\log(\delta/r)$ compared to using $\log(z/r)$. The latter was previously used to collapse the structure functions $\langle (u(z,x) - u(z,x+\mathbf{i}r))^{2p} \rangle^{1/p}$, see Ref.[95]). It is possible that the discrepancies could be due to coherent motions in the logarithmic layer. That is to say, a lack of correlations among the random additive terms may be responsible for the differences between HRAP model predictions and experimental observations. Besides the lack in accounting for correlations among eddies of different

sizes in the hierarchy, HRAP as presented does not include magnitude modulation of small scales velocity fluctuations near the wall by larger-scale eddies further above the wall, a mechanism that is found to be prevalent in high Reynolds number wall bounded flows.[195,196] However, the "outer peak" which is responsible for the modulation of the near-wall motions corresponds, in the current version of HRAP, to the last step in the hierarchy. One can view the outcome of HRAP as the outer scale input to the wall modulation approach.[196]

Hence more refined eddy models and extensions of the HRAP approach including more detailed physics beyond the simple additive superposition of independent eddy-induced velocity fluctuations can be considered in the future. We believe that the more advanced statistical diagnostic tools provided here by the new generalized two point moments (S_1, S_2, S_3, S_4 etc.) can be used to test those possible extensions.

As logarithmic scalings with respect to the wall normal distance can be found in the even order moments of the spanwise velocity components, i.e. $\langle v^2 \rangle \sim \log(\delta/z)$, it could be expected that the spanwise velocity fluctuation should follow a similar additive process, and the derived scalings here may be observed also for the spanwise velocity. Moreover, because the attached eddies have a finite span in the transverse direction, those two-point logarithmic scalings are expected to hold if the two-point displacement is instead in the transverse direction. For the data sets used in this work, those ideas cannot be studied. Further investigations with additional data should examine the detailed structure of the spanwise velocity and two-point logarithmic

scalings that involves a spanwise displacements. Based also on previous work,[95] while we do expect the log dependencies to exist for v, we do not expect to see the for w (the wall-normal component).

Chapter 6

Moment-generating-functions in wall-bounded flows

6.1 Introduction

It was shown in the last chapter that new logarithmic laws for statistical moments could be derived from the HRAP approach. We now ask the question whether more statistical objects of more general character than simple moments may also be studied in turbulent boundary layers and may be amenable for predictions using HRAP.

The specific statistical tool explored here is provided by the exponential of the random variable of interest, and then considering various moments of this new random variable. More specifically, considering streamwise velocity fluctuations in a boundary layer at a height z, and point-pair distances r in the streamwise direction, we consider

the following statistical objects:

$$W(q;z) \equiv \langle \exp(q\,u^+) \rangle, \quad W(q,q';z,r) \equiv \langle \exp[q\,u^+(x) + q'\,u^+(x+r)] \rangle. \tag{6.1}$$

These are the single and two-point moment generating functions (MGF), respectively. The parameter q, a real number, serves as a "dial" to emphasize different parts of the signal such as high and low-speed regions, for positive and negative values of q, respectively. For two-point statistics, choosing different values of q and q' enables one to emphasize particular behaviors at points separated by a distance r. One natural consequence of the definition of MGFs is that single and two-point moments can be directly computed from the curvatures of the MGFs at the origin, according to

$$\begin{aligned} \langle u^{+p} \rangle &= \left. \frac{\partial^p W(q;z)}{\partial q^p} \right|_{q=0}, \\ \langle u^+(x)^p u^+(x+r)^{p'} \rangle &= \left. \frac{\partial^{p'}}{\partial q'^{p'}} \frac{\partial^p}{\partial q^p} W(q,q';z,r) \right|_{q=0,q'=0}. \end{aligned} \tag{6.2}$$

It is worth noting here that central moments are solely determined by the single-point moment generating function at $q = 0$.

It is also useful to mention that $W(q;z)$ as defined corresponds to a highly simplified and real-valued subset of the more general object described by the Hopf equation. This equation describes the full N-point joint PDF of velocity fluctuations, where N is the total number of different spatial points needed to describe the flow. Basic interest in the Hopf equation follows from the fact that it is a linear equation and therefore

self-contained requiring no closure. It describes the time evolution of the generalized moment generating function $\Psi(\boldsymbol{\theta}) = \langle \exp(i \int \boldsymbol{\theta}(\mathbf{x}) \cdot \mathbf{u}(\mathbf{x}) d^3\mathbf{x}) \rangle$, where $\mathbf{u}$ is the velocity field, $i\boldsymbol{\theta}(\mathbf{x})$ is a complex "test-field" which serves as (very high-dimensional) independent variable taking on specified values at every point in the flow. As mentioned before, the Hopf equation is a *linear* equation for $\Psi(\boldsymbol{\theta})$. However, it includes *functional derivatives* with respect to the entire test-field $\boldsymbol{\theta}(\mathbf{x})$ and solving such functional equations remains an unattainable theoretical goal. The new quantity $W(q; z)$ may be considered to be a highly simplified version, a 'subset', of $\Psi(\boldsymbol{\theta})$ in which we take a special-case test field $i\theta_j(\mathbf{x}) = q\delta(\mathbf{x} - z\hat{\mathbf{k}})\delta_{j1}$, and similarly for the two-point MGF $i\theta_j(\mathbf{x}) = q\delta(\mathbf{x} - z\hat{\mathbf{k}})\delta_{j1} + q'\delta(\mathbf{x} - r\hat{\mathbf{i}} - z\hat{\mathbf{k}})\delta_{j1}$ (where $\hat{\mathbf{k}}$ and $\hat{\mathbf{i}}$ are the unit vectors in the wall-normal and streamwise directions, respectively).

Another connection with prior approaches can be highlighted. In the study of small-scale intermittency and anomalous scaling, high-order moments of turbulent kinetic energy dissipation normalized by its mean, $\varepsilon/\langle\varepsilon\rangle$, such as $\langle(\varepsilon/\langle\varepsilon\rangle)^q\rangle$ with $q > 0$ are used to emphasize the highly intermittent peaks in dissipation, while the low-dissipation regions can be highlighted by moments of negative order $q < 0$ (see e.g.Refs. 189). The analogy is then between u^+ and the variable $\ln(\varepsilon/\langle\varepsilon\rangle)$. As will be seen in the discussion in §6.2, 6.3, an analogy between the momentum cascade and the energy cascade can be formally made, providing helpful insights for the study of wall bounded flows.

The discussion here focuses on boundary layer flows. For the variance of the

streamwise velocity fluctuations to exhibit logarithmic scaling one may hypothesize that $\langle \exp(qu^+) \rangle$ exhibits power-law scaling with respect to z near $q = 0$, since

$$W(q;z) \sim \left(\frac{z}{\delta}\right)^{-\tau(q)} \rightarrow \langle {u^+}^2 \rangle = \left.\frac{\partial^2 W(q;z)}{\partial q^2}\right|_{q=0} = B_2 - \left.\frac{d^2\tau(q)}{dq^2}\right|_{q=0} \log\left(\frac{z}{\delta}\right). \quad (6.3)$$

However, the known logarithmic behavior of $\langle {u^+}^2 \rangle$ does not imply power-law scaling of $W(q;z)$ for q values away from $q = 0$ so that this must be tested based on data.

The rest of the chapter is organized as follows: the scaling behavior of the single-point MGF is investigated in section 6.2, including empirical evidence of power-law scaling as function of height z, for q both positive and negative. Experimental measurements of flow at $Re_\tau \approx 13,000$ from the Melbourne high Reynolds number boundary layer wind tunnel (HRNBLWT) are considered for this purpose. In section 6.3, we consider two-point MGFs and in particular provide an 'attached eddy' model based prediction of a scaling transition for $W(q,-q;z,r)$. This behavior is confirmed by analysis of experimental data. Statistical convergence of the data is examined in section 6.4, and conclusions are provided in §6.5. Throughout the chapter, u^+ is the streamwise velocity fluctuation normalized by friction velocity and z is the wall-normal coordinate. The overall picture of wall bounded flows provided by the Townsend attached eddy hypothesis[15] is found useful in the discussion and is often invoked (or implied). In Ref. 15, as well as in Ref. 14, 96, the boundary layer is hypothesized to consist of attached eddies whose sizes scale with their distance from

the wall and whose population density scales inversely with distance from the wall.

6.2 Scaling of single-point MGFs

We present results of the MGFs from high Reynolds number boundary layer turbulence. Hot-wire streamwise velocity measurements at $Re_\tau = 13,000$ from the Melbourne HRNBLWT are analyzed (with $U_\infty = 20$ (m/s), u_τ =0.639 (m/s), and $\delta = 0.319$ (m), see[197] for further details of the dataset). The MGFs are computed for various q-values in a range between ± 2. Statistics are evaluated at the 50 measurement heights averaging over a time interval of approximately $T_{\text{data}} = 11200\delta/U_\infty$. The measured MGFs as function of wall distance in inner units are shown in figure 6.1 (a) for representative values of q. In the range $610 < z^+$, $z < 0.2\delta$ (see Ref. 90 for detailed discussion on the range of the log layer), power law behavior is observed. Moreover, there is significant difference in the scaling exponents of $W(q; z)$ for positive and negative q values of the same magnitude. This is especially the case for high $|q|$. The respective scaling ranges differ depending on the sign of q: for $q > 0$, the power-law region extends down to heights $z^+ \approx 400$ while for $q < 0$, the power-law region is shorter, down only to wall distances of about $z^+ \approx 600$. Note that $z^+ \approx 400$ corresponds nominally to the lower limit $3Re_\tau^{0.5}$ identified in Ref. 90 as appropriate for the logarithmic scaling range of the variance. This appears appropriate for the $q > 0$ cases, but for $q < 0$, the range is more consistent with $z^+ = 600$. Since negative

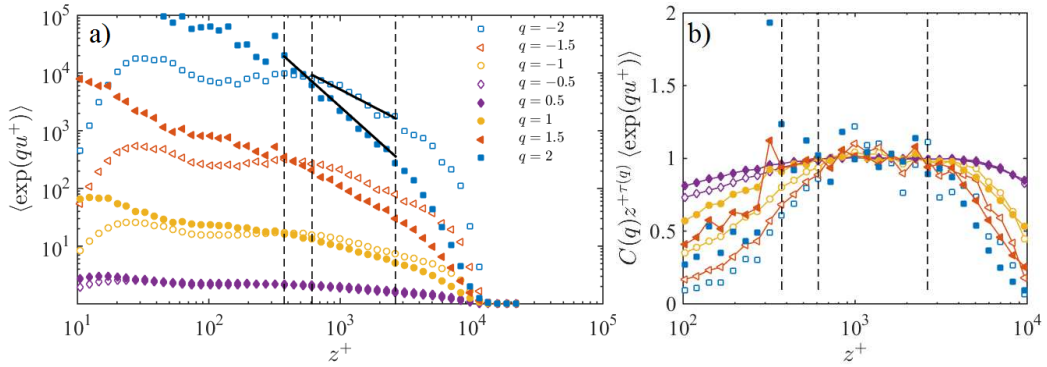

Figure 6.1: a) Log-log plot of $\langle \exp(qu^+) \rangle$ against z^+ for $q = \pm 0.5, \pm 1, \pm 1.5 \pm 2$. Solid symbols are used for positive q's and hollow symbols are used for negative q values. The extent of the scaling regions, $375 < z^+$, $z < 0.2\delta$ for $q > 0$ and $610 < z^+$, $z < 0.2\delta$ for $q < 0$ are indicated by vertical dashed lines. (b) Pre-multiplied single-point MGF, $C(q)z^{+\tau(q)} \cdot \langle \exp(qu^+) \rangle$. The pre-factor $C(q)$ is determined from the power-law fitting (such that in the fitted range $C(q)z^{+-\tau(q)} \approx \langle \exp(qu^+) \rangle$). $\tau(q)$ used in the pre-multiplied quantites are $\tau = 0.17, 0.54, 0.91, 1.18$ for $q = -0.5, -1, -1.5, -2$ and $\tau = 0.17, 0.63, 1.27, 2.04$ for $q = 0.5, 1, 1.5, 2$.

q emphasizes the scaling behavior of the low-speed regions of the flow, it is concluded that these are affected by wall and viscous effects up to larger distances from the wall, consistent with those regions being associated more prevalently with positive vertical velocities.

Eq. 6.3 suggests power-scaling of $W(q; z)$ near $q = 0$ and for z values where the $\langle u^{+2} \rangle$ has logarithmic scaling. Such scaling can also be obtained by considering the velocity fluctuations as resulting from a sum of discrete random contributions from attached eddies:

$$u^+ = \sum_{i=1}^{N_z} a_i. \tag{6.4}$$

Here a_i's are random additives, assumed to be identically and independently distributed, each associated with an attached eddy of size $\sim \delta/2^i$ if for simplicity we

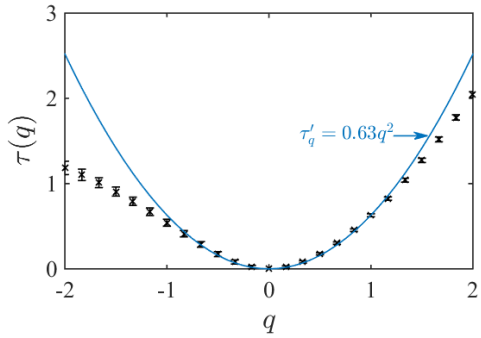

Figure 6.2: Measured scaling exponents $\tau(q)$ (symbols), obtained from fitting $W(q;z)$ as function of z, in the range $610 < z^+$ and $z < 0.2\delta$. Error bars show the uncertainty in the obtained exponents. A quadratic fit around the origin yields $\tau(q) = 0.63q^2$ (blue solid line).

choose a scale ratio of 2. The number of additives N_z is taken to be proportional to the number of attached eddies at any given height z. If the eddy population density is inversely proportional to z according to the attached eddy hypothesis,[15] then N_z is proportional to:

$$N_z \sim \int \frac{1}{z} dz \sim \log\left(\frac{\delta}{z}\right). \tag{6.5}$$

As a result, the exponential moment can be evaluated

$$\left\langle \exp(qu^+) \right\rangle = \left\langle \exp(qa) \right\rangle^{N_z} = \left(\frac{z}{\delta}\right)^{-C_e \log\langle \exp(qa)\rangle}, \tag{6.6}$$

where C_e is some constant. Eq. 6.6 provides a prediction for the scaling exponents $\tau(q)$:

$$\tau(q) = C_e \log\left\langle \exp(qa) \right\rangle. \tag{6.7}$$

$\tau(q)$ is determined by the p.d.f. of the random additives a's, representing the velocity

field induced by a typical attached eddy. If these eddies are assumed to be purely inertial without dependence on viscosity, then $\tau(q)$ would be expected to be Reynolds number independent. Furthermore, if a is assumed to be a Gaussian variable, then Eq. 6.7 leads to the quadratic law

$$\tau(q) = Cq^2, \tag{6.8}$$

where C is another constant. In order to compare this behavior with measurements, we fit $\tau(q)$ from data (as shown in Fig. 6.1, a) in the relatively narrow and conservative range $600 < z^+$, $z < 0.2\delta$ the common range where both positive and negative q display good scaling. The quality of the power-law fitting is further examined in Fig. 6.1, b, where the pre-multiplied single-point MGFs are plotted against the wall normal distance. The fitted $\tau(q)$ curve is plotted against q in Fig. 6.2, including error bars determined by the ratio of the root-mean-square of the variation in $\log(\exp(qu^+)) - \tau(q)\log(z^+)$ in the fitted range of z^+ to the corresponding expected increase (or decrease) in $\langle \exp(qu^+) \rangle$ indicated by the fitted paramter. Due to statistical convergence issues, evaluation of $\tau(q)$ is limited to $|q| < 2$. A quadratic fit around $q = 0$ is shown with the solid line in figure 6.2. The fit yields $\tau(q) = 0.63q^2$. According to Eq. 6.3,

$$A_1 = \left. \frac{d^2\tau(q)}{dq^2} \right|_{q=0} = 2C = 1.26. \tag{6.9}$$

This is consistent with the prior measurements of the "Perry-Townsend" constant

$A_1 \approx 1.25$.[90,93,94] Studying possible Reynolds number effects falls beyond the scope of this chapter.

We can also compute $\langle u^{+2p}\rangle^{1/p}$ using the single-point MGF $\langle \exp(qu^+)\rangle$. Eqs. 6.2, 6.3, and 6.8 lead to $\langle u^{+2}\rangle = 1 \times 2C\log(\delta/z)$, $\langle u^{+4}\rangle^{1/2} = 3^{1/2} \times 2C\log(\delta/z)$, $\langle u^{+6}\rangle^{1/3} = 15^{1/3} \times 2C\log(\delta/z)$, and $\langle u^{+8}\rangle^{1/4} = 105^{1/4} \times 2C\log(\delta/z)$, recovering the scaling of generalized logarithmic laws.[94] Because of the Gaussianity that underlies Eq. 6.8, it is not surprising that $A_p/A_1 = [(2p-1)!!]^{1/p}$ (see Refs. 14, 94). But as can be discerned in Fig. 6.2 the quadratic fit becomes highly inaccurate away from $q = 0$, consistent with known deviations from Gaussian behavior of velocity fluctuations in wall boundary layer turbulence. Also the data are asymmetric, showing significantly stronger deviations from the Gaussian prediction for $q < 0$ than for $q > 0$. These results constitute new information about the flow and may prove important in comparing with models.

6.3 Two-point MGFs and scaling transition

In this section, the scaling behavior of the two-point moment generating function $W(q, q'; z, r) = \langle \exp[qu^+(x, z)+q'u^+(x+r, z)]\rangle$ in the logarithmic region (for moments as function of z) and in the relevant range of the two-point separation distance r is investigated. Note that here we indicate z explicitly to avoid confusion. Before

analyzing the data, predictions of scaling behavior exploiting the assumed hierarchical tree-structure of attached eddies are presented. Figure 6.3 shows a sketch of attached eddies. We consider 2 points at a wall distance z that are separated by a distance r in the flow (x) direction. Velocity fluctuations at the two points are given by the random additives a_i corresponding to all the eddies "above" a given point. As a result, two points at a distance r will share a subset of common additives from the larger eddies that contain both points, while each contains independent additives from eddies that are not common to both points. This consideration then enables one to factor the exponentials to separate common and separate contributions. The approach follows that of Refs. 188, 189 who considered such factorizations of two-point moments of dissipation rate, and a crucial concept is that of the size of the smallest common eddy, r_c. To find the scaling for $W(q, q'; z, r)$, the quantity $\exp(qu^+(x, z) + q'u^+(x + r, z))$ is conditioned based on the size of the smallest common eddy r_c of the points under consideration, and the final result is given by the sum over all possible common eddy sizes r_c:

$$W(q, q'; z, r) = \sum_{r_c=r}^{\delta/\tan\theta} \left\langle \exp[qu^+(x, z)] \exp[q'u^+(x + r, z)] \;\middle|\; r_c \right\rangle P_{r_c}, \tag{6.10}$$

where P_{r_c} is the probability that the smallest common eddy shared by the two points (x, z), $(x + r, z)$ is of size r_c. Eddies of size larger than r_c affect both points equally.

Also, we make the association that eddy-size of r_c in the horizontal direction has a

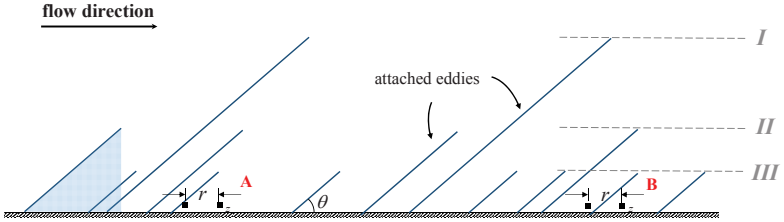

Figure 6.3: Conceptual sketch of a boundary layer with 3 hierarchies of attached eddies (I, II, III). $\theta \approx 17°$ is the inclination angle of a typical attached eddy; consistent with a packet structure.[14] Both points in set A as well as in set B are at a height z above the wall and are separated by a distance r in the flow direction. An attached eddy affects the region beneath it, as is indicated by the shaded region.[15]

height $z_c = r_c \tan\theta$. Factorizing the exponential at both points to contributions from eddies of size larger than r_c (heights above z_c) and eddies smaller than r_c (heights less than z_c) leads to

$$\left\langle e^{qu^+(x,z)+q'u^+(x+r,z)} \;\middle|\; r_c \right\rangle = \left\langle e^{(q+q')u^+(x,z_c)} \, \frac{e^{qu^+(x,z)}}{e^{qu^+(x,z_c)}} \, \frac{e^{q'u^+(x+r,z)}}{e^{q'u^+(x+r,z_c)}} \;\middle|\; r_c \right\rangle. \quad (6.11)$$

Eddies of size smaller than r_c cannot affect both points at the same time, therefore the difference $u^+(x,z) - u^+(x,z_c)$ and $u^+(x+r,z) - u^+(x+r,z_c)$ (or the ratio of the exponentials), which according to the random additive ansatz (Eq. 6.4) contain only contributions (additives) from eddies of size smaller than r_c, can be assumed to be statistically independent. Also, they are independent of the additives corresponding to the velocity difference $u^+(x,\delta) - u^+(x,z_c)$. These arguments lead to

$$\left\langle e^{qu^+(x,z)+q'u^+(x+r,z)} \;\middle|\; r_c \right\rangle = \left\langle e^{(q+q')u^+(x,z_c)} \right\rangle \left\langle \frac{e^{qu^+(x,z)}}{e^{qu^+(x,z_c)}} \right\rangle \left\langle \frac{e^{q'u^+(x+r,z)}}{e^{q'u^+(x+r,z_c)}} \right\rangle. \quad (6.12)$$

Following the same arguments that lead to Eq 6.6, we have

$$\left\langle \frac{e^{qu^+(x,z)}}{e^{qu^+(x,z_c))}} \right\rangle \sim \left(\frac{z_c}{z}\right)^{\tau(q)} \tag{6.13}$$

and similarly at $x+r$ involving $\tau(q')$. Substituting Eq. 6.13 into Eq. 6.11 leads to

$$\left\langle e^{qu^+(x,z)+q'u^+(x+r,z)} \;\middle|\; r_c \right\rangle \sim P_{r_c} \left(\frac{z}{z_c}\right)^{-\tau(q)-\tau(q')} \left(\frac{z_c}{\delta}\right)^{-\tau(q+q')} \tag{6.14}$$

To estimate P_{r_c} for some height z, we follow Refs. 188, 189 and argue that P_{r_c} is proportional to the area of a strip of thickness r along the perimeter of an eddy of size r_c (area $\sim r\, r_c$), divided by the total area of such an eddy in the plane ($\sim r_c^2$). For point pairs falling within such a strip, the two points typically pertain to different eddies of size r_c. Hence $P_{r_c} \sim r/r_c$, and after replacing $z_c = r_c \tan\theta$, we can write

$$\left\langle e^{qu^+(x,z)+q'u'(x+r,z)} \right\rangle \sim \sum_{r_c=r}^{\delta/\tan\theta} \left(\frac{r_c}{\delta}\right)^{\tau(q)+\tau(q')-\tau(q+q')-1} \left(\frac{r}{\delta}\right) \left(\frac{z}{\delta}\right)^{-\tau(q)-\tau(q')}, \tag{6.15}$$

where a prefactor depending on $\tan\theta$ has been omitted for simplicity. At high Reynolds numbers, we can consider the situation $\delta/\tan\theta >> r$. Thinking in terms of a discrete hierarchy of eddies, the sum in Eq.6.15 becomes a geometric one. It is dominated either by the value at small scales $r_c \sim r$ or at large scales $r_c \sim \delta/\tan\theta$, depending on the sign of the exponent. Therefore, two asymptotic regimes can then

be identified:

$$\begin{aligned} W(q,q';z,r) &\sim (z/\delta)^{-\tau(q)-\tau(q')}\,(r/\delta)^{\tau(q)+\tau(q')-\tau(q+q')}, && \text{if } \tau(q)+\tau(q')-\tau(q+q')-1<0, \\ W(q,q';z,r) &\sim (z/\delta)^{-\tau(q)-\tau(q')}\,(r/\delta)^{1}, && \text{if } \tau(q)+\tau(q')-\tau(q+q')-1>0, \end{aligned} \tag{6.16}$$

indicating a "scaling transition" with respect to r when q and q' are such that $\tau(q)+\tau(q')-\tau(q+q')-1=0$.

To examine whether such a scaling transition exists in the measurements, we consider the specific case $q'=-q$, for which the predicted scaling behavior with respect to r is:

$$W(q,-q;z,r)\sim\left(\frac{r}{\delta}\right)^{\Phi(q)}, \quad \text{where} \quad \Phi(q)=\min[\tau(q)+\tau(-q),1], \tag{6.17}$$

since $\tau(0)=0$ by construction. It is worth noting here that such a scaling transition is indicative of the 'tree-like' or hierarchical and space-filling structure on which the attached eddies are organized and since the transition occurs away from $q=0$, it cannot be diagnosed using traditional two-point moments.

Based on the dataset described before, $W(q,-q;z,r)$ is evaluated and plotted against r^+ in figure 6.4 (a) for a specific wall normal position in the log region (here taken at $z^+=600$) and for various values of q. We evaluate two-point correlations using direct summation (and checked that FFT gives essentially the same results). The relevant range in r for the scaling predicted in Eq. 6.16 is between $r=z/\tan(\theta)$ (any r below this value corresponds to eddies of size smaller than z and is thus

not relevant) and $0.15\delta/\tan\theta$ (this is more conservative compared to $0.2\delta/\tan\theta$). For the specific height considered in figure 6.4, this range corresponds to $2000 < r^+ < 6500$ and is indicated by the solid vertical lines. As can be seen, $W(q,-q;z,r)$ does exhibit power-law scaling in the relevant range of r. The quality of the power-law fitting is further exmined in figure 6.4, b, where the premultiplied two-point MGFs are plotted against the two-point distance r^+. Moreover, as is already clear in figure 6.4 (a), the scaling exponent gradually increases as q increases but then the slope ceases to increase further with increasing q. We fit for $\Phi(q)$ in the range of r indicated by the two vertical solid lines in figure 6.4. Figure 6.5 compares the measured $\Phi(q)$ and the prediction made in Eq. 6.17. Measured values for $\tau(q)$ and $\tau(-q)$ are used in Eq. 6.17. As can be seen from figure 6.5 a scaling transition exists and it appears to be correctly predicted by the scaling analysis leading to Eq. 6.16. The error-bars for the fitted slopes are estimated as the ratio of the root-mean-square of the variations in $\log(W(q,-q;z,r)) - \Phi(q)\log(r)$ in the fitting range of r to the expected change indicated by the fitted parameter, i.e error $= rms[\log(W(q,-q;z,r)) - \Phi(q)\log(r)]/(\Phi(q)\log(\Delta r))$, where Δr is range of r used in fitting.

Furthermore, the scaling of $W(q,q';z,r)$ can be used to compute general moments such as $\langle u^m(x,z)u^n(x+r,z)\rangle$, and $\left\langle (u(x,z)-u(x+r,z))^{2n}\right\rangle$ (the latter are simply combinations of $\langle u_z^m(x)u_z^n(x+r)\rangle$). As an example, we compute $\langle u^+(x)u^+(x+r)\rangle$ using

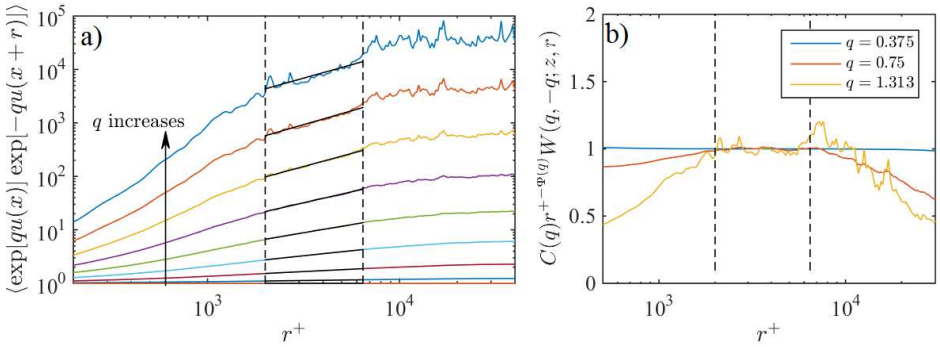

Figure 6.4: Log-log plot of $W(q,-q;z,r)$ against r at $z^+ = 600$, for 9 values of q ranging from 0 to 1.5 (shown values are q =0, 0.188, 0.375, 0.563, 0.75, 0.938, 1.125, 1.313 and 1.5). The range of r chosen to determine the power law scaling exponent (relevant for the log region) is $z/\tan\theta$, to $0.15\delta/\tan\theta$. At $z^+ = 600$, this range corresponds to (approximately) $2000 < r^+ < 6500$. This range is indicated by two thin solid vertical lines. The fits are indicated by dashed lines. (b) Pre-multiplied two-point MGFs $C(q)r^{+-\Phi(q)} \cdot W(q,-q;z,r)$ for representative q values. The pre-factor $C(q)$ is determined from the power-law fitting. $\Phi(q)$ used in the pre-multiplied quantities are 0.18, 0.61, 1.04 for q being 0.375, 0.75, 1.313.

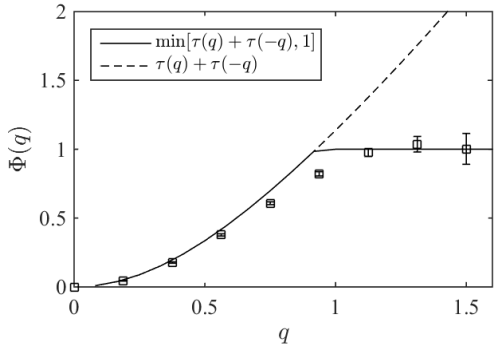

Figure 6.5: A comparison of the experimental measurements and model predictions of $\Phi(q)$ (symbols and solid line) against q. $\Phi(q)$ is the exponent on r in the predicted scaling behavior of $W(q,-q;z,r)$.

Eqs. 6.2, 6.16:

$$\left\langle u^+(x)u^+(x+r)\right\rangle = \frac{\partial}{\partial q}\frac{\partial}{\partial q'}\left\langle e^{qu^+(x)+q'u^+(x+r)}\right\rangle\Big|_{q=q'=0} = 2C\log(r/\delta) = A_1\log(r/\delta). \tag{6.18}$$

This logarithmic scaling is not unexpected since it is consistent with the -1 power law in the energy spectrum. With $\langle u^+(x)u^+(x+r)\rangle$ known, we can compute the structure function as

$$\left\langle (u^+(x)-u^+(x+r))^2\right\rangle = 2\langle {u^+}^2\rangle - 2\left\langle u^+(x)u^+(x+r)\right\rangle = 2A_1\log\left(\frac{r}{z}\right). \tag{6.19}$$

This recovers the observation made in Ref.[95] Higher order structure function can be calculated and logarithmic scalings can be recovered within in this framework (not shown here for succinctness).

6.4 Data convergence

Statistical convergence of the statistical moments measured in this work can be verified by examining the pre-multiplied probability density function (pdf). In particular, we examine $e^{\pm u^+}P(u^+)$ and $e^{\pm 2u^+}P(u^+)$, where $P(u^+)$ is the single-point pdf of the velocity at a representative wall normal height $z^+ = 610$ (which is above $3Re^{0.5}$ and is still deep into the log region). For the two-point MGF considered in section 6.3, we evaluate the two-point joint pdf $P(u_1, u_2)$ where u_1 and u_2 are velocities at

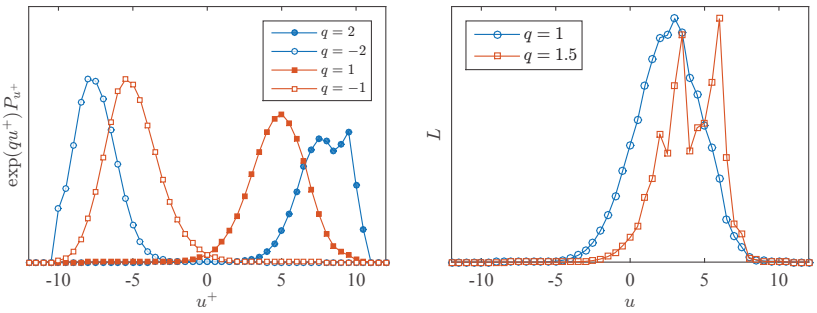

Figure 6.6: Pre-mulitplied p.d.f $exp(u^+)P(u^+)$ (left) and L (right).

two points x and $x + r$, and examine the quantity $L(u_1)$ defined as

$$L(u_1) = \exp(qu_1) \int_{u_2} \exp(-qu_2) P(u_1, u_2) du_2. \tag{6.20}$$

Since $W(q, -q; z, r) = \int L(u_1) du_1$, examination of the tails of $L(u_1)$ provides information about statistical convergence in measurements of $W(q, -q; z, r)$. We examine $L(u_1)$ at the same wall normal height $z^+ = 610$ and a representative $r^+ = 2500$ (which is within the relevant range $z/\tan\theta < r < 0.15\delta/\tan\theta$).

As can be seen in figure 6.6, the quantities of interest, i.e. $\langle e^{qu^+} \rangle$ and $\langle e^{q(u^+(x) - u^+(x+r))} \rangle$, which are equal to the area under these curves, are well captured by the data available, at least for those q values considered in section 6.2 and 6.3. Additionally, these figures illustrate the properties of MGFs that by raising $\exp(u^+)$ to positive or negative powers, regions of high or low velocity are highlighted respectively (as is seen in figure 6.6, left) and show distinctly asymmetric behavior.

6.5 Conclusions

Introducing a new framework for the study of turbulence statistics in the logarithmic region in boundary layers, basic properties of the single-point and two-point moment generating function have been investigated. Power law behaviors are observed in relevant ranges of z, and r (the latter for two-point moment generating functions) during analysis of experimental measurements. By taking negative or positive values of the parameter q, the single-point moment generating function $W(q; z)$ can be used to investigate separately the properties of low velocity regions and high velocity regions. Such distinctions are not easily accessible when using traditional moments. A scaling transition in the two-point MGF, $W(q, -q; z, r)$, is predicted based on a simplified model inspired by the attached eddy hypothesis. Such a transition is indeed observed in the measurements and provides quantifiable evidence that the attached eddies through the log region are organized in a 'tree-like' or hierarchical and space-filling manner. Such an organization was always assumed in previous attached eddy modeling efforts.[14] Deviations from Gaussian statistics are visible in the scaling behavior of the MGFs for q away from $q = 0$. Various turbulence statistics can be derived from the MGF and known logarithmic scaling laws in single-point even-order moments and structure functions can be recovered.

Chapter 7

Concluding remarks

In this thesis, we have presented work on turbulent boundary layers. In order to enable a large number of LES applications that can be run economically , we have developed a new wall model that provides beneficial Reynolds number scaling and is based on first-principles. To simulate spatially developing turbulent boundary layers over rough walls, including resolved roughness elements, we have developed an integral wall model and a rescaling-recycling inflow generation technique. LES results of rough wall boundary layers are presented for surface roughness ranging from cubes to 2D transverse bars and to arrays with Gaussian height distribution. Analyzing the measured rough wall aerodynamic properties z_o, d, an analytical rough wall model is proposed based on a quantatitive description of flow sheltering. The roughness elements considered in this work, so far, are restricted to low-rise rectangular prisms. Extensions of the analytical model to account for high-rise rectangular prisms, a

type of roughness element that is quite relevant to urban boundary layers, have been treated in Ref. 175 and is not discussed here. For general roughness, the sheltering is not restricted to roughness elements of the same scale but among all scales. Modelling flow sheltering of multi-scale roughness remains a challenge and is of interest for futher investigation.

In Chaps 5, 6, a hierarchical random additive model is developed and tested against wind tunnel measurements from the Melbourne HRNBLWT. In the present formulation, HRAP provides a description to the log region. Validity of the random additive formalism (without assuming the random additives being i.i.d.) to the near wall viscosity-affected region and to the bulk region has not been assessed and is of interest for further investigation (some initial efforts in this direction are presented in Ref. 198). It must be pointed out that the HRAP neglects any correlations among wall attached eddies that belong to different hierarchies and the that HRAP model is Gaussian in nature. While it is not conclusively known whether the boundary layer becomes Gaussian or not in the infinite Reynolds number limit, based on available data and known evidence of non-Gaussian behavior, e.g. the presence of coherent strucures, it is of interest to include non-Gaussian behavior in the HRAP model in future work. Besides, the work presented in this thesis has focused on the streamwise velocity fluctuations. Based on geometric arguments about wall-attached eddies , one may argue that the spanwise component is expected to have the same structure as the streamwise component. It is therefore of interest to examine whether the scalings

observed here for the streamwise velocity fluctuations can still be observed for the spanwise component.

Chapter 8

Appendix

8.1 Appendixes for the integral wall model

8.1.1 Mixing length and roughness model

In this work we assume mixing length modeling in two contexts: First, it is used directly in the wall model during LES. Second, it is used in the context of numerically solving the RANS boundary layer equations using a grid to provide direct comparisons to the assumed profiles in the wall model.

In the iWMLES model, the mixing length enters when evaluating the stress at $y = \Delta_y$ (Eq.2.9) and at the wall $y = 0$ for the case of roughness modeling (Eq.2.10). For smooth walls ($k = 0$), the mixing length that is consistent with a linear profile in

the near-wall sublayer and with the logarithmic scaling above is given by

$$\ell_m = \begin{cases} 0 & y \leq \delta_i \\ \kappa y & y > \delta_i. \end{cases} \tag{8.1}$$

For the case of rough surfaces in the model we use $\delta_i = k$ and

$$\ell_m = \begin{cases} \alpha k & y \leq \delta_i \\ \kappa(y - d') & y > \delta_i, \end{cases} \tag{8.2}$$

where $d' = \alpha/\kappa$.

Now, for testing the approach (see Appendix 8.1.2) by comparing the assumed velocity profiles to actual numerical integrations of the boundary layer equations, we prefer to specify more realistic, smoother functional forms for $\ell_m(y)$. For smooth surfaces, a classical inertial scaling combined with Van-Driest damping function, $h_D(y^+) = 1 - \exp(-y^+/Y^+)$ for the viscous sublayer transition can be used, where $y^+ = yu_\nu/\nu$ and u_ν is the viscous friction velocity. We use the usual value $Y^+ = 25$.

For the case of rough surfaces, the mixing length ℓ_m is taken to be constant proportional to k within a layer of height on the order of k.[199] Above this layer, we aim to recover the classical inertial scaling $\ell_m = \kappa(y - d)$, where κ is the von Karman constant and d some displacement height. Then, the mixing length can be expressed

conveniently as

$$\ell_m = \begin{cases} \alpha k & y \le \delta_i \\ \kappa\,(y-d)\,h_D(y^+) & y > \delta_i, \end{cases} \quad , \tag{8.3}$$

where $\delta_i = k$, $d = k(1-q)$, and $q = \alpha/\left(\kappa h_D(k^+)\right)$ to ensure continuity of ℓ_m at $y = k$. Based on empirical information,[199] $\alpha = 0.2$ is chosen in this work. By using this mixing length model, we found that the velocity profile typically contains a linear region and a log region (see appendix B), and we have used assumed the velocity profile accordingly.

The filtered form drag force terms used in Eq. 2.3 are expressed according to:

$$\langle f_x \rangle = -C_d a_{\mathrm{Lx}}\ |\langle U \rangle|\,\langle u \rangle, \qquad \langle f_z \rangle = -C_d a_{\mathrm{Lz}}\ |\langle U \rangle|\,\langle w \rangle, \tag{8.4}$$

where C_d is the drag coefficient. We note that C_d is both flow- and surface-dependent and may require calibration from case to case. a_{Lx}, a_{Lz} is the roughness area density, defined as

$$a_{\mathrm{Lx}}(y) = \frac{\mathrm{d}a_{\mathrm{fx}}}{\mathrm{d}y}\frac{1}{\Delta_x \Delta_z}, \qquad a_{\mathrm{Lz}}(y) = \frac{\mathrm{d}a_{\mathrm{fz}}}{\mathrm{d}y}\frac{1}{\Delta_x \Delta_z}, \tag{8.5}$$

where $\mathrm{d}a_{\mathrm{fx}}(y), \mathrm{d}a_{\mathrm{fz}}(y)$ are the frontal areas between heights y and $y + \mathrm{d}y$ in the direction of x and z, respectively.

8.1.2 Numerical integration of BL equations and comparisons with assumed profiles

In this section, we solve the boundary layer equation Eq.2.3 numerically to explore typical shapes to guide the selection of appropriately general test functions to represent the vertical structure of $\langle u \rangle$ (and $\langle w \rangle$).

We point out that an ansatz suitable for $\langle U \rangle$ applies equally to $\langle u \rangle$ and $\langle w \rangle$ because the latter are just projections of $\langle U \rangle$. Therefore in this sub-section, we consider 2D flow with $\langle u \rangle$ aligned with $\langle U \rangle$. Any term that contains w is dropped and no subscripts are used. We return to the boundary layer streamwise-direction momentum equation without the vertical integration and consider solutions of this equation under a variety of conditions in order to guide the formulation of suitably general test functions later on.

The 2D boundary layer equation reads:

$$\frac{\partial \langle u \rangle}{\partial t} + \frac{\partial \langle u \rangle \langle u \rangle}{\partial x} + \frac{\partial \langle u \rangle \langle v \rangle}{\partial y} = -\frac{1}{\rho}\frac{d\langle p \rangle}{dx} + \frac{\partial}{\partial y}\left[(\nu + \nu_T)\frac{\partial \langle u \rangle}{\partial y}\right] - C_d a_L \langle u \rangle \langle u \rangle. \quad (8.6)$$

In order to explore the basic structure of possible solutions, we assume that the unsteady, convective and pressure gradient terms can be conveniently grouped into a

single parameter N, whose dependence upon y is neglected.[118] Specifically, we have:

$$\frac{\partial}{\partial y}\left[(\nu+\nu_T)\,\frac{\partial\langle u\rangle}{\partial y}\right]-C_d a_L\langle u\rangle^2=N \tag{8.7}$$

as the equation to be solved, where

$$N=\frac{\partial\,\langle u\rangle}{\partial t}+\frac{\partial\,\langle u\rangle\,\langle u\rangle}{\partial x}+\frac{\partial\,\langle u\rangle\,\langle v\rangle}{\partial y}+\frac{1}{\rho}\frac{d\,\langle p\rangle}{dx} \tag{8.8}$$

represents the effect of convective term, unsteady term and pressure gradient. N is treated as a given parameter coming from the outer part of the flow (LES).

Boundary conditions for the solution $\langle u\rangle$ from eqn.(8.7) are specified as no-slip at the bottom boundary and merging with some known velocity U_{LES} at the top:

$$\langle u\rangle|_{y=0}=0, \tag{8.9}$$

and

$$\langle u\rangle|_{y=\Delta_y}=U_{LES}. \tag{8.10}$$

Now we can solve Eq.(8.7) numerically for various N, C_d, $a_L(y)$, and k values. For numerical integration, it is convenient to non-dimensionalize the problem as follows:

$$\hat{u}=\frac{\langle u\rangle}{U_{LES}},\quad \hat{y}=\frac{y}{\Delta_y},\quad \hat{\ell}_m=\frac{\ell_m}{\Delta_y},\quad Re_y=\frac{U_{LES}\;\Delta_y}{\nu},\quad \hat{N}=N\;\frac{\Delta_y}{U_{LES}^2}\;\;\&\;\;\hat{a}_L=a_L\Delta_y. \tag{8.11}$$

Then the equation to be integrated numerically reads:

$$\frac{\partial}{\partial \hat{y}}\left[\left(\hat{\ell}_m^{\,2}\left|\frac{\partial \hat{u}}{\partial \hat{y}}\right| + \frac{1}{Re_y}\right)\frac{\partial \hat{u}}{\partial \hat{y}}\right] - \; C_d\; \hat{a}_L\; \hat{u}^2 = \hat{N}\;, \tag{8.12}$$

where Re_y and $\hat{N}$ are prescribed parameters. The solution is subject to $\hat{u}(0) = 0$, $\hat{u}(1) = 1$. To solve Eq.8.12, we use Matlab with its built-in differential equation solver function bvp4c. Notice that u_τ in Van-Driest damping function must be calculated from the profile and is not known a priori. Hence the solution needs to be obtained in a prediction-correction manner.

Typical values of interest for some parameters are taken to be $C_d \sim 0.1$ and $\hat{a}_L \sim 1$. We first consider a roughness height $\hat{k} \sim O(0.1)$. Wide ranges of Re_y can be considered, depending on the problem. The range for $\hat{N}$ is set to be between $[-0.01, 0.01]$. This range is estimated by recalling that pressure drop per unit length in channel flow is proportional to u_τ^2, and typically $\hat{u}_\tau$ is $O(0.1)$ times the outer velocity scale. This corresponds to a dimensionless pressure drop of $O(0.01)$. Similar values can be expected for the unsteady and advective terms.

We first solve Eq.8.12 with those typical values ($C_d = 0.1$, $\hat{a}_L = 1$, for $y < k$, $\hat{k} = 0.1$, $\hat{N} = 0$, and $Re_y = 10^4$ (Fig.8.1). It is observed that in this case a nearly linear profile for $y < k$ is followed by the classic log-region for $y > k$ (as expected given the mixing length prescription).

We then examine how this profile is affected by various choices of C_d, $\hat{a}_L$, $\hat{k}$, and

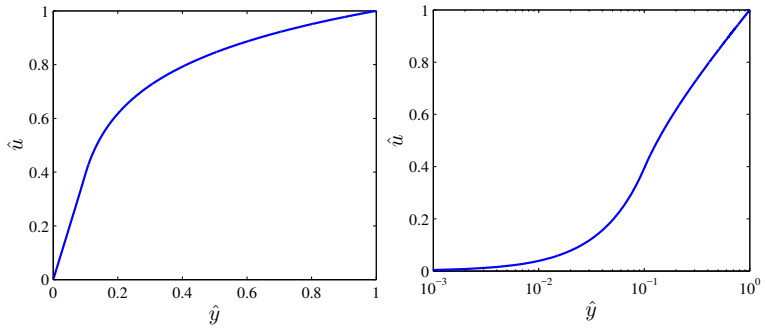

Figure 8.1: Velocity profile obtained from integrating Eq. (8.12) using $Re_y = 10^4$, $\hat{N} = 0$, $C_d = 0.1$, $\hat{a}_L = 1$, for $y < k$ and $\hat{k} = 0.1$. The left figure is in linear axes while the right figure shows same results in linear-log.

.

Re_y. First we look at the effect of different types of roughness. Fig.8.2 shows the effect of changing the detailed functional form of $\hat{a}_L$ (the distribution of roughness area). Three functional forms for $\hat{a}_L(y)$ are tested:

$$\begin{aligned} \hat{a}_{L_1}(y) &= \hat{a}_{Lm} \times 1 & y < k \\ \hat{a}_{L_2}(y) &= \hat{a}_{Lm} \times \sin\left(\pi \tfrac{y}{k}\right) & y < k \\ \hat{a}_{L_3}(y) &= \hat{a}_{Lm} \times \left(1 - \tfrac{y}{k}\right) & y < k \end{aligned} \tag{8.13}$$

where $\hat{a}_{Lm}$ is the maximum value of $\hat{a}_L(y)$. $\hat{a}_L$ is set to be 0 beyond $y = k$. It is clear that the detailed function form does not affect the general shape of the profile significantly, and that in each case we have a nearly linear profile near the wall followed by a logarithmic profile.

Figure 8.3 shows the effect of varying the roughness height $\hat{k}$, confirming a linear trend for $y < k$. Next, figure 8.4 shows the effect of varying the maximum value of $\hat{a}_L(y)$. The effect of C_d is of course similar. Figure 8.5 shows the effect of changing

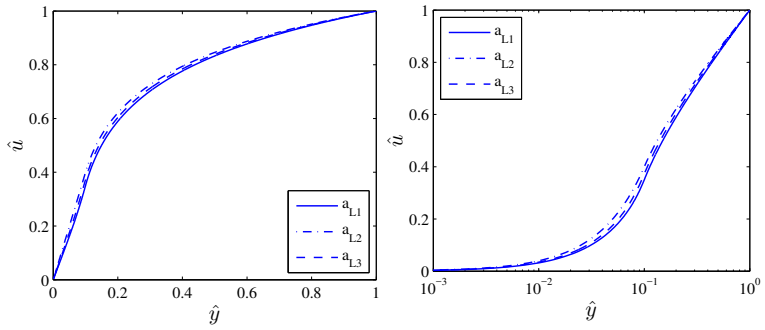

Figure 8.2: Velocity profile for different forms of $\hat{a}_L(y)$. $\hat{a}_{Lm}$ is set to be 10. All other parameters as the same as in Fig. 8.1.

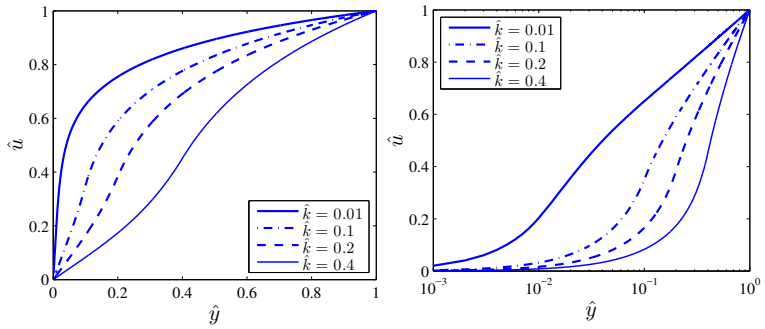

Figure 8.3: Velocity profile for different $\hat{k} = k/\Delta_y$. All other parameters are the same as the reference case shown in Fig. 8.1.

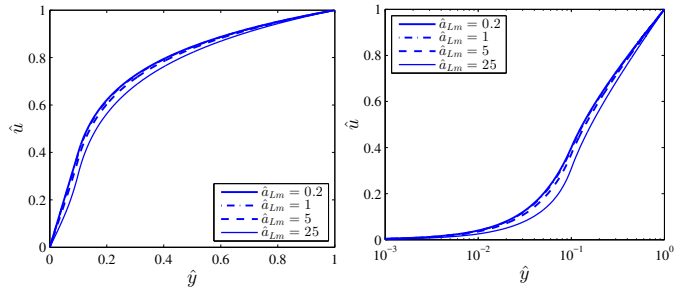

Figure 8.4: Velocity profile for different $\hat{a}_{Lm} = a_{Lm}\Delta_y$. All other parameters are the same as the reference case shown in Fig. 8.1.

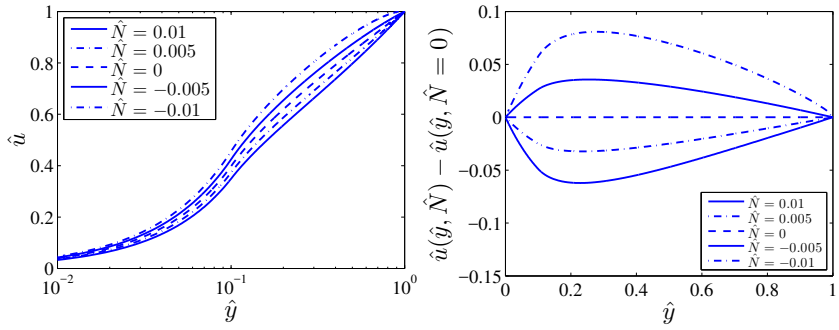

Figure 8.5: Velocity profiles for different $\hat{N}$ (left) in semi-log axes. All other parameters are the same as the reference case shown in Fig. 8.1. The right figure shows the difference in velocity with $\hat{N} \neq 0$ and $\hat{N} = 0$, resulting in region that may be approximated as linear in the meso-layer, with a slope whose sign depends on the sign of $\hat{N}$.

$\hat{N}$. We note that for non-zero $\hat{N}$ the difference with the logarithmic trend can be approximated reasonably well by a linear trend for $y > k$.

So far, we have assumed a fairly large Reynolds number, $Re_y = 10^4$, and a roughness height k only an order of magnitude smaller than Δ_y. We therefore have ensured the existence of a base-line logarithmic region. Next, we further consider cases with relatively low Re_y and surfaces that are hydrodynamically smooth or transitional. Fig.8.6 shows the profile for various Re_y. The roughness height $\hat{k}$ is kept equal to 0.1, while the k^+ values for $Re_y = 10^1, 10^2, 10^3$ are, respectively, $k^+ = 0.32, 1.16, 8.57$, i.e. smooth and transitionally rough.

We observe that for all different situations considered, the profile continues to be composed, qualitatively, of a linear region near the origin, and a log region in the upper part with a possible linear correction.

We then put the proposed velocity profile to test by comparing the numerically

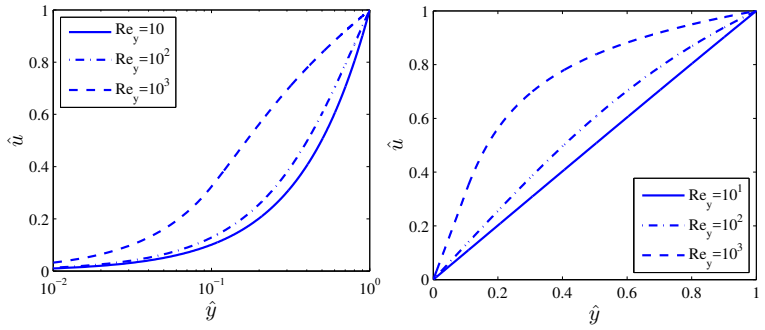

Figure 8.6: Velocity profiles for different Re_y in linear-linear axes and semi-log axes. $k = 0.1$ for all three cases. All other parameters are kept the same as the reference case shown in Fig. 8.1. The various Reynolds numbers lead to k^+ that are $0.32, 1.16, 8.75$.

integrated profile from Eq.8.12 with that obtained from enforcing the assumed profile from the main text including the 6 conditions and constraints. Solid lines shown in Fig.8.7 are from the numerical integration while the dashed lines are the assumed functional forms in iWMLES. First we consider $\hat{k} = 0.1$ and two values of $\hat{N}$ corresponding to non-equilibrium cases, namely $\hat{N}$=0.01 and -0.005 (comparison shown in left top figure). We then consider the case of $\hat{N} = 0$, with $\hat{k} = 0.01$ and 0.2 (top right). In the main text, Fig. 2.2 showed such a comparison for $\hat{k} = 0.1$. The assumed profile shape is compared with the numerical integration for various more cases including rough surface with $\hat{k} = 0.1$ at two Reynolds numbers and varying the C_d (or a_{LM} parameter), and results are shown in Fig. 8.7, bottom figures. It is apparent that the assumed velocity profile coupled with the conditions used in iWMLES is able to capture the main behaviors of Eq.8.12.

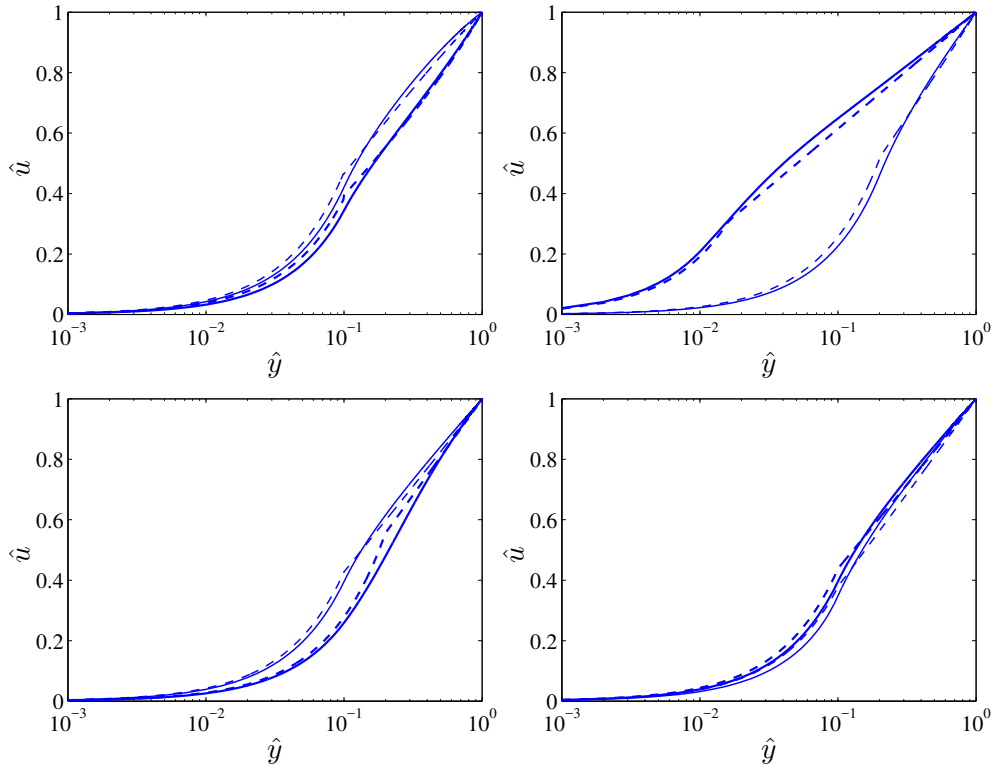

Figure 8.7: Comparison of velocity profile solved numerically from Eq.8.12 and that from the iWMLES formulae. The top left case shows the comparison when $N \neq 0$. $\hat{N}$ is 0.01 and -0.005 respectively. Top right figure shows two cases with different roughness height, $\hat{k} = 0.01, 0.2$. Two profiles with different Reynolds numbers are shown in the bottom left figure (namely for $Re_y = 0.5 \times 10^2$ for the thick line and $Re_y = 5 \times 10^3$ for the thin line). Lastly, the bottom right figure shows the comparison when the drag coefficient changes, namely $C_d = 0.1, 1$ for the thick line and thin line respectively, but using the same k value.

8.1.3 Projection onto X,Z directions

8.1.3.1 Velocity Profile

Both x and z components of the wall stress needs to be obtained in wall-modeled LES. For the general case in which $W_{LES} \neq 0$ and when pressure gradients in the z direction exist, we begin by projecting Eq.2.12, the assumed velocity profile from 2D analysis, onto the x and z component. We define the total LES velocity as $U_{tot}^2 = U_{LES}^2 + W_{LES}^2$. We consider the meso-layer ($\delta_i < y < \Delta_y$) first. Projection is included by $U_{LES}/U_{tot}, W_{LES}/U_{tot}$.

$$\begin{aligned} \langle u \rangle &= u_\tau \frac{U_{LES}}{U_{tot}} \left[\frac{1}{\kappa} \log \frac{y}{\Delta_y} \right] + u_\tau \left[A_x \frac{y}{\Delta_y} + C_x \right] \\ \langle w \rangle &= u_\tau \frac{W_{LES}}{U_{tot}} \left[\frac{1}{\kappa} \log \frac{y}{\Delta_y} \right] + u_\tau \left[A_z \frac{y}{\Delta_y} + C_z \right] \end{aligned} \tag{8.14}$$

Since C_x, C_z, A_x, A_z need to be determined from boundary conditions and other constraints, it is not necessary to place U_{LES}/U_{tot}, or W_{LES}/U_{tot} in front of the constant offset or linear terms represented already by C_x, C_z and A_x, A_z, respectively.

Next, consider the inner layer. We notice that the viscous momentum fluxes in x, z directions at $y = 0$ are simply projections of the total momentum flux τ_ν:

$$\tau_\nu = u_\nu^2 = (\nu + \nu_{T,y=0}) \frac{\partial \langle U \rangle}{\partial y}|_{y=0} \tag{8.15}$$

on to x, z, where $\langle U \rangle = \langle u \rangle^2 + \langle w \rangle^2$. We further define

$$u_{\nu,x}^2 = (\nu + \nu_{T,y=0}) \frac{\partial \langle u \rangle}{\partial y}|_{y=0}, \qquad u_{\nu,z}^2 = (\nu + \nu_{T,y=0}) \frac{\partial \langle w \rangle}{\partial y}|_{y=0}. \tag{8.16}$$

Then we have

$$u_\nu^4 = u_{\nu,x}^4 + u_{\nu,z}^4, \tag{8.17}$$

and the profile for the inner layer($0 < y < \delta_i$) can be written as

$$\langle u \rangle = u_{\nu,x} \frac{y}{\delta_\nu}, \qquad \langle w \rangle = u_{\nu,z} \frac{y}{\delta_\nu} \tag{8.18}$$

8.1.3.2 Constraints to determine parameters

Note that we now have eleven parameters, i.e. $\tau_{w,x}$, $\tau_{w,z}$, u_τ, $u_{\nu,x}$, $u_{\nu,z}$, δ_ν, δ_i, A_x, A_z, C_x, C_z, to be determined to fully describe the assumed velocity profiles for $\langle u \rangle$ and $\langle w \rangle$. The conditions are the following:

1. Two matching condition at $y = \Delta_y$:

$$\begin{aligned} u_\tau \left[C_x + A_x \right] &= U_{LES} \\ u_\tau \left[C_z + A_z \right] &= W_{LES}, \end{aligned} \tag{8.19}$$

   where U_{LES}, and W_{LES} are the horizontal velocities assumed to be known from LES (time filtered as described in main text).

2. The height δ_i is defined as in main text, i.e. Eq.2.15 (repeated below for completeness):

$$\delta_i = \min\left[\max\left(k, 11\frac{\nu}{u_\tau}\right), \Delta_y\right], \tag{8.20}$$

If $\delta_i = \Delta_y$, the inner region penetrates into $y = \Delta_y$ and no meso layer is included. The entire profile reduces to a linear profile.

3. Two conditions from the fact that at $y = \delta_i$ the velocity profiles must be continuous (note that the derivative is not continuous):

$$\begin{aligned} u_{\nu,x}\frac{\delta_i}{\delta_\nu} &= u_\tau \frac{U_{LES}}{U_{\text{tot}}}\left[\frac{1}{\kappa}\log\frac{\delta_i}{\Delta_y}\right] + u_\tau\left[A_x\frac{\delta_i}{\Delta_y} + C_x\right] \\ u_{\nu,z}\frac{\delta_i}{\delta_\nu} &= u_\tau \frac{W_{LES}}{U_{\text{tot}}}\left[\frac{1}{\kappa}\log\frac{\delta_i}{\Delta_y}\right] + u_\tau\left[A_z\frac{\delta_i}{\Delta_y} + C_z\right] \end{aligned} \tag{8.21}$$

4. δ_ν is determined via a consistent relation:

$$u_{\nu,x}^4 + u_{\nu,z}^4 = \left[\left(\nu + \alpha k\left(u_{\nu,x}^4 + u_{\nu,z}^4\right)^{1/4}\right)\frac{u_{\nu,x}}{\delta_\nu}\right]^2 + \left[\left(\nu + \alpha k\left(u_{\nu,x}^4 + u_{\nu,z}^4\right)^{1/4}\right)\frac{u_{\nu,z}}{\delta_\nu}\right]^2. \tag{8.22}$$

5. The definitions of total wall stress in each direction, thus providing 2 more conditions, are given by

$$\begin{aligned} \tau_{w,x} &= \left[u_{\nu,x}^2 + \int_0^k C_d a_L \left|u_{\nu,x}\right| \sqrt{u_{\nu,x}^2 + u_{\nu,z}^2}\left(y/\delta_\nu\right)^2 dy\right]\text{sign}(u_{\nu,x}), \\ \tau_{w,z} &= \left[u_{\nu,z}^2 + \int_0^k C_d a_L \left|u_{\nu,z}\right| \sqrt{u_{\nu,x}^2 + u_{\nu,z}^2}\left(y/\delta_\nu\right)^2 dy\right]\text{sign}(u_{\nu,z}). \end{aligned} \tag{8.23}$$

Note that we have replaced the velocity profile with the linear form since the

drag integral only extends, by definition, over the roughness layer up to $y = k$. The total stress magnitude involves the total friction velocity u_τ according to Eq.2.11. I.e. knowing $\tau_{w,x}$ and $\tau_{w,z}$, we determine $u_\tau = (\tau_{w,x}^2 + \tau_{w,z}^2)^{1/4}$.

6. The integrated momentum equations, Eq.(2.6), are also needed, providing and additional set of 2 equations.

$$\begin{aligned} \frac{\partial L_x}{\partial t} + M_x &= \tau_{\Delta_y,x} - \tau_{w,x} \\ \frac{\partial L_z}{\partial t} + M_z &= \tau_{\Delta_y,z} - \tau_{w,z} \end{aligned} \tag{8.24}$$

Again, $\tau_{\Delta_y,x}, \tau_{w,x}$ and $\tau_{\Delta_y,z}, \tau_{w,z}$ are momentum fluxes through $y = \Delta_y$ and at the wall, as defined in Eq.2.10. In the case of $\delta_i < \Delta_y$, where a log region is present, we have:

$$\begin{aligned} \tau_{\Delta_y,x} &= \left(\nu + \nu_{T,y=\Delta_y}\right) \left(\frac{1}{\kappa}\frac{U_{LES}}{U_{tot}} + A_x\right) \frac{u_\tau}{\Delta_y}, \\ \tau_{\Delta_y,x} &= \left(\nu + \nu_{T,y=\Delta_y}\right) \left(\frac{1}{\kappa}\frac{W_{LES}}{U_{tot}} + A_z\right) \frac{u_\tau}{\Delta_y}, \end{aligned} \tag{8.25}$$

where

$$\nu_{T,y=\Delta_y} = \left[\kappa(\Delta_y - d)\right]^2 \left.\frac{\partial U}{\partial y}\right|_{y=\Delta_y}. \tag{8.26}$$

Above, d is the displacement height defined in Appendix A, and $\partial U/\partial y|_{y=\Delta_y}$ is:

$$\left.\frac{\partial U}{\partial y}\right|_{y=\Delta_y} = \frac{U_{LES}}{U_{tot}} \left(\frac{U_{LES}}{U_{tot}}\frac{1}{\kappa} + A_x\right) \frac{u_\tau}{\Delta_y} + \frac{W_{LES}}{U_{tot}} \left(\frac{W_{LES}}{U_{tot}}\frac{1}{\kappa} + A_z\right) \frac{u_\tau}{\Delta_y} \tag{8.27}$$

When $\delta_i = \Delta_y$, only the linear inner region survives. The expressions for $\tau_{w,x}$, $\tau_{w,z}$ are unchanged and the expressions of τ_{x,Δ_y}, τ_{z,Δ_y} are simply given by:

$$\tau_{x,\Delta_y} = \nu \frac{U_{LES}}{\Delta_y}, \qquad \tau_{z,\Delta_y} = \nu \frac{W_{LES}}{\Delta_y}. \tag{8.28}$$

These provide 11 coupled nonlinear equations to fully determine the 11 unknown parameters.

Further simplifications are convenient, to combine several of the prior coupled equations: Most parameter can be expressed analytically via $u_{\nu,x}$, $u_{\nu,z}$. First, using (8.22) we can express δ_ν in terms of $u_{\nu,x}$, $u_{\nu,z}$:

$$\delta_\nu = \left[\frac{\left(\nu + \alpha k \left(u_{\nu,x}^4 + u_{\nu,z}^4 \right)^{1/4} \right)^2}{\left(u_{\nu,x}^4 + u_{\nu,z}^4 \right) / \left(u_{\nu,x}^2 + u_{\nu,z}^2 \right)} \right]^{1/2} \tag{8.29}$$

u_τ then can be computed from Eq.2.11. δ_i is in turn determined from Eq.(8.20). In order to express C_x, C_z, A_x, A_z in terms of $u_{\nu,x}$, $u_{\nu,z}$, we first separate C_x, C_z out in Eq.(8.19).

$$\begin{aligned} C_x &= \frac{U_{LES}}{u_\tau} - A_x \\ C_z &= \frac{W_{LES}}{u_\tau} - A_z \end{aligned} \tag{8.30}$$

Replacing Eq.(8.30) into Eq.(8.21), we have A_x, A_z expressed in terms of $u_{\nu,x}$, $u_{\nu,z}$.

$$\begin{aligned} A_x &= \left[\frac{U_{LES}}{u_\tau} + \frac{U_{LES}}{U_{tot}}\frac{1}{\kappa}\log\frac{\delta_i}{\Delta_y} - \frac{\delta_i}{\delta_\nu}\frac{u_{\nu,x}}{u_\tau}\right] / \left[1 - \frac{\delta_i}{\Delta_y}\right] \\ A_z &= \left[\frac{W_{LES}}{u_\tau} + \frac{W_{LES}}{U_{tot}}\frac{1}{\kappa}\log\frac{\delta_i}{\Delta_y} - \frac{\delta_i}{\delta_\nu}\frac{u_{\nu,z}}{u_\tau}\right] / \left[1 - \frac{\delta_i}{\Delta_y}\right] \end{aligned} \tag{8.31}$$

The parameters A, C and δ_i are required in the determination of the vertically integrated quantities L_x, L_{xx}, etc that enter into the momentum equation in condition (6), Eq. 8.24.

8.1.3.3 Evaluation of Vertical Integrals

Evaluation of M_x, M_z requires calculation of integrals like L_x, L_z, L_{xx}, L_{zz}, and L_{xz}. We list all involved integrals here.

$$\begin{aligned} L_x =& \int_0^{\Delta_y} \langle u\rangle \ \mathrm{d}y = \int_0^{\delta_i} \langle u\rangle \ \mathrm{d}y + \int_{\delta_i}^{\Delta_y} \langle u\rangle \ \mathrm{d}y \\ =& \frac{1}{2}u_{\nu,x}\frac{\delta_i^2}{\delta_\nu} + u_\tau\Delta_y\left[\frac{1}{2}A_x\left(1-\frac{\delta_i^2}{\Delta_y^2}\right) + C_x\left(1-\frac{\delta_i}{\Delta_y}\right) - \frac{1}{\kappa}\frac{U_{LES}}{U_{tot}}\left(1-\frac{\delta_i}{\Delta_y}+\frac{\delta_i}{\Delta_y}\log\frac{\delta_i}{\Delta_y}\right)\right]. \end{aligned} \tag{8.32}$$

L_z can be obtained similarly by replacing x subscript with z and U_{LES} with W_{LES}. Then,

$$\begin{aligned} L_{xx} =& \int_0^{\Delta_y} \langle u\rangle^2 \ \mathrm{d}y = \int_0^{\delta_i} \langle u\rangle^2 \ \mathrm{d}y + \int_{\delta_i}^{\Delta_y} \langle u\rangle^2 \ \mathrm{d}y \\ =& \frac{1}{3}u_{\nu,x}^2\frac{\delta_i^3}{\delta_\nu^2} + u_\tau^2\Delta_y\left[-A_x\frac{U_{\mathrm{LES}}}{U_{tot}}\frac{1}{\kappa}\frac{\delta_i^2}{\Delta_y^2}\log\frac{\delta_i}{\Delta_y} + A_x\left(C_x - \frac{1}{2\kappa}\frac{U_{\mathrm{LES}}}{U_{tot}}\right)\left(1-\frac{\delta_i^2}{\Delta_y^2}\right) + \frac{A_x^2}{3}\left(1-\frac{\delta_i^3}{\Delta_y^3}\right)\right. \\ &\left. + \left(C_x - \frac{1}{\kappa}\frac{U_{\mathrm{LES}}}{U_{tot}}\right)^2 - \frac{\delta_i}{\Delta_y}\left(C_x - \frac{U_{\mathrm{LES}}}{U_{tot}}\frac{1}{\kappa} + \frac{U_{\mathrm{LES}}}{U_{tot}}\frac{1}{\kappa}\log\frac{\delta_i}{\Delta_y}\right)^2 + \frac{1}{\kappa^2}\frac{U_{\mathrm{LES}}^2}{U_{tot}^2}\left(1-\frac{\delta_i}{\Delta_y}\right)\right] \end{aligned} \tag{8.33}$$

L_{zz} can be obtained similarly by replacing x subscript with z and U_{LES} with W_{LES}. Finally we need:

$$
\begin{aligned}
L_{xz} &= \int_0^{\Delta_y} \langle u \rangle \langle w \rangle \ \ \mathrm{d}y = \int_0^{\delta_i} \langle u \rangle \langle w \rangle \ \ \mathrm{d}y + \int_{\delta_i}^{\Delta_y} \langle u \rangle \langle w \rangle \ \ \mathrm{d}y \\
&= \frac{1}{3} u_{\nu,x} u_{\nu,z} \frac{\delta_i^3}{\delta_\nu^2} + u_\tau^2 \Delta_y \left[-\frac{1}{\kappa} \left(A_x \frac{W_{\mathrm{LES}}}{U_{tot}} + A_z \frac{U_{\mathrm{LES}}}{U_{tot}} \right) \left(\frac{1}{4} - \frac{1}{4} \frac{\delta_i^2}{\Delta_y^2} + \frac{1}{2} \frac{\delta_i^2}{\Delta_y} \log \frac{\delta_i}{\Delta_y} \right) \right. \\
&- \frac{1}{\kappa} \left(C_x \frac{W_{\mathrm{LES}}}{U_{tot}} + C_z \frac{U_{\mathrm{LES}}}{U_{tot}} \right) \left(1 - \frac{\delta_i}{\Delta_y} + \frac{\delta_i}{\Delta_y} \log \frac{\delta_i}{\Delta_y} \right) - \frac{U_{\mathrm{LES}}}{U_{tot}} \frac{W_{\mathrm{LES}}}{U_{tot}} \frac{1}{\kappa^2} \left(\frac{\delta_i}{\Delta_y} - 2 + \frac{\delta_i}{\Delta_y} \left(\log \frac{\delta_i}{\Delta_y} - 1 \right)^2 \right) \\
&\left. + \frac{1}{3} A_x A_z \left(1 - \frac{\delta_i^3}{\Delta_y^3} \right) + \frac{1}{2} \left(A_x C_z + A_z C_x \right) \left(1 - \frac{\delta_i^2}{\Delta_y^2} \right) + C_x C_z \left(1 - \frac{\delta_i}{\Delta_y} \right) \right]
\end{aligned}
\tag{8.34}
$$

8.1.3.4 Solution Procedure

Note that except for Eq. (8.24), every condition or physical constraint in this section is local and instantaneous in the sense that they don't involve spatial or temporal derivatives. Different discretization schemes can be used for Eq. (8.24). We use forward Euler for simplicity and denote the current time-step as n, and the wall-model integration time step as δt.

$$
\begin{aligned}
L_x^n &= L_x^{n-1} + \delta t \left(-M_x^{n-1} + \tau_{\Delta_y,x}^{n-1} - \tau_{w,x}^{n-1} \right), \\
L_z^n &= L_z^{n-1} + \delta t \left(-M_z^{n-1} + \tau_{\Delta_y,z}^{n-1} - \tau_{w,z}^{n-1} \right).
\end{aligned}
\tag{8.35}
$$

Since all terms on the right hand side are known from the previous time step, Eq.(8.35) provides the value for L_x, L_z at time step n. It is those two equations that needs to be solved simultaneously. The Newton method works well to solve this coupled system at every surface point.

We summarize the procedure here.

1. Based on the known information at the prior time step (U_{LES}^{n-1}, U_{LES}^{n-1}, $\partial\langle p\rangle^{n-1}/\partial x$ and $\partial\langle p\rangle^{n-1}/\partial z$, and all parameters A^{n-1}, C^{n-1}, u_ν^{n-1}, etc..), evaluate M_x^{n-1}, M_z^{n-1} (from Eqs. 2.7, 8.32, 8.33, etc.), $\tau_{\Delta_y,x}^{n-1}$, $\tau_{\Delta_y,z}^{n-1}$ (from Eqs. 8.25), and $\tau_{w,x}^{n-1}$ and $\tau_{w,z}^{n-1}$ (from Eqs. 8.23).

2. At the current time-step n, obtain LES velocities U_{LES}^n, W_{LES}^n and pressure gradients $\partial\langle p\rangle^n/\partial x$ and $\partial\langle p\rangle^n/\partial z$ above every surface grid point (at a distance Δ_y above).

3. With these values, set up a system of equations for 11 unknown parameters A_x^n, A_z^n, C_x^n, C_z^n, $u_{\nu,x}^n$, $u_{\nu,z}^n$, δ_ν^n, δ_i^n, $\tau_{w,x}$, $\tau_{w,z}$ and u_τ. Two of the equations are obtained from the momentum equation by equating the right hand side of Eq. 8.35 with the values from the integrals evaluated at time-step n. Specifically, we have

$$\frac{1}{2}u_{\nu,x}^n\frac{\delta_i^{n2}}{\delta_\nu^n}+u_\tau^n\Delta_y\left[\frac{1}{2}A_x^n\left(1-\frac{\delta_i^{n2}}{\Delta_y^2}\right)+C_x^n\left(1-\frac{\delta_i^n}{\Delta_y}\right)-\frac{1}{\kappa}\frac{U_{LES}^n}{U_{tot}^n}\left(1-\frac{\delta_i^n}{\Delta_y}+\frac{\delta_i^n}{\Delta_y}\log\frac{\delta_i^n}{\Delta_y}\right)\right]$$

$$=L_x^{n-1}+\delta t\left(-M_x^{n-1}+\tau_{\Delta_y,x}^{n-1}-\tau_{w,x}^{n-1}\right), \qquad (8.36)$$

$$\frac{1}{2}u_{\nu,z}^n\frac{\delta_i^{n2}}{\delta_\nu^n}+u_\tau^n\Delta_y\left[\frac{1}{2}A_z^n\left(1-\frac{\delta_i^{n2}}{\Delta_y^2}\right)+C_z^n\left(1-\frac{\delta_i^n}{\Delta_y}\right)-\frac{1}{\kappa}\frac{W_{LES}^n}{U_{tot}^n}\left(1-\frac{\delta_i^n}{\Delta_y}+\frac{\delta_i^n}{\Delta_y}\log\frac{\delta_i^n}{\Delta_y}\right)\right]$$

$$=L_z^{n-1}+\delta t\left(-M_z^{n-1}+\tau_{\Delta_y,z}^{n-1}-\tau_{w,z}^{n-1}\right). \qquad (8.37)$$

Other equations are repeated below for completeness. We have

$$\delta_i^n = \min\left[\max\left(k, 11\frac{\nu}{u_\tau^n}\right), \Delta_y\right], \tag{8.38}$$

$$\delta_\nu^n = \left[\frac{\left(\nu + \alpha k\left((u_{\nu,x}^n)^4 + (u_{\nu,z}^n)^4\right)^{1/4}\right)^2}{\left((u_{\nu,x}^n)^4 + (u_{\nu,z}^n)^4\right) / \left((u_{\nu,x}^n)^2 + (u_{\nu,z}^n)^2\right)}\right]^{1/2}. \tag{8.39}$$

Also

$$\begin{aligned} A_x^n &= \left[\frac{U_{LES}^n}{u_\tau^n} + \frac{U_{LES}^n}{U_{tot}^n}\frac{1}{\kappa}\log\frac{\delta_i^n}{\Delta_y} - \frac{\delta_i^n}{\delta_\nu^n}\frac{u_{\nu,x}^n}{u_\tau^n}\right] / \left[1 - \frac{\delta_i^n}{\Delta_y}\right], \\ A_z^n &= \left[\frac{W_{LES}^n}{u_\tau^n} + \frac{W_{LES}^n}{U_{tot}^n}\frac{1}{\kappa}\log\frac{\delta_i^n}{\Delta_y} - \frac{\delta_i^n}{\delta_\nu^n}\frac{u_{\nu,z}^n}{u_\tau^n}\right] / \left[1 - \frac{\delta_i^n}{\Delta_y}\right], \end{aligned} \tag{8.40}$$

and

$$\begin{aligned} C_x^n &= \frac{U_{LES}}{u_\tau^n} - A_x^n, \\ C_z^n &= \frac{W_{LES}}{u_\tau^n} - A_z^n. \end{aligned} \tag{8.41}$$

Also,

$$\begin{aligned} \tau_{w,x}^n &= \left[(u_{\nu,x}^n)^2 + \int_0^k C_d a_L \left|u_{\nu,x}^n\right| \sqrt{(u_{\nu,x}^n)^2 + (u_{\nu,z}^n)^2}\,(y/\delta_\nu^n)^2\, dy\right] \mathrm{sign}(u_{\nu,x}^n), \\ \tau_{w,z}^n &= \left[(u_{\nu,z}^n)^2 + \int_0^k C_d a_L \left|u_{\nu,z}^n\right| \sqrt{(u_{\nu,x}^n)^2 + (u_{\nu,z}^n)^2}\,(y/\delta_\nu^n)^2\, dy\right] \mathrm{sign}(u_{\nu,z}^n), \end{aligned} \tag{8.42}$$

and

$$u_\tau^n = \left[(\tau_{w,x}^n)^2 + (\tau_{w,z}^n)^2\right]^{1/4}. \tag{8.43}$$

These 11 coupled nonlinear equations are solved using Newton iteration at every point. Convergence is quite fast.

4. Apply wall stress components $\tau_{w,x}$ and $\tau_{w,z}$ in the LES at the wall, and forward to the next time step.

8.1.4 Prescribed roughness length or velocity defect ΔU^+

When the roughness length y_0 is prescribed and known (this length is usually called z_0 but we will use the notation y_0 to be consistent with y representing the wall-normal direction), the approach reverts to requiring that $\langle u \rangle (y = y_0) = 0$. If instead of y_0 one wishes to use correlations for the velocity defect ΔU^+, the usual relationship between y_0 and ΔU^+ must be used, Eq.(2.23). No "inner layer" is needed in this approach. The assumed profile, therefore, becomes

$$\begin{aligned} \langle u \rangle &= \frac{u_{\tau,x}}{\kappa} \log(\frac{y}{y_0}) + u_{\tau,x}\ A_x \left(\frac{y}{\Delta_y} - \frac{y_0}{\Delta_y} \right), \\ \langle w \rangle &= \frac{u_{\tau,z}}{\kappa} \log(\frac{y}{y_0}) + u_{\tau,z}\ A_z \left(\frac{y}{\Delta_y} - \frac{y_0}{\Delta_y} \right). \end{aligned} \tag{8.44}$$

Unlike the case in which the assumed profiles included some information about the surface (either smooth or with a prescribed distribution of $a_L(y)$, k, etc.), here we are assuming that the entire roughness information can be contained in a single parameter y_0 irrespective of direction. It turns out that the velocity scale for the logarithmic

portion of the profile, whenever we have non-equilibrium conditions with A_x or A_z not equal to zero, cannot be simply $u_\tau U_{LES}/U_{tot}$ and $u_\tau W_{LES}/U_{tot}$, i.e. parameterized by a single u_τ for an imposed outer LES velocity. In that case we must allow for different friction velocities in the x and z directions. Therefore, we have introduced $u_{\tau,x}$, $u_{\tau,z}$. This enables more flexibility for the profile, which is needed when a single y_0 is prescribed for both x, z direction. We note that in the case of equilibrium conditions ($A_i = 0$), it is still the case that $u_{\tau,x} = u_\tau U_{LES}/U_{tot}$ and $u_{\tau,z} = u_\tau W_{LES}/U_{tot} u_\tau$.

Two matching conditions and vertically integrated momentum equations in x and z directions are used to determine four unknown parameters $u_{\tau,x}$, $u_{\tau,z}$, A_x and A_z. First we use two matching conditions at $y = \Delta_y$ to express A_x, and A_z in terms of $u_{\tau,x}$, $u_{\tau,z}$ and the LES velocities:

$$\begin{aligned} A_x &= \left[\frac{U_{\text{LES}}}{u_{\tau,x}} - \frac{1}{\kappa}\log\frac{\Delta_y}{y_0}\right] \Big/ \left[1 - \frac{y_0}{\Delta_y}\right] \\ A_z &= \left[\frac{W_{\text{LES}}}{u_{\tau,z}} - \frac{1}{\kappa}\log\frac{\Delta_y}{y_0}\right] \Big/ \left[1 - \frac{y_0}{\Delta_y}\right] \end{aligned} \tag{8.45}$$

Then two additional equations come, as before, from the vertically integrated momentum equations but now with the stress at the wall evaluated at $y = y_0$ according to

$$\begin{aligned} \frac{\partial L_x}{\partial t} + M_x &= \tau_{\Delta_y x} - \tau_{y_o x} \\ \frac{\partial L_z}{\partial t} + M_z &= \tau_{\Delta_y z} - \tau_{y_o z} \end{aligned} \tag{8.46}$$

The vertically integrated momentum equation requires momentum flux from $y = \Delta_y$ and $y = y_0$ in both x, z directions. The expressions for the momentum flux in x direction are:

$$\tau_{\Delta_y x} = \kappa^2 \Delta_y^2 \left|\frac{\partial U}{\partial y}\right|_{\Delta_y} \frac{\partial \langle u \rangle}{\partial y}\bigg|_{\Delta_y}, \qquad \tau_{y_0 x} = \kappa^2 y_0^2 \left|\frac{\partial U}{\partial y}\right|_{y_0} \frac{\partial \langle u \rangle}{\partial y}\bigg|_{y_0} \tag{8.47}$$

and similarly in the z direction. Each term can be expressed via $u_{\tau,x}$, $u_{\tau,z}$:

$$\frac{\partial \langle u \rangle}{\partial y}\bigg|_{\Delta_y} = \frac{u_{\tau,x}}{\Delta_y}\left(\frac{1}{\kappa} + A_x\right), \qquad \frac{\partial \langle u \rangle}{\partial y}\bigg|_{y_0} = \frac{u_{\tau,x}}{y_0}\left(\frac{1}{\kappa} + A_x \frac{y_0}{\Delta_y}\right). \tag{8.48}$$

and

$$\left|\frac{\partial U}{\partial y}\right|_{\Delta_y} = \left|\frac{U_{\mathrm{LES}}}{U_{tot}} \frac{\partial \langle u \rangle}{\partial y}\bigg|_{\Delta_y} + \frac{W_{\mathrm{LES}}}{U_{tot}} \frac{\partial \langle w \rangle}{\partial y}\bigg|_{\Delta_y}\right| \qquad \left|\frac{\partial U}{\partial y}\right|_{y_0} = \sqrt{\frac{\partial \langle u \rangle}{\partial y}\bigg|_{y_0}^2 + \frac{\partial \langle w \rangle}{\partial y}\bigg|_{y_0}^2}. \tag{8.49}$$

The numerical treatment is the same as that described in Appendix C, in which the four parameters $u_{\tau,x}^n$, $u_{\tau,z}^n$, A_x^n and A_z^n are solved from four equations in which the momentum equations 8.46 are discretized using forward Euler, and the integrals needed to evaluate L_x, L_{xx} etc. involve the previous time values and the integrations are evaluated only in the logarithmic layer. In this case the profile contains only the meso layer, and the analytical integration is simpler than in the case with two layers.

We provide the integrals here:

$$L_x = u_{\tau,x}\Delta_y \left[\frac{1}{2}A_x\left(1-\frac{y_0}{\Delta_y}\right)^2 - \frac{1}{\kappa}\left(1-\frac{y_0}{\Delta_y}+\log\frac{y_0}{\Delta_y}\right)\right] \tag{8.50}$$

$$\begin{aligned} L_{xx} = u_{\tau,x}^2\Delta_y \Bigg[&\left(\frac{1}{\kappa}\log\frac{y_0}{\Delta_y}+\frac{1}{\kappa}\right)^2 + \frac{1}{\kappa^2} - \frac{2}{\kappa^2}\frac{y_0}{\Delta_y} + \frac{1}{3}A_x^2\left(1-\frac{y_0}{\Delta_y}\right)^3 \\ &-\frac{A_x}{\kappa}\left(1-\frac{y_0}{\Delta_y}\right)^2 + \frac{A_x}{2\kappa}\left(1-\frac{y_0^2}{\Delta_y^2}\right) - \frac{A_x}{\kappa}\log\frac{y_0}{\Delta_y}\left(1-2\frac{y_0}{\Delta_y}\right)\Bigg], \end{aligned} \tag{8.51}$$

nd similarly for L_z and L_{zz}. For the cross term we have:

$$\begin{aligned} L_{xz} = u_{\tau,x}u_{\tau,z}\Delta_y \Bigg[&\left(\frac{1}{\kappa}\log\frac{y_0}{\Delta_y}+\frac{1}{\kappa}\right)^2 + \frac{1}{\kappa^2} - \frac{2}{\kappa^2}\frac{y_0}{\Delta_y} + \frac{1}{3}A_xA_y\left(1-\frac{y_0}{\Delta_y}\right)^3 \\ &-\frac{A_x+A_y}{2\kappa}\left(1-\frac{y_0}{\Delta_y}\right)^2 + \frac{A_x+A_y}{4\kappa}\left(1-\frac{y_0^2}{\Delta_y^2}\right) - \frac{A_x+A_y}{2\kappa}\log\frac{y_0}{\Delta_y}\left(1-2\frac{y_0}{\Delta_y}\right)\Bigg] \end{aligned} \tag{8.52}$$

8.2 Appendixes for the rescaling-recycling method

8.2.1 Dynamic approach for λ

We follow Ref. 143 and assume:

$$\frac{u_\tau}{U} \sim Const\ Re_\delta^{-\gamma}, \tag{8.53}$$

where $Re_\delta = U\delta/\nu$ but γ is not necessarily known *a-priori*. We place the test plane at equal distance from the inlet and the recycle planes. Denoting the inlet plane to be plane 1, the test plane to be plane 2, and the recycle plane to be plane 3, we have:

$$\begin{aligned} \frac{u_{\tau,1}}{u_{\tau,2}} &= \left(\frac{\delta_2}{\delta_1}\right)^\gamma, \\ \frac{u_{\tau,2}}{u_{\tau,3}} &= \left(\frac{\delta_3}{\delta_2}\right)^\gamma. \end{aligned} \tag{8.54}$$

Because the boundary layer thickness grows nearly linearly in x, we have:

$$\begin{aligned} \frac{\delta_2}{\delta_1} &= \frac{x_0 + x_{1,2}}{x_0} = 1 + \frac{x_{1,2}}{x_0}, \\ \frac{\delta_3}{\delta_2} &= \frac{x_0 + x_{1,3}}{x_0 + x_{2,3}} = \frac{x_0 + 2x_{1,2}}{x_0 + x_{1,2}} = 1 + \frac{x_{1,2}}{x_0} + O\left[\left(\frac{x_{1,2}}{x_0}\right)^2\right], \end{aligned} \tag{8.55}$$

where x_0 is the distance of the computational inlet location to the virtual origin, $x_{i,j}$ is the distance between planes i and j. Therefore we obtain

$$\lambda = \frac{u_{\tau,1}}{u_{\tau,3}} = \frac{u_{\tau,1}}{u_{\tau,2}}\frac{u_{\tau,2}}{u_{\tau,3}} = \left(\frac{u_{\tau,2}}{u_{\tau,3}}\right)^2 = \frac{D_2}{D_3} \tag{8.56}$$

where D is the drag force on a given area of the surface. D can be measured within the simulation via integrating the pressure force (form drag) on the resolved roughness elements (neglecting the contribution from the sub-grid roughness) and then averaging in the streamwise direction for one repeating roughness tile to eliminate any variation due to single roughness elements. Since D_2, D_3 can be directly measured from the

simulation, λ can in turn be determined. We thus set

$$\lambda = \frac{\bar{D}_2}{\bar{D}_3}, \tag{8.57}$$

where the temporally averaged value (following Eq. 3.11) is used to reduce fluctuations.

8.2.2 A validation case

The finite difference incompressible Navier-Stokes solver Vicar3D has already been extensively validated in prior work.[136] We present one validation that is of particular interest to this study. The experimental data set we validate against is developing turbulent boundary layer over a surface mounted with perfectly staggered cubes (figure 8.8).[16] The experiment is conducted in a low speed wind tunnel. The cube height is $20mm$ and the surface solidity is 0.25. The free stream velocity is $10.15m/s$. The Reynolds number based on free stream and cube height is 1.2×10^4. At the streamwise location where the velocity profile is measured, the ratio between the boundary layer thickness and roughness height (i.e. the cube height) is $\delta/k = 7$. The mean velocity profile is measured at the locations marked in figure 8.8 by blue circles and then the profiles are averaged over the four locations. The simulation is performed with the inflow generation technique developed. Periodic boundary conditions are used in the spanwise direction. A zero-gradient condition is imposed at the top boundary. The

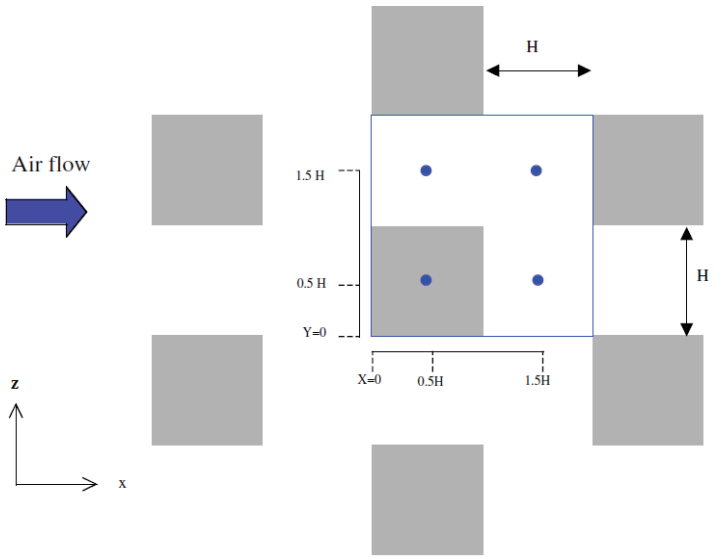

Figure 8.8: The surface roughness element distribution and geometry corresponding to the experiment.[16]

mean velocity is taken at the streamwise location where local δ/k is 7. We compare the mean velocity as well as $\overline{u'u'}$ profile obtained from the experiment and the simulation in figure. 8.9. The drag coefficient (defined $C_d = 2f/\rho U^2$, where ρ is the fluid density, f is the drag force per planar area and U is the free stream velocity) is 0.042 while the computed drag from the simulation is 0.043.

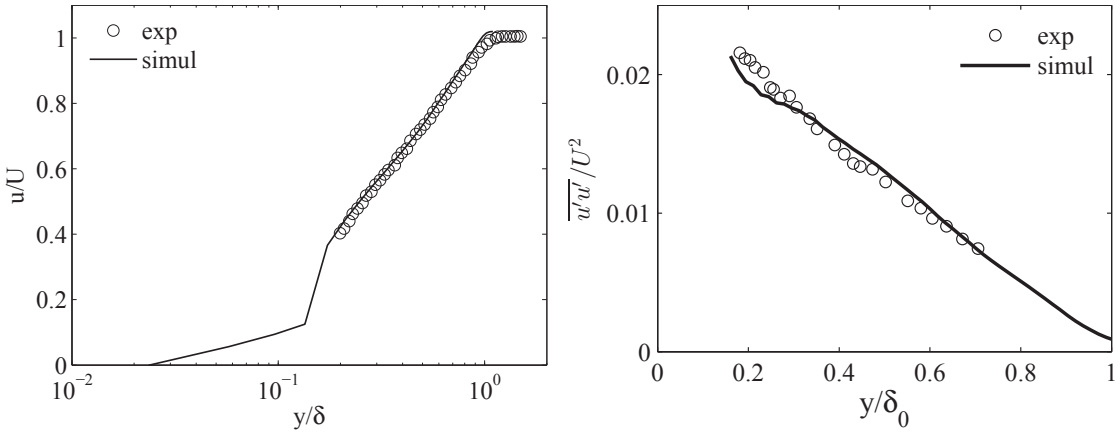

Figure 8.9: A comparison of the mean profile (left) as well as the profile of $\overline{u'u'}$ from simulation and experiment.[16] The velocity is normalized by the free stream velocity and y by the local boundary layer thickness.

8.3 Appendixes for the analytical rough wall model

8.3.1 Further examples of sheltered area evaluations

We have already considered aligned cube arrays in §4.3.2. Here we provide additional two examples of calculating the sheltered area analytically for regular, simple roughness arrangements. Then we briefly discuss how to implement a simple numerical code to do this geometrical calculation for more complicated cases.

First we consider fully staggered cube arrays. Because all roughness elements will be equally sheltered, we only need to consider one element. We begin by identifying

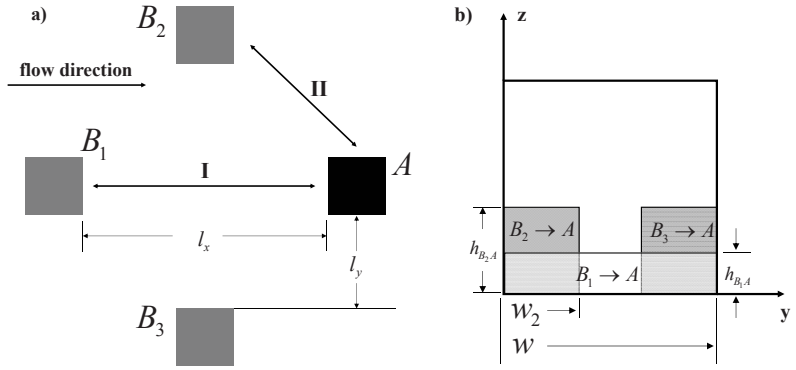

Figure 8.10: a) A sketch of the roughness interaction in fully staggared cube arrays. Cube A can be sheltered by B_1, B_2, B_3. b) a sketch of the frontal area of A.

the upstream elements that could shelter the particular element under consideration. Figure 8.10 sketches the interactions that need to be considered. The sheltering due to B_1 is $S_{B_1A} = h_{B_1A}[\mathcal{H}(y) - \mathcal{H}(y-w)]$, where $h_{B_1A} = \max[0, h - l_x \tan(\theta)]$, $l_x = 2h/\sqrt{\lambda_f} - h$, $w = h$. The sheltered area due to B_2 is $S_{B_2A} = h_{B_2A}[\mathcal{H}(y) - \mathcal{H}(y-w_2)]$, where $h_{B_2A} = \max[0, h - \tan(\theta)(l_x - h)/2]$, $w_2 = \max[\tan(\theta)(l_x - h)/2 - l_y, 0]$, $l_y = h/\sqrt{\lambda_f} - h$. Because of symmetry, sheltering due to B_3 is $S_{B_3A} = h_{B_2A}[\mathcal{H}(y-w+w_2) - \mathcal{H}(y-w)]$. The sheltered area of A is then determined by $A_{s,A} = \int_0^w \max[S_{B1A}, S_{B2A}, S_{B3A}]dy = (w - 2w_2)h_{B_1A} + 2w_2 h_{B_2A}$.

Second we consider roughness with staggered bi-modal height distribution. The interactions that need to be considered are sketched in figure 8.11(a). This time, we need to calculate the sheltered area for both the lower-rising and higher-rising elements separately. For the higher-rising elements A_1, these could be sheltered by the lower-rising roughness upstream B_2 and by the higher-rising element further upstream A_3, as well as by the one that is diagonally upstream A_2. Notice the interactions

among A_1, A_2, A_3 is quite like the interaction among the staggered arrays. The interaction between B_2, A_1 and A_2, B_1 on the other hand, are just like aligned cubes.

The flow sheltering in the canopy layer is sketched in figure 8.11(b). The sheltered projected frontal area in the example sketched in figure 8.11 is $A_{f,s}/A_T = \lambda_f(h_B w + h_{s,A} w)/(h_B w + h_A w)$, where $h_A = h_m + std(h)$, $h_B = h_m - std(h)$, $h_{s,B}$, $h_{s,A}$ are the height of the sheltered area for the low and high rising roughness respectively. The height of the equivalent sheltered layer h_s is then simply $h_s = (h_{s,A} + h_B)/2$.

In general the equivalent sheltered layer height is

$$h_s = \mathcal{H}\left(\frac{h_{s,A}+h_{s,B}}{2} - h_B\right)(h_{s,A}+h_{s,B}-h_B) + \left[1 - \mathcal{H}\left(\frac{h_{s,A}+h_{s,B}}{2} - h_B\right)\right]\frac{h_{s,A}+h_{s,B}}{2}. \tag{8.58}$$

To determine $h_{s,B}$, $h_{s,A}$, the wake interaction among the roughness elements need to be considered. In general, interaction between higher roughness-higher roughness, higher roughness-lower roughness, lower roughness-lower roughness needs to be considered, but since lower roughness elements are separated by higher roughness, there is no need to consider lower roughness-lower roughness interactions. With u_τ/U_h known as a function of a, h_s expressed with a via Eq. 8.58. Eq. 4.17 can be then used to solve a. With a known, U_h, u_τ, z_o, d can again be solved via Eq. 4.4, 4.6, 4.7, 4.8.

For more complex cases, such as the example with a Gaussian distribution of heights, the geometric calculations must be done by a code. The method is based on discretizing the upstream and downstream edges of the base of roughness elements. A sketch is provided in figure 8.12. Because of the rectangular shape of the roughness,

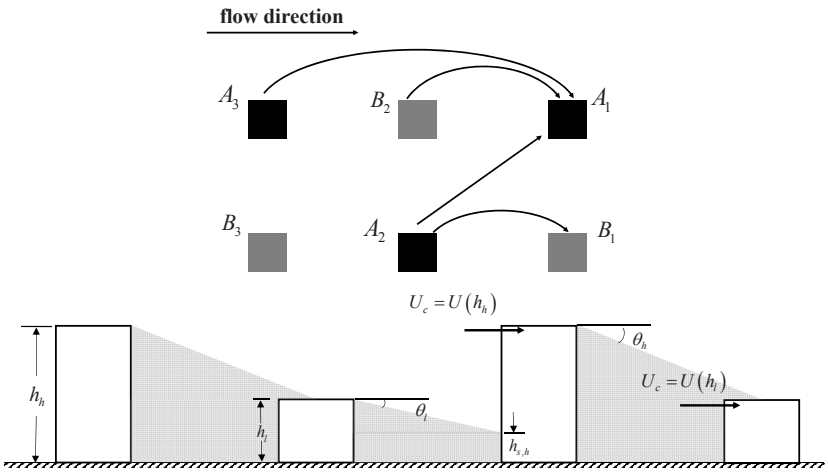

Figure 8.11: (a) Sketch of the interaction among roughness elements for roughness of bimodal height distribution. A_i, $i = 1, 2, 3$ are higher-rise roughness and B_i, $i = 1, 2, 3$ are lower-rise roughness. (b) sketch of the wake interaction among roughness elements. In the case shown the roughness of height h_l is completely sheltered from the wake behind the roughness of height h_h and no sheltering occurs among the higher roughness elements. But parts of the higher roughness elements are sheltered by the lower roughness elements. Because the number of roughness of height h_h and roughness of height h_l is the same, the equivalent sheltered layer height is given by $h_s = (h_{s,A} + h_B)/2$.

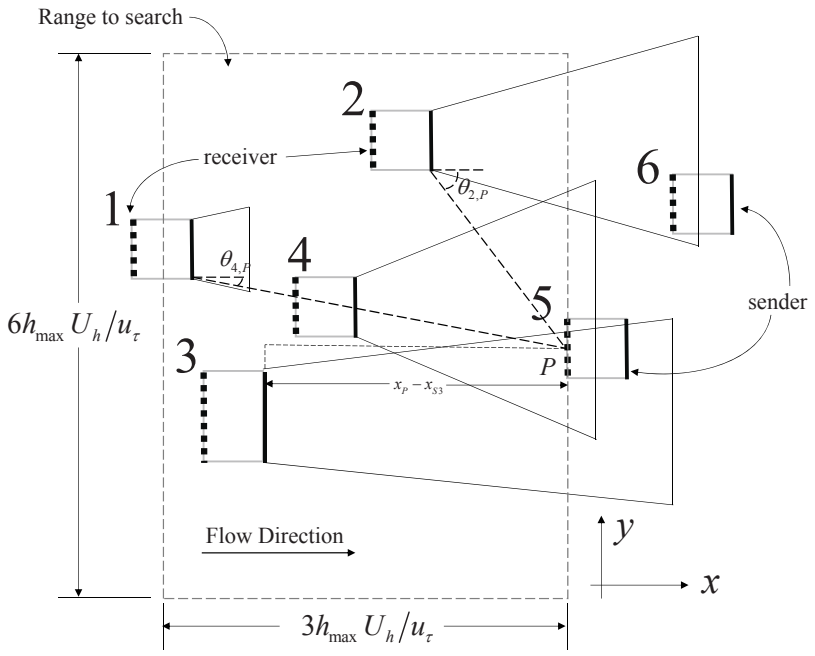

Figure 8.12: A sketch of the rough wall with rectangular roughness elements. Each element is indicated by a rectangle and given a number (from 1 to 6). The 'senders' are highlighted with thick lines and the 'receivers' with thick dotted lines. The point P of the 'receiver' of element 5 is under consideration. The domain to search for roughness elements that could shelter P is enclosed by dashed lines. It is $3h_{\max}U_h/u_\tau$ upstream and on both sides. $h_{\max}$ is the height of the highest roughness element. The sheltering of the 'senders' within the search domain is indicated by thin solid line.

only the base plane needs to be considered. First, for all rectangular roughness elements, the windward faces are identified, i.e. its projection on the ground, a segment of line. These lines will be called 'receivers' (because they receive sheltering). The height h of the receiver element is associated to it in order to make sure sheltering does not go beyond the height of the sheltered roughness. Second, we identify all leeward faces, and group their projections on the ground into a 'emitters' set. We too keep track of their heights to calculate the sheltering height to any downstream roughness element (if the downstream (receiver) element is δx downstream, the sheltering height on the receiver segment is $h_s = h - \delta x \tan(\theta)$). Both receiver and emitter lines are discretized (here we use 100 points per line).

The task now is to loop through all points in each member of 'receivers' and calculate how it is sheltered by each member in the set of 'emitters'. To calculate how a particular 'emitter' member S is sheltering a particular point P in a line that belongs to the 'receiver' set, we take the minimum between the height of the volumetric sheltering of S at P and the height of element P. This height is then compared among sheltering by all 'emitters' members and the maximum value of the sheltering height at P is the sheltering height at P. By doing this, the sheltering height for each of the 'receiver points' can be calculated and an integral of sheltering height at each point across the receiver line leads to A_s.

For example, consider the point P in figure 8.12. Within the searching domain (the domain enclosed by the dashed box and is $3h_{\max}U_h/u_\tau$ upstream and on both

sides), there are four 'sender' members: 1, 2, 3, 4. Element 2 cannot shelter P because $\tan(\theta_{2,P}) > \tan(\theta_2)$, where $\tan(\theta_2)$ is the wake expansion rate of roughness 2. Element 1 cannot shelter P because $x_P - x_{S1} > h_1/\tan(\theta_1)$, where x_P, x_{S1} are streamwise coordinates of point P and the 'sender' of element 1. Both elements 4 and 3 can shelter P. Their sheltering height at P can be calculated: $S_{4,P} = \min[h_4 - (x_P - x_{S4})\tan(\theta_4), h_5]$, $S_{3,P} = \min[h_3 - (x_P - x_{S3})\tan(\theta_3), h_5]$, where $S_{i,P}$ is the sheltering from i to P, h_i is the height of element i, i is 3, 4, or 5. The sheltered height of P is $h_P = \max[h_{4,P}, h_{3,P}]$.

8.3.2 Including surface friction drag for $\lambda_f \to 0$

A conceptual difficulty occurs in the model for d as $\lambda_f \to 0$ namely that d does not tend to 0. This difficulty arises because we assumed the bottom surface to be smooth, and we have made the assumption of a fully rough flow regime in which friction drag is entirely neglected. As $\lambda_f \to 0$ viscous friction drag on the smooth portions of the surface must become comparatively relevant. Therefore we must consider how the drag is partitioned between roughness elements and underlying surface.[7]

We describe the contribution of the bottom surface and top of roughness elements (i.e. the planform surfaces) to the overall momentum loss as coming from either 'unresolved roughness' form drag or viscous drag on the bottom surface. We assume that the hydrodynamic roughness height of that unresolved roughness, z_o', is known a-priori, or in the case of viscous drag it can be determined iteratively as

$z_o' = \nu/u_\tau \exp(-\kappa B_0)$ (where $B_0 = 5$ is the usual offset of the smooth-wall log law and u_τ is part of the solution). The force on the overall planform surface is modeled as $F_s = C_s U_h^2 A_T$ with $C_s = [\kappa/\ln(h/z_0')]^2$. And, the force on the frontal surface is modeled according to $F_R = \frac{1}{2} C_{HD} U_h^2 A_f = C_R U_h^2 \lambda_f A_T$ with $C_R = \frac{1}{2} C_{DH}$, valid for low coverage fraction according to the derivation presented in §4.3.2. Thus the ratio of forces is:

$$\frac{F_s}{F_R} = \frac{1}{\lambda_f \beta}, \tag{8.59}$$

where $\beta = C_R/C_s = 2[\kappa/\ln(h/z_0')]^2/C_{DH}$ with $C_{DH} = 1.4$ as before. This simple estimate of the force or stress partition derivation is valid for low packing densities. In fact, a similar estimate to Eq. 8.59 can be justified also for higher packing ratios since then sheltering reduces both the numerator and denominator in similar fashion.[7] The momentum balance Eq. 4.4 is then augmented by considering $u_\tau^2 A_T = F_R(F_s/F_R + 1) = F_R(1 + \beta\lambda_f)/(\beta\lambda_f)$, i.e.

$$u_\tau^2 A_T = \frac{1 + \beta\lambda_f}{\beta\lambda_f} \int_{A_f} C_d U^2 dA. \tag{8.60}$$

Eq. 4.8 can also be corrected as:

$$d = \frac{\beta\lambda_f}{1 + \beta\lambda_f} \frac{\int_{A_f} C_d U^2 z dA}{\int_{A_f} C_d U^2 dA} \tag{8.61}$$

Equations 4.6 and 4.7 remain unaffected provided the corrected values of z_0 and d are used.

For illustration purposes, consider for example that the underlying surface includes an unresolved roughness with element height $h' = 0.02h$. The typical rule of thumb is $z'_o \sim 0.06h'$,[77] leading to $C_s = 0.00357$. With $C_R = 1.4$ the ratio is, in this case, $\beta = 196$. The predictions of the model with drag partition correction in this case are plotted in Figs. 4.15(b) and 4.16(b) that had been shown previously. It is observed that with this correction, $\lim_{\lambda_f \to 0} d = 0$, $\lim_{\lambda_f \to 0} z_o = z'_o$, while this correction is negligible for packing densities $\lambda_f > 0.1$ where the fully rough condition is more closely reproduced.

Bibliography

[1] E. Meinders and K. Hanjalić, "Vortex structure and heat transfer in turbulent flow over a wall-mounted matrix of cubes," *Int J Heat Fluid Flow*, vol. 20, no. 3, pp. 255–267, 1999.

[2] T. S. Lund, X. Wu, and K. D. Squires, "Generation of turbulent inflow data for spatially-developing boundary layer simulations," *J Comput Phys*, vol. 140, no. 2, pp. 233–258, 1998.

[3] A. Hagishima, J. Tanimoto, K. Nagayama, and S. Meno, "Aerodynamic parameters of regular arrays of rectangular blocks with various geometries," *Boundary-Layer Meteorol.*, vol. 132, no. 2, pp. 315–337, 2009.

[4] H. Cheng, P. Hayden, A. Robins, and I. Castro, "Flow over cube arrays of different packing densities," *Journal of Wind Engineering and Industrial Aerodynamics*, vol. 95, no. 8, pp. 715–740, 2007.

[5] D. Hall, R. Macdonald, and S. Walker, *Measurements of dispersion within sim-*

ulated urban arrays: a small scale wind tunnel study. Building Research Establishment, 1996.

[6] S. Leonardi and I. P. Castro, "Channel flow over large cube roughness: a direct numerical simulation study," *J. Fluid Mech.*, vol. 651, pp. 519–539, 2010.

[7] M. Raupach, "Drag and drag partition on rough surfaces," *Boundary-Layer Meteorol.*, vol. 60, no. 4, pp. 375–395, 1992.

[8] O. Coceal and S. Belcher, "A canopy model of mean winds through urban areas," *Quarterly Journal of the Royal Meteorological Society*, vol. 130, no. 599, pp. 1349–1372, 2004.

[9] R. Macdonald, "Modelling the mean velocity profile in the urban canopy layer," *Boundary-Layer Meteorol.*, vol. 97, no. 1, pp. 25–45, 2000.

[10] T. Ikeda and P. A. Durbin, "Direct simulations of a rough-wall channel flow," *J. Fluid Mech.*, vol. 571, pp. 235–263, 2007.

[11] J. Cui, V. Patel, C.-l. Lin, and V. Patel, *Large-eddy simulation of turbulent flow over rough surfaces.* Iowa Institute of Hydraulic Research, College of Engineering, University of Iowa, 2000.

[12] S. Leonardi, P. Orlandi, R. Smalley, L. Djenidi, and R. Antonia, "Direct numerical simulations of turbulent channel flow with transverse square bars on one wall," *J. Fluid Mech.*, vol. 491, pp. 229–238, 2003.

BIBLIOGRAPHY

[13] S. Coleman, V. Nikora, S. McLean, and E. Schlicke, "Spatially averaged turbulent flow over square ribs," *Journal of Engineering Mechanics*, vol. 133, no. 2, pp. 194–204, 2007.

[14] J. Woodcock and I. Marusic, "The statistical behaviour of attached eddies," *Phys. Fluids*, vol. 27, no. 1, p. 015104, 2015.

[15] A. Townsend, "The structure of turbulent shear flow," *Cambridge UP, Cambridge*, 1976.

[16] H. Cheng and I. P. Castro, "Near wall flow over urban-like roughness," *Boundary-Layer Meteorol.*, vol. 104, no. 2, pp. 229–259, 2002.

[17] D. K. Chapman, "Computatisnal aerodynamics development and outlook," *AIAA journal*, vol. 17, no. 12, pp. 1293–1313, 1979.

[18] U. Piomelli, "Wall-layer models for large-eddy simulations," *Progress in aerospace sciences*, vol. 44, no. 6, pp. 437–446, 2008.

[19] U. Piomelli and E. Balaras, "Wall-layer models for large-eddy simulations," *Ann. Rev. Fluid Mech.*, vol. 34, no. 1, pp. 349–374, 2002.

[20] U. Piomelli, J. Ferziger, P. Moin, and J. Kim, "New approximate boundary conditions for large eddy simulations of wall-bounded flows," *Phys. Fluids*, vol. 1, no. 6, pp. 1061–1068, 1989.

BIBLIOGRAPHY

[21] I. Marusic, G. J. Kunkel, and F. Porte-Agel, "Experimental study of wall boundary conditions for large-eddy simulation," *J. Fluid Mech.*, vol. 446, pp. 309–320, 2001.

[22] J. W. Deardorff, "Numerical investigation of neutral and unstable planetary boundary layers," *J. Atmos. Sci.*, vol. 29, no. 1, pp. 91–115, 1972.

[23] C.-H. Moeng, "A large-eddy-simulation model for the study of planetary boundary-layer turbulence," pp. 2052–2062, 1984.

[24] P. J. Mason and D. Thomson, "Stochastic backscatter in large-eddy simulations of boundary layers," *J. Fluid Mech.*, vol. 242, pp. 51–78, 1992.

[25] F. Porté-Agel, C. Meneveau, and M. B. Parlange, "A scale-dependent dynamic model for large-eddy simulation: application to a neutral atmospheric boundary layer," *J. Fluid Mech.*, vol. 415, pp. 261–284, 2000.

[26] E. Bou-Zeid, C. Meneveau, and M. Parlange, "A scale-dependent lagrangian dynamic model for large eddy simulation of complex turbulent flows," *Phys. Fluids*, vol. 17, no. 2, p. 025105, 2005.

[27] W. Anderson and C. Meneveau, "Dynamic roughness model for large-eddy simulation of turbulent flow over multiscale, fractal-like rough surfaces," *J. Fluid Mech.*, vol. 679, pp. 288–314, 2011.

BIBLIOGRAPHY

[28] E. Balaras and C. Benocci, "Subgrid-scale models in finite-difference simulations of complex wall bounded flows," *AGARD CP*, vol. 551, no. 2.1, 1994.

[29] E. Balaras, C. Benocci, and U. Piomelli, "Two-layer approximate boundary conditions for large-eddy simulations," *AIAA journal*, vol. 34, no. 6, pp. 1111–1119, 1996.

[30] A. R. Kerstein, W. T. Ashurst, S. Wunsch, and V. Nilsen, "One-dimensional turbulence: vector formulation and application to free shear flows," *J. Fluid Mech.*, vol. 447, pp. 85–109, 2001.

[31] A. R. Kerstein, "One-dimensional turbulence: model formulation and application to homogeneous turbulence, shear flows, and buoyant stratified flows," *J. Fluid Mech.*, vol. 392, pp. 277–334, 1999.

[32] T. M. Smith and S. Menon, "One-dimensional simulations of freely propagating turbulent premixed flames," *Combustion Science and Technology*, vol. 128, no. 1-6, pp. 99–130, 1997.

[33] P. R. Spalart, "Detached-eddy simulation," *Ann. Rev. Fluid Mech.*, vol. 41, pp. 181–202, 2009.

[34] P. Sagaut, *Large eddy simulation for incompressible flows*. Springer, 2002.

[35] U. Piomelli, E. Balaras, H. Pasinato, K. D. Squires, and P. R. Spalart, "The

inner–outer layer interface in large-eddy simulations with wall-layer models," *Int J Heat Fluid Flow*, vol. 24, no. 4, pp. 538–550, 2003.

[36] G. Elsinga and I. Marusic, "Universal aspects of small-scale motions in turbulence," *J. Fluid Mech.*, vol. 662, pp. 514–539, 2010.

[37] I. Marusic, R. Mathis, and N. Hutchins, "Predictive model for wall-bounded turbulent flow," *Science*, vol. 329, no. 5988, pp. 193–196, 2010.

[38] F. Nicoud, J. Baggett, P. Moin, and W. Cabot, "Large eddy simulation wall-modeling based on suboptimal control theory and linear stochastic estimation," *Phys. Fluids*, vol. 13, no. 10, pp. 2968–2984, 2001.

[39] M. Milano and P. Koumoutsakos, "Neural network modeling for near wall turbulent flow," *J Comput Phys*, vol. 182, no. 1, pp. 1–26, 2002.

[40] S. Bose and P. Moin, "A dynamic slip boundary condition for wall-modeled large-eddy simulation," *Phys. Fluids*, vol. 26, no. 1, p. 015104, 2014.

[41] M. Raupach, R. Antonia, and S. Rajagopalan, "Rough-wall turbulent boundary layers," *Applied Mechanics Reviews*, vol. 44, no. 1, pp. 1–25, 1991.

[42] J. Jiménez, "Turbulent flows over rough walls," *Annu. Rev. Fluid Mech.*, vol. 36, pp. 173–196, 2004.

[43] H. Schlichting, "Boundary-layer theory," 1968.

BIBLIOGRAPHY

[44] M. Raupach and A. S. Thom, "Turbulence in and above plant canopies," *Ann. Rev. Fluid Mech.*, vol. 13, no. 1, pp. 97–129, 1981.

[45] J. Finnigan, "Turbulence in plant canopies," *Ann. Rev. Fluid Mech.*, vol. 32, no. 1, pp. 519–571, 2000.

[46] R. Britter and S. Hanna, "Flow and dispersion in urban areas," *Ann. Rev. Fluid Mech.*, vol. 35, no. 1, pp. 469–496, 2003.

[47] A. Monin, "The atmospheric boundary layer," *Ann. Rev. Fluid Mech.*, vol. 2, no. 1, pp. 225–250, 1970.

[48] J. Counihan, "Adiabatic atmospheric boundary layers: a review and analysis of data from the period 1880–1972," *Atmospheric Environment*, vol. 9, no. 10, pp. 871–905, 1975.

[49] S. Leonardi, B. Cruz Perez, and J. Lucena, "Effect of surface roughness on heat transfer in a turbulent channel flow," in *APS Division of Fluid Dynamics Meeting Abstracts*, vol. 1, 2010.

[50] J. P. Bons, "A review of surface roughness effects in gas turbines," *Journal of Turbomachinery*, vol. 132, no. 2, p. 021004, 2010.

[51] D. G. Bogard, D. L. Schmidt, and M. Tabbita, "Characterization and laboratory simulation of turbine airfoil surface roughness and associated heat transfer," *Journal of Turbomachinery*, vol. 120, no. 2, pp. 337–342, 1998.

[52] J. Boynton, R. Tabibzadeh, and S. Hudson, "Investigation of rotor blade roughness effects on turbine performance," *Journal of Turbomachinery*, vol. 115, no. 3, pp. 614–620, 1993.

[53] G. Tabor and M. Baba-Ahmadi, "Inlet conditions for large eddy simulation: a review," *Computers & Fluids*, vol. 39, no. 4, pp. 553–567, 2010.

[54] K. Kondo, S. Murakami, and A. Mochida, "Generation of velocity fluctuations for inflow boundary condition of LES," *Journal of Wind Engineering and Industrial Aerodynamics*, vol. 67, pp. 51–64, 1997.

[55] A. Smirnov, S. Shi, and I. Celik, "Random flow generation technique for large eddy simulations and particle-dynamics modeling," *Journal of Fluids Engineering*, vol. 123, no. 2, pp. 359–371, 2001.

[56] L. Davidson, "HYBRID LES-RANS: Inlet boundary conditions for flows with recirculation," in *Advances in Hybrid RANS-LES Modelling*. Springer, 2008, pp. 55–66.

[57] P. Druault, S. Lardeau, J.-P. Bonnet, F. Coiffet, J. Delville, E. Lamballais, J.-F. Largeau, and L. Perret, "Generation of three-dimensional turbulent inlet conditions for large-eddy simulation," *AIAA journal*, vol. 42, no. 3, pp. 447–456, 2004.

[58] L. Perret, J. Delville, R. Manceau, and J.-P. Bonnet, "Generation of turbu-

lent inflow conditions for large eddy simulation from stereoscopic piv measurements," *Int J Heat Fluid Flow*, vol. 27, no. 4, pp. 576–584, 2006.

[59] P. S. Johansson and H. I. Andersson, "Generation of inflow data for inhomogeneous turbulence," *Eur. J. Mech. B-Fluid*, vol. 18, no. 5, pp. 371–389, 2004.

[60] L. Di Mare, M. Klein, W. Jones, and J. Janicka, "Synthetic turbulence inflow conditions for large-eddy simulation," *Phys. Fluids*, vol. 18, no. 2, p. 025107, 2006.

[61] M. Klein, A. Sadiki, and J. Janicka, "A digital filter based generation of inflow data for spatially developing direct numerical or large eddy simulations," *J Comput Phys*, vol. 186, no. 2, pp. 652–665, 2003.

[62] Z.-T. Xie and I. P. Castro, "Efficient generation of inflow conditions for large eddy simulation of street-scale flows," *Flow, turbulence and combustion*, vol. 81, no. 3, pp. 449–470, 2008.

[63] N. Jarrin, S. Benhamadouche, D. Laurence, and R. Prosser, "A synthetic-eddy-method for generating inflow conditions for large-eddy simulations," *Int J Heat Fluid Flow*, vol. 27, no. 4, pp. 585–593, 2006.

[64] J. Schlüter, H. Pitsch, and P. Moin, "Large-eddy simulation inflow conditions for coupling with Reynolds-averaged flow solvers," *AIAA journal*, vol. 42, no. 3, pp. 478–484, 2004.

[65] P. Wang, X.-S. Bai, M. Wessman, and J. Klingmann, "Large eddy simulation and experimental studies of a confined turbulent swirling flow," *Phys. Fluids*, vol. 16, no. 9, pp. 3306–3324, 2004.

[66] P. R. Spalart and J. H. Watmuff, "Experimental and numerical study of a turbulent boundary layer with pressure gradients," *J. Fluid Mech.*, vol. 249, pp. 337–371, 1993.

[67] R. J. Stevens, J. Graham, and C. Meneveau, "A concurrent precursor inflow method for large eddy simulations and applications to finite length wind farms," *Renewable energy*, vol. 68, pp. 46–50, 2014.

[68] K. Nozawa and T. Tamura, "Large eddy simulation of the flow around a low-rise building immersed in a rough-wall turbulent boundary layer," *Journal of Wind Engineering and Industrial Aerodynamics*, vol. 90, no. 10, pp. 1151–1162, 2002.

[69] J. Nikuradse, *Laws of flow in rough pipes*. National Advisory Committee for Aeronautics Washington, 1950.

[70] C. F. Colebrook, "Turbulent flow in pipes, with particular reference to the transition region between the smooth and rough pipe laws." *Journal of the ICE*, vol. 11, no. 4, pp. 133–156, 1939.

[71] L. F. Moody, "Friction factors for pipe flow," *Trans. Asme*, vol. 66, no. 8, pp. 671–684, 1944.

BIBLIOGRAPHY

[72] R. Simpson, "A generalized correlation of roughness density effects on the turbulent boundary layer," *AIAA Journal*, vol. 11, no. 2, pp. 242–244, 1973.

[73] E. Napoli, V. Armenio, and M. De Marchis, "The effect of the slope of irregularly distributed roughness elements on turbulent wall-bounded flows," *J. Fluid Mech.*, vol. 613, pp. 385–394, 2008.

[74] M. Schultz and K. Flack, "Turbulent boundary layers on a systematically varied rough wall," *Phys. Fluids*, vol. 21, no. 1, p. 015104, 2009.

[75] K. A. Flack and M. P. Schultz, "Review of hydraulic roughness scales in the fully rough regime," *Journal of Fluids Engineering*, vol. 132, no. 4, p. 041203, 2010.

[76] K. Flack, M. Schultz, and T. Shapiro, "Experimental support for Townsend's Reynolds number similarity hypothesis on rough walls," *Phys. Fluids*, vol. 17, no. 3, p. 035102, 2005.

[77] C. Grimmond and T. R. Oke, "Aerodynamic properties of urban areas derived from analysis of surface form," *Journal of Applied Meteorology*, vol. 38, no. 9, pp. 1262–1292, 1999.

[78] J. F. Barlow and O. Coceal, "A review of urban roughness sublayer turbulence," *Met Office Research and Development–Technical Report*, vol. 1, no. 527, 2009.

BIBLIOGRAPHY

[79] M. Kanda, "Progress in the scale modeling of urban climate: Review," *Theoretical and Applied Climatology*, vol. 84, no. 1-3, pp. 23–33, 2006.

[80] A. J. Arnfield, "Two decades of urban climate research: a review of turbulence, exchanges of energy and water, and the urban heat island," *International Journal of Climatology*, vol. 23, no. 1, pp. 1–26, 2003.

[81] S. Vardoulakis, B. E. Fisher, K. Pericleous, and N. Gonzalez-Flesca, "Modelling air quality in street canyons: a review," *Atmospheric Environment*, vol. 37, no. 2, pp. 155–182, 2003.

[82] H. Lettau, "Note on aerodynamic roughness-parameter estimation on the basis of roughness-element description," *Journal of Applied Meteorology*, vol. 8, no. 5, pp. 828–832, 1969.

[83] J. Counehan, "Wind tunnel determination of the roughness length as a function of the fetch and the roughness density of three-dimensional roughness elements," *Atmospheric Environment*, vol. 5, no. 8, pp. 637–642, 1971.

[84] R. Macdonald, R. Griffiths, and D. Hall, "An improved method for the estimation of surface roughness of obstacle arrays," *Atmospheric Environment*, vol. 32, no. 11, pp. 1857–1864, 1998.

[85] B.-G. Kim, C. Lee, S. Joo, K.-C. Ryu, S. Kim, D. You, and W.-S. Shim,

"Estimation of roughness parameters within sparse urban-like obstacle arrays," *Boundary-Layer Meteorol.*, vol. 139, no. 3, pp. 457–485, 2011.

[86] S. Di Sabatino, E. Solazzo, P. Paradisi, and R. Britter, "A simple model for spatially-averaged wind profiles within and above an urban canopy," *Boundary-Layer Meteorol.*, vol. 127, no. 1, pp. 131–151, 2008.

[87] I. N. Harman and J. J. Finnigan, "A simple unified theory for flow in the canopy and roughness sublayer," *Boundary-Layer Meteorol.*, vol. 123, no. 2, pp. 339–363, 2007.

[88] J. Millward-Hopkins, A. Tomlin, L. Ma, D. Ingham, and M. Pourkashanian, "Estimating aerodynamic parameters of urban-like surfaces with heterogeneous building heights," *Boundary-Layer Meteorol.*, vol. 141, no. 3, pp. 443–465, 2011.

[89] A. J. Smits, B. J. McKeon, and I. Marusic, "High-Reynolds number wall turbulence," *Ann. Rev. Fluid Mech.*, vol. 43, pp. 353–375, 2011.

[90] I. Marusic, J. P. Monty, M. Hultmark, and A. J. Smits, "On the logarithmic region in wall turbulence," *J. Fluid Mech.*, vol. 716, p. R3, 2013.

[91] A. Perry, S. Henbest, and M. Chong, "A theoretical and experimental study of wall turbulence," *J. Fluid Mech.*, vol. 165, pp. 163–199, 1986.

[92] I. Marusic and G. J. Kunkel, "Streamwise turbulence intensity formulation for flat-plate boundary layers," *Phys. Fluids*, vol. 15, no. 8, pp. 2461–2464, 2003.

[93] M. Hultmark, M. Vallikivi, S. Bailey, and A. Smits, "Turbulent pipe flow at extreme Reynolds numbers," *Phys. Rev. Lett.*, vol. 108, no. 9, p. 094501, 2012.

[94] C. Meneveau and I. Marusic, "Generalized logarithmic law for high-order moments in turbulent boundary layers," *J. Fluid Mech.*, vol. 719, p. R1, 2013.

[95] C. de Silva, I. Marusic, J. Woodcock, and C. Meneveau, "Scaling of second-and higher-order structure functions in turbulent boundary layers," *J. Fluid Mech.*, vol. 769, pp. 654–686, 2015.

[96] A. Perry and M. Chong, "On the mechanism of wall turbulence," *J. Fluid Mech.*, vol. 119, pp. 173–217, 1982.

[97] I. Marusic and N. Hutchins, "Study of the log-layer structure in wall turbulence over a very large range of Reynolds number," *Flow Turbul. Combust.*, vol. 81, no. 1-2, pp. 115–130, 2008.

[98] J. Jimenez and S. Hoyas, "Turbulent fluctuations above the buffer layer of wall-bounded flows," *J. Fluid Mech.*, vol. 611, pp. 215–236, 2008.

[99] S. K. Robinson, "Coherent motions in the turbulent boundary layer," *Ann. Rev. Fluid Mech.*, vol. 23, no. 1, pp. 601–639, 1991.

[100] J. Jiménez, "Cascades in wall-bounded turbulence," *Ann. Rev. Fluid Mech.*, vol. 44, no. 1, p. 27, 2011.

BIBLIOGRAPHY

[101] M. Head and P. Bandyopadhyay, "New aspects of turbulent boundary-layer structure," *J. Fluid Mech.*, vol. 107, pp. 297–338, 1981.

[102] R. Adrian, C. Meinhart, and C. Tomkins, "Vortex organization in the outer region of the turbulent boundary layer," *J. Fluid Mech.*, vol. 422, pp. 1–54, 2000.

[103] N. Hutchins, W. Hambleton, and I. Marusic, "Inclined cross-stream stereo particle image velocimetry measurements in turbulent boundary layers," *J. Fluid Mech.*, vol. 541, pp. 21–54, 2005.

[104] X. Wu and P. Moin, "Direct numerical simulation of turbulence in a nominally zero-pressure-gradient flat-plate boundary layer," *J. Fluid Mech.*, vol. 630, pp. 5–41, 2009.

[105] P. Schlatter, Q. Li, R. Örlü, F. Hussain, and D. S. Henningson, "On the near-wall vortical structures at moderate Reynolds numbers," *Eur. J. Mech. B-Fluid*, vol. 48, pp. 75–93, 2014.

[106] A. Grass, R. Stuart, and M. Mansour-Tehrani, "Vortical structures and coherent motion in turbulent flow over smooth and rough boundaries," *Philos. Trans. R. Soc. London, Ser. A*, vol. 336, no. 1640, pp. 35–65, 1991.

[107] K. Christensen and R. J. Adrian, "Statistical evidence of hairpin vortex packets in wall turbulence," *J. Fluid Mech.*, vol. 431, pp. 433–443, 2001.

[108] C. D. Tomkins and R. J. Adrian, "Spanwise structure and scale growth in turbulent boundary layers," *J. Fluid Mech.*, vol. 490, pp. 37–74, 2003.

[109] B. Ganapathisubramani, E. K. Longmire, and I. Marusic, "Characteristics of vortex packets in turbulent boundary layers," *J. Fluid Mech.*, vol. 478, pp. 35–46, 2003.

[110] J. del Álamo, J. Jimenez, P. Zandonade, and R. D. Moser, "Self-similar vortex clusters in the turbulent logarithmic region," *J. Fluid Mech.*, vol. 561, pp. 329–358, 2006.

[111] R. J. Adrian, "Hairpin vortex organization in wall turbulencea)," *Phys. Fluids*, vol. 19, no. 4, p. 041301, 2007.

[112] A. Lozano-Durán and J. Jiménez, "Time-resolved evolution of coherent structures in turbulent channels: characterization of eddies and cascades," *J. Fluid Mech.*, vol. 759, pp. 432–471, 2014.

[113] J. Jimenez, J. C. Del Alamo, and O. Flores, "The large-scale dynamics of near-wall turbulence," *J. Fluid Mech.*, vol. 505, pp. 179–199, 2004.

[114] J. C. Del Alamo, J. Jiménez, P. Zandonade, and R. D. Moser, "Scaling of the energy spectra of turbulent channels," *J. Fluid Mech.*, vol. 500, pp. 135–144, 2004.

[115] J. del Álamo and J. Jimenez, "Linear energy amplification in turbulent channels," *J. Fluid Mech.*, vol. 559, pp. 205–213, 2006.

[116] A. Perry and I. Marusic, "A wall-wake model for the turbulence structure of boundary layers. part 1. extension of the attached eddy hypothesis," *J. Fluid Mech.*, vol. 298, pp. 361–388, 1995.

[117] I. Marusic and A. Perry, "A wall-wake model for the turbulence structure of boundary layers. part 2. further experimental support," *J. Fluid Mech.*, vol. 298, pp. 389–407, 1995.

[118] D. Chung and D. Pullin, "Large-eddy simulation and wall modelling of turbulent channel flow," *J. Fluid Mech.*, vol. 631, pp. 281–309, 2009.

[119] M. Inoue and D. Pullin, "Large-eddy simulation of the zero-pressure-gradient turbulent boundary layer up to Re_θ= O (1012)," *J. Fluid Mech.*, vol. 686, pp. 507–533, 2011.

[120] M. Inoue, D. Pullin, Z. Harun, and I. Marusic, "LES of the adverse-pressure gradient turbulent boundary layer," *Int J Heat Fluid Flow*, vol. 44, pp. 293–300, 2013.

[121] A. Misra and D. I. Pullin, "A vortex-based subgrid stress model for large-eddy simulation," pp. 2443–2454, 1997.

[122] R. L. Panton, *Incompressible flow*. John Wiley & Sons, 2013.

[123] Y. Shi, Z. Xiao, and S. Chen, "Constrained subgrid-scale stress model for large eddy simulation," *Phys. Fluids*, vol. 20, no. 1, p. 011701, 2008.

[124] X. I. A. Yang, J. Sadique, R. Mittal, and C. Meneveau, "Integral wall model for large eddy simulations of wall-bounded turbulent flows," *Phys. Fluids*, vol. 27, no. 2, p. 025112, 2015.

[125] R. H. Shaw and U. Schumann, "Large-eddy simulation of turbulent flow above and within a forest," *Boundary-Layer Meteorol.*, vol. 61, no. 1-2, pp. 47–64, 1992.

[126] S. B. Pope, *Turbulent flows*. Cambridge university press, 2000.

[127] H. Schlichting, *Boundary-layer theory*. McGraw-Hill, 1968.

[128] I. Marusic, J. P. Monty, M. Hultmark, and A. J. Smits, "On the logarithmic region in wall turbulence," *J. Fluid Mech.*, vol. 716, p. R3, 2013.

[129] C. Meneveau, T. S. Lund, and W. H. Cabot, "A lagrangian dynamic subgrid-scale model of turbulence," *J. Fluid Mech.*, vol. 319, pp. 353–385, 1996.

[130] R. Mittal, H. Dong, M. Bozkurttas, F. Najjar, A. Vargas, and A. von Loebbecke, "A versatile sharp interface immersed boundary method for incompressible flows with complex boundaries," *J Comput Phys*, vol. 227, no. 10, pp. 4825–4852, 2008.

[131] M. Calaf, C. Meneveau, and J. Meyers, "Large eddy simulation study of fully developed wind-turbine array boundary layers," *Phys. Fluids*, vol. 22, no. 1, p. 015110, 2010.

[132] M. Calaf, M. B. Parlange, and C. Meneveau, "Large eddy simulation study of scalar transport in fully developed wind-turbine array boundary layers," *Phys. Fluids*, vol. 23, no. 12, p. 126603, 2011.

[133] W. Anderson and C. Meneveau, "A large-eddy simulation model for boundary-layer flow over surfaces with horizontally resolved but vertically unresolved roughness elements," *Boundary-Layer Meteorol.*, vol. 137, no. 3, pp. 397–415, 2010.

[134] W. Anderson, P. Passalacqua, F. Porté-Agel, and C. Meneveau, "Large-eddy simulation of atmospheric boundary-layer flow over fluvial-like landscapes using a dynamic roughness model," *Boundary-Layer Meteorol.*, vol. 144, no. 2, pp. 263–286, 2012.

[135] D. You and P. Moin, "A dynamic global-coefficient subgrid-scale eddy-viscosity model for large-eddy simulation in complex geometries," *Phys. Fluids*, vol. 19, no. 6, p. 065110, 2007.

[136] R. Mittal, H. Dong, M. Bozkurttas, F. Najjar, A. Vargas, and A. von Loebbecke, "A versatile sharp interface immersed boundary method for incompressible flows

with complex boundaries," *J Comput Phys*, vol. 227, no. 10, pp. 4825–4852, 2008.

[137] B. Vreman, B. Geurts, and H. Kuerten, "On the formulation of the dynamic mixed subgrid-scale model," *Phys. Fluids*, vol. 6, no. 12, pp. 4057–4059, 1994.

[138] D. You and P. Moin, "A dynamic global-coefficient subgrid-scale eddy-viscosity model for large-eddy simulation in complex geometries," *Phys. Fluids*, vol. 19, no. 6, p. 065110, 2007.

[139] R. Mittal and G. Iaccarino, "Immersed boundary methods," *Annu. Rev. Fluid Mech.*, vol. 37, pp. 239–261, 2005.

[140] X. I. Yang and C. Meneveau, "Recycling inflow method for simulations of spatially evolving turbulent boundary layers over rough surfaces," *J. Turbul*, vol. 17, no. 1, pp. 75–93, 2015.

[141] X. Wu, "Inflow generation methods for spatially developing turbulence simulation," *Ann. Rev. Fluid Mech.*, vol. 49, no. 1, 2016.

[142] H. Schlichting, K. Gersten, and K. Gersten, *Boundary-layer theory*. Springer Science & Business Media, 2000.

[143] G. Araya, L. Castillo, C. Meneveau, and K. Jansen, "A dynamic multi-scale approach for turbulent inflow boundary conditions in spatially developing flows," *J. Fluid Mech.*, vol. 670, pp. 581–605, 2011.

BIBLIOGRAPHY

[144] W. Anderson and C. Meneveau, "Dynamic roughness model for large-eddy simulation of turbulent flow over multiscale, fractal-like rough surfaces," *J. Fluid Mech.*, vol. 679, pp. 288–314, 2011.

[145] A. E. Perry, W. H. Schofield, and P. N. Joubert, "Rough wall turbulent boundary layers," *J. Fluid Mech.*, vol. 37, no. 02, pp. 383–413, 1969.

[146] I. Tani, "Some equilibrium turbulent boundary layers," *Fluid Dynamics Research*, vol. 1, no. 1, p. 49, 1986.

[147] J. H. Lee, H. J. Sung, and P.-Å. Krogstad, "Direct numerical simulation of the turbulent boundary layer over a cube-roughened wall," *J. Fluid Mech.*, vol. 669, pp. 397–431, 2011.

[148] J. Ahn, J. H. Lee, and H. J. Sung, "Statistics of the turbulent boundary layers over 3d cube-roughened walls," *Int J Heat Fluid Flow*, vol. 44, pp. 394–402, 2013.

[149] I. P. Castro, "Rough-wall boundary layers: mean flow universality," *J. Fluid Mech.*, vol. 585, pp. 469–485, 2007.

[150] M. Schultz, personal communication.

[151] M. Raupach and R. Shaw, "Averaging procedures for flow within vegetation canopies," *Boundary-Layer Meteorol.*, vol. 22, no. 1, pp. 79–90, 1982.

[152] M. Raupach, P. Coppin, and B. Legg, "Experiments on scalar dispersion within a model plant canopy part i: The turbulence structure," *Boundary-Layer Meteorol.*, vol. 35, no. 1-2, pp. 21–52, 1986.

[153] D. Poggi and G. G. Katul, "The effect of canopy roughness density on the constitutive components of the dispersive stresses," *Experiments in Fluids*, vol. 45, no. 1, pp. 111–121, 2008.

[154] O. Coceal, T. G. Thomas, and S. E. Belcher, "Spatial variability of flow statistics within regular building arrays," *Boundary-Layer Meteorol.*, vol. 125, no. 3, pp. 537–552, 2007.

[155] S. Moltchanov, "Dispersive stresses in canopy flows," Ph.D. dissertation, Technion-Israel Institute of Technology, Faculty of Civil and Environmental Engineering, 2013.

[156] J. Hong, J. Katz, C. Meneveau, and M. P. Schultz, "Coherent structures and associated subgrid-scale energy transfer in a rough-wall turbulent channel flow," *J. Fluid Mech.*, vol. 712, pp. 92–128, 2012.

[157] C. Meneveau, T. S. Lund, and W. H. Cabot, "A lagrangian dynamic subgrid-scale model of turbulence," *J. Fluid Mech.*, vol. 319, pp. 353–385, 1996.

[158] R. Smalley, R. Antonia, and L. Djenidi, "Self-preservation of rough-wall tur-

bulent boundary layers," *Eur. J. Mech. B-Fluid*, vol. 20, no. 5, pp. 591–602, 2001.

[159] R. J. Stevens, M. Wilczek, and C. Meneveau, "Large-eddy simulation study of the logarithmic law for second-and higher-order moments in turbulent wall-bounded flow," *J. Fluid Mech.*, vol. 757, pp. 888–907, 2014.

[160] K. Pohlhausen, "On the approximate integration of the differential equations of laminar shear layers," *ZAMM*, vol. 1, 1921.

[161] R. M. Cionco, "A mathematical model for air flow in a vegetative canopy," DTIC Document, Tech. Rep., 1966.

[162] X. I. Yang, J. Sadique, R. Mittal, and C. Meneveau, "Exponential roughness layer and analytical model for turbulent boundary layer flow over rectangular-prism roughness elements," *J. Fluid Mech.*, vol. 789, pp. 127–165, 2016.

[163] A. Vreman, "An eddy-viscosity subgrid-scale model for turbulent shear flow: Algebraic theory and applications," *Phys. Fluids*, vol. 16, no. 10, pp. 3670–3681, 2004.

[164] D. Jiang, W. Jiang, H. Liu, and J. Sun, "Systematic influence of different building spacing, height and layout on mean wind and turbulent characteristics within and over urban building arrays," *Wind and Structures*, vol. 11, no. 4, pp. 275–289, 2008.

BIBLIOGRAPHY

[165] D. Coles, "The law of the wake in the turbulent boundary layer," *J. Fluid Mech.*, vol. 1, no. 02, pp. 191–226, 1956.

[166] M. Raupach, J. Finnigan, and Y. Brunei, "Coherent eddies and turbulence in vegetation canopies: the mixing-layer analogy," *Boundary-Layer Meteorol.*, vol. 78, no. 3-4, pp. 351–382, 1996.

[167] P. Jackson, "On the displacement height in the logarithmic velocity profile," *J. Fluid Mech.*, vol. 111, pp. 15–25, 1981.

[168] J. Santiago, O. Coceal, A. Martilli, and S. Belcher, "Variation of the sectional drag coefficient of a group of buildings with packing density," *Boundary-Layer Meteorol.*, vol. 128, no. 3, pp. 445–457, 2008.

[169] Y. Shao and Y. Yang, "A scheme for drag partition over rough surfaces," *Atmospheric Environment*, vol. 39, no. 38, pp. 7351–7361, 2005.

[170] ——, "A theory for drag partition over rough surfaces," *Journal of Geophysical Research: Earth Surface*, vol. 113, no. F2, 2008.

[171] S. Leonardi, P. Orlandi, and R. Antonia, "Properties of d-and k-type roughness in a turbulent channel flow," *Phys. Fluids*, vol. 19, no. 12, p. 125101, 2007.

[172] R. E. Akins, J. A. Peterka, and J. E. Cermak, "Mean force and moment coefficients for buildings in turbulent boundary layers," *Journal of Wind Engineering and Industrial Aerodynamics*, vol. 2, no. 3, pp. 195–209, 1977.

[173] M. Hussain and B. Lee, "A wind tunnel study of the mean pressure forces acting on large groups of low-rise buildings," *Journal of Wind Engineering and Industrial Aerodynamics*, vol. 6, no. 3, pp. 207–225, 1980.

[174] A. Curley and M. Uddin, "Direct numerical simulation of turbulent flow around a surface mounted cube," *AIAA paper*, no. 3431, 2015.

[175] J. Sadique, Y. X. I. A., C. Meneveau, and R. Mittal, "Aerodynamic properties of rough surfaces with high aspectratio roughness elements effect of aspectratio and arrangements (submitted)," *Boundary-Layer Meteorol.*, 2016.

[176] M. Kanda, R. Moriwaki, and F. Kasamatsu, "Large-eddy simulation of turbulent organized structures within and above explicitly resolved cube arrays," *Boundary-Layer Meteorol.*, vol. 112, no. 2, pp. 343–368, 2004.

[177] S. A. Zaki, A. Hagishima, J. Tanimoto, and N. Ikegaya, "Aerodynamic parameters of urban building arrays with random geometries," *Boundary-Layer Meteorol.*, vol. 138, no. 1, pp. 99–120, 2011.

[178] C. Vanderwel and B. Ganapathisubramani, "Effects of spanwise spacing on large-scale secondary flows in rough-wall turbulent boundary layers," *J. Fluid Mech.*, vol. 774, p. R2, 2015.

[179] M. Placidi and B. Ganapathisubramani, "Investigation of wall-bounded turbu-

lence over sparsely distributed roughness," in *APS Division of Fluid Dynamics Meeting Abstracts*, vol. 1, 2011, p. 7004.

[180] M. Schultz, M. Schatzmann, and B. Leitl, "Effect of roughness inhomogeneities on the development of the urban boundary layer," *Int J. Environ Pollut*, vol. 25, no. 1-4, pp. 105–117, 2005.

[181] T. von Kármán, "Mechanische aehnlichkeit und turbulenz," *Proc. 3. Int. Cong. Appl. Mech*, vol. 1, pp. 79–93, 1930.

[182] L. Prandtl, "Bericht ueber untersuchungen zur ausgebildeten turbulenz." *Z. Angew. Math. Mech.*, vol. 5, pp. 136–139, 1961.

[183] X. I. Yang, I. Marusic, and C. Meneveau, "Moment generating functions and scaling laws in the inertial layer of turbulent wall-bounded flows," *J. Fluid Mech.*, vol. 791, p. R2, 2016.

[184] I. Marusic, "The logarithmic region of wall turbulence: Universality, structure and interactions," in *Proc. 18th Aust. Fluid Mech. Conf.*, 2012.

[185] M. Hultmark, "A theory for the streamwise turbulent fluctuations in high Reynolds number pipe flow," *J. Fluid Mech.*, vol. 707, pp. 575–584, 2012.

[186] G. I. Taylor, "The spectrum of turbulence," in *Proceedings of the Royal Society of London A: Mathematical, Physical and Engineering Sciences*, vol. 164, no. 919. The Royal Society, 1938, pp. 476–490.

[187] N. Hutchins, T. B. Nickels, I. Marusic, and M. Chong, "Hot-wire spatial resolution issues in wall-bounded turbulence," *J. Fluid Mech.*, vol. 635, pp. 103–136, 2009.

[188] C. Meneveau and A. B. Chhabra, "Two-point statistics of multifractal measures," *Physica A*, vol. 164, no. 3, pp. 564–574, 1990.

[189] J. O'Neil and C. Meneveau, "Spatial correlations in turbulence: Predictions from the multifractal formalism and comparison with experiments," *Phys. Fluids*, vol. 5, no. 1, pp. 158–172, 1993.

[190] U. Piomelli, J.-L. Balint, and J. M. Wallace, "On the validity of taylors hypothesis for wall-bounded flows," *Phys. Fluids*, vol. 1, no. 3, pp. 609–611, 1989.

[191] G. L. Brown and A. S. Thomas, "Large structure in a turbulent boundary layer," *Phys. Fluids*, vol. 20, no. 10, pp. S243–S252, 1977.

[192] S. K. Robinson, "Instantaneous velocity profile measurements in a turbulent boundary layer," *Chem. Eng. Commun.*, vol. 43, no. 4-6, pp. 347–369, 1986.

[193] R. Boppe, W. Neu, and H. Shuai, "Large-scale motions in the marine atmospheric surface layer," *Boundary-Layer Meteorol.*, vol. 92, no. 2, pp. 165–183, 1999.

[194] I. Marusic and W. D. Heuer, "Reynolds number invariance of the structure

inclination angle in wall turbulence," *Phys. Rev. Lett.*, vol. 99, no. 11, p. 114504, 2007.

[195] I. Marusic, R. Mathis, and N. Hutchins, "Predictive model for wall-bounded turbulent flow," *Science*, vol. 329, no. 5988, pp. 193–196, 2010.

[196] R. Mathis, N. Hutchins, and I. Marusic, "A predictive inner–outer model for streamwise turbulence statistics in wall-bounded flows," *J. Fluid Mech.*, vol. 681, pp. 537–566, 2011.

[197] I. Marusic, K. Chauhan, V. Kulandaivelu, and N. Hutchins, "Evolution of zero-pressure-gradient boundary layers from different tripping conditions," *J. Fluid Mech.*, vol. 783, pp. 379–411, 2015.

[198] X. I. A. Yang, C. Meneveau, I. Marusic, and L. Biferale, "Extended self-similarity in moment-generating-functions in wall-bounded turbulence at high Reynolds number (submitted)," *Physical Review Fluids*, 2016.

[199] D. Poggi, A. Porporato, L. Ridolfi, J. Albertson, and G. Katul, "The effect of vegetation density on canopy sub-layer turbulence," *Boundary-Layer Meteorol.*, vol. 111, no. 3, pp. 565–587, 2004.

Vita

Xiang Yang was born in Yuyao, Zhejiang, China, 1989. For his undergraduate studies, he attended the Peking University in Beijing, China and graduated with a Bachelor of Science degree in Mechanical Engineering in 2012. He began attending the Johns Hopkins University in 2012 and received a Master of Science in Engineering degree in 2015.